NUREG/CR-3900
BMI-2127
Vol. 4

Long-Term Performance of Materials Used for High-Level Waste Packaging

Annual Report, Year Three
April 1984 - April 1985

Compiled by D. Stahl, N. E. Miller

Battelle's Columbus Laboratories

Prepared for
U.S. Nuclear Regulatory
Commission

NOTICE

This report was prepared as an account of work sponsored by an agency of the United States Government. Neither the United States Government nor any agency thereof, or any of their employees, makes any warranty, expressed or implied, or assumes any legal liability of responsibility for any third party's use, or the results of such use, of any information, apparatus, product or process disclosed in this report, or represents that its use by such third party would not infringe privately owned rights.

NOTICE

Availability of Reference Materials Cited in NRC Publications

Most documents cited in NRC publications will be available from one of the following sources:

1. The NRC Public Document Room, 1717 H Street, N.W.
   Washington, DC 20555
2. The Superintendent of Documents, U.S. Government Printing Office, Post Office Box 37082,
   Washington, DC 20013-7082
3. The National Technical Information Service, Springfield, VA 22161

Although the listing that follows represents the majority of documents cited in NRC publications, it is not intended to be exhaustive.

Referenced documents available for inspection and copying for a fee from the NRC Public Document Room include NRC correspondence and internal NRC memoranda; NRC Office of Inspection and Enforcement bulletins, circulars, information notices, inspection and investigation notices; Licensee Event Reports; vendor reports and correspondence; Commission papers; and applicant and licensee documents and correspondence.

The following documents in the NUREG series are available for purchase from the NRC/GPO Sales Program: formal NRC staff and contractor reports, NRC-sponsored conference proceedings, and NRC booklets and brochures. Also available are Regulatory Guides, NRC regulations in the *Code of Federal Regulations*, and *Nuclear Regulatory Commission Issuances*.

Documents available from the National Technical Information Service include NUREG series reports and technical reports prepared by other federal agencies and reports prepared by the Atomic Energy Commission, forerunner agency to the Nuclear Regulatory Commission.

Documents available from public and special technical libraries include all open literature items, such as books, journal and periodical articles, and transactions. *Federal Register* notices, federal and state legislation, and congressional reports can usually be obtained from these libraries.

Documents such as theses, dissertations, foreign reports and translations, and non-NRC conference proceedings are available for purchase from the organization sponsoring the publication cited.

Single copies of NRC draft reports are available free, to the extent of supply, upon written request to the Division of Technical Information and Document Control, U.S. Nuclear Regulatory Commission, Washington, DC 20555.

Copies of industry codes and standards used in a substantive manner in the NRC regulatory process are maintained at the NRC Library, 7920 Norfolk Avenue, Bethesda, Maryland, and are available there for reference use by the public. Codes and standards are usually copyrighted and may be purchased from the originating organization or, if they are American National Standards, from the American National Standards Institute, 1430 Broadway, New York, NY 10018.

NUREG/CR-3900
BMI-2127
Vol. 4

Long-Term Performance of Materials Used for High-Level Waste Packaging

Annual Report, Year Three
April 1984 - April 1985

Manuscript Completed: June 1985
Date Published: July 1985

Compiled by
D. Stahl, N. E. Miller

Battelle's Columbus Laboratories
505 King Avenue
Columbus, OH 43201-2693

Prepared for
Division of Radiation Programs and Earth Sciences
Office of Nuclear Regulatory Research
U.S. Nuclear Regulatory Commission
Washington, D.C. 20555
NRC FIN B6764
Under Contract No. NRC-04-82-015

CONTRIBUTORS

J. A. Beavers
H. J. Cialone
A. J. Markworth
J. K. McCoy
J. L. Means
S. L. Nicolosi
M. R. Pascucci
S. W. Rust
E. D. Spinosa
N. G. Thompson

ABSTRACT

As part of the Nuclear Regulatory Commission's requirement to assess the Department of Energy's application to construct geologic repositories for high-level radioactive waste, Battelle's Columbus Laboratories is investigating the long-term performance of materials used for high-level waste packages. Waste form experimentation has focused on borosilicate glass, using the reference composition MCC 76-68. An experiment investigated the influence of continuous contact between the glass specimen and the leachate on the results of corrosion studies. It was found that precipitates formed during cooling can affect the results. Other experiments evaluated the influence of crystallization on glass waste-form performance and the influence of organic acid on the waste-form and radionuclide mobility in groundwater. Models were used to analyze glass dissolution, including the reprecipitation of dissolved glass species. The effect of groundwater species on the electrochemistry of steels is being analyzed to evaluate susceptability to pitting and stress-corrosion cracking. Species identified as potential cracking agents are being investigated by slow strain rate experiments. Hydrogen embrittlement studies of steel showed annealed cast steel to be more sensitive to embrittlement. Realistic general and pitting corrosion models are being developed, based on known principles of mass transport and radiolytic production. Mechanical and water-chemistry-related stresses which influence mechanical degradation were evaluated. Groundwater-radiolysis and water-chemistry studies are continuing as part of the integrated system performance task.

This report documents investigations performed during the period April, 1984 to April, 1985.

TABLE OF CONTENTS

	Page
Executive Summary	xxii
1. INTRODUCTION	1-1
1.1 Individual Program Tasks	1-2
1.1.1 Waste Forms	1-2
1.1.1.1 Glass-Dissolution Experiments	1-3
1.1.1.2 Glass-Dissolution Model	1-4
1.1.1.3 Spent Fuel	1-4
1.1.2 Container Materials	1-4
1.1.2.1 External Overpack Corrosion	1-5
1.1.2.2 Hydrogen Embrittlement	1-6
1.1.2.3 Modeling of General Corrosion and Pitting	1-7
1.1.3 Integrated System Performance	1-8
1.2 Overall Program Objectives	1-9
2. WASTE FORMS	2-1
2.1 Glass/Water Contact Experiment	2-1
2.1.1 Procedure	2-1
2.1.2 Results	2-4
2.1.3 Discussion and Conclusions	2-11
2.1.4 Implications for Radionuclide Isolation	2-12
2.2 Glass-Crystallinity Experiment	2-12
2.2.1 Summary of Experimental Results	2-14
2.2.2 Implications for Waste Form Performance	2-16
2.3 Experimental Verification of the Glass Dissolution/Reprecipitation Model	2-16
2.3.1 Experimental Results	2-16
2.3.2 Conclusion	2-22
2.4 Organic Acid Experiment	2-22
2.5 Spent Fuel Experiments	2-23
2.5.1 Leach Testing	2-24
2.5.2 Radionuclide Distribution	2-25

TABLE OF CONTENTS
(Continued)

		Page
2.6	Waste-Form Modeling	2-26
2.6.1	Glass Dissolution/Reprecipitation Modeling	2-26
2.6.2	Inclusion of Water-Chemistry Effects in Glass-Dissolution Modeling	2-36
2.7	Future Work	2-45
2.8	References for Section 2	2-46
3.	CONTAINER MATERIALS	3-1
3.1	Overpack Corrosion	3-1
3.1.1	Potentiodynamic Polarization Studies	3-2
3.1.1.1	Metallurgical Studies	3-4
3.1.1.2	Environmental Studies	3-14
3.1.2	Slow Strain Rate Studies	3-41
3.1.3	Pitting-Kinetics Studies	3-52
3.1.3.1	Exposures of Prepitted Specimens	3-52
3.1.3.2	Electrochemical Pit-Propagation Experiments	3-55
3.1.4	Future Work	3-65
3.2	Hydrogen Embrittlement	3-69
3.2.1	Verification Tests on Cast Steel	3-69
3.2.2	Commercial-Purity Iron	3-72
3.2.2.1	Tensile Properties of Iron	3-75
3.2.2.2	Fracture-Toughness Properties of Iron	3-75
3.2.2.3	Subcritical Crack Growth in Iron	3-79
3.2.3	Future Work	3-79
3.3	Corrosion Correlations	3-79
3.3.1	Analysis of General Corrosion	3-80
3.3.1.1	One Chemical Species, Maximum-Rate Kinetics	3-81

TABLE OF CONTENTS
(Continued)

	Page
3.3.1.2 Two Chemical Species, Maximum-Rate Kinetics	3-84
3.3.1.3 Inclusions of Film-Growth Kinetics	3-89
3.3.2 Analysis of Pitting Corrosion	3-91
3.3.2.1 Pit-Generation Kinetics	3-91
3.3.2.3 Pitting Current	3-97
3.3.3 Future Work	3-103
3.4 Mechanical Degradation Analyses	3-103
3.4.1 Water Chemistry and Temperature	3-105
3.4.2 Radiolysis	3-106
3.4.3 Stresses	3-109
3.4.4 Future Work	3-109
3.5 References for Section 3	3-109
4. Integrated System Performance	4-1
4.1 Water Chemistry	4-1
4.2 Groundwater Radiolysis	4-3
4.2.1 Radiolysis of Alkaline Ferrous Systems	4-4
4.2.2 Mechanism for the Radiolysis of Solutions Containing Chloride	4-8
4.3 Integral Experiments	4-8
4.4 References for Section 4	4-11
5. QUALITY ASSURANCE	5-1
APPENDIX A. GLASS-CRYSTALLINITY EXPERIMENT SAMPLE PREPARATION	A-1
1. INTRODUCTION	A-1
2. LABORATORY PROCEDURE	A-1
3. EXPERIMENTAL RESULTS	A-8
4. STATISTICAL ANALYSIS	A-8
5. CRYSTALLIZATION PATH	A-12
6. CONCLUSIONS	A-14

LIST OF FIGURES

		Page
Figure 2.1.	Schematic representation of method used to isolate glass sample from leachate	2-3
Figure 2.2.	Typical heating and cooling profiles	2-5
Figure 2.3.	Scanning electron micrograph of: (a) unleached glass; (b) glass leached at 90 C and isolated from leachate during cooling; and (c) glass leached at 90 C and cooled in continuous contact with leachate.	2-7
Figure 2.4.	Scanning electron micrographs of: (a) glass leached at 190 C and isolated from leachate during cooling; and (b), (c), and (d) glass leached at 190 C and cooled in continuous contact with leachate.	2-8
Figure 2.5.	Coordinates and levels of central composite design	2-15
Figure 2.6.	pH of leachant after exposure of sample at MCC-1P conditions	2-19
Figure 2.7.	Percent specimen weight loss after exposure to MCC-1P conditions.	2-20
Figure 2.8.	Analyzed concentration of silica in leachant after sample exposure to MCC-1P conditions	2-21
Figure 2.9.	Variation of s and q with τ for $\beta = 0.0$, $r = 0.2$, and for selected values of γ.	2-32
Figure 2.10.	Variation of s and q with τ for $\beta = 0.5$, $r = 0.2$, and for selected values of γ.	2-33
Figure 2.11.	Variation of s and q with τ for $\beta = 1.0$, $r = 0.2$, and for selected values of γ.	2-34
Figure 2.12.	Variation of s and q with τ for $\beta = 0.5$, $r = 0.1$, and for selected values of γ.	2-35
Figure 2.13.	Glass-dissolution rate in pure water as a function of time	2-39
Figure 2.14.	Glass-dissolution rate in synthetic basalt groundwater as a function of time.	2-39

LIST OF FIGURES
(Continued)

		Page
Figure 2.15.	pH as a function of time as glass dissolves in pure water.	2-40
Figure 2.16.	pH as a function of time as glass dissolves in synthetic basalt groundwater	2-40
Figure 2.17.	pH as a function of silicon concentration as glass dissolves in pure water.	2-41
Figure 2.18.	Silicon concentration as a function of pH as glass dissolves in pure water.	2-41
Figure 2.19.	Silicon concentration at saturation as a function of instantaneous silicon concentration as glass dissolves in pure water.	2-42
Figure 2.20.	Silicon concentration as a function of time as glass dissolves in pure water.	2-42
Figure 2.21.	pH as a function of silicon concentration as glass dissolves in synthetic basalt groundwater. .	2-43
Figure 2.22.	Silicon concentration at saturation as a function of pH as glass dissolves in synthetic basalt groundwater.	2-43
Figure 2.23.	Silicon concentration at saturation as a function of instantaneous silicon concentration as glass dissolves in synthetic basalt groundwater.	2-44
Figure 2.24.	Silicon concentration as a function of time as glass dissolves in synthetic basalt groundwater. .	2-44
Figure 3.1.	Schematic of typical anodic potentiodynamic polarization curves.	3-3
Figure 3.2.	Potentiodynamic polarization curve for cast, doped BCL steel in basalt groundwater at 90 C polarized with a scan rate of 0.6 V/hr	3-7
Figure 3.3.	Potentiodynamic polarization curve for clean wrought BCL steel in basalt groundwater at 90 C polarized with a scan rate of 0.6 V/hr	3-8

LIST OF FIGURES
(Continued)

		Page
Figure 3.4.	Potentiodynamic polarization curve for Specimen 1 for Ferrovac E in basalt groundwater at 90 C polarized with a scan rate of 0.6 V/hr	3-10
Figure 3.5.	Potentiodynamic polarization curve for Specimen 2 of Ferrovac E in basalt groundwater at 90 C polarized with a scan rate of 0.6 V/hr	3-11
Figure 3.6.	Optical photographs of Ferrovac E Specimen 1 following potentiodynamic polarization testing in deaerated 1X basalt groundwater at 90 C	3-12
Figure 3.7.	Optical photographs of Ferrovac E Specimen 2 following potentiodynamic polarization testing in deaerated 1X basalt groundwater at 90 C	3-13
Figure 3.8.	Electrochemical potential parameters taken from potentiodynamic polarization curves for wrought doped BCL steel and clean cast BCL steel in deaerated simulated basalt groundwater at 90 C.	3-15
Figure 3.9.	Current parameters taken from potentiodynamic polarization curves for wrought doped BCL steel and clean cast BCL steel in deaerated simulated basalt groundwater at 90 C	3-16
Figure 3.10.	Effect of scan rate on the polarization behavior of cast doped BCL steel in deaerated basalt groundwater at 90 C.	3-18
Figure 3.11.	Effect of scan rate on the polarization behavior of clean wrought BCL steel in deaerated basalt groundwater at 90 C.	3-19
Figure 3.12.	Potentiodynamic polarization curve for the wrought doped BCL steel in basalt groundwater at 250 C with a scan rate of 0.6 V/hr.	3-21
Figure 3.13.	Optical photograph of metallographic section of hot-rolled 1020 carbon steel specimen which was tested in 0.001 M $FeCl_3$ at 315 C and a strain rate of 1×10^{-8}/s.	3-45

LIST OF FIGURES
(Continued)

		Page
Figure 3.14.	Optical photograph of metallographic section of hot rolled 1020 carbon steel specimen which was tested in 0.0005 M $FeCl_3$ at 315 C and a strain rate of 1 x 10^{-7}/s.	3-47
Figure 3.15.	Effect of temperature on the maximum depth of cracking in slow strain rate specimens of hot-rolled 1020 carbon steel tested in 5 x 10^{-4} M $FeCl_3$ at a strain rate of 1 x 10^{-7} sec^{-1}	3-48
Figure 3.16.	Effect of temperature on the cracking velocity in slow strain rate specimens of hot-rolled 1020 carbon steel tested in 5 x 10^{-4} M $FeCl_3$ at a strain rate of 1 x 10^{-7} sec^{-1}	3-49
Figure 3.17.	Optical photograph of metallographic section of hot-rolled 1020 carbon steel specimen which was tested in 0.005 M $FeCl_3$ at 175 C and a strain rate of 1 x 10^{-7}/sec.	3-50
Figure 3.18.	Higher power optical photograph of one of the pits shown in Figure 3.17.	3-51
Figure 3.19.	Electrochemical potential as a function of exposure time for mechanically prepitted 1018 carbon steel containing crushed basalt at 90 C.	3-54
Figure 3.20.	Low-power photograph of prepitted hot-rolled 1018 steel specimens following exposure in oxygenated and deaerated simulated basalt groundwater containing crushed basalt at 90 C. . .	3-56
Figure 3.21.	Low-power optical photograph of metallographic section of prepitted (2.54-mm-diameter) specimen of hot-rolled carbon steel following exposure in oxygenated simulated basalt groundwater containing crushed basalt.	3-57
Figure 3.22.	Optical photograph of 2:1 aspect-ratio 0.53-mm-diameter pit	3-58
Figure 3.23.	Optical photograph of 5:1 aspect-ratio 0.53-mm-diameter pit	3-58

LIST OF FIGURES
(Continued)

		Page
Figure 3.24.	Higher-power optical photograph of pit shown in Figure 3.22	3-59
Figure 3.25.	Higher-power optical photograph of pit shown in Figure 3.23	3-59
Figure 3.26.	Schematic of pit-propagation monitor	3-60
Figure 3.27.	Current density as a function of exposure time for pit propagation experiments performed at aspect ratios of 1:1, 1:5, and 1:10 in aerated 1X basalt groundwater at 75 C.	3-64
Figure 3.28.	Potentiodynamic polarization curve for 1:1 aspect ratio pit in aerated 1X basalt groundwater at 75 C following 1-week exposure; scan rate 0.6 V/hr.	3-66
Figure 3.29.	Potentiodynamimc polarization curve for 1:5 aspect ratio pit in aerated 1X basalt groundwater at 75 C following 1-week exposure; scan rate 0.6 V/hr.	3-67
Figure 3.30.	Potentiodynamic polarization curve for 1:10 aspect ratio pit in aerated 1X basalt groundwater at 75 C following 1-week exposure; scan rate 0.6 V/hr.	3-68
Figure 3.31.	Transverse section through iron ingot from which tensile specimens were parpared.	3-73
Figure 3.32.	Microstructure of iron ingot in Figure 3.31.	3-73
Figure 3.33.	Photomicrographs of iron ingot showing fine precipitates at grain boundaries and in the matrix	3-74
Figure 3.34.	J-resistance curves for iron specimens	3-78
Figure 3.35.	Calculated rates of general corrosion as a function of time	3-83
Figure 3.36.	Calculated depth of penetration by general corrosion as a function of time.	3-83

LIST OF FIGURES
(Continued)

		Page
Figure 3.37.	Concentration profiles for the oxidizing radiolytic species, as calculated by the one-species model using maximum-rate kinetics for corrosion.	3-86
Figure 3.38.	Concentration profiles for the reducing radiolytic species, as calculated by the two-species model using maximum-rate kinetics for corrosion.	3-86
Figure 3.39.	Concentration profiles for the oxidizing radiolytic species, as calculated by the one-species model using maximum-rate kinetics for corrosion.	3-87
Figure 3.40.	Corrosion rate as a function of time as calculated by the one-species model (solid) and two-species model (dash) using maximum-rate kinetics for corrosion.	3-87
Figure 3.41.	Corrosion depth as a function of time as calculated by the one-species model (solid) and two-species model (dash) using maximum-rate kinetics for corrosion.	3-88
Figure 3.42.	Corrosion rate as a function of time as calculated by the one-species model using the point-defect model for film growth	3-92
Figure 3.43.	Corrosion depth as a function of time as calculated by the one-species model using the point-defect model for film growth	3-92
Figure 3.44.	Concentration profiles for the oxidizing radiolytic species, as calculated by the one-species model using the point-defect model for film growth.	3-93
Figure 3.45.	Variation of pit-generation rate and pit concentration with time, as calculated by the pitting-corrosion model.	3-98
Figure 3.46.	Calculated pit-depth distributions (F vs. H, after Equation 3-20) for m = 2 and selected values of I.	3-99

LIST OF FIGURES
(Continued)

		Page
Figure 3.47.	Calculated pit-depth distributions (F vs. H, after Equation 3-20) for m = 3 and selected values of T.	3-100
Figure 3.48.	Calculated pit-depth distributins (F vs. H, after Equation 3-20) for m = 4 and selected values of T.	3-101
Figure A.1.	Coordinates and levels of central composite design	A-2
Figure A.2.	Photomicrographs of thin sections of RuO_2-doped MCC 76-68.	A-5
Figure A.3.	Photomicrograph of thin sections of RuO_2 doped MCC 76-68.	A-6
Figure A.4.	Typical reflection micrographs from crystallinity experiment (500X).	A-9
Figure A.5.	SEM micrograph and EDX spectrum for condition (-1,-1,-1)	A-15
Figure A.6.	SEM micrograph and EDX spectrum for condition (0,0,0).	A-16
Figure A.7.	SEM micrograph showing crystalline morphologies A to D for condition (1,1,1)	A-17
Figure A.8.	EDX spectra for crystalline morphologies A and B in Figure A.7.	A-18
Figure A.9.	EDX spectra for crystalline morphologies C and D in Figure A.7.	A-19
Figure A.10.	SEM micrograph and EDX spectrum for "native" crystal in MCC 76-68	A-20
Figure A.11.	EDX spectra for bulk glass in untreated MCC 76-68 and specimen treated at (1,1,1) condition. .	A-21

LIST OF TABLES

		Page
Table 2.1.	Glass/water contact experimental matrix	2-2
Table 2.2.	Summary of results of glass-water contact experiments	2-6
Table 2.3.	Analysis of variance (ANOVA) summaries for glass-water contact experiment.	2-6
Table 2.4.	Chemical compositions of glass surface layers determined by energy-dispersive x-ray analysis. . .	2-10
Table 2.5.	Chemical compositions of glass surface layers (0.3 nm) determined by electron spectroscopy for chemical analysis	2-11
Table 2.6.	Coordinates and levels of central composite design.	2-15
Table 2.7.	Silica-dissolution-model experimental matrix. . . .	2-17
Table 2.8.	Results of glass corrosion model experiment	2-18
Table 2.9.	Organic acid test conditions.	2-24
Table 3.1.	Chemical compositions and other data on steels used in the corrosion studies	3-6
Table 3.2.	Summary of results of potentiodynamic polarization tests performed on cast and wrought steels in deaerated basalt groundwater at 90 C and a scan rate of 0.6 V/hr.	3-9
Table 3.3.	Summary of results of potentiodynamic polarization tests performed on doped cast BCL steel and clean wrought steel in deaerated basalt groundwater at 90 C comparing fast scan rate and slow scan rate data	3-20
Table 3.4.	High and low concentrations of species selected for evaluation in the electrochemical experiments .	3-23
Table 3.5.	Concentrations of species in basalt groundwater or in actual or simulated basalt repository environments.	3-24

LIST OF TABLES
(Continued)

		Page
Table 3.6.	Experimentally measured polarization parameters for solution 33 which represented the mid-point concentration of species defined in Table 3.4 (4 replicates, A-D)	3-26
Table 3.7.	Results of statistical analysis indicating the effect of each chemical species on the polarization parameters measured by potentiodynamic polarization.	3-27
Table 3.8.	Summary of results of statistical analysis for the main effects of the chemical species based on a 90-percent or greater probability of significance.	3-28
Table 3.9.	Main effects and interactions selected from screening tests to be examined in main test matrix.	3-30
Table 3.10.	Experimental design developed utilizing COED for main matrix of experiments.	3-31
Table 3.11.	Main effects, intercept terms, and correlation coefficients resulting from statistical analysis of the combined preliminary and main-matrix data. .	3-32
Table 3.12.	Interaction effects resulting from statistical analysis of the combined preliminary and main matrix data	3-33
Table 3.13.	Summary of results of statistical analysis comparing main matrix with preliminary matrix . . .	3-37
Table 3.14.	Two-factor interactions as determined by main matrix analysis (based on 85 percent or greater probability of significance).	3-38
Table 3.15.	Effect of various solutions and slurries containing Fe (III) and/or chloride on cracking at 316 C.	3-43
Table 3.16.	Summary of results of slow strain rate experiments performed on hot-rolled 1020 carbon steel in $FeCl_3$ solutions	3-46
Table 3.17.	pH as a function of exposure time for simulated basalt groundwater solutions in contact with basalt rock and 1018 carbon steel specimens	3-53

LIST OF TABLES
(Continued)

		Page
Table 3.18.	Revised fracture-toughness data for clean and doped steels.	3-71
Table 3.19.	Composition of iron ingot from which specimens were prepared	3-72
Table 3.20.	Tensile properties of iron.	3-76
Table 4.1.	Reactions added to the Rosinger and Dixon mechanism which complement the description of groundwaters containing iron	4-5
Table 4.2.	Fe^{2+} oxidation in radiolysis of an aqueous system containing dissolved oxygen.	4-6
Table 4.3.	Aqueous ferric species present during radiolysis of an aqueous solution containing dissolved oxygen.	4-6
Table 4.4.	Effect of initial dissolved oxygen concentration on radiolytic oxidation of ferrous ions	4-7
Table 4.5.	Reactions to account for interactions between chlorides and radiolytic species.	4-9
Table 4.6.	Rate constants at 298 K for reactions shown in Table 4.5.	4-10
Table 5.1.	Status of NRC waste packaging program QA procedures.	5-2
Table A.1.	Coordinates and levels of central composite design.	A-2
Table A.2.	Additions of RuO_2 suspensions	A-7
Table A.3.	Quantitative microscopy results for treated MCC 76-68 glass (800X).	A-10
Table A.4.	Quantitative microscopy results for reference samples	A-11
Table A.5.	Regression coefficients with their corresponding T-tests and significance probabilities resulting from a stepwise regression of V_C and log (V_C) on full second-order models	A-13

PREVIOUS REPORTS IN SERIES

NUREG/CR-3405, Volume 1: "Long-Term Performance of Materials Used for High-Level Waste Packaging: Annual Report, March 1982-April 1983."

NUREG/CR-3427, Volume 1: "Long-Term Performance of Materials Used for High-Level Waste Packaging: Quarterly Report, April-June 1983."

NUREG/CR-3427, Volume 2: "Long-Term Performance of Materials Used for High-Level Waste Packaging: Quarterly Report, July-September 1983."

NUREG/CR-3427, Volume 3: "Long-Term Performance of Materials Used for High-Level Waste Packaging: Quarterly Report, October-December 1983."

NUREG/CR-3427, Volume 4: "Long-Term Performance of Materials Used for High-Level Waste Packaging: Annual Report, April 1983-April 1984."

NUREG/CR-3900, Volume 1: "Long-Term Performance of Materials Used for High-Level Waste Packaging: Quarterly Report, April-June 1984."

NUREG/CR-3900, Volume 2: "Long-Term Performance of Materials Used for High-Level Waste Packaging: Quarterly Report, July-September 1984."

NUREG/CR-3900, Volume 3: "Long-Term Performance of Materials Used for High-Level Waste Packaging: Quarterly Report, October-December 1984."

EXECUTIVE SUMMARY

The Department of Energy (DOE) is conducting a large program for the disposal of high-level radioactive wastes in deep-mined geologic repositories. The Nuclear Regulatory Commission (NRC), being responsible for regulating high-level radioactive waste disposal, will review DOE's application for the construction and operation of the repositories. To assist in evaluating DOE's application, the NRC's Office of Nuclear Regulatory Research is developing an understanding of the long-term performance of geologic repositories. As part of this effort, Battelle's Columbus Laboratories has been awarded a five-year contract to investigate the long-term performance of materials used for high-level waste packages.

The program is being conducted in three parallel efforts: waste-form studies, container-material studies, and waste-package system studies. This report summarizes the results obtained during the second year of the program.

Waste-Form Studies

The waste-form studies are aimed at describing and modeling those mechanisms that will alter or "age" the waste form during the containment period, and identifying and describing those processes that will influence dissolution of the waste-form after it is exposed to groundwater. During the first three years of the program, the waste-form studies have centered largely on borosilicate glasses.

During the third year, an experiment was conducted to assess the uncertainty associated with glass-corrosion data that results from an experimental difficulty inherent in most waste-form leaching experiments. The effect involves the precipitation of chemical constituents upon the glass specimen during cooling. Results indicate that this phenomenon may have some significance, particularly at higher temperatures.

An analysis of canister cooling rates has indicated that these rates may allow some volume fraction of crystals to be produced by devitrification of the waste form during cooling. An experiment was performed to prepare glass samples with different degrees of devitrification. These samples are planned to be used to evaluate the effect of devitrification on the dissolution of the glass.

The development of a glass-dissolution model began with some simplified assumptions about the rate of glass dissolution. The model is being modified by including phenomena known to affect dissolution processes. Mathematical expressions were added to the model to describe the actual dissolution of the glass by transport of glass species across the glass/groundwater interface, the convective flow of the groundwater, and the reprecipitation of dissolved glass species as a more stable phase than the original glass; the latter point is believed to be very

important in controlling the rate of glass dissolution. The glass-dissolution model studies (along with the water chemistry model) are being used to identify the parameters of groundwater composition that may influence glass dissolution. Experimental data are being collected to verify the modeling studies.

Large quantities of spent fuel will be available for disposal when a repository is ready for operation; thus, data on its performance will be needed by the NRC. An information base on spent fuel as a waste form has been developed to identify available data on the interactions of spent fuel with groundwater. With the aid of this information, an experimental plan was developed to examine spent fuel dissolution under prototypic conditions. Two tests were planned to provide information on the applicability of a solubility-limited release model to the estimation of the long-term release of radionuclides from spent fuel.

Container-Material Studies

The container studies are focused on those processes that can cause degradation of the metallic waste-package overpack. During the second year, studies focused on cast low-carbon steel for use in a basalt environment. The dominant processes identified for degradation of the steel overpack are general corrosion, stress-corrosion cracking, pitting, crevice corrosion, hydrogen attack, and mechanical stress.

In studying external-overpack corrosion, we investigated general corrosion, pitting, crevice corrosion, and stress-corrosion cracking of cast low-carbon steel in anticipated repository environments. Two steel castings with compositions similar to ASTM Standard A216 were cast: one with low sulfur and phosphorus, and the other with sulfur and phosphorus comparable to normal foundry castings. One-half of each casting was hot rolled, resulting in four types of low-carbon steel for testing. These were tested for general corrosion, pitting, crevice corrosion and stress-corrosion cracking in two deaerated solutions (a simulated basalt groundwater and a simulated concentrated (10X) basalt groundwater) at 250 C. These experiments did not identify any corrosion mechanism which would indicate that steel could not be used as a container material.

A comprehensive literature review was conducted to identify chemical species known to have caused stress-corrosion cracking in low-carbon steel in some environments. The basalt repository environment was characterized by data from the literature and by data from our water-chemistry and radiolysis models. The effects of certain species on steels were analyzed by potentiodynamic polarization techniques and were further studied using slow strain rate tests. The studies demonstrated that $FeCl_3$ can cause stress-corrosion cracking of carbon steel at chloride concentrations typical of groundwaters. Also, the results of the polarization experiments and autoclave exposures suggest that pit initiation in low-carbon steels is likely in basalt groundwater. Experiments conducted to determine the potential for hydrogen embrittlement of overpack steel indicate that hydrogen can significantly reduce

the cracking resistance of the steel. This effect is especially evident in specimens that are annealed after casting. The embrittlement of overpack material could be significant to long-term performance in a repository. Thus, more studies are planned which will use welded steel samples to investigate the impact of localized heating on the susceptibility of steel to hydrogen embrittlement.

In the corrosion modeling effort, studies of corrosion correlations were continued in the areas of general corrosion and pitting corrosion of container materials. Efforts were directed toward developing a physically realistic model that would include processes of major importance in a repository environment. The model was applied to specific examples to illustrate the effects caused by varying certain parameters. Studies in pitting corrosion analyzed the propagation of pit-depth distribution based on specific factors and rates of growth.

Integrated System Performance

At the beginning of the second year, the programming of the system computer model was removed from the scope of study by the NRC, with greater emphasis being placed on providing information for a better understanding of the processes involved in waste-package system degradation.

During the third year, emphasis has been placed on water-chemistry studies and the radiolysis of aqueous solutions containing ferric and ferrous species. Calculations were performed using the radiolysis mechanism developed this year for iron. Effort was also directed toward the development of a mechanism for the radiolysis of solutions containing chloride species.

Integral experiments were planned and assembled to provide a means of assessing the relative importance of various combined-effects processes which may affect the long-term performance of nuclear waste packages. These experiments will provide information on the performance of spent fuel waste forms in environments approximating that of a potential repository. They will also provide data which can be used to benchmark the radiolysis and water-chemistry models which are under development.

1. INTRODUCTION: PROJECT OBJECTIVES AND APPROACH

The Waste Policy Act of 1982 delegates to the Department of Energy (DOE) the authority for siting, construction, and operation of deep-mined geologic repositories for the disposal of high-level waste and spent fuel. The Nuclear Regulatory Commission (NRC) has the responsibility to regulate the activities of DOE to assure that the health and safety of the repository workers and of the public are adequately protected. Prior to construction, the DOE will submit a license application to the NRC describing in detail the proposed repository. The DOE has been directed to take a multiple-barrier approach to the isolation of radioactive wastes, with the waste package, the engineered facility, and the natural geohydrologic features of the site being the major barriers. Since NRC's compliance assessment requires the technical capability to understand relevant phenomena and processes relating to the long-term performance of the multiple barriers, the NRC's Office of Nuclear Regulatory Research (RES) has established this waste-package performance program at Battelle's Columbus Laboratories to provide that part of the input to the assessment. As an important aid to this understanding, Battelle is evaluating total system performance to integrate separate effects and improve our understanding of the long-term performance of waste-package materials. This will also assist in identifying and evaluating research needs.

It is generally accepted that after repository closure the dominant mechanism to cause the release of radionuclides from the repository is groundwater transport. Considerable attention has been given to this phenomenon and many processes have been identified that affect groundwater transport. Simplistically, the water must first contact the waste, the radionuclides must be mobilized by the water from the waste, and finally, the radionuclides must be transported by the water from the repository to be accessible to the environment of humans.

The generally accepted approach to minimizing the release is to provide a number of different obstacles or barriers to the dissolution and transport of radionuclides by the groundwater. For a deep-mined repository, the geohydrologic features of the earth itself are expected to be a major barrier to the release of radionuclides. The repository site will be selected to have properties to optimize isolation of the wastes. Of major importance are initial groundwater chemistry that will inhibit dissolution of the radionuclides and water flow rates and pathways that will require very long times (>1000 yr) to reach the accessible environment.

In addition to the natural barrier to radionuclide release offered by the geohydrologic features of the site, engineered features of the repository and of the waste package will provide additional barriers to the release of radionuclides. The repository will be constructed in such a manner as to minimize disturbing the adjacent rock and will attempt to accommodate the thermomechanical effects of the emplaced wastes with a minimum of degration to its geohydrologic properties.

Upon closure, the underground openings and shafts to the surface will be backfilled and sealed to minimize groundwater flow paths.

From early waste-management studies, it has been recognized that the radioactive waste should be in a physically stable and chemically inert form which will resist physical degradation and dissolution by groundwater after disposal. More recently, it has been decided to add more confidence in isolating the waste by packaging the waste in a container that will provide essentially complete containment of the radionuclides through the period of time in which the repository is heated significantly above its ambient temperature by the heat from decaying fission products. After the container is eventually breached by some process, the waste form must remain sufficiently resistant to groundwater attack to provide high retention of the radionuclides and, together with the repository, to control the release of radionuclides for thousands of years.

The waste package is the center of study of this research program. The objective of the study is to provide an improved understanding of the long-term performance of the materials used for the high-level waste package. More specifically, we are identifying those processes that tend to degrade the performance of the waste-package materials, performing experiments to produce data where data are otherwise lacking on material performance, and analytically modeling the processes to utilize the data to better understand how the processes will affect the material's future performance.

1.1 Individual Program Tasks

The program is being conducted in three parallel efforts: waste-form studies, container studies, and integrated waste-package system studies.

1.1.1 Waste Forms

The waste-form studies are aimed at first describing and modeling those mechanisms that will alter or "age" the waste form during the containment period, and second, identifying and describing those processes that will influence waste-form dissolution after it is exposed to groundwater. During the first three years of the program, the waste-form studies have been largely centered on borosilicate glasses for both defense and commercial high-level wastes. These waste forms are similar, with the defense wastes having higher concentrations of iron, aluminum, and zirconium from metallic matrices and claddings, and commercial wastes having higher concentrations of radioactive waste products. Some effort has also been directed toward evaluating spent fuel as a waste form.

The glass-forming agents added to each waste type can be expected to be tailored to optimize the waste-form properties for each type of high-level waste. After the waste forms are produced, particularly during the very long period of time after disposal while sealed in their

container, they will experience processes that will change them. These changes can be detrimental or beneficial. A beneficial change is the decay of most of the fission products in the waste which will greatly reduce the heat output (and temperature) of the waste package, reduce the radiation levels which can affect the dissolution process, and reduce the quantity of radionuclides which must be controlled. Detrimental effects are those that will increase the dissolution rate of the glass and hence increase the release of radionuclides.

One detrimental effect is devitrification of the glass, which can lead both to new phases with increased solubility and to cracking of the glass (which is detrimental because it allows a greater surface area of the glass to be contacted by the groundwater). A model has been developed to predict the degree of devitrification that will occur from thermal effects during the post-fabrication cooling period and the subsequent reheating in the repository after disposal. During the third year, glass specimens were prepared with differing degrees of crystallization and different crystallite sizes. These specimens will be tested in year four to examine the effects of devitrification upon glass dissolution.

Cracking can also be caused by thermal stresses and by mechanical stresses. The latter may occur because of external forces in the adjacent rock being applied to the waste form, because of the density change in the container materials as they corrode, or because of internal forces such as density change from radiation effects. A study of the radiation effects on glass has failed to reveal any new approach to evaluating this phenomenon experimentally. We are largely dependent upon the existing literature which indicates that radiation effects in glass have a small effect on its performance.

1.1.1.1 Glass-Dissolution Experiments

During the second year of the program, experiments were conducted to determine the relative effect of pressure, temperature, solution chemistry, and the ratio of glass surface area to solution volume on the dissolution of samples of borosilicate glass. These experimental efforts have also been valuable to establish many procedures necessary for glass dissolution studies and have formed a base of experience for future experiments.

Glass dissolution experiments begun during year three have three distinct objectives. The first is to evaluate the most common leach-testing procedure to determine whether some types of data from those tests require unique interpretation. The second is to evaluate parameters of groundwater composition that may influence glass dissolution. The last objective of these experiments is to evaluate our analytical model of the glass dissolution process.

1.1.1.2 Glass-Dissolution Model

The development of a glass-dissolution model began with the assumptions that with a high groundwater flow rate, the glass-dissolution rate is the same as the initial glass-dissolution rate in unaltered groundwater, and with a low flow rate the glass-dissolution rate is determined by the equilibrium solubility of the glass. These oversimplified assumptions are being modified by including those phenomena that are known to affect the processes. For example, if precipitation occurs, the solute concentration in the groundwater falls below that of equilibrium with the glass and the glass can continue to dissolve. Next, mathematical expressions were added to the model to describe the actual dissolution of the glass by transport of glass species across the glass/groundwater interface, the convective flow of the groundwater, and the reprecipitation of dissolved glass species as a more stable phase than the original glass. The latter point is believed to be very important in controlling the rate of glass dissolution. As mentioned in the previous section, this aspect of the glass-dissolution model is being investigated by a carefully planned series of experiments.

The glass dissolution modeling effort is playing an increased role in planning the experimental studies for glass dissolution. In addition to the reprecipitation evaluation described above, the glass-dissolution model studies, along with the water chemistry model (described in Section 4.1), will be used to identify the parameters of groundwater composition that may influence glass dissolution. The ultimate goal in all of the above studies is to provide a base of integrated information to be used by the NRC in evaluating the long-term performance of glass waste forms after disposal.

1.1.1.3 Spent Fuel

Spent fuel will be the primary high-level waste form available for disposal when a repository is ready for operation; thus, data on its performance will be needed by the NRC. Beginning in the second year of our program, we began to develop an information base to include spent fuel as a waste form in future studies. The immediate objective of this effort was to identify the data that are available on the interactions of spent fuel with groundwater to develop a plan for future experimental and analytical studies. In the third year, a group of experiments using actual spent fuel specimens was planned and the equipment for the in-cell testing was assembled. These tests will be conducted during years four and five.

1.1.2 Container Materials

The container studies focus on those processes that can cause degradation of the metallic waste package overpack. The objectives are to collect data on the parameters that influence the degradation processes, to identify the controlling parameters, and ultimately to model the degradation processes that determine the long-term performance of the

overpack. The scope of the studies is limited to the materials which are indicated by DOE to be their candidate materials. During the first year of study, a titanium alloy was the candidate material. Beginning in the second year, studies were redirected to cast low-carbon steel for use in a basalt environment.

The dominant processes which have been identified as causing degradation of the steel overpack are general corrosion, stress-corrosion cracking, pitting, crevice corrosion, hydrogen attack, and mechanical stress. These processes may occur individually or in combination. The parameters that affect these processes include chemical composition and physical state of the steel, groundwater composition and flow rate, temperature, radiation intensity, availability of air, lithostatic forces, redox state, alkalinity/acidity, and availability of hydrogen. A study was also completed on the corrosion of the Type 304L stainless steel canister by hot glass.

1.1.2.1 External Overpack Corrosion

The use of low-carbon steel in a wet environment for a long-life container requires that the steel be thick enough to sustain the loss of metal by corrosion without penetration over the period of interest. If general corrosion dominates the process, the rate of general corrosion will determine the necessary wall thickness. If localized attack such as pitting or crevice corrosion occurs, then the rate of the localized attack and the container life must be used to establish the wall thickness. However, if the steel is susceptible to cracking in the anticipated environment, the rate of cracking is so rapid relative to required container life that the corrosion-allowance approach cannot be used to achieve acceptable performance. What is important is the susceptibility of the metal to crack initiation. Cracking may result from stress-corrosion cracking or from reduction in fracture toughness from hydrogen attack.

A large amount of data is available from the literature on the general corrosion of low-carbon steel in a variety of environments. This is also true for pitting attack, and some data are available for crevice corrosion and stress-corrosion cracking. Data are also available for hydrogen effects on wrought steel, but there are essentially none on cast steels. Much of the data on the corrosion of steel are for salt-water environments and shallow soil burial (such as pipe lines), but few data are directly applicable to the environments expected in a repository. With the current interest in cast steel for a long-life waste container, corrosion studies have begun in simulated repository environments at several laboratories.

Our initial experimental approach was to investigate general corrosion, pitting, crevice corrosion, and stress-corrosion cracking in anticipated repository environments. Two steel castings with compositions similar to ASTM Standard A216 were cast: one a "clean" steel, with low sulfur and phosphorus, and the other "doped" with sulfur and phosphorus

comparable to normal foundry castings. One-half of each casting was hot rolled, resulting in four types of low-carbon steel for testing: a wrought and a cast "clean" and "doped" steel. Specimens of these steels were tested for general corrosion, pitting, crevice corrosion and stress-corrosion cracking in two deaerated solutions, a simulated basalt groundwater and a simulated concentrated (10X) basalt groundwater, at 250 C. The concentrated solution was to simulate a solution that could occur from groundwater boiling during the early high temperatures in an unsealed repository. These experiments did not identify any corrosion mechanisms which would indicate that steel could not be used as a corrosion-allowance container material.

Subsequent experimental efforts are being directed at identifying parameters which may cause poor corrosion performance of low-carbon steel, with emphasis on stress-corrosion cracking. A comprehensive literature review has been conducted to identify chemical species known to have caused stress-corrosion cracking in low-carbon steels in some environments. The repository environment is being characterized by data from the literature and by data from our water-chemistry and radiolysis models. Chemical species which have caused stress-corrosion cracking of steel in environments similar to that of the repository are being examined by laboratory experiments. First, electrochemical experiments are being conducted with steel specimens in simulated groundwater containing the chemical species suspected of causing the attack. Data from these experiments will show the steel's relative susceptibility to cracking and the electrochemical conditions under which it is most likely to occur. Those conditions under which the electrochemical tests show that cracking of steel may occur are used for additional slow strain rate tests. These latter experiments give more definitive data on the susceptibility of low-carbon steel to stress-corrosion cracking and the conditions under which it may be expected to occur. Electrochemical studies of pit initiation and propagation are being conducted to provide data for modeling of container pitting.

1.1.2.2 Hydrogen Embrittlement

Cracking of metals can also occur from degraded strength by hydrogen attack. There are essentially no data in the literature on the effects of hydrogen on the properties of cast steels, although there are considerable data on its effects on wrought steels. The initial efforts in our program were made to determine whether cast steels could be expected to react in a manner similar to that of wrought steels to hydrogen attack. If they would react similarly, then the abundant data for wrought steels could be applied to cast steels.

To compare the performance of cast and wrought steels, two castings were prepared as described above. The variation in the sulfur and phosphorous was included because it was suspected that these two elements may play a significant role in hydrogen attack and corrosion. Both cast and wrought samples of the clean and doped steel compositions are available for testing.

The susceptibility of the steels to hydrogen uptake was evaluated by measuring the hydrogen content of samples of each of the four steels in their as-fabricated condition, after exposure to an outgassing procedure, and to a corrosion environment in basalt groundwater. The data showed that cast steel was more susceptible to hydrogen uptake than wrought steel.

The sensitivity of low-carbon steel to hydrogen embrittlement has been evaluated by conducting tensile and fracture-toughness tests in gaseous hydrogen and an inert environment and measuring the extent of degradation of the properties by hydrogen. Tests were conducted on a pure iron as well as steels in the as-fabricated condition and some which were annealed. Some degradation was found in steels in the as-fabricated condition; however, severe degradation was found in steels that were annealed.

1.1.2.3 Modeling of General Corrosion and Pitting

A comprehensive mathematical model is under development for use in understanding the corrosion processes associated with the waste-container materials in a repository environment. The foundation of the model for the general-corrosion process is a set of mass-transport equations which can be used to compute the fluxes of corrosion species to the container surface, taking into account the fact that certain corrosive species may be generated by radiolysis. The model accounts for diffusion and convective flow to transport the species.

Preliminary computations have been performed to test parts of the model. The computations have proven quite successful. Applications of the model are very dependent upon realistic input data. Experiments are planned in a gamma radiation field to provide data on the enhancement of corrosion by radiation. Also, data will be sought on the rate and composition of surface film growth.

Battelle's modeling effort is also being applied to pitting attack, which may be an important mechanism for the ultimate loss of container integrity. The model being developed considers three different aspects of the overall pitting process: pit-initiation kinetics, pit-growth kinetics, and the evolution of the pit-depth distribution. Many investigators have studied the metal-pitting process, and much information is available from the literature. However, few data are available for the waste-package environment in the repository. One series of experiments planned by our experimental and analytic staff is expected to provide data specifically applicable to the pitting model.

The experimental and analytical efforts in the container-materials task are well integrated and are being directed to providing an understanding of the long-term performance of the overpack materials, with emphasis on those processes that can lead to poor performance.

1.1.3 Integrated System Performance

The waste-package system studies interact with the waste-form studies and the container-material studies to provide an improved understanding of the performance of the total waste-package system. During the first year of the program, the major objective of this task was to develop a waste-package system model incorporating all the separate- and multiple-effects models for waste-form and container performance into one computer model. Indeed, at the end of the first year the first-generation system model was developed and operable. At the beginning of the second year, the programming of the system computer model was removed from the scope of study by the NRC, with greater emphasis being placed on providing information for a better understanding of the processes involved in waste-package system degradation.

One aspect of the total system under study is the production of radiolysis products in the groundwater by gamma radiation from the waste. This is of major importance in modeling the corrosion of the container and in planning experiments to determine the effects of radiolysis. The gamma fluxes and energy deposition rates as a function of time in the materials of the waste package and very-near-field basalt environment have been calculated for both commercial high-level waste and spent fuel as gamma sources. These data are being used to calculate the radiolysis products in the groundwater surrounding the waste package. To simplify the calculation, it was initially assumed that the groundwater was pure water. Next, various chemical species, beginning with iron, are being added to the reaction descriptions to be able to apply the analytical method to various groundwater compositions. The output of the radiolysis model calculations provide input to the water-chemistry model, which is a fundamental part of the glass-dissolution model and the general-corrosion model.

A general purpose water-chemistry code, WATEQ, was evaluated for use as a basis for the glass-dissolution model and found not directly applicable, although the WATEQ data set is of value. The water-chemistry model which we initially developed for our use has intentionally been kept simple. Only a limited set of chemical species was included. The set includes the basic water species, the species which dominate most natural groundwaters, and certain species which are assumed to result from the corrosion of iron-based metallic containers and from the dissolution of borosilicate glass. The reactions among the aqueous species are assumed to equilibrate rapidly. Any other reactions are excluded by the choice of species. Input to the model includes temperature, oxidation potential, volume of water, and amounts of each of the elements in solution (including those species from the radiolysis code). The water-chemistry model calculates the concentration and activity of each of the water species. The results are used for the glass-dissolution and corrosion models.

A series of integral experiments was planned during the third year. These experiments are to use samples of real spent fuel with intact

cladding and various degrees of failed claddings exposed to simulated deoxygenated groundwater at 90 C. Selected experiments have spent fuel specimens embedded in packing material or container corrosion products. The water will be pumped over each specimen at a nominal rate of 1 m/yr and collected for analysis of radionuclide content. These tests are performed to identify multiple effects which may affect container and waste form performance and to obtain qualitative data or the release of radionuclides from spent fuel with failed cladding. The experiments will be conducted during the fourth and fifth years of the project.

1.2 Overall Program Objectives

In all the program tasks, the ultimate objective is to develop a base of information to assist the NRC in evaluating the performance of the waste package proposed in DOE's license application. A near-term objective is to provide information to allow the NRC to prepare position papers on the information required of DOE for evaluation of their waste package. Of significance here is identifying sensitive parameters affecting the performance of materials and identifying data requirements.

To achieve the above objectives, the waste-form task is providing information to give a better understanding of the release of radionuclides from the waste form, beginning at the time it is first contacted by groundwater, through the 10,000-year period defined in the draft EPA Standard. This includes an understanding of the probable physiochemical condition of the waste form when it is contacted by groundwater, as well as the parameters of waste-form composition and environmental conditions which will cause changes from its state at the time of disposal. In addition, we are producing experimental data on the parameters that affect dissolution of the waste form, including composition of the groundwater and environmental conditions. The waste-form dissolution process is also being mathematically modeled to allow analysis of the performance of the waste form under specific input conditions.

The information on the performance of the overpack materials relates to the required containment period of 300 to 1000 years. Overpack performance is expected to be most affected by corrosion and hydrogen-attack processes. We are attempting to provide information on the parameters of overpack-material composition, groundwater composition, and environmental conditions that are most significant in these processes. Our preliminary study of the titanium alloy in brine did not reveal any conditions that would cause general corrosion, pitting, crevice corrosion, or stress-corrosion cracking to affect the good performance of the material as claimed in the literature. However, vapor-phase attack was identified; this could degrade the material and should be more thoroughly investigated if the DOE selects the material for use.

Our studies of cast low-carbon steel in a basalt environment are currently focused on the susceptibility of the metal to stress-corrosion cracking under repository conditions, because steel is known to fail by this process in some environments. We are studying the chemical species

and environmental conditions that cause cracking to determine whether this mode of failure is expected under credible repository conditions. Our experimental studies on general and localized corrosion, together with our comprehensive general-corrosion model, will assist in evaluating the corrosion-allowance approach for the use of steel as a long-life container.

Although the development of an integrated waste-package system model is no longer included in the scope of this project, modeling efforts in the integrated system-performance task are contributing significant information to studies of general corrosion and glass dissolution. These studies require knowledge of the amount and kind of chemical species that may be produced by radiolysis of the groundwater near the waste package as a result of gamma radiation from the enclosed waste. To obtain this information, energy deposition and radiolysis codes are used. To determine how these radiolysis products may affect the performance of the canister and waste form, it is necessary to determine their chemical activities. These are calculated by the water-chemistry model, using as input data from experiments and from the groundwater-radiolysis model. The output from the water-chemistry model is the concentration and activity of each chemical species in the groundwater near the waste package. This information is used not only as input to the general-corrosion and glass-dissolution models but also as a point of reference in directing the experimental efforts in corrosion and dissolution. Some effects of radiolysis may be observed in the integral experiments to be conducted during the fourth year of the program. The primary objectives of the integral experiments is to identify combined effects, possibly synergistic in nature, that affect the performance of the overpack and waste form, and to provide some insight into the role of cladding in the release of radionuclides from spent fuel.

2. WASTE FORMS

Waste-form experimentation in this third project year has focused on waste-form glass, using the reference composition MCC 76-68. Four experiments have been conducted: (1) an assessment of the influence of experimental design--specifically, the continuous contact between the glass specimen and the leachate--on the results of static leaching or corrosion at 90 and 190 C; (2) an experimental validation of the dissolution/precipitation degradation model; (3) an evaluation of the influence of crystallization on glass waste-form performance; and (4) an evaluation, initiated at the end of this project year, of the influence of organic acid on waste-form performance and radionuclide mobility in groundwater. Because of the shift in program emphasis toward evaluation of spent fuel as a waste form, these experiments will conclude the glass waste-form work. However, the glass/water contact experiment is the only one completed in this program year; the remaining experiments will be completed in the first half of the fourth year.

The experiments yet to be completed address model verification, organic-acid effects, and glass-crystallinity effects. At the conclusion of these experiments, a topical report will be prepared describing the results of the glass waste-form task.

During the year, a program plan was defined for the initial experiments on spent fuel. This included a series of leaching tests and a determination of the location of radionuclides in spent fuel. Because the emphasis on waste forms has shifted to spent fuel, this plan will be modified early in year four of the program. Concurrently, the matrix for the in-cell integral tests will be modified to reflect this shift.

2.1 Glass/Water Contact Experiment

The objective of this experiment is to assess the uncertainty associated with glass-leaching data that results from an analytical difficulty inherent in static waste-form leaching experiments. The potential problem is precipitation of chemical constituents upon the glass specimen during cooling at the end of the experiment. The MCC-1P and MCC-2P protocols used by most experimenters in this field require that the reaction vessels be cooled to room temperature prior to withdrawing solution and glass specimens for analysis. With these and similar procedures, waste-form constituents whose solubilities are temperature-dependent and that are in solution at elevated temperature may nucleate and precipitate upon the glass specimen during cooling, thereby changing the solution composition and the glass-surface properties from those at the test condition.

2.1.1 Procedure

In this experiment, a number of samples were in continuous contact with the attacking solution during the entire experiment, while other samples were exposed to the solution only during the isothermal treatment time.

The experimental matrix is shown in Table 2.1. In all cases, either MCC-1P or MCC-2P protocols[2.1] were followed, except for separating some of the samples of glass from the simulated basalt water[2.2] during the heating and cooling periods.

Table 2.1. Glass/water contact experimental matrix.

Glass/Water	MCC-1P[b]	MCC-2P[c]
Isothermal[a] contact	XXX	XXXX
Continuous[a] contact	XXX	XXXX
Blank[a]	XXX	XXX

[a] X = Replicate samples
[b] 90 C, S/V = 0.01/mm
[c] 190 C, S/V = 0.01/mm.

To separate glass specimen and water, 120-ml acid digestion bombs (Parr Bomb Model 4748) were modified to accommodate the glass sample at heights approximately 1/3 of the distance from the bottom or 1/3 of the distance from the top. In all cases, the glass samples, cut into 1-cm cubes with a 200 grit diamond saw, were placed between the two perforated TEFLON* discs and all the containers were filled with approximately 60 ml, or half their volume, of simulated basalt water. The volume was adjusted to obtain a surface-to-volume ratio of 0.01/mm at the experimental temperature. Some bombs were inverted during the heating and cooling periods so that the solution contacted the glass only during the isothermal period; the other bombs continuously exposed the glass to that solution. This procedure is represented in Figure 2.1.

*TEFLON is a registered trademark of the DuPont de Nemours Company.

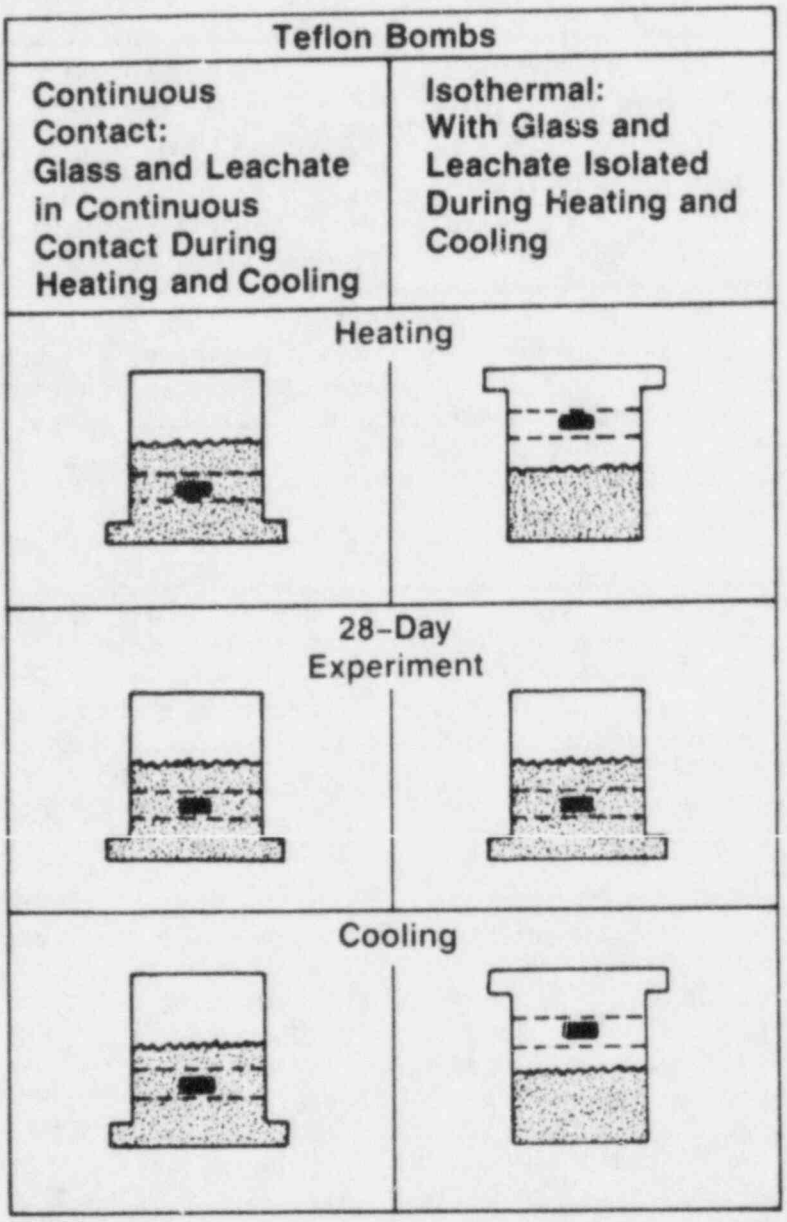

Figure 2.1. Schematic representation of method used to isolate glass sample from leachate.

All containers were placed in two ovens that were maintained at 90 C and 190 C as determined by a calibrated, Type K thermocouple placed in contact with one of the blank containers in each oven. When this thermocouple reached the experimental temperature, the isothermal contact containers were inverted to expose the glass to the basalt water. At the end of the 28-day exposure period, these containers were returned to their original upright position to discontinue contact between the water and the glass samples. They remained in this position for approximately 1 hour to allow evaporation of surface water, then, all bombs were removed and cooled to room temperature. Typical heating and cooling profiles are shown in Figure 2.2.

Once cool, the glass specimens were removed, weighed, and subjected to surface analyses by appropriate methods such as scanning electron microscopy, ESCA, and Auger spectroscopy. After acid digestion, the solution chemistry was determined.

2.1.2 Results

Data on the percent change in weight are shown in Table 2.2. To evaluate the presence of statistically significant differences between continuous-contact samples and isothermal samples, standard analyses of variance (ANOVAs) have been performed on these data. The 90 C and 190 C data are analyzed separately because different variances are expected to be induced by a more aggressive attack at 190 C. A summary of these ANOVAs is presented in Table 2.3. The data at 90 C indicate that for the 28-day tests no effect is present. At 190 C, the weight loss changes show a statistically significant influence of continuous and isothermal contact.

Selected scanning electron micrographs of glass-specimen surfaces are shown in Figures 2.3 and 2.4. Figure 2.3a illustrates an unleached glass sample at 500X, showing the 200 grit grinding striations on the surface. Surfaces of glass samples leached at 90 C are illustrated in Figures 2.3b and 2.3c. The "honeycomb" structure apparent in both results from the leaching of more soluble glass constituents, leaving the less soluble constituents behind. The glass sample in continuous contact with the leachate during cooling (Figure 2.3c) is morphologically very similar to the glass sample isolated from the leachate during cooling (Figure 2.3b), suggesting very minor precipitation of solutes during cooling from 90 C.

The surfaces of glass samples leached at 190 C, illustrated in Figure 2.4, show very different morphological characteristics. The glass cooled in isolation from the leachate (Figure 2.4a) exhibits a "honeycomb" structure similar to those in Figures 2.3b and 2.3c, except that the leached layer appears to be deeper, a result consistent with greater dissolution at the higher temperature. However, glass samples allowed to remain in contact with the leachate during cooling from 190 C

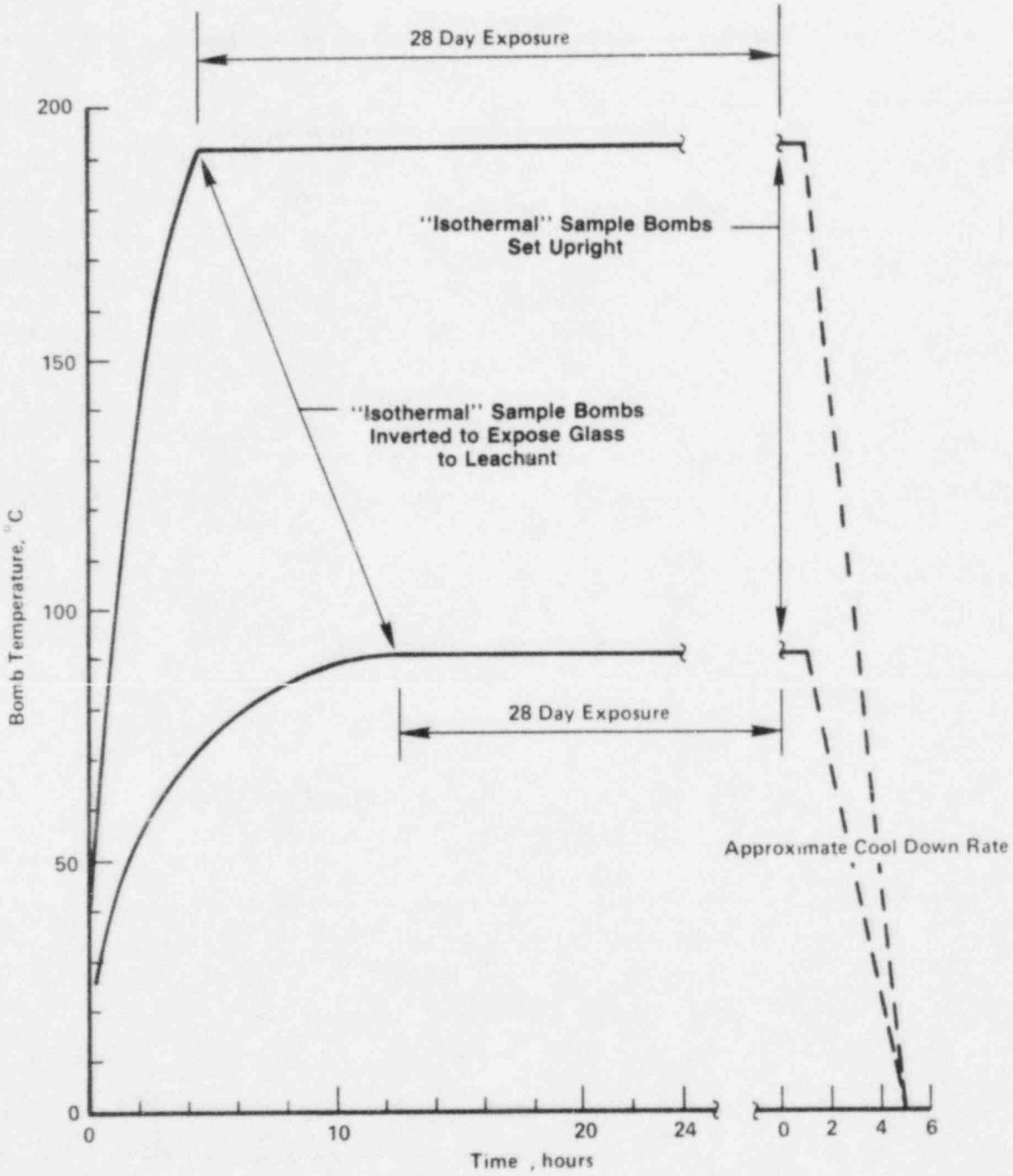

Figure 2.2. Typical heating and cooling profiles.

Table 2.2. Summary of results of glass-water contact experiments.

		Temperature (C)	
		90	190
Continuous Contact	Percent weight change	0.083	1.182
		0.054	1.135
		0.073	1.139
			1.108
	average	0.070	1.141
Isothermal contact	Percent weight change	0.083	1.167
		0.079	1.199
		0.079	1.334
			1.204
	average	0.080	1.226

Table 2.3. Analysis of variance (ANOVA) summaries for glass-water contact experiment.

	Temperature (C)	Calculated F-Statistic	Probability of No Effect
Percent weight change	90	1.441	29.7%
	190	4.552	7.6%

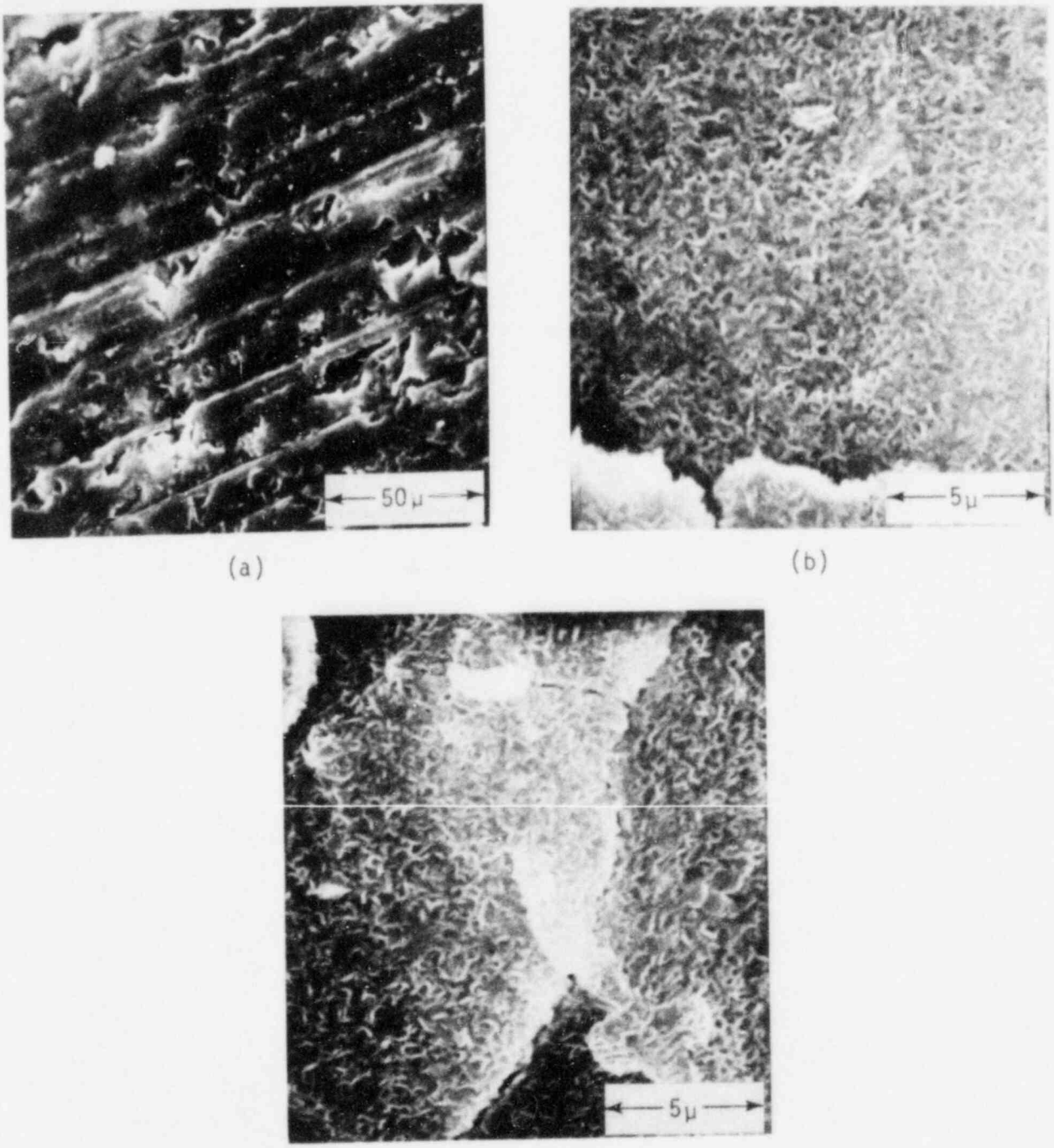

(a) (b)

(c)

Figure 2.3. Scanning electron micrograph of: (a) unleached glass; (b) glass leached at 90 C and isolated from leachate during cooling; and (c) glass leached at 90 C and cooled in continuous contact with leachate.

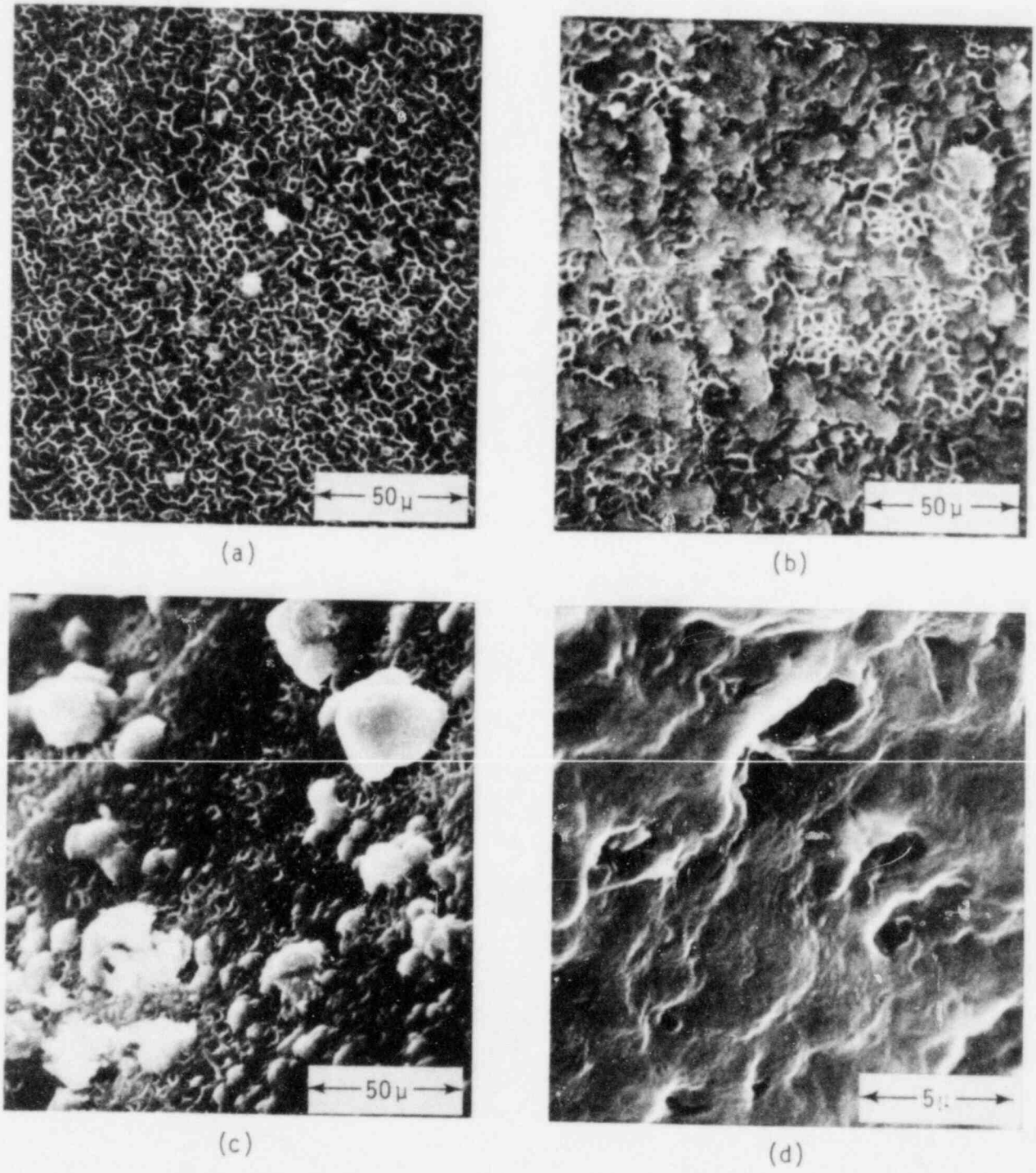

Figure 2.4. Scanning electron micrographs of: (a) glass leached at 190 C and isolated from leachate during cooling; and (b), (c), and (d) glass leached at 190 C and cooled in continuous contact with leachate.

(Figure 2.4b-d) show distinct precipitates on the outer surface of the honeycomb structures. These precipitates apparently formed predominantly during cooling from 190 C to room temperature by the deposition of chemical constituents which were soluble at 190 C but, being insoluble at lower temperature, precipitated onto the glass surface. Figure 2.4b shows nodule-like precipitates covering about 50 percent of the glass surface area. In Figure 2.4c, the honeycomb layer is almost completely covered by a thin film, and large nodules were deposited onto the film. Figure 2.4d shows the film in greater magnificiation with traces of the honeycomb structure showing through, but with most of the structure filled in by the precipitated material.

Leached glass samples have been analyzed by energy-dispersive x-ray analysis (EDAX) and electron spectroscopy for chemical analysis (ESCA). Selected EDAX analyses are reported in Table 2.4. The values are normalized to 100 percent for the five elements listed. Their actual concentrations are lower because other elements are present but are either not detected by EDAX (e.g., oxygen) or are detected in trace or irregular concentrations (e.g., titanium and magnesium). The data discussed in the text are underlined.

Consistent with the SEM data, the EDAX analyses show no significant compositional differences between glasses in continuous contact or isolated from leachates during cooling in the 90 C experiments. Areal scan data on specimens at 190 C show that glasses in continuous contact with leachates are enriched in iron and zinc. Data taken on selected nodules indicate calcium and phosphorus enrichment of glasses in continuous contact with the leachate. All four elements are MCC 76-68 glass constituents, and calcium is also present in the synthetic groundwater. This enrichment is interpreted to be indicative of precipitation of these elements onto the alteration layers during cooling. Note, however, that the 190 C glasses isolated from the leachate are somewhat enriched in zinc (areal acquisition) and calcium and phosphorus (nodule acquisition) relative to unleached controls and glasses leached at 90 C. One interpretation of these observations is that zinc, calcium, and phosphorus concentrate in the alteration layer during the 28-day experiment, and then iron, zinc, calcium, and phosphorus further nucleate and precipitate upon the glass sample during cooling.

ESCA data show similar compositional trends and are reported in Table 2.5. These data include oxygen and do not necessarily add up to 100 percent because several trace elements of little importance, such as nickel and titanium, are not reported. Again, the more significant compositional differences are between samples isolated and in continuous contact with leachates at 190 C. Calcium, phosphorus, and zinc appear to precipitate in the alteration layer during the cooling phase at the conclusion of the experiment. However, these elements are already slightly enriched on glass surfaces that were isolated from leachate during cooling.

Table 2.4. Chemical compositions of glass surface layers determined by energy-dispersive x-ray analysis.

Glass Sample	Relative Weight Percent[a]				
	Si	P	Ca	Fe	Zn
Areal Acquisition Unexposed MCC 76-68	54.6	5.4	6.5	19.6	13.9
Areal Acquisition 90 C Isothermal	36.3	5.0	9.5	27.5	21.7
Areal Acquisition 90 C Continuous Contact	35.4	--	9.3	30.8	24.6
Areal Acquisition 190 C Isothermal	47.7	--	7.8	18.0	27.2
Areal Acquisition 190 C Continuous Contact	23.6	--	5.3	29.3	41.7
Nodule 190 C Isolated	38.6	9.4[b]	12.7	12.3	27.0
Nodule 190 C Continuous Contact	25.3	22.0	27.2	9.4	16.1

(a)Normalized to 100 percent.
(b)Underlined data are discussed in the text.

Table 2.5. Chemical compositions of glass surface layers (0-3 nm) determined by electron spectroscopy for chemical analysis.

Glass Sample	Weight Percent					
	Si	P	Ca	Fe	Zn	O
Unleached Control	20.4	--	2.3	2.9	1.5	67.7
90 C, Isothermal	13.0	--	--	3.6	0.2	82.0
90 C, Continuous Contact	17.5	--	2.0	2.6	2.2	75.5
190 C, Isothermal	17.1	1.7*	2.7	2.7	4.5	67.8
190 C, Continuous Contact	14.9	2.7	3.7	2.1	6.5	69.1

*Underlined data are discussed in the text.

In summary, the films and nodules shown in Figure 2.4b-d that coat the leached honeycomb structure shown in Figure 2.4a are composed primarily of iron and zinc oxides and a $Ca{\cdot}PO_4$ species. They appear to be an artifact produced when the leachate is in contact with the glass specimens during cooling from 190 C. These elements are also enriched in the alteration layer during the 28-day 190 C experiments, and their presence facilitates further nucleation and precipitation during cooling.

2.1.3 Discussion and Conclusions

SEM analyses show that certain elements precipitate in the glass alteration layer upon cooling in 28-day tests at 190 C when glass specimens and leachate are cooled in continuous contact. Precipitates are not observed in the 28-day tests at 90 C. Small nodule-like and flocculated precipitates are commonly observed on glass surfaces exposed to static leachates for a period of time sufficient for saturation to occur[2.3]. However, the precipitates that we report are clearly artifacts of the experimental design because they form during cooling to room temperature at the conclusion of the experiment. These precipitates are comprised of a thin film that coats the "honeycomb" alteration layer and larger nodules that reside on the outer surface of the thin film. EDAX and ESCA analyses indicate that the precipitates are largely composed of the oxides of iron and zinc and of a $Ca{\cdot}PO_4$ compound. The precipitation phenomenon gives rise to a small but statistically significant weight

gain in the affected glasses. Any effect on leachate composition is too small to be discerned analytically.

The results of these experiments are specific to MCC 76-68 simulated waste glass exposed to synthetic basalt groundwater at 90 C and 190 C in 28-day static tests. Longer test durations would be expected to increase the magnitude of the precipitation effect and might permit the phenomenon to be operative at lower temperatures. Low velocity, flow-through experiments may also be susceptible to similar experimental artifacts. Similar effects may be expected for other nuclear waste borosilicate glasses, such as the Defense Waste Reference Glass (DWRG), SRL TDS-131, and SRL-165, which contain varying amounts of iron, zinc, calcium, and/or phosphorus[2.3]. The precipitation effect may have contributed to the irreproducibility of Ca and Zn concentrations in leachates during the study of a precise static leach test for simulated nuclear waste glass materials[2.4].

2.1.4 Implications for Radionuclide Isolation

The precipitation effect may have significant ramifications regarding the behavior of actinides and other radionuclides during static leaching of fully-loaded high-level waste glasses. Calcium phosphates, which are very insoluble[2.5], particularly at alkaline pH, may absorb or coprecipitate uranium, radium, strontium, and other trace elements[2.6-2.9]. Furthermore, iron oxides and oxyhydroxides are strong absorbents for a wide variety of trace elements[2.10]. Artifact precipitates may, therefore, modify the partitioning of radionuclides between the surface layers of glass and their aqueous leachates.

The precipitation phenomenon described herein is of interest in that it may lead to incorrect interpretation of alteration layer morphology and composition and also of leach rates as measured by glass weight loss or leachate composition. The use of the simple experimental approach outlined in Figure 2.1 will minimize the opportunity for their formation. The results of this study suggest that some data from the commonly used leach tests may require special interpretation.

2.2 Glass-Crystallinity Experiment

A detailed analysis of canister cooling rates has indicated that these rates may allow some significant volume fraction of crystals to be produced by devitrification of the waste form[2.11]. A recent report[2.12] indicates that these calculations may overestimate the rate of cooling by approximately 75 percent. In other words, experimentally measured cooling rates are slower than those calculated, further compounding the potential devitrification problem.

Before undertaking a detailed description of this crystallinity, its detrimental character needs to be determined. The work of Hench and Clark[2.13] showed that volume fractions of crystallinity from 35 to 100 percent could reduce the durability of SRL 131-29.8 percent TDS-3A

waste glass to as little as 1/40 of its original durability. They further discussed a mechanism of preferential attack at the glass/crystal interface[2.14]. Therefore two parameters, the volume fraction crystallized and the grain size of the resultant crystals, could influence the corrosion characteristics of devitrified glass. To assess these characteristics, an experiment which exposes two different volume-fractions crystallized at two different crystal sizes was planned. To conduct this experiment, a means of generating those specimens was needed.

Heterogenous nucleation is the best means of fixing crystal sizes and volume fractions under isothermal heat-treatment conditions. The occurrence of RuO_2 as a melt insoluble in MCC 76-68 glass provides an intrinsic nucleation site that should not distort subsequent leaching results. Furthermore, isothermal crystallization experiments by Uhlmann and coworkers[2.15] have shown that time, temperature, and the number of nucleating particles per unit volume determine the volume fraction crystallized.

By choosing different concentrations of nucleating particles, the crystal size may be limited by impingement. For instance, crystal grain diameters of 10 μm and 1 μm should require respective concentrations of 10^6 and 10^9 particles per cubic centimeter. These concentrations can be obtained by mixing commercial RuO_2 with MCC 76-68 in weight ratios of 20 mg RuO_2 per gram of glass and 20 μg per gram of glass, if a 0.2 μm mean diameter is assumed for RuO_2.

The temperature range for developing the samples should be between the glass transition temperature for MCC 76-68 (i.e., T_g = 450 C), a temperature at which crystal growth stops, and the liquidus temperature (T_ℓ = 950 C), the temperature at which growth begins. A temperature range of (T_g + 100 C) $\leq$ T $\leq$ (T_ℓ 00 C) should be an appropriate starting point.

The isothermal treatment time must also be established. The data of Bickford and Jantzen[2.16] indicate that various defense waste compositions will be significantly devitrified if isothermally treated between 4 and 44 hours at temperatures between T_g and T_ℓ for those glasses. Those glasses are somewhat more resistant to devitrification than MCC 76-68 because of their high Al_2O_3 content, so isothermal treatment times of 4 and 44 hours should also suffice for MCC 76-68 glass.

The method of response-surface exploration can be used to develop the time, temperature, and nuclei concentrations that should lead to the required volume-fractions-crystallized and crystal sizes. This method is a statistical design that can be used to find maximum and minimum response conditions without knowledge of exact, functional relationships. For the variables to be explored, a central composite design[2.17] can be used to accommodate quadratic effects in all the variables and should be adequate for the present purposes. This design

is presented pictorially in Figure 2.5; the corresponding coordinates are presented in Table 2.6. As previously discussed, they are based on the following initial values of the experimental variables:

Variable	Low	High
T (C)	550	850
t (hours)	4	44
N_p (#/cc)	10^6	10^9 .

2.2.1 Summary of Experimental Results

The details of the experimental procedures and results are presented in Appendix A. The inclusion of heterogeneous nuclei of RuO_2 in MCC 76-68 glass changes the cause of crystallization. Also, they induce numerous, small crystals in this glass as compared to the untreated MCC 76-68 reference. However, within the ranges of experimental conditions, the influence of temperature, time, and the concentration of nucleation particles, N_p, on the mean crystal diameter is small.

The inclusion of heterogeneous nuclei in MCC 76-68 glass heat treated at temperatures and times comparable to those present during waste form cooling can significantly change the volume fraction of crystals. The ranges of temperature and time explored to date indicate that 5 percent, by volume, of a crystalline phase can be easily produced. The volume fraction crystallized, V_c, is statistically related to T, t, and N_p as follows:

$$\log (V_c) = 0.14 + 0.28\ T - 0.15\ T^2 + 0.22 \log (N_p) + 0.27\ [T \log(N_p)].$$

The lack of a statistically significant time variable likely results from slow growth in the temperature regime explored in this experiment. Furthermore, initial data indicate that changes in crystal morphology and composition are brought about by heterogeneous nucleation onto RuO_2 particles.

The ranges of temperature, time, and RuO_2 concentration that have been explored have not yielded data that can be used to generate specimens with V_c in excess of 5 percent or with two distinctly different crystal sizes. However, a preliminary empirical equation describing crystallization has been developed. Therefore, to improve this equation and, as a result, to produce the specimens needed for leaching/corrosion experiments, this effort should continue.

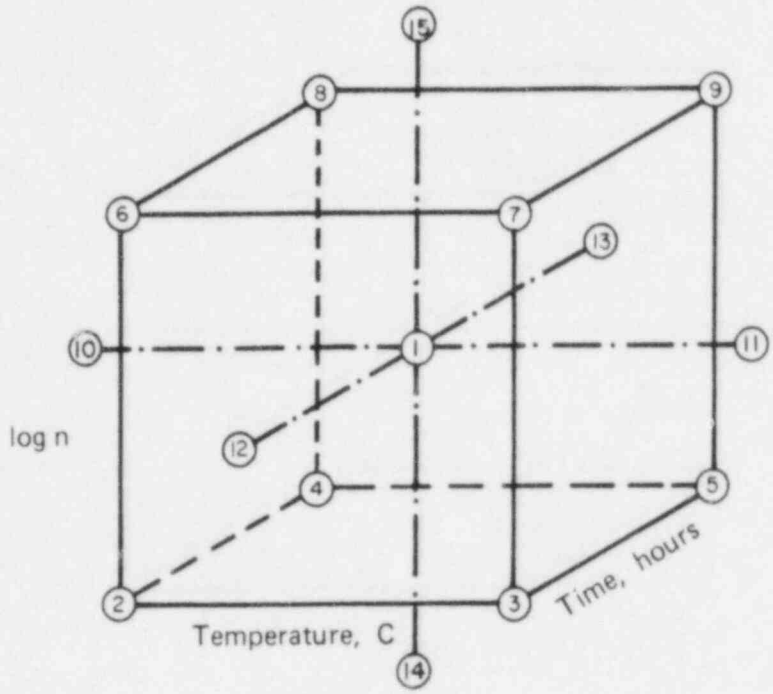

Figure 2.5. Coordinates and levels of central composite design.

Table 2.6. Coordinates and levels of central composite design.

Point	Coordinates	T (C)	t (hours)	log N_p
1	(0,0,0)	700	24	7.5
2	(-1,-1,-1)	610	12	6.6
3	(1,-1,-1)	790	12	6.6
4	(-1,1,-1)	610	36	6.6
5	(1,1,-1)	790	36	6.6
6	(-1,-1,1)	610	12	8.4
7	(1,-1,1)	790	12	8.4
8	(-1,1,1)	610	36	8.4
9	(1,1,1)	790	36	8.4
10	(-1.68,0,0)	550	24	7.5
11	(1.68,0,0)	850	24	7.5
12	(0,-1.68,0)	700	4	7.5
13	(0,1.68,0)	700	44	7.5
14	(0,0,-1.68)	700	24	6
15	(0,0,1.68)	700	24	9

2.2.2 Implications for Waste Form Performance

The striking change in crystal morphology and volume fraction induced by heterogeneous nucleation may have an influence on waste form behavior. These results are especially important because the heterogeneous nuclei used are an intrinsic melt insoluble in MCC 76-68 glass. The empirical relationship developed for V_C indicates a complex behavior between cooling rate and the concentration of heterogeneous nuclei. The form of this equation implies that the slowly cooling, central portion of the waste form may have a significant volume fraction of crystals, perhaps 5 percent or greater.

Radioactive species such as those simulated by lanthanides and molybdenum (i.e., technetium) in MCC 76-68 glass tend to concentrate in these crystals. A combination of high V_C, which could lead to cracking of the waste form, and radionuclides concentrated in soluble crystals could have an impact on radionuclide release to groundwater. Clearly, experimentation that will better define the influence of heterogeneous crystal nucleation and growth is warranted.

2.3 Experimental Verification of the Glass Dissolution/Reprecipitation Model

The dissolution/reprecipitation model interprets the rate of glass waste-form dissolution as being controlled by the dissolution of the least dissolvable glass species into the groundwater and the precipitation of a more stable solid form of that species once its solubility limit, C_o', has been reached. Using the model, the instantaneous concentration of the rate-controlling species, dC/dt, can be expressed as:

$$\frac{dC}{dt} = \left(\frac{S}{V}\right) K (C_o - C) + K' (C_o' - C) \quad . \qquad (2\text{-}1)$$

In this equation, K and K' are the rate constants for glass dissolution and solid precipitation, respectively; C_o is the solubility limit with respect to the glass; and S/V is the ratio of the glass surface area to the volume of solution.

2.3.1 Experimental Results

In an experiment for evaluating this model, specimens of MCC 76-68 glass, crystalline quartz (α-quartz), and amorphous silica (a-SiO_2) have been exposed to reagent-grade water under MCC-1P conditions. The exposure time to date has varied between 1 and 70 days. To ensure the best possible accuracy in measurement of SiO_2 concentration, the experiment has been conducted at 90 C in bombs containing reagent-grade water with cubic specimens 1 cm on a side to maintain a surface-to-volume ratio of 0.01/mm, the MCC-1P condition. Because continuous

glass-water contact is undesirable (refer to Section 2.1), all bombs have been inverted to prevent such contact during heating and cooling. To reach thermal equilibrium, the bombs were placed in the oven for 24 hours before inversion to obtain glass/water contact. To prevent contact on cooling, they were reinverted upon removal from the oven.

The experimental matrix is shown in Table 2.7. The numbers in this table refer to the bombs, numbered 1 to 21. At the end of the 35th day, Bombs 1 to 9 were cleaned and returned to the oven to provide additional samples. In this way, reasonably accurate measures of the dissolution/precipitation curves for MCC 76-68 glass, fused silica, and α-quartz can be obtained.

After treatment, the glass specimens are removed and weighed. The pH of the leachant is measured, and the leachant is treated with high-purity $NaCO_3$ to ensure that all silicon is dissolved. The concentration of monomeric silica in this solution is determined by an ammonium molybdate colorimetric procedure. The results of the analyses are presented in Table 2.8 and Figures 2.6-2.8.

Table 2.7. Silica-dissolution-model experimental matrix.(a)

	Exposure Time, Days											
Sample	1	3	5	8(b)	11	14(b)	21	28(b)	35	42	56	70
MCC 76-68	1	2	3	4	5	6	7	8	9	10	11	12
Fused silica				1		4		7		13	16	19
α-quartz				2		5		8		14	17	20
Blank				3		6		9		15	18	21

(a) Numerals in table are bomb identification numbers.

(b) Bombs 1-9 will be subjected to digestion and cleaning procedures before being returned to the oven on the 49th day. After their return to the oven, Bombs 1-3 will be removed on Day 57, Bombs 4-6 on Day 63, and Bombs 7-9 on Day 77, counting from the beginning of the experiment.

Table 2.8. Results of glass corrosion model experiment.

	MCC 76-68			α-quartz			amorphous SiO_2			blank		
Exposure, days	pH(a)	%ΔW(b)	(SiO_2), ppm	pH(a)	%ΔW(b)	(SiO_2), ppm	pH(a)	%ΔW(b)	(SiO_2), ppm	pH(a)	%ΔW(b)	(SiO_2), ppm
1	8.3	0.0172	9.19	-	-	-	-	-	-	-	-	-
3	8.5	0.0572	18.77	-	-	-	-	-	-	-	-	-
5	8.7	0.0654	22.41	-	-	-	-	-	-	-	-	-
8	8.7	0.1044	33.04	5.415	0.0037	0.54	5.970	-0.0046	0.94	5.935	-	0.37
11	8.8	0.1217	38.90									
14	8.9	0.1128	41.14	5.861	0.0114	0.57	5.910	0.[illegible]45	0.55	5.794	-	0.18
21	9.0	0.1392	46.33									
28	8.9	0.2833	60.50	5.850	0.0075	0.93	5.769	0.0228	2.30	5.790	-	0.48
35	9.0	0.2550	40.74									
42	8.8	0.2319	78.78	5.875	-0.0068	0.89	5.115	-0.0046	1.33	5.425	-	0.075
56	9.0	0.3174	85.92	5.605	-0.0036	0.93	5.725	0.0000	1.89	5.535	-	0.155
70	9.1	0.5183	149.62	5.960	0.0000	1.80	5.840	0.0502	8.72	5.521		0.50

(a)Final pH when reagent water starts: pH = 5.0.

(b)Percent weight change. (+) = loss, (-) = gain.

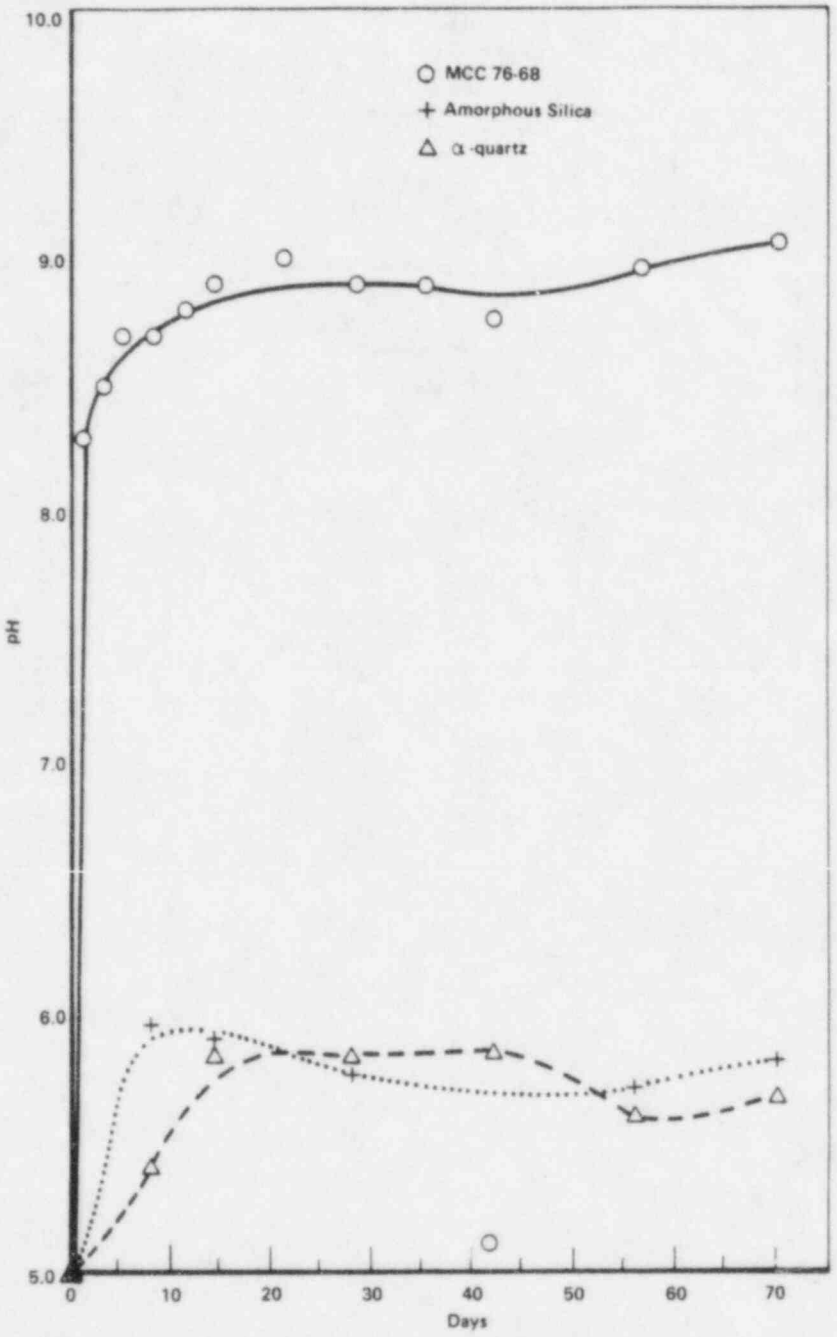

Figure 2.6. pH of leachant after exposure of sample at MCC-1P conditions.

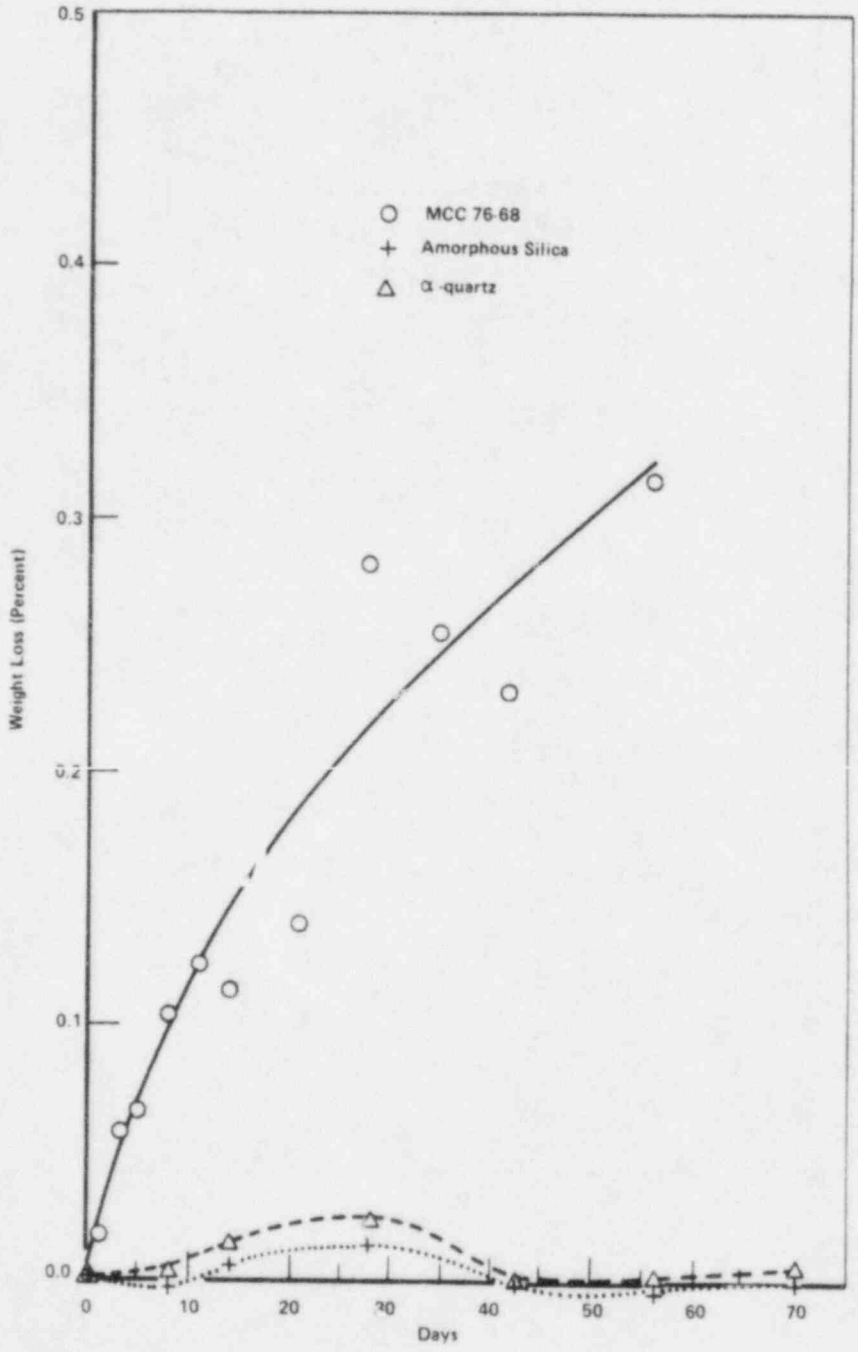

Figure 2.7. Percent specimen weight loss after exposure to MCC-1P conditions.

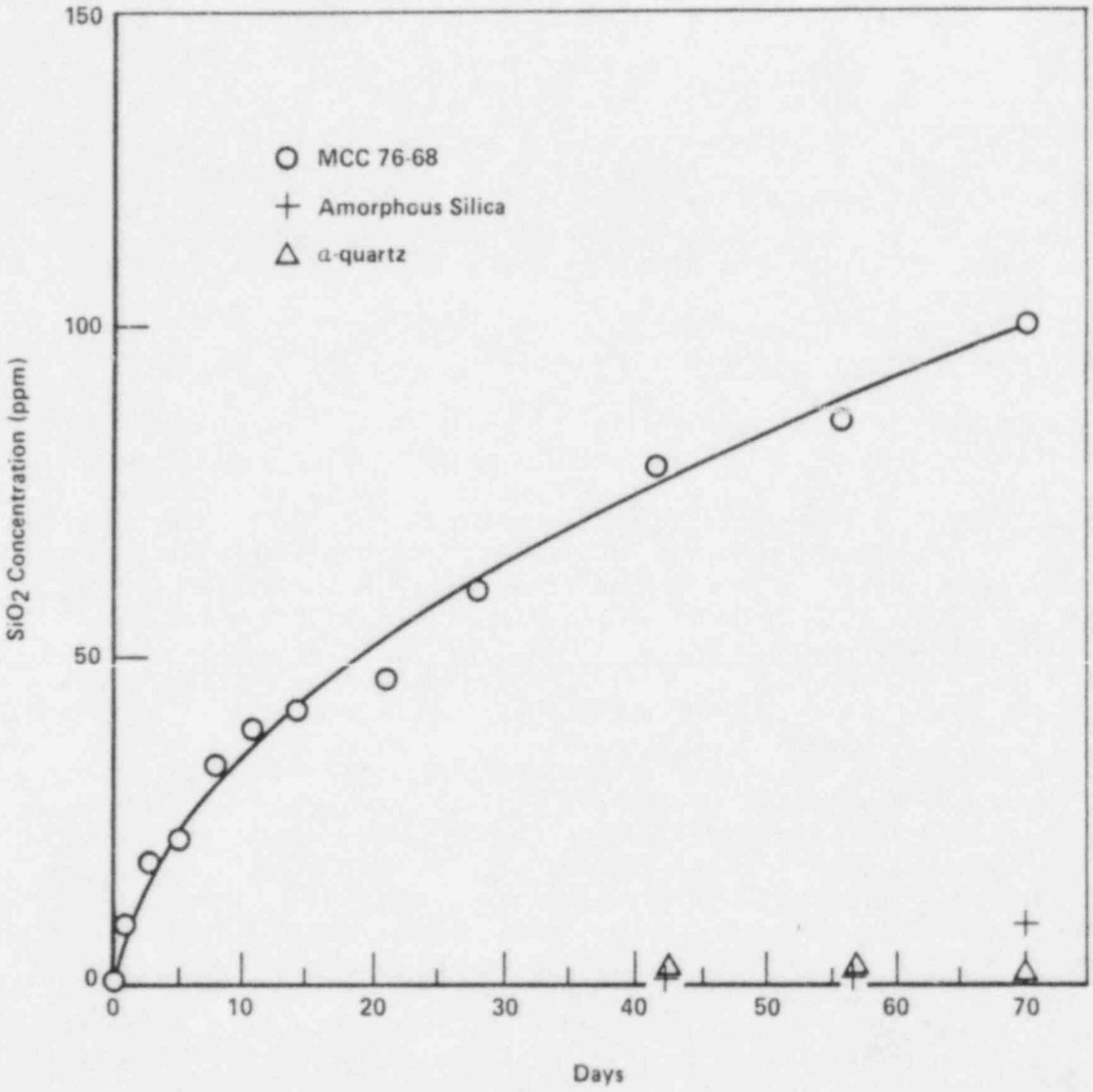

Figure 2.8. Analyzed concentration of silica in leachant after sample exposure to MCC-1P conditions.

As can be seen in Figure 2.6, the pH change is much greater for MCC 76-68 than for either of the silica references. The pH for MCC 76-68 tends toward an equilibrium value of approximately 8.8, while the pH of the reference specimens tends toward an equilibrium value of around 5.6. The data on weight loss and silica concentration, shown in Figures 2.7 and 2.8, respectively, are consistent with these pH data and with each other. However, neither of these latter graphs yet show the peak in silica concentration predicted by the proposed model.

2.3.2 Conclusion

The dissolution/precipitation reactions have not reached dynamic equilibrium after 70 days of exposure. Six more bombs, each containing MCC 76-68 specimens, have been returned to the experiment. These will be removed at 14-28 day intervals starting with the 84th day. As these data become available, the dissolution/precipitation model will be evaluated.

2.4 Organic Acid Experiment

The objective of this experiment is to identify factors that, if operative in a repository environment, may accelerate glass leaching rates. Such factors may include components of the physicochemical composition of the groundwater in contact with the waste package--such as pH, Eh, and the presence of complexing ions such as F^-, Cl^-, and organic acids--as well as processes that may affect glass integrity, such as devitrification. For third-year and early fourth-year testing we have chosen to concentrate on the effects of natural organic acids, which are common groundwater constituents but whose effects on glass leaching have not yet, to our knowledge, been experimentally addressed.

Natural organic acids in deep groundwaters may include compounds with a wide range of compositions. We have chosen to evaluate two species that typify two groups of organic acids frequently encountered in the natural environment: acetic acid and fulvic acid. Acetic acid is one of the principal microbiological breakdown products of numerous natural organic compounds. It occurs widely in oil field waters[2.18] and has recently been identified in deep groundwaters from the Palo Duro Basin, Texas[2.19]--one of the sites recently selected as a potential high-level nuclear-waste repository. Acetic acid was found in concentrations ranging up to 225 mg/liter in Palo Duro groundwaters, along with other short-chain, aliphatic acid anions such as propionate, n- and iso-butyrate, and n-valerate, which were present in concentrations up to 23 mg/liter. In oil-field brines, acetic acid concentrations can range to more than 4,000 mg/liter[2.19]. Humic species form mainly in soils and swamps and occur widely in surface and shallow groundwaters and occasionally in deep groundwaters. For example, fulvic acid, a slightly more oxygenated form of humic acid, has been identified in concentrations ranging up to 20 mg/liter in deep groundwaters from the Finnsjon and Sterno areas of Sweden, both of which are prospective radioactive-waste disposal sites in granitic media[2.20].

Thus, acetic acid and fulvic acid are representative of the types of natural organic compounds that may occur in groundwaters in basaltic lithologies--fulvic acid because soils and associated vegetation are frequently buried by basalt flows, and acetic acid because it is one of the principal breakdown products of more complex organic compounds. Acetic and fulvic acids are also appropriate selections for testing because they represent limiting ranges of metal-complexing capacities for natural organic ligands. Acetic acid is a monodentate ligand with relatively weak metal-complexing capacity, and fulvic acid is a complex polydentate ligand with strong metal-binding characteristics.

The concentrations of organic ligands used in the glass-corrosion experiments are intended to bracket the extremes of their expected concentrations in the actual waste-disposal environment. For acetic acid, concentrations of 200 and 2,000 mg/liter are appropriate. To evaluate possible nonlinearity of concentration influences, the geometric mean of the concentrations was also used--632 mg/liter. Fulvic acid values are an order of magnitude lower in all cases, i.e., 20, 63.2, and 200 mg/liter.

The radiation stabilities of these organic compounds are not clearly understood. Similar organic acids, such as EDTA (ethylenediaminetetra-acetic acid), have been reported to decompose partially when exposed to intense radiation fields and high temperatures[2.21]. However, the present experiments are intended to simulate glass/water interactions after package failure, which is not expected to occur until more than a thousand years after disposal when the radiation field surrounding the waste has diminished significantly.

The test plan, which was initiated late in this program year, is to dope simulated Grande Ronde basalt water with the required concentrations of fulvic acid and acetic acid. This doped water will be used in the modified MCC-1P test (see Section 2.1). Chemical analyses of radioactive simulants released to the leachant and surface analyses will be used to evaluate the influences of these two acids. Table 2.9 is a summary of the test.

Once the MCC-1P exposure period has expired, the samples will be removed and pH and weight changes will be measured. Chemical analyses of the solutions will be directed toward evaluating the capacity of these organic ligands for complexing multivalent cations removed from the glass specimen. In particular, the complexation of molybdenum, which is a simulant for technetium, and actinides will be evaluated.

2.5 Spent Fuel Experiments

Since spent fuel is a likely waste form for emplacement in a repository, activity was initiated last year to characterize the state of knowledge regarding the degradation of cladding and fuel under expected repository conditions. The literature review, completed last year,[2.11] indicated

that much more work needs to be performed in order to understand the leaching/dissolution behavior of irradiated UO_2 fuel under prototypic repository conditions. In addition, some work is needed in understanding localized attack, e.g., stress-corrosion cracking and pitting, on Zircaloy cladding.

Table 2.9. Organic acid test conditions.

Dopant[a]	Dopant Concentration (mg/l)	Purpose	Replicates
None	--	Reference	XX
Acetic Acid	200	Low	XX
	632	Middle	XX
	2000	High	XX
Fulvic Acid	20	Low	XX
	63.2	Middle	XX
	200	High	XX

[a]Added to simulated basalt groundwater.

This year, with the aid of the literature review, we developed an experimental plan to examine spent fuel leaching dissolution under prototypic conditions. As part of that plan, a small effort was devoted to determining the location of radionuclides, including the surface, grain boundaries, and grains, in order to understand the leaching/corrosion data obtained.

2.5.1 Leach Testing

In the evaluation of a licensing application it is likely that some type of solubility-limited dissolution model will be assumed for the long-term release of radionuclides from spent fuel waste forms. This dissolution model may relate the expected solubility-limited dissolution rate of a species such as uranium, as UO_2, with the release of all other radionuclides in ratios determined from analysis of short-term experimental data. Two tests were planned to provide information on the applicability of such a solubility-limited release model to the estimation of the long-term release of radionuclides from spent fuel.

A loop test was planned to investigate the release of radionuclides from spent fuel fragments. These tests would be performed under prototypic repository conditions for temperature, pressure, and groundwater chemistry. During the dissolution process, fluid samples will be withdrawn to provide information on the relative release rates of radionuclides. This experiment was designed to provide information on how the release rates of radionuclides change when the dissolution of the waste form becomes appreciable.

Studies were also planned for the determination of activation energies for the release of radionuclides from spent fuel due to leaching and/or dissolution as a function of time and temperature regime. This would have provided a means for assessing the applicability of high temperature tests to predictions of spent fuel performance at lower temperatures. This information could also provide a means for quantitatively accounting for effects of temperature on the predicted release rates of radionuclides from spent fuel.

To supplement this work, data was to be used from some of the isothermal leach tests reported in the literature. Measured release rates as a function of temperature would be used to determine activation energies for the release of radionuclides as a function of time and temperature regime.

As noted earlier, the emphasis on spent fuel has been increased. As a result of this action, the above plans for leach testing have been revised. The plan now calls for dissolution experiments, utilizing precise redox control, to be performed under prototypic repository conditions.

2.5.2 Radionuclide Distribution

Justification for a model for the long-term release of radionuclides from spent fuel will require information on the microscopic distribution of radionuclides in the fuel material. If the grain boundary and surface inventory is removed during the initial leach period, a case can be made for a solubility-limited long-term radionuclide release model. The actual assessment of such a model, however, would require information on the distributions of radionuclides as well as results of other studies, such as the leach tests described in Section 2.5.1.

After a review of existing literature data, the distribution of radionuclides in residence in grains and grain boundaries will be determined using an electron microprobe. The radial distribution of radionuclides will be determined using an electron microprobe as well as an anastigmatic SIMS apparatus. These distributions will be determined for unleached fuel and fuel which has undergone various degrees of leaching.

2.6 Waste-Form Modeling

During the past year, modeling studies of waste-form degradation were devoted to glass waste forms and entailed two principal subjects: effects of reprecipitation of dissolved glass species on the overall kinetics of glass dissolution, and the infuence of water chemistry on glass dissolution. The results are presented below.

2.6.1 Glass Dissolution/Reprecipitation Modeling

When a glass waste form undergoes dissolution into the groundwater with which it presumably is in contact, it is possible that some of the dissolved species may reprecipitate as more stable minerals, e.g., as layers on surrounding surfaces or as colloids distributed within the water. As a result, the concentration of these dissolved species within the water is reduced, which in turn causes the glass to dissolve to a further extent in an attempt to approach thermodynamic equilibrium with the water. Thus, the overall effect of reprecipitation is to enhance the extent to which glass dissolution takes place. Results of leaching experiments using a simple borosilicate glass have, for example, been so interpreted by Petit and coworkers.[2.22]

In the Annual Report for the second year of this program,[2.23] results were presented of some initial modeling studies relative to the reprecipitation of dissolved glass species as part of a more stable phase. As discussed therein, the simultaneous occurrence of glass dissolution and precipitate growth takes place when $C_o' < C < C_o$. Here, C is the instantaneous, time-dependent concentration, within a closed volume V of groundwater, of the glass component that controls dissolution. C_o' and C_o are the saturation concentrations of this particular species relative to the precipitate and the glass, respectively. Within this regime, the rate at which C changes with time t was taken as

$$\frac{dC}{dt} = \frac{KS}{V} (C_o - C) + K' (C_o' - C) \qquad (2\text{-}2)$$

where K is a rate constant for glass dissolution, S is the surface area of glass exposed to the groundwater, and K' is an effective rate constant for growth of the precipitate.

In the original calculations[2.23], K' was chosen to be time-independent, and the predicted variation of C with t that resulted did indeed exhibit behavior that has been observed experimentally (e.g., nepheline dissolution with gibbsite precipitation, as reviewed by Lasaga[2.24]), i.e.,

- $C\ (t \to \infty) = \text{constant}$
- $C_o' < C\ (t \to \infty) < C_o$.

During the past year, calculations were carried out in which K' was no longer treated as a constant, but rather as an increasing function of time. Such behavior might be expected, for example, for the growth of colloidal particles from solution, which, as they grow, present an increasing amount of surface area to the surrounding ground water and thus are able to transport the dissolved species from solution at faster net rates. On the other hand, treatment of K' as a constant may be more characteristic of growth of the precipitate as layers on adjacent surfaces, for which the amount of exposed area remains approximately constant.

The particular form assumed for K' was

$$K'(t) = a + b\,(t - t_p) \tag{2-3}$$

where a and b are time-independent parameters (but possibly temperature-dependent, although temperature variations are not being considered here), and the time t_p is defined such that

$$C(t_p) = C_o' \quad .$$

Thus, times within the range $t > t_p$ are of interest in solving Equations 2-2 and 2-3. Clearly, the special case for which b = 0 corresponds to that which had been previously treated.(2.23)

Equation 2-3 was cast in linear form for simplicity in accounting for a K' parameter that increases with time, rather than for a physically realistic representation of actual reprecipitation kinetics. Unfortunately, however, even the simple form of Equation 2-3 yields results that are rather complex, as compared to the case for which b = 0.

Proceeding with the analysis, Equations 2-2 and 2-3 can be combined and expressed in terms of dimensionless variables and parameters to yield

$$\frac{ds}{d\xi} + \gamma\xi s = 1 + (\gamma\xi - 1)r \tag{2-4}$$

where

$$s \equiv C/C_o \tag{2-5a}$$

$$r \equiv C_o'/C_o \tag{2-5b}$$

$$\gamma \equiv b\left(\frac{V}{KS}\right)^2 \tag{2-5c}$$

$$\xi \equiv \frac{1+\beta}{\gamma} + \tau - \tau_p \tag{2-5d}$$

with

$$\beta \equiv \frac{aV}{KS} \tag{2-5e}$$

$$\tau \equiv KSt/V \tag{2-5f}$$

$$\tau_p \equiv KSt_p/V \quad . \tag{2-5g}$$

The definitions of s, r, β, τ, and τ_p given here are consistent with those presented in Reference 2.23. The explicit dependence of τ_p upon r is given in Equation 2.20 of that reference.

Equation 2-4 can be easily solved, subject to the initial condition $s(\xi_p) = r$, where $\xi_p \equiv \xi(\tau = \tau_p)$, to yield the rather complex expression

$$s = r + (1 - r)\left(\frac{2}{\gamma}\right)^{1/2}\left\{F\left[\left(\frac{\gamma}{2}\right)^{1/2}\xi\right]\right. \tag{2-6}$$

$$\left. - F\left[\left(\frac{\gamma}{2}\right)^{1/2}\xi_p\right]\exp\left[\frac{\gamma}{2}\left(\xi_p^2 - \xi^2\right)\right]\right\}$$

where F is Dawson's integral, defined in general[2.25] as

$$F(z) = e^{-z^2}\int_0^z e^{u^2}\,du \quad . \tag{2-7}$$

Unfortunately, F(z) is not an elementary function; its values must be computed numerically.

Analysis of the properties of $s(\xi)$ is presented below. However, one particular feature that can readily be deduced is the behavior of s at

asymptotic times, i.e., $\xi \to \infty$. Toward this end, we use a well-known relation[2.25],

$$F(z) = \frac{\pi^{1/2}}{2i} e^{-z^2} \operatorname{erf}(iz) \tag{2-8}$$

together with the asymptotic expansion for the complement of the error function[2.26],

$$\operatorname{erfc}(z) \sim \frac{e^{-z^2}}{z\pi^{1/2}} \left[1 + 0\left(\frac{1}{z^2}\right)\right] . \tag{2-9}$$

Equation 2-9 is valid for $z \to \infty$ and $|\arg(z)| < 3\pi/4$. Noting that $\operatorname{erf}(z) = 1 - \operatorname{erfc}(z)$, one can combine Equations 2-8 and 2-9 to obtain

$$F(z) \sim \frac{\pi^{1/2} e^{-z^2}}{2i} + \frac{1}{2z}\left[1 + 0\left(\frac{1}{z^2}\right)\right] . \tag{2-10}$$

If z is real,

$$F(z) \sim \frac{1}{2z} . \tag{2-11}$$

From Equations 2-6 and 2-11, we obtain

$$s \sim r \tag{2-12}$$

in the limit as $\xi \to \infty$. Consequently, we see from Equations 2-5a, 2-5b, and 2-12 that

$$C \sim C_o' \tag{2-13}$$

as $t \to \infty$. Therefore, as the time becomes asymptotically large, the concentration of the species controlling glass dissolution, within the closed volume of groundwater, gradually approaches the saturation level of that species relative to the precipitate. Of course, such behavior is expected, since from Equation 2-3, K' becomes very large as t

increases. In turn, from Equation 2-2, C must approach C_o' in order to maintain dC/dt at a finite level.

There are essentially two ways that one could proceed to apply this model to explicitly determine the variation of s (that is, C) with time. One method is to use the analytic solution expressed in Equation 2-6 in conjunction with some type of numerical routine to calculate the Dawson's integral contained therein. The other method would involve direct application of a numerical integration procedure to the original differential equation, Equation 2-4. The latter approach was used in the calculations reported below.

It is convenient, at this point, to re-express Equation 2-4 using the variable τ rather than ξ as a measure of time. This is clearly a minor modification, as can be seen from Equation 2-5d, since these two variables differ from one another only by an additive constant. Thus, combining Equations 2-4 and 2-5d,

$$\frac{ds}{d\tau} = 1 - r - \left[1 + \beta + \gamma\,(\tau - \tau_p)\right](s - r) \quad . \tag{2-14}$$

For times within the interval $0 \leq t < t_p$, both β and γ are zero, and taking $s(\tau = 0) = 0$, the solution of Equation 2-14 becomes

$$s = 1 - \exp(-\tau) \quad . \tag{2-15}$$

Equation 2.20 of Reference 2.23 is seen to follow directly by setting $s = r$ and $\tau = \tau_p$ in Equation 2-15. In addition, the solution of Equation 2-14 for the special case $\gamma = 0$ (i.e., for which K' is time-independent) can be expressed in terms of elementary functions (Equation 2.24 of Reference 2.23).

We can also calculate the total amount, Q, of the species controlling glass dissolution that has actually gone into solution. In general,

$$\frac{dQ}{dt} = KS\,(C_o - C) \quad . \tag{2-16}$$

Equation 2-16 can be expressed in terms of dimensionless quantities using Equations 2-5a and 2-5f i.e.,

$$\frac{dq}{d\tau} = 1 - s \qquad (2\text{-}17)$$

where

$$q \equiv \frac{Q}{C_o V} \quad . \qquad (2\text{-}18)$$

Equations 2-16 and 2-18 are consistent with the terminology used in Reference 2.23.

Closed-form expressions for $q(\tau)$ were developed in Reference 2.23 for two cases: $K' = 0$, and K' being time-independent (Equations 2.27 and 2.29 of Ref. 2.23, respectively). During the past year, a numerical approach was used to obtain $q(\tau)$ for cases in which both β and γ are greater than zero; for such cases, a fourth-order Runge-Kutta procedure was used to integrate Equations 2-14 and 2-17 simultaneously.

The results of some specific numerical examples are illustrated in Figures 2.9 to 2.12. Some general observations, based on these figures, are as follows:

- Reprecipitation results in a decrease of the instantaneous concentration of glass in solution and an increase of the net amount of dissolved glass, as compared to the case for which no reprecipitation occurs. Indeed, the added amount of glass that has dissolved due to reprecipitation effects can be appreciable.

- An increase of γ (i.e., b) at constant β and r (i.e., a and C_o', respectively) results in an enhancement of the overall reprecipitation effect.

- Likewise, an increase of β at constant γ and r also enhances the overall reprecipitation effect, although the relative enhancement becomes less pronounced for the larger γ and τ values, for which the time-dependent term in K' dominates the time-independent term.

- A decrease of r at constant β and γ causes the reprecipitation effect to be enhanced.

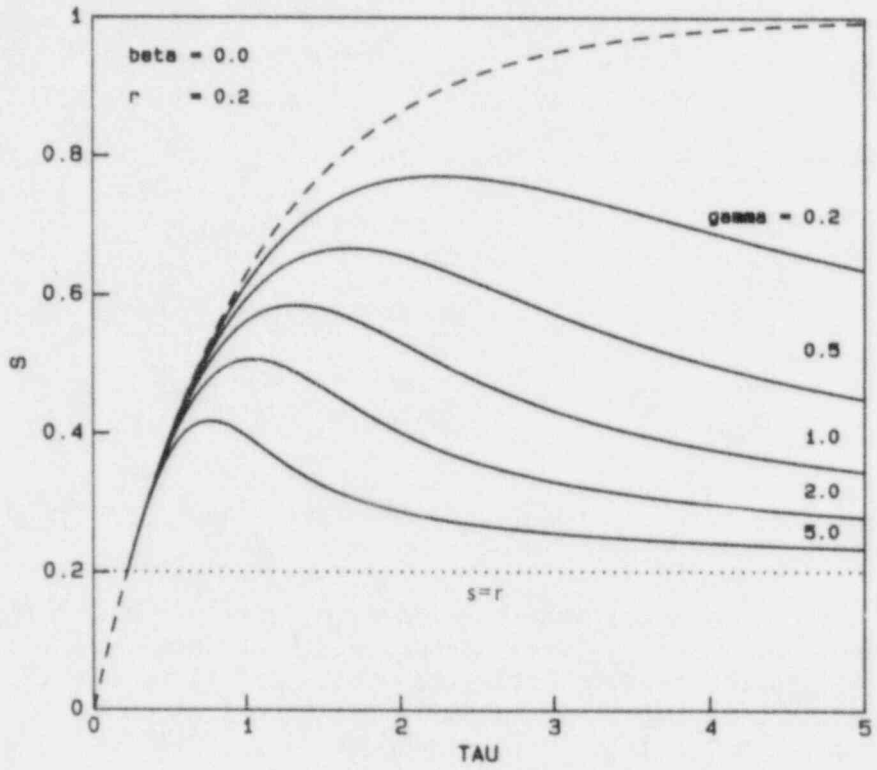

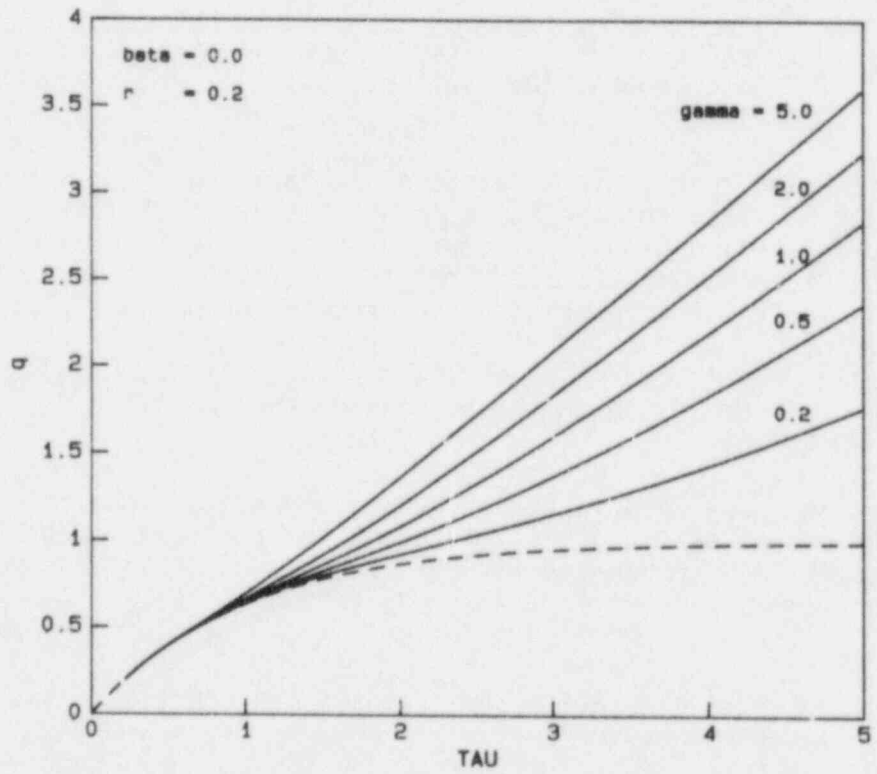

Figure 2.9. Variation of s and q with τ for $\beta = 0.0$, $r = 0.2$, and for selected values of γ.

The dashed curves correspond to $\beta = \gamma = 0$, i.e., no reprecipitation.

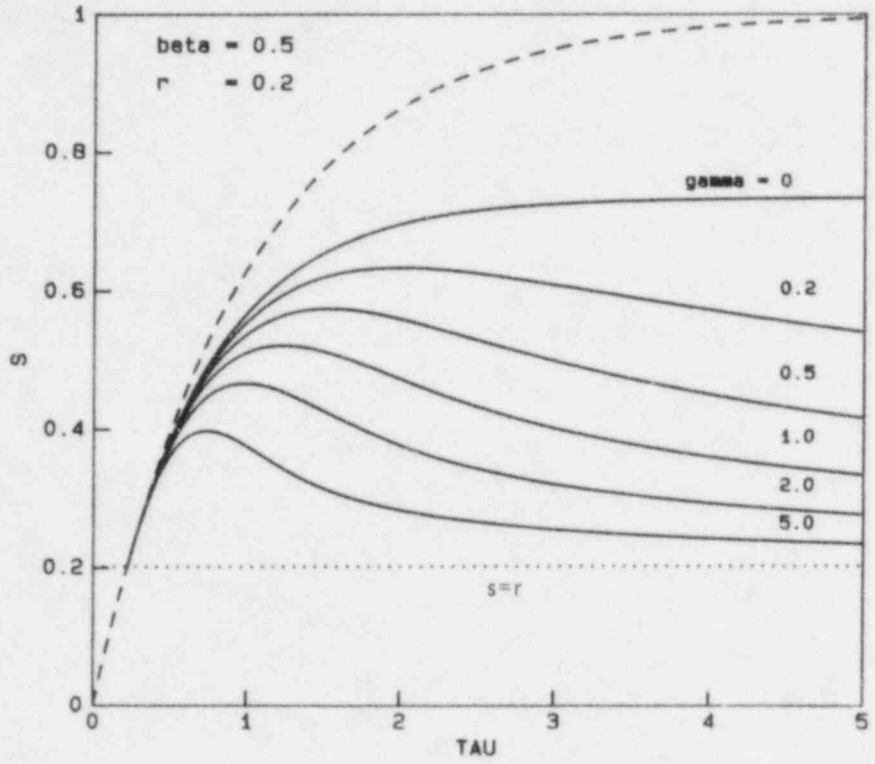

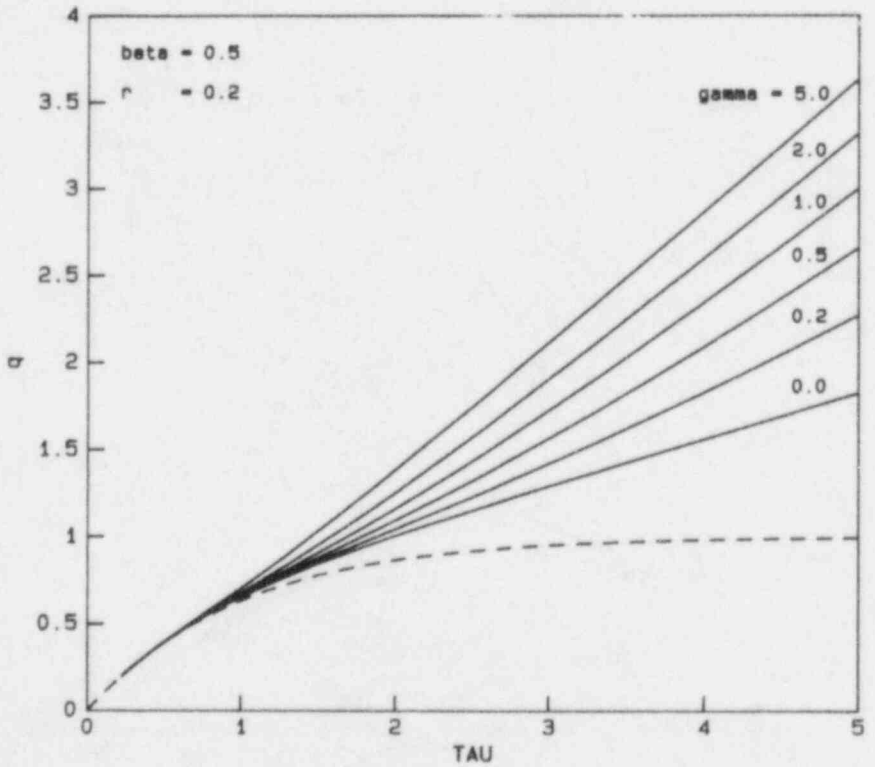

Figure 2.10. Variation of s and q with τ for $\beta = 0.5$, $r = 0.2$, and for selected values of γ.

The dashed curves correspond to $\beta = \gamma = 0$, i.e., no reprecipitation.

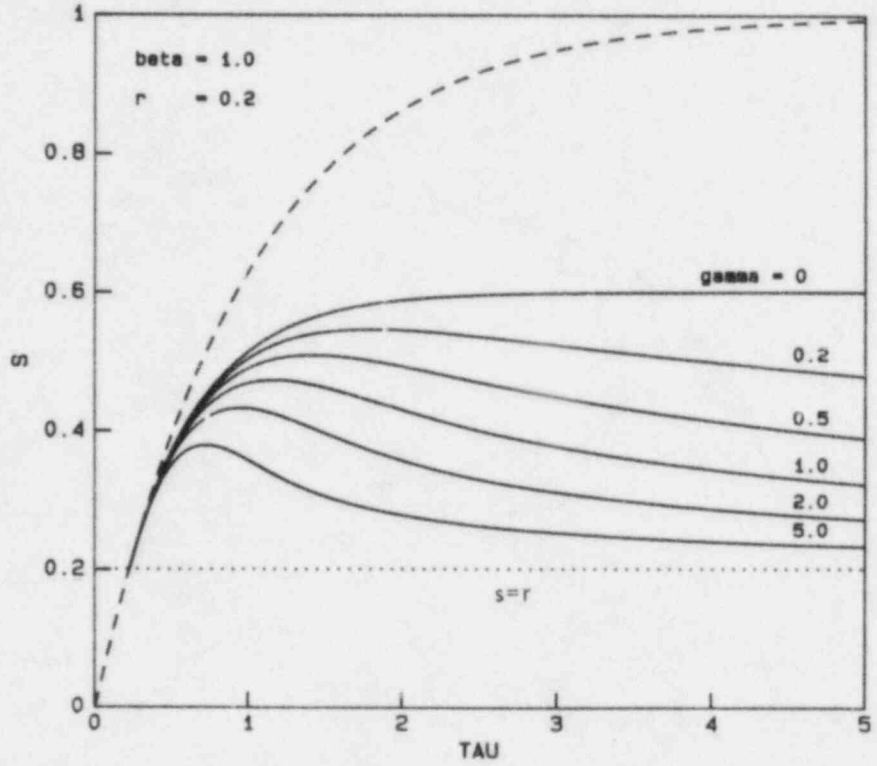

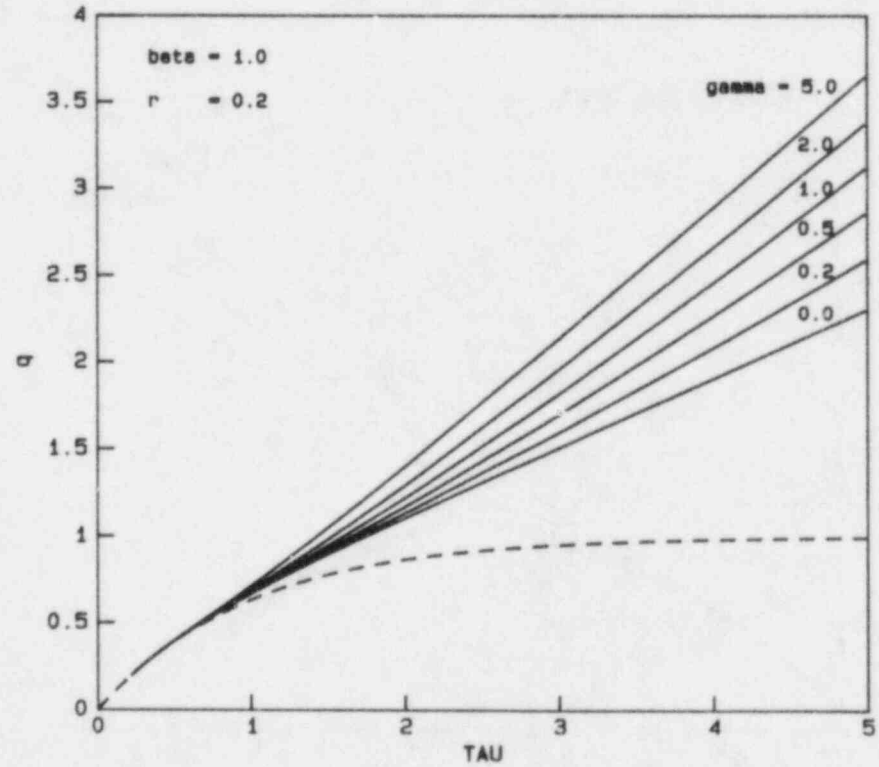

Figure 2.11. Variation of s and q with τ for $\beta = 1.0$, $r = 0.2$, and for selected values of γ.

The dashed curves correspond to $\beta = \gamma = 0$, i.e., no reprecipitation.

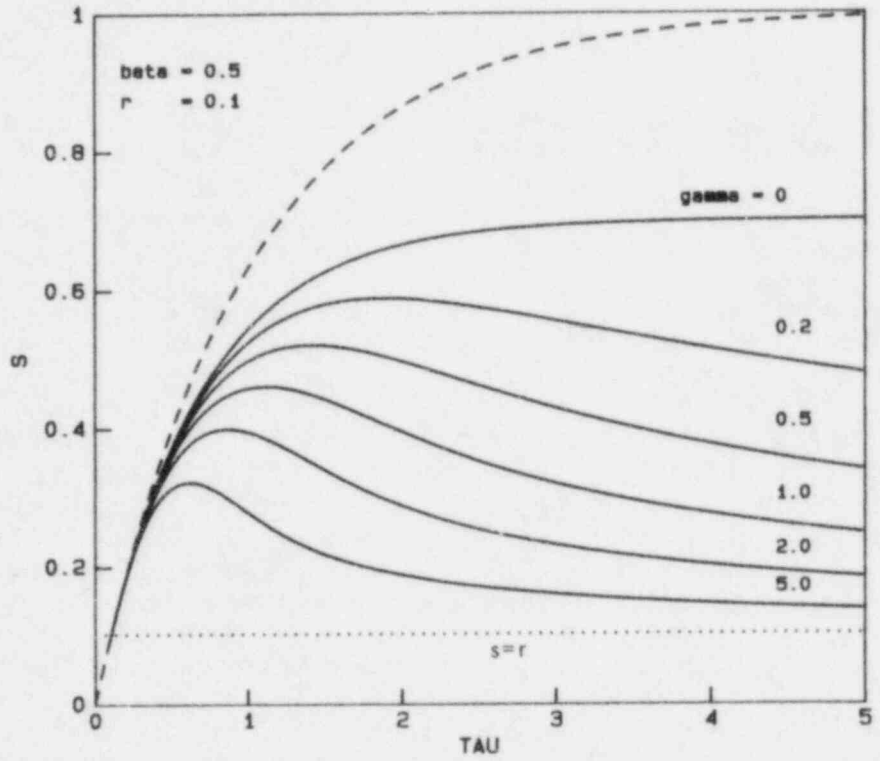

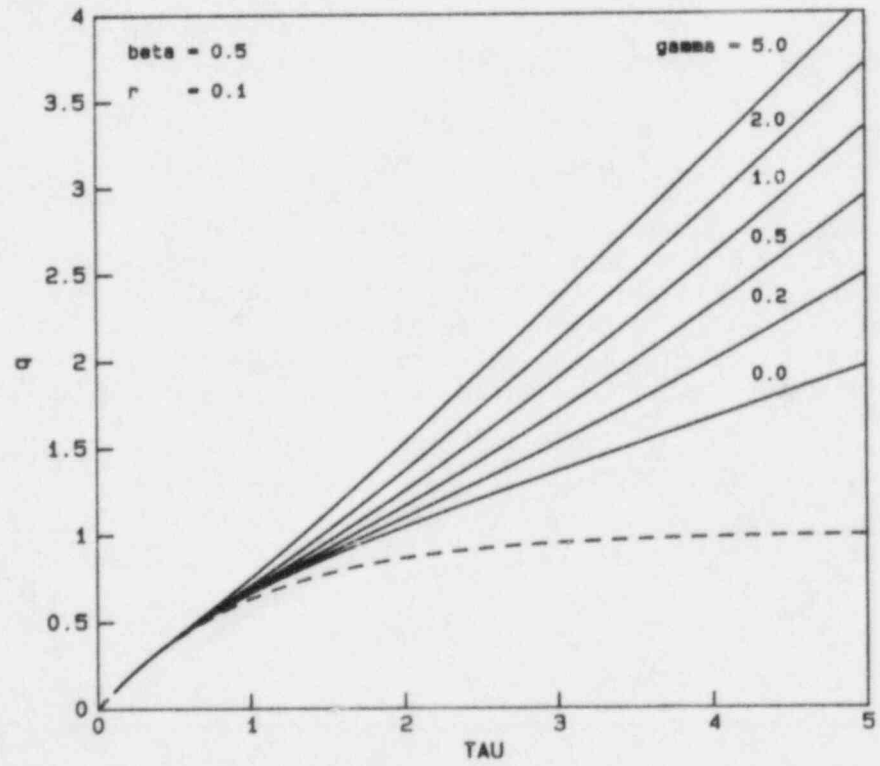

Figure 2.12. Variation of s and q with τ for $\beta = 0.5$, $r = 0.1$, and for selected values of γ.

The dashed curves correspond to $\beta = \gamma = 0$, i.e., no reprecipitation.

- For $\beta \neq 0$, $\gamma = 0$, the value of s asymptotically approaches a constant value that is greater than r but less than 1.

- For $\beta \neq 0$, $\gamma > 0$, the value of s attains a maximum and then asymptotically approaches the constant value s = r.

The last two observations are, in general, consistent with analogous experimental studies[2.24] and modeling studies[2.27,2.28] pertaining to various geological processes.

It must be emphasized that the mathematical form for K' used in this analysis was selected on a largely empirical basis. It should, however, present a reasonable description of gross features of the reprecipitation process.

Further studies in this area will include continued correlation of these modeling studies with analogous studies reported in the literature for geological systems. In addition, an experimental program of this general nature is in progress at Battelle and should lend further insight into both the kinetics of the process and the associated physical mechanisms. It is also anticipated that water-chemistry considerations will be included in the overall dissolution/reprecipitation model, following a procedure analogous to that used to describe glass-dissolution kinetics, as described below.

2.6.2 Inclusion of Water-Chemistry Effects in Glass-Dissolution Modeling

One would expect that the rate of dissolution of a waste-form glass would vary with both the glass composition and the groundwater composition. Moreover, as the glass dissolves, the groundwater composition is continuously altered as species are added thereto from the dissolved glass, which in turn would affect the instantaneous rate of dissolution. This behavior was investigated, during the past year, using the water-chemistry model that had been developed under this program[2.29].

The glass-dissolution model that was used for these studies is described by Equation 2-2 (with K' = 0 for the present analyses) or Equation 2-16, i.e.,

$$\frac{dC}{dt} = k\ (C_o - C) \qquad (2\text{-}19)$$

where the parameter k in Equation 2-19 represents the quantity KS/V in Equation 2-17. For the calculations summarized below, normalization of time was introduced by setting k = 1. This is equivalent to using a new, dimensionless time variable, τ, as defined in Equation 2-5f.

Actually, this approach to describing heterogeneous-reaction kinetics has been in use for many years, a review of some of the earlier studies having been presented by Moelwyn-Hughes[2.30]. More recently, the specific problem of leaching of nuclear-waste-containing glasses has been addressed[2.31,2.32] with varying degrees of complexity, using a glass-dissolution model of this fundamental type.

The basic assumptions upon which the calculations reported here were based are the following:

- Glass dissolution occurs congruently and is limited by the rate at which silicon dissolves.
- No spatial variation of the silicon concentration in the volume V of groundwater around the glass exists.
- The instantaneous rate of glass dissolution is proportional to the difference between the saturation concentration of silicon in aqueous solution, with respect to the glass, and its actual concentration.
- The solution into which the glass dissolves occupies a constant, closed volume.

Clearly, Equation 2-19 is consistent with these assumptions.

All the above assumptions are more or less standard for glass-dissolution calculations. The feature that makes this calculation significantly more realistic than others is that C_0 is not assumed to be constant. Instead, it is assumed that the activity of nonionized silicic acid (H_4SiO_4) is independent of pH and that the increase in silica solubility at high pH is due to ionization. This is in good agreement with experimental data[2.33] on silica solubility.

The calculations reported here were based on one waste-form composition: the PNL 77-260 glass. Actually, a simplified glass composition was used, containing oxides of silicon, boron, sodium, and calcium in the mole ratios:

$$Si/B/Na/Ca = 1.0/0.432/0.431/0.0709 \quad .$$

Two different waters were used in our calculations: pure water and Grande Ronde basalt groundwater[2.34]. Actually, the basalt-groundwater composition that we used was modified by lumping sodium and potassium as sodium, and fluorine and chlorine as chlorine. Treating potassium the same as sodium is expected to have a negligible effect on pH calculations, since both NaOH and KOH are strong alkalis. Treating fluorine the same as chlorine is less justified since HF is a relatively weak acid while HCl is a strong acid. However, the pH as calculated using this scheme was compared with the pH calculated by a more complete

water-chemistry program which did not require lumping of elements, and the difference was about 0.02 pH units.[2.35]. This is considered to be sufficiently accurate for our purposes.

The differential equation for glass dissolution (Equation 2-19) was solved by the following conceptual process. From the composition of the initial groundwater, the pH was calculated, and this was used to calculate C_o. The initial rate of dissolution could then be calculated from Equation 2-19. The waste form was allowed to dissolve congruently for a short period of time, thus changing the composition of the groundwater. The process above was then repeated for the modified groundwater composition. In general, it was to be expected that C_o would change with time and that the dissolution rate would not follow a simple exponential curve. This was indeed the case, as shown in Figures 2.13 and 2.14. (The dissolution rates in those two figures are normalized to unity at time t = 0.) In the case of pure water, the dissolution rate reached a maximum at a normalized time of about 0.07. For the synthetic basalt groundwater, however, the dissolution rate dropped monotonically from its initial value. The reason for these two very different behaviors can be seen from Figures 2.15 and 2.16. As the waste form dissolved in pure water, its pH rapidly increased from its initial value of 7, and the total concentration of silicon at saturation, C_o, also increased, raising the dissolution rate. In contrast, the pH of the synthetic basalt groundwater dropped as the waste form dissolved. That reduced the saturation concentration of silicon, resulting in a lower dissolution rate.

From these results, it is apparent that short-term glass degradation data must be interpreted with caution. In the case of pure water, the theory predicts that the dissolution rate will increase with time, at least at short times. Such experimental data might be incorrectly interpreted as suggesting that the waste form is undergoing catastrophic degradation. In the case of synthetic basalt groundwater, the theory predicts a rapid decrease of the dissolution rate with time. This might lead to an overestimate of the stability of the waste form.

Some additional calculated characteristics of the glass-dissolution process for these two groundwaters are illustrated in Figures 2.17 to 2.24. In all these figures, time is again normalized as given by Equation 2-5f, and all concentrations are in units of molality. These figures are largely self-explanatory. However, it should be noted that, in general, silicon concentration at saturation, C_o, is a function of pH and ionic strength; but since ionic-strength effects are not large, C_o is a function mostly of pH, in which case Figures 2.18 and 2.22 should represent segments of the same curve. Comparison of these two figures shows that such is indeed the case.

Continued efforts in this area, during the fourth year, will include effects of different glass compositions (e.g., PNL 76-68 and SRL 165) as well as other groundwaters (e.g., tuff). In addition, this general approach will also be applied to spent-fuel waste forms.

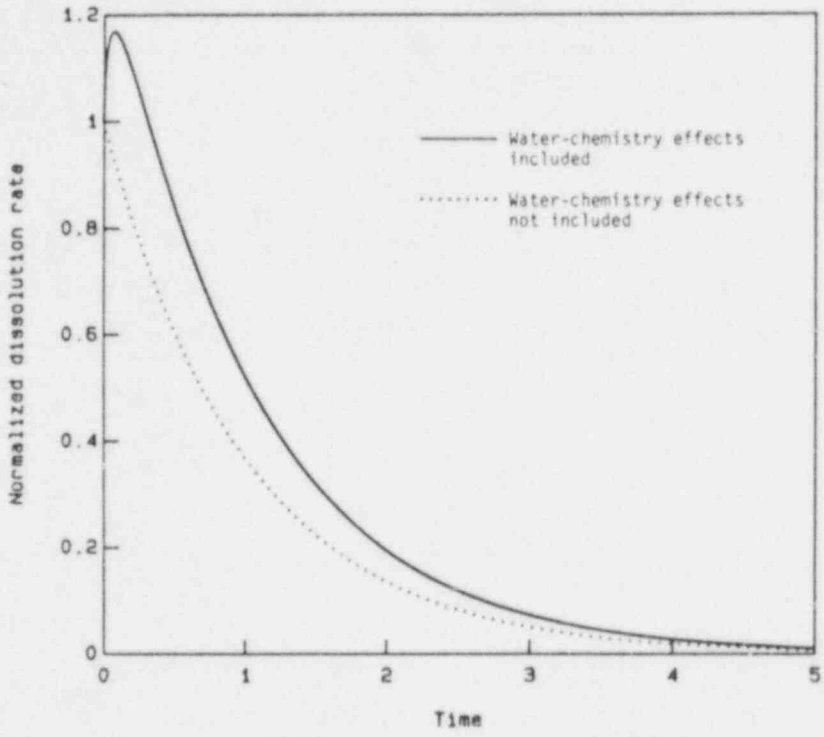

Figure 2.13. Glass-dissolution rate in pure water as a function of time.

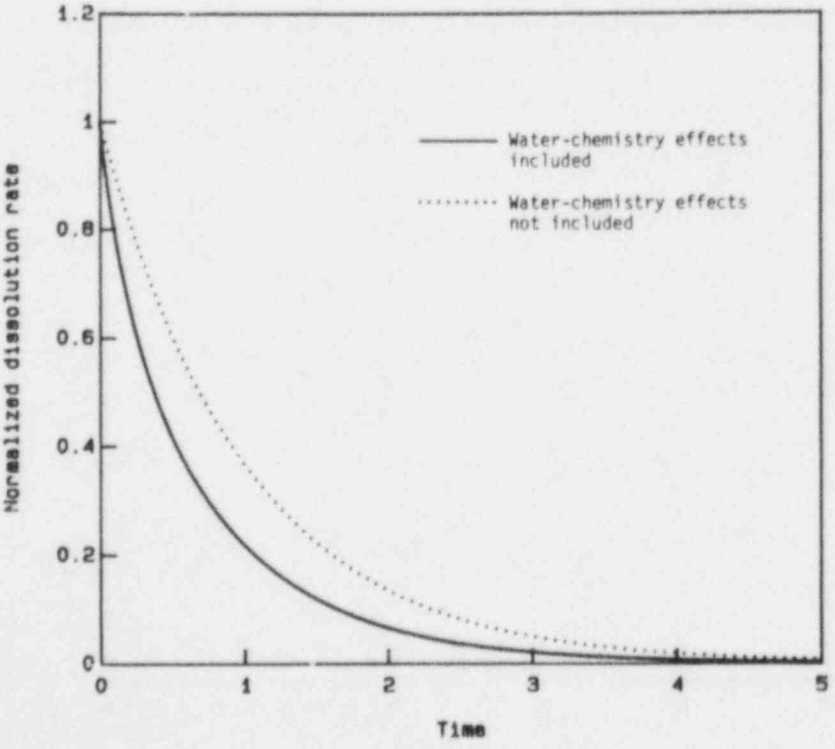

Figure 2.14. Glass-dissolution rate in synthetic basalt groundwater as a function of time.

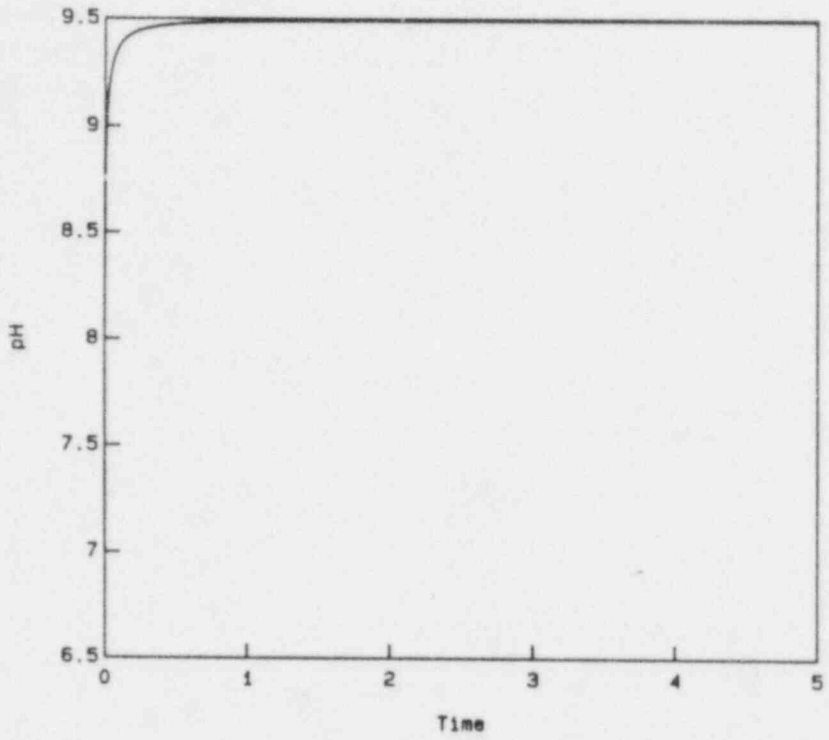

Figure 2.15. pH as a function of time as glass dissolves in pure water.

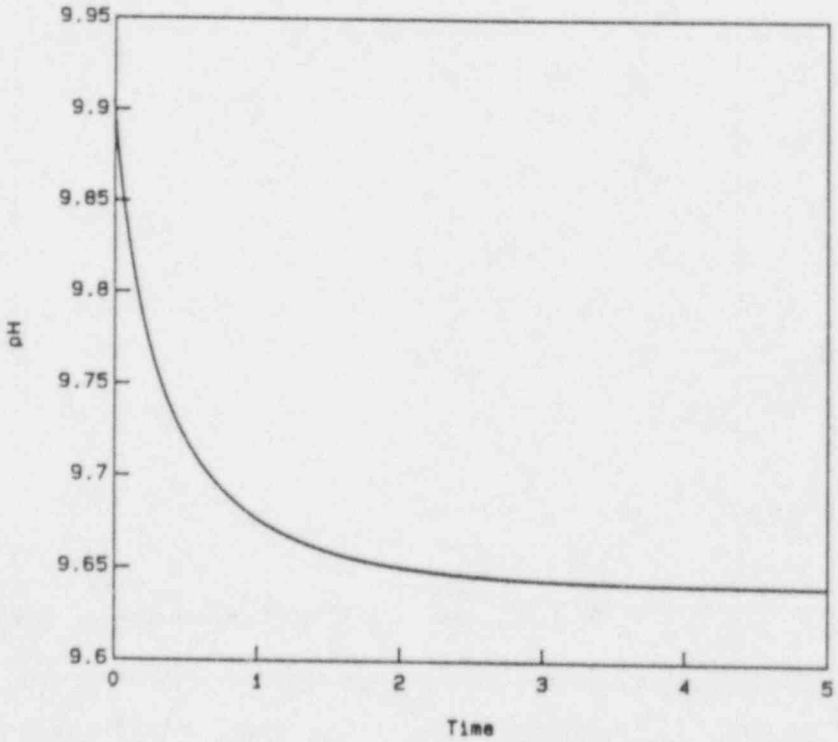

Figure 2.16. pH as a function of time as glass dissolves in synthetic basalt groundwater.

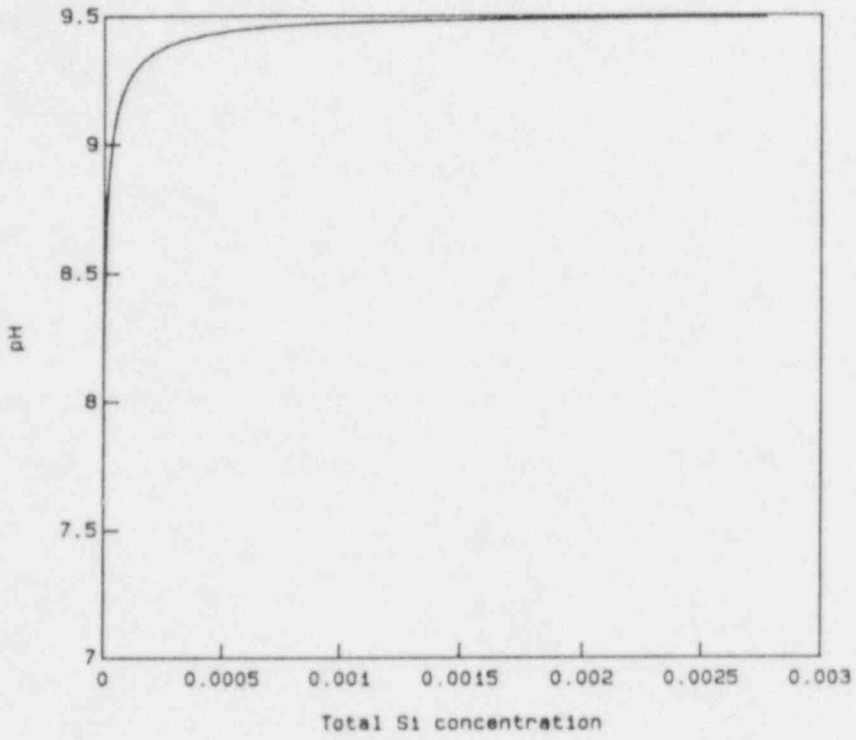

Figure 2.17. pH as a function of silicon concentration as glass dissolves in pure water.

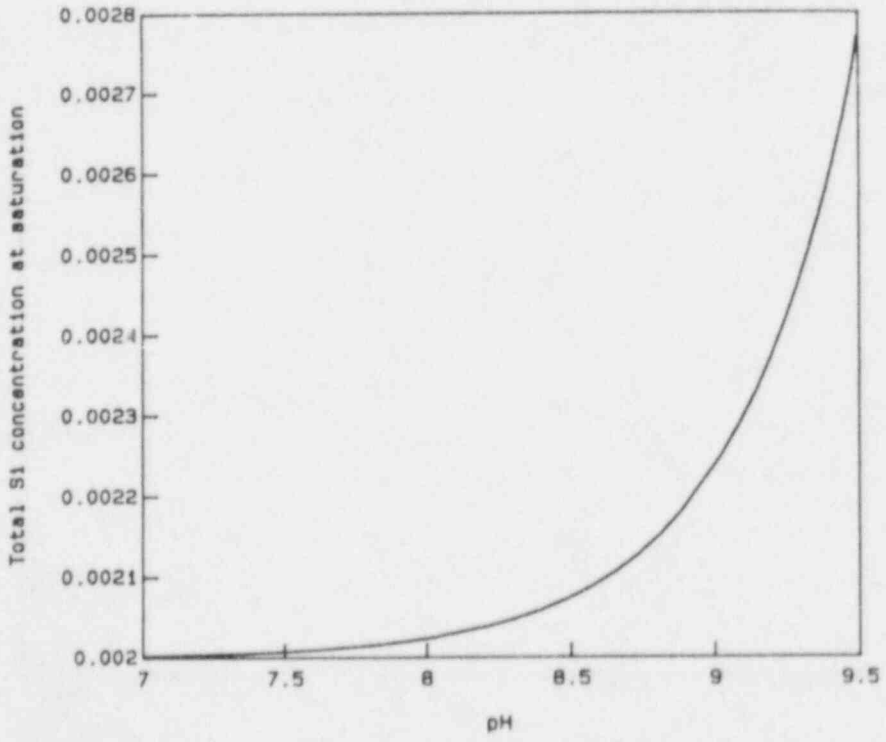

Figure 2.18. Silicon concentration as a function of pH as glass dissolves in pure water.

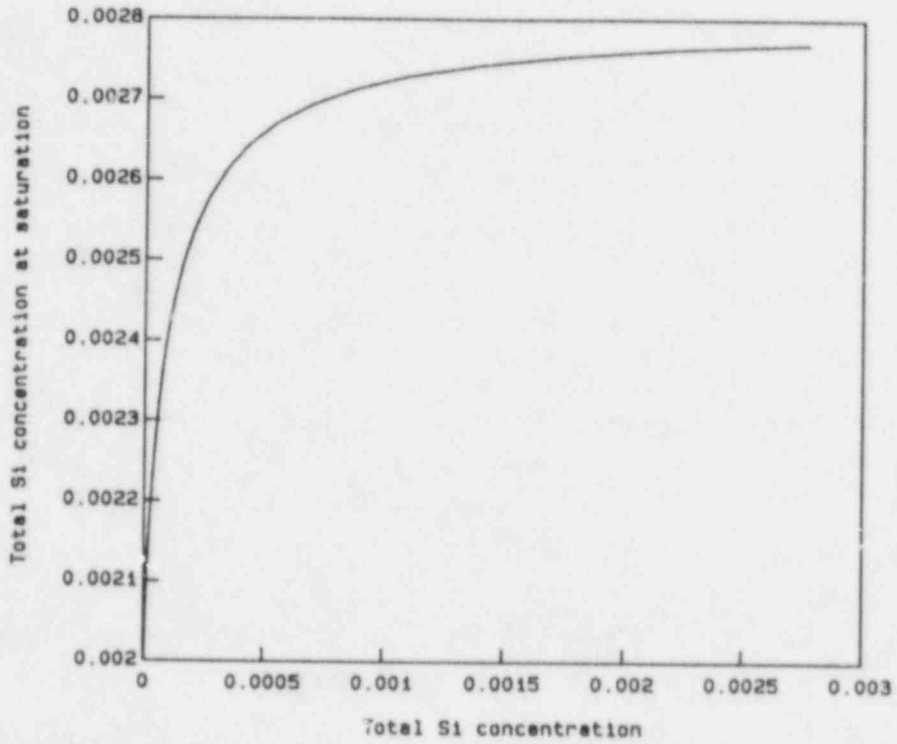

Figure 2.19. Silicon concentration at saturation as a function of instantaneous silicon concentration as glass dissolves in pure water.

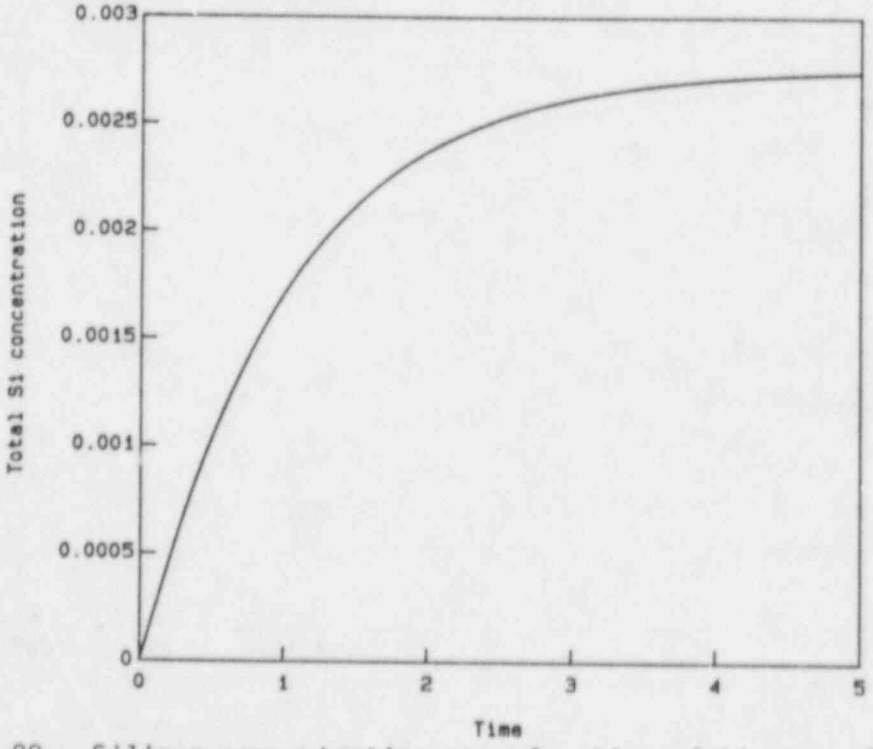

Figure 2.20. Silicon concentration as a function of time as glass dissolves in pure water.

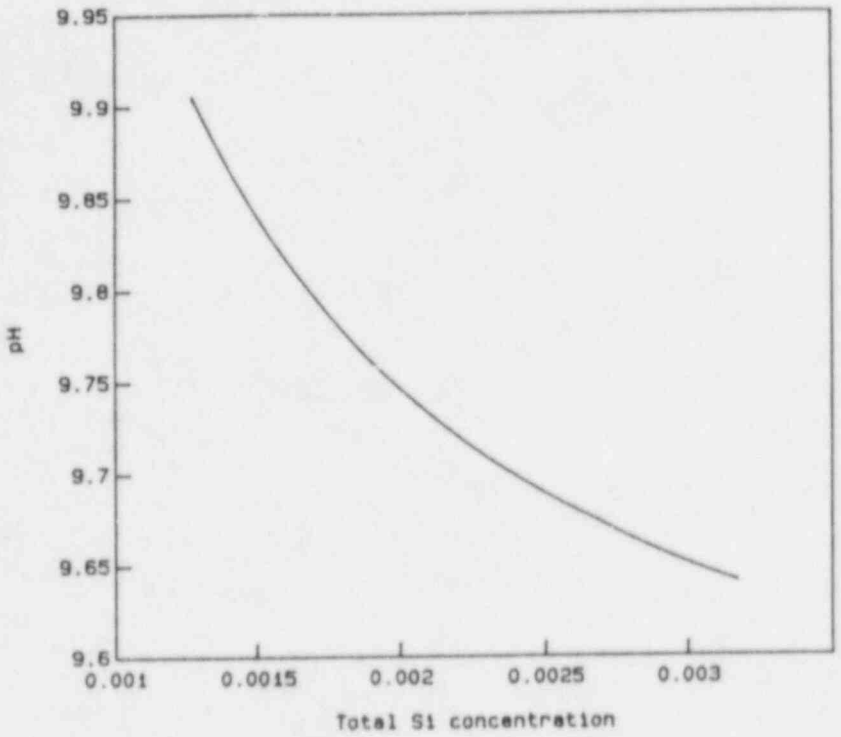

Figure 2.21. pH as a function of silicon concentration as glass dissolves in synthetic basalt groundwater.

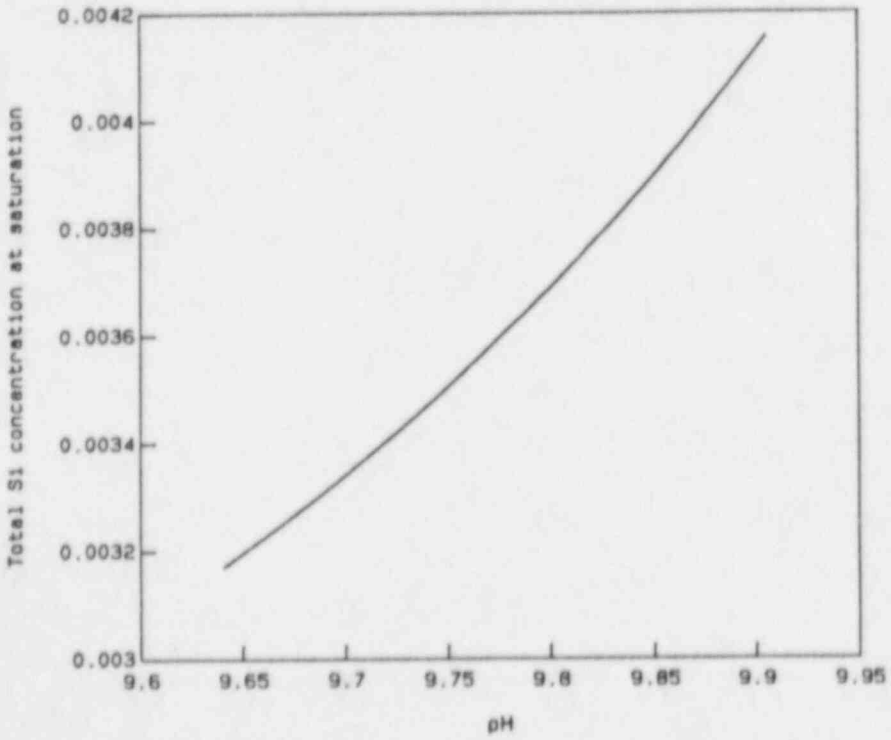

Figure 2.22. Silicon concentration at saturation as a function of pH as glass dissolves in synthetic basalt groundwater.

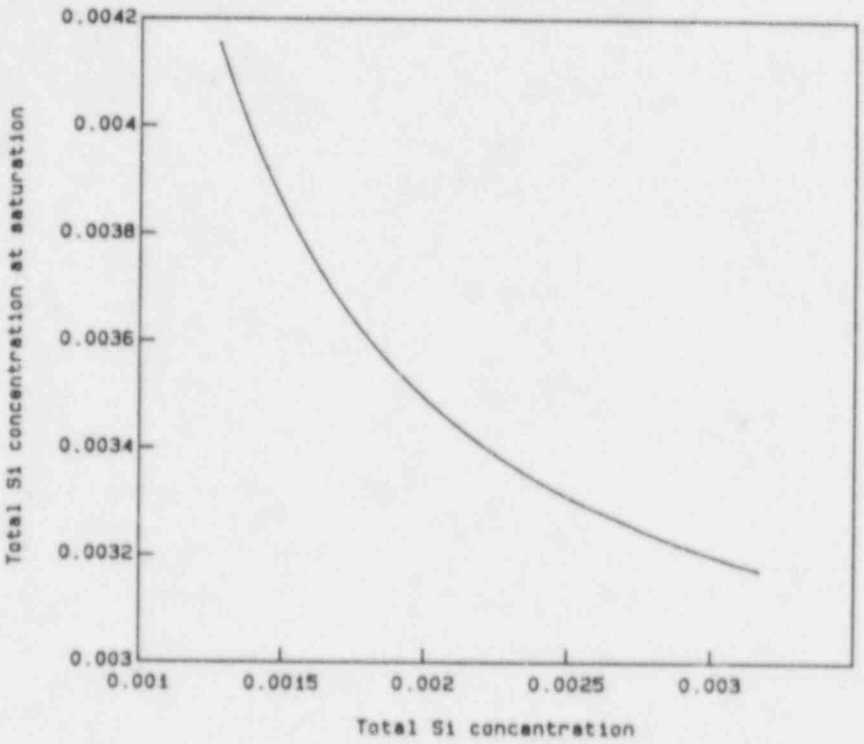

Figure 2.23. Silicon concentration at saturation as a function of instantaneous silicon concentration as glass dissolves in synthetic basalt groundwater.

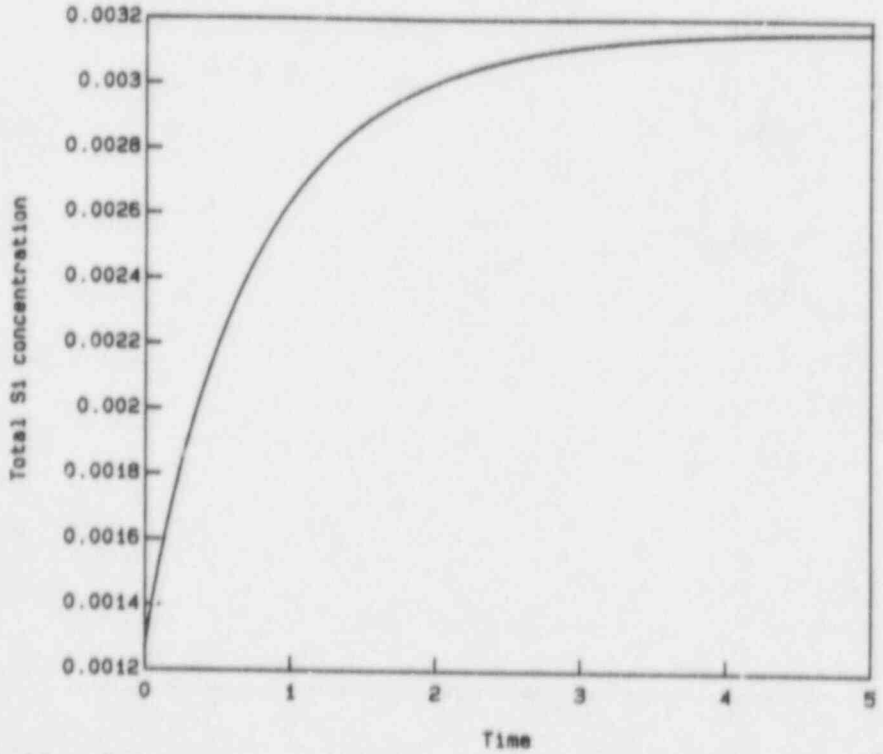

Figure 2.24. Silicon concentration as a function of time as glass dissolves in synthetic basalt groundwater.

2.7 Future Work

Studies of dissolution and reprecipitation phenomena in the glass waste form will be completed during the coming year. The role of silica solubility in glass leaching will be evaluated experimentally to provide analytical verification of the waste-form dissolution model. The effects of factors that may accelerate glass dissolution in a repository environment will also be examined; these factors include the degree of crystallinity of the glass and the presence of natural organic acids in groundwater.

Spent-fuel studies in the coming year will focus on understanding the dissolution of UO_2 under prototypic long-term repository conditions. An experimental matrix has been prepared. The distribution of radionuclides will be examined through a literature search in preparation for future experimentation.

During the next year, waste-form modeling efforts will address both borosilicate glass and spent fuel. The glass-dissolution model will be extended by including the effects of specific groundwater composition on dissolution/reprecipitation kinetics. Efforts in modeling spent-fuel degradation will be initiated. Existing models for environmentally enhanced fracture of glass and ceramic materials will also be evaluated in terms of their applicability to waste-form fracture in a repository environment.

2.8 References for Section 2

(2.1) J. E. Mendel (Manager), The Nuclear Waste Materials Handbook, DOE/TIC-11400, prepared by the Materials Characterization Center (undated).

(2.2) T. E. Jones, Reference Material Chemistry--Synthetic Ground Water Formation, RHO-BW-ST-37P, prepared by Rockwell Hanford Operations for the U.S. Department of Energy (1982).

(2.3) J. E. Mendel, Final Report of the Defense High-Level Waste Leaching Mechanisms Program, PNL-5157 (August, 1984).

(2.4) H. M. Kingston, D. J. Cronin, and M. S. Epstein, "Investigation of a Precise Static Leach Test for the Testing of Simulated Nuclear Waste Materials", Nucl. Chem. Waste Management, 5, 3-15 (1984).

(2.5) W. Stumm and J. J. Morgan, Aquatic Chemistry, Wiley-Interscience, N.Y., 1970; p. 521.

(2.6) Z. S. Altschuler, R. S. Clark, Jr., and E. S. Young, Geochemistry of Uranium in Apatite and Phosphorite, U.S. Geological Survey Professional Paper 314-D, 50 pp (1958).

(2.7) C. E. Roessler, Z. A. Smith, W. E. Bolch, and R. J. Prince, "Uranium and Radium-226 in Florida Phosphate Materials", Health Phys., 37, 269-277 (1979).

(2.8) R. A. Gulbrandsen, "Chemical Composition of Phosphorites of the Phosphoria Formation", Geochem. Cosmochim. Acta, 30, 769-778 (1966).

(2.9) V. Z. Bliskovskiy, V. A. Yefimova, and L. V. Romanova, "The Sr^{+2} Content of Phosphorites", Geochem. International, 4, 1186-1190 (1967).

(2.10) J. L. Means, D. A. Crerar, and M. P. Borcsik, "Adsorption of Co and Selected Actinides by Mn and Fe Oxides in Soils and Sediments", Geochem. Cosmochim Acta, 42, 1763-1773 (1978).

(2.11) D. Stahl and N. E. Miller, "Long-Term Performance of Materials Used for High-Level Waste Packaging", NUREG/CR-3427, BMI-2113, Vol. 4, prepared by Battelle's Columbus Laboratories for the U.S. Nuclear Regulatory Commission, pp 2-37 to 2-51.

(2.12) D. M. Martin, "Fracture in Glass/High Level Waste Canisters", NUREG/CR-4198, pp 17-18 (April, 1985).

(2.13) L. L. Hench and D. E. Clark, "Surface Properties and Performance Prediction of Alternative Waste Forms", report to NRC (Contract NRC-04-78-252) (March, 1983).

(2.14) W. J. McCracken, D. E. Clark, and L. L. Hench, "Aqueous Durability of Lithium Disilicate Glass Ceramics", Ceram. Bull. 61 (11), pp 1218-1223 (1982).

(2.15) H. Yinnon and D. R. Uhlmann, "A Kinetic Treatment of Glass Formation V. Surface and Bulk Heterogeneous Nucleation", J. Non-Cryst. Solids, 44 (1), pp 37-55 (1981).

(2.16) D. F. Bickford and C. M. Jantzen, "Devitrification Behavior of Defense Waste Glass", paper presented at Materials Research Society Annual Meeting, (November, 1983).

(2.17) C. R. Hick, Fundamental Concepts in the Design of Experiments, Holt, Rinehart, and Winston (1964).

(2.18) W. W. Carothers and Y. K. Kharaka, "Aliphatic Acid Anions in Oil-Field Waters--Implications for Origin of Natural Gas", American Association of Petroleum Geologists Bulletin, 62, (12), pp 2441-2453 (1978).

(2.19) J. L. Means and N. J. Hubbard, "The Organic Geochemistry of Deep Ground Waters from the Palo Duro Basin, Texas: Implications for Radionuclide Complexation, Ground Water Origin, and Petroleum Exploration", prepared by Battelle's Columbus Laboratories for the Office of Nuclear Waste Isolation, Battelle Memorial Institute, Columbus, Ohio (in review).

(2.20) J. L. Means, "The Organic Geochemistry of Deep Ground Waters", ONWI-268, prepared by Battelle's Columbus Laboratories for the Office of Nuclear Waste Isolation, Battelle Memorial Institute, Columbus, Ohio (1982).

(2.21) S. N. Bhattacharyya and K. P. Kandu, "Radiolysis of Aqueous Solutions of Nickel (II) EDTA", Radiation Research, 51, pp. 45-55 (1972).

(2.22) J. C. Petit, Y. Langevin, J. M. Lameille, and J. C. Dran, "On the Leaching Behavior of a Simple Borosilicate Glass in a Confined Environment", in Scientific Basis for Nuclear Waste Management V, W. Lutze (editor), Elsevier Science Publishing Co., Inc., New York, p. 203 (1982).

(2.23) "Long-Term Performance of Materials Used for High-Level Waste Packaging", D. Stahl and N. E. Miller (Compilers), NUREG/CR-3427, Vol 4, BMI-2113 (June, 1984), pp 2-58 ff.

(2.24) A. C. Lasaga, in Reviews in Mineralogy, Vol. 8: Kinetics of Geochemical Processes, A. C. Lasaga and R. J. Kirkpatrick (editors), Mineralogical Soc. of America (Washington, D.C., 1981), pp. 10-11.

(2.25) F.W.J. Olver, Asymptotics and Special Functions, Academic Press, Inc. (New York, 1974), pp. 43-44.

(2.26) W. Gautschi, in Handbook of Mathematical Functions with Formulas, Graphs, and Mathematical Tables, M. Abramowitz and I. A. Stegun (editors), National Bureau of Standards, Applied Mathematics Series-55 (Washington, D.C., 1964), p. 298.

(2.27) R. Wollast, "Kinetics of the Alteration of K-Feldspar in Buffered Solutions at Low Temperatures", Geochim. et Cosmochim. Acta, 31 (1967) 635.

(2.28) R. Wollast, "The Silica Problem", in The Sea, E. W. Goldberg (editor), Vol. 5, John Wiley & Sons, Inc. (New York, 1974), p. 359.

(2.29) "Long-Term Performance of Materials Used for High-Level Waste Packaging", D. Stahl and N. E. Miller (Compilers), NUREG/CR-3405, BMI-2105 (July, 1983), pp. 6-1 ff.

(2.30) E. A. Moelwyn-Huges, The Kinetics of Reactions in Solution, 2nd Edition (Oxford University Press, London, 1947), pp. 367 ff.

(2.31) W. L. Kuhn, R. D. Peters, and S. A. Simonson, "Development of a Leach Model for a Commercial Nuclear Waste Glass", Nucl. Technol. 63 (1983)82.

(2.32) K. B. Harvey, "A Semiunified Approach to Leach Testing of Nuclear Waste Forms", Nucl. Chem. Waste Manag. 4 (1983)201.

(2.33) G. B. Alexander, W. M. Heston, and R. K. Iler, "The Solubility of Amorphous Silica in Water", J. Chem. Phys., 58 (1954)453.

(2.34) T. E. Jones, "Reference Material Chemistry--Synthetic Groundwater Composition", RHO-BW-ST-37 P (April, 1982).

(2.35) "Long-Term Performance of Materials Used for High-Level Waste Packaging", D. Stahl and N. E. Miller (Compilers), NUREG/CR-3427, Vol. 1 (August, 1983), pp. 5-1 ff.

3. CONTAINER MATERIALS

The container consists of two or more concentric metallic enclosures that act as a barrier against the ingress of groundwater or brine to the waste form and the egress of radionuclides to the repository.

The general and localized corrosion of the outer metallic enclosure, or overpack, by water in the repository has also been under study. At the outset of the project, a potential overpack consisted of a thick-walled steel container covered by a thin shell of a titanium alloy for use in a salt repository. To study overpack corrosion in the titanium-salt system, coupons of Titanium Grade 12 were exposed in an autoclave to high-temperature simulated brines. However, the use of a titanium shell has subsequently been in less favor by the DOE, so the effort has shifted from titanium to cast and wrought low-carbon steels, which are being considered for use in a basalt repository. To study corrosion in the steel-basalt system, steel coupons were exposed in an autoclave to high-temperature simulated basalt groundwaters of varying concentration. The effect of groundwater species on the relevant electro-chemical behavior of steels is being evaluated to indicate susceptibility to localized corrosion, specifically pitting and stress-corrosion cracking. Where electrochemical results indicate that stress-corrosion cracking may occur, a more thorough investigation is being conducted using slow strain rate studies. The possible embrittlement of a cast steel overpack by hydrogen generated during corrosion reactions and radiolysis is also being investigated.

Closely related to these experimental efforts is the ongoing development of a mathematical description of general corrosion and pitting corrosion of overpack materials. This research is being directed toward development of a physically realistic model that includes processes of major importance in an actual repository. Efforts in developing the pitting-corrosion correlation have focused on the kinetics of pit generation and pit growth. Analysis of mechanical degradation of waste-package components has continued, with specific effort directed toward analyzing sources of mechanical stress that, in combination with water-chemistry-related factors, may contribute to the susceptibility of a steel to stress-corrosion cracking.

3.1 Overpack Corrosion

Studies of overpack corrosion have focused this year on three areas: potentiodynamic polarization studies, slow strain rate studies, and pitting-kinetics studies. All of the studies have examined the carbon steel-basalt rock system. The objective of the potentiodynamic polarization studies is to evaluate the influence of metallurgy and groundwater chemistry on stress-corrosion cracking (SCC) and pitting susceptibility. The objective of the slow strain rate studies is to confirm the results of the electrochemistry with regard to SCC and to investigate the effect of electrochemical potential, temperature, and

environment composition in detail for the identified cracking agents. The objective of the pitting kinetics studies is to investigate the effects of geometrical and environmental variables on pit propagation. Discussion of progress on these tasks are given below.

3.1.1 Potentiodynamic Polarization Studies

In this task, potentiodynamic polarization techniques are being used to evaluate the influence of metallurgical and environmental variables on the electrochemical behavior of carbon steels in simulated basalt repository environments. The results of these analyses are then used to assess the tendency for stress-corrosion cracking and pitting.

The potentiodynamic polarization procedure is explained in the 1984 annual report.(3.1) In this procedure, the polarity and magnitude of the current density between a specimen of the material of interest and an inert counter electrode are measured as a function of electrochemical potential. For the anodic portions of the curve, the current measured is equal to the corrosion rate of the specimen if two conditions are met: (1) the electrochemical potential is far enough away from the open-circuit potential that the rate of the cathodic reaction is negligible; and (2) the rates of parasitic oxidation reactions are negligible.

Schematics of anodic polarization curves showing several types of behavior are given in Figure 3.1. For the active-corrosion case, the anodic curve is linear on an E-log i plot, and the forward and reverse scans are coincident. The presence of a peak in the anodic portion of the curve, followed by decreasing current, is generally indicative of the onset of passivation. The occurrence of hysteresis between the forward and reverse scans is indicative of pitting. Where the hysteresis loop is very large, the protection potential may be very close to the open-circuit potential, indicating a high probability of pitting in that particular environment.

The potentiodynamic polarization technique also has been found to be useful in identifying potential stress-corrosion cracking (SCC) environments for carbon steels. It has been shown(3.2) that SCC is associated with environments that promote active-passive behavior and that the electrochemical potential range for SCC is near to and more noble than E_{max}. Moreover, severe cracking has been observed(3.2) in environments when i_{max} on the fast scan is greater than about $1 \times 10^{-3} A/cm^2$ and when the fast scan exhibits at least an order of magnitude higher currents than the slow scan.

The polarization behavior of the candidate alloys was determined using conventional polarization techniques. The specific polarization equipment used for these experiments included a PAR Model 173 potentiostat with an ECO Model 567 function generator, coupled to a computer data-acquisition system. For the ambient pressure tests, a three-compartment

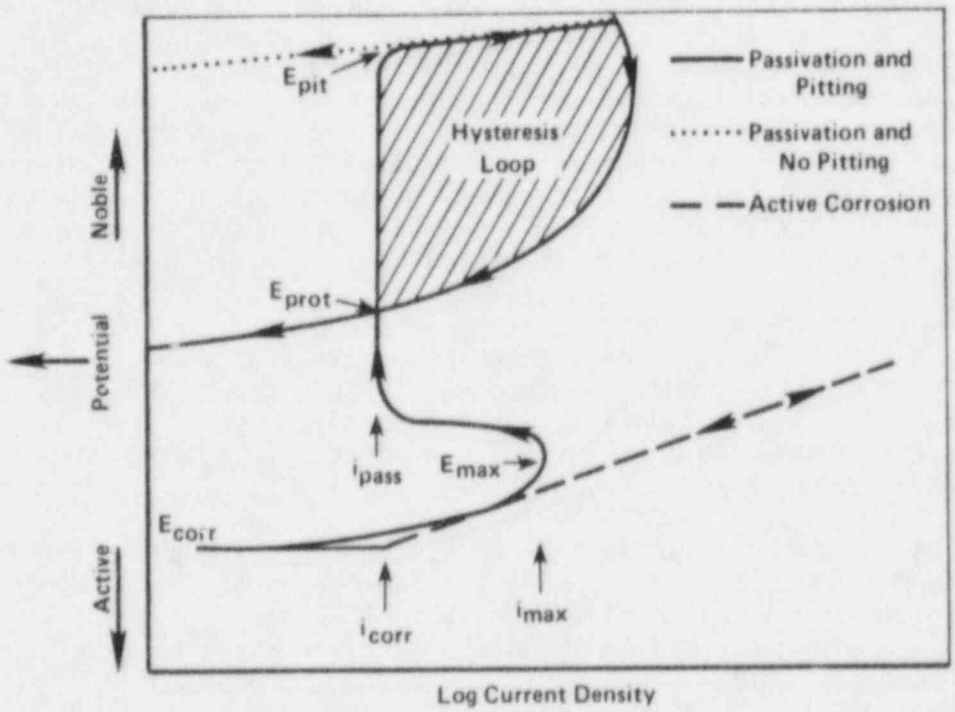

Figure 3.1. Schematic of typical anodic potentiodynamic polarization curves.

E_{corr} = corrosion potential; E_{pitt} = potential at which pits initiate on forward scan; E_{prot} = potential at which pits repassivate on reverse scan; i_{cor} = current density at the free-corrosion potential; i_{max} = current density at active peak; i_{pass} = current density in passive range.

electrochemical cell was employed that utilized a saturated calomel reference electrode (SCE) and a platinum counter electrode. The three-compartment electrochemical cell separates the working electrode from the counter electrode, preventing mixing of the solutions in the counter-electrode and the working-electrode compartments. The working-electrode specimens, hot-rolled 1020 carbon steel, were cylindrical rods drilled and tapped at both ends and sealed off using TEFLON* gaskets. The specimens were typically 0.6 cm in diameter and 1.9 cm in length; the actual area of each specimen was measured prior to immersion in the electrochemical cell. The electrodes were polished with successively finer grades of silicon carbide paper, finishing with a 600-grit grade.

Prior to testing, the working electrode remained in the test solution overnight while the solution was sparged with the desired gas mixture. The polarization scans were then performed approximately 16 hours after immersion of the working electrode in the cell. Partial cathodic and full anodic polarization curves were obtained by scanning at a rate of 0.6 V/h and beginning the scan approximately 100 mV more negative than the free-corrosion potential. The current for the anodic curve was scanned until a current density of approximately 3×10^{-3} A/cm^2 was attained; the potential scan was then reversed until repassivation occurred and the current changed polarity, becoming cathodic. At the completion of the polarization curve, a new steel specimen was inserted into the polarization cell and immediately polarized to a potential of approximately -0.90 V SCE. Within five minutes of immersion, a fast anodic scan was performed using a potential scan rate of 18 V/hr.

A few potentiodynamic polarization curves were obtained in an autoclave at 250 C. In these tests, a pressure-balanced external Ag/AgCl reference electrode and an internal platinum counter electrode were used. With the exception of the modifications necessitated by the cell design, the experimental procedure used for the high pressure test was similar to that used at ambient pressure.

After completion of the polarization scans, the following polarization parameters were obtained from the polarization curves of potential (E) versus logarithm of current density (log i): i_{cor}, E_{cor}, i_{pas}, E_{pit}, E_{prot}, and i_{max} (i_{max} was typically obtained from fast scan curve only).

3.1.1.1 Metallurgical Studies

The majority of the metallurgical studies were performed in a single groundwater composition (referred to in the previous reports as 1X basalt groundwater) which is prepared according to a published procedure.(3.3)

---

*TEFLON is a registered trademark of the E. I. duPont de Nemours Company.

The electrochemical studies focused on the effects of steel cleanliness and structure on electrochemical behavior. Two steel compositions were examined, one ("doped" with phosphorus and sulfur) which is comparable to a 1018 composition and one ("clean") having low phosphorus and sulfur (see Table 3.1). These two steels were tested in the as-cast condition and in the hot-rolled condition, giving four combinations. Information on the preparation procedures and characterization of these materials is provided in the 1983-1984 Annual Report.[3.1]

Results of polarization tests performed on the materials at a scan rate of 0.6 V/hour in deaerated 1X basalt groundwater at 90 C are summarized in Table 3.2. Typical polarization curves are given in Figures 3.2 and 3.3. These data show that neither the cleanliness nor the structure of the steel had a pronounced effect on its electrochemical behavior in basalt groundwater.

As an extension of this work, polarization tests were run, in duplicate, on Ferrovac E in 1X basalt groundwater at 90 C. Ferrovac E is a high-purity iron containing only trace quantities of impurities (see Table 3.1) and represents an upper bound in cleanliness for a ferrous canister material. The results are summarized in Table 3.2 and Figures 3.4 and 3.5. Several features of the data are noteworthy. First of all, two types of behavior are readily apparent. In Specimen 1, the appearance of the polarization curve is similar to that reported for the other steels, exhibiting an active-to-passive transition, a passive region, and definite pitting and protection potentials. Values of the parameters for Ferrovac E were comparable to those previously reported for the other steels (see Table 3.2). On the other hand, the curve for Specimen 2 does not exhibit an active-to-passive transition, and the free-corrosion potential was in the passive potential range. A pitting potential is evident and hysteresis occurred on the reverse scan, indicating that pitting had occurred on the specimen. The protection and pitting potentials for Specimen 1 and 2 were similar, whereas the value for E_{corr} for Specimen 2 was more noble than that or Specimen 1. The most reasonable explanation for this behavior is that the solution in the cell containing the latter sample was contaminated with trace quantities of O_2 which spontaneously passivated the specimen.

The standard procedure used for these electrochemical experiments was to allow the specimens to equilibrate in the solution overnight before beginning the polarization experiment. Periodically, during this equilibration period, the specimens of Ferrovac E were visually examined, and evidence of pit initiation was found on the polished surfaces of both specimens. Following the polarization test, the attack on the specimen surfaces was somewhat greater, as one would expect based on the polarization behavior. Optical photographs of the specimens after testing, given in Figures 3.6 and 3.7, show small distinct pits, which were associated with deposit buildup on the specimen surfaces.

In summary, the results of these experimental studies indicate that variation in the composition of the steels from high-purity Ferrovac E

Table 3.1. Chemical compositions and other data on steels used in the corrosion studies.

SAE Number or Designation	Thermomechanical Treatment	Tests Used In	Dimensions	Composition, weight percent										
				C	Mn	P	S	Si	Cu	Sn	Ni	Cr	Mo	Al
1018	Hot-Rolled	Pitting Exposures	7.6 cm x 15.2 cm strip	0.18	0.77	0.017	0.019	0.22	--	--	--	--	--	--
1020[a]	Hot-Rolled	Electrochemical Pitting Monitor, Potentiodynamic Polarization	1.27 cm rod	0.20	0.46	0.011	0.032	0.17	0.38	0.027	0.014	0.018	0.024	--
1020[a]	Hot-Rolled	Slow Strain Rate	0.635 cm dia. rod	0.22	0.55	0.01	0.037	--	--	--	--	--	--	--
Clean BCL Steel	Cast or Hot-Rolled	Potentiodynamic Polarization	Ingot	0.18	0.49	0.004	0.002	0.30	0.006	--	0.002	0.007	0.00	0.10
Doped BCL Steel	Cast or Hot-Rolled	Potentiodynamic Polarization	Ingot	0.17	0.55	0.029	0.036	0.35	0.007	--	0.004	0.011	0.00	0.14
Ferrovac E	Cast	Potentiodynamic Polarization	Ingot	0.003	Tr[b]	--	--	Tr	--	--	Nil[c]	Nil	Tr	Nil

(a)Hot-rolled 1018 carbon steel not available in rod form.
(b)Tr = Trace.
(c)Nil = None detected.

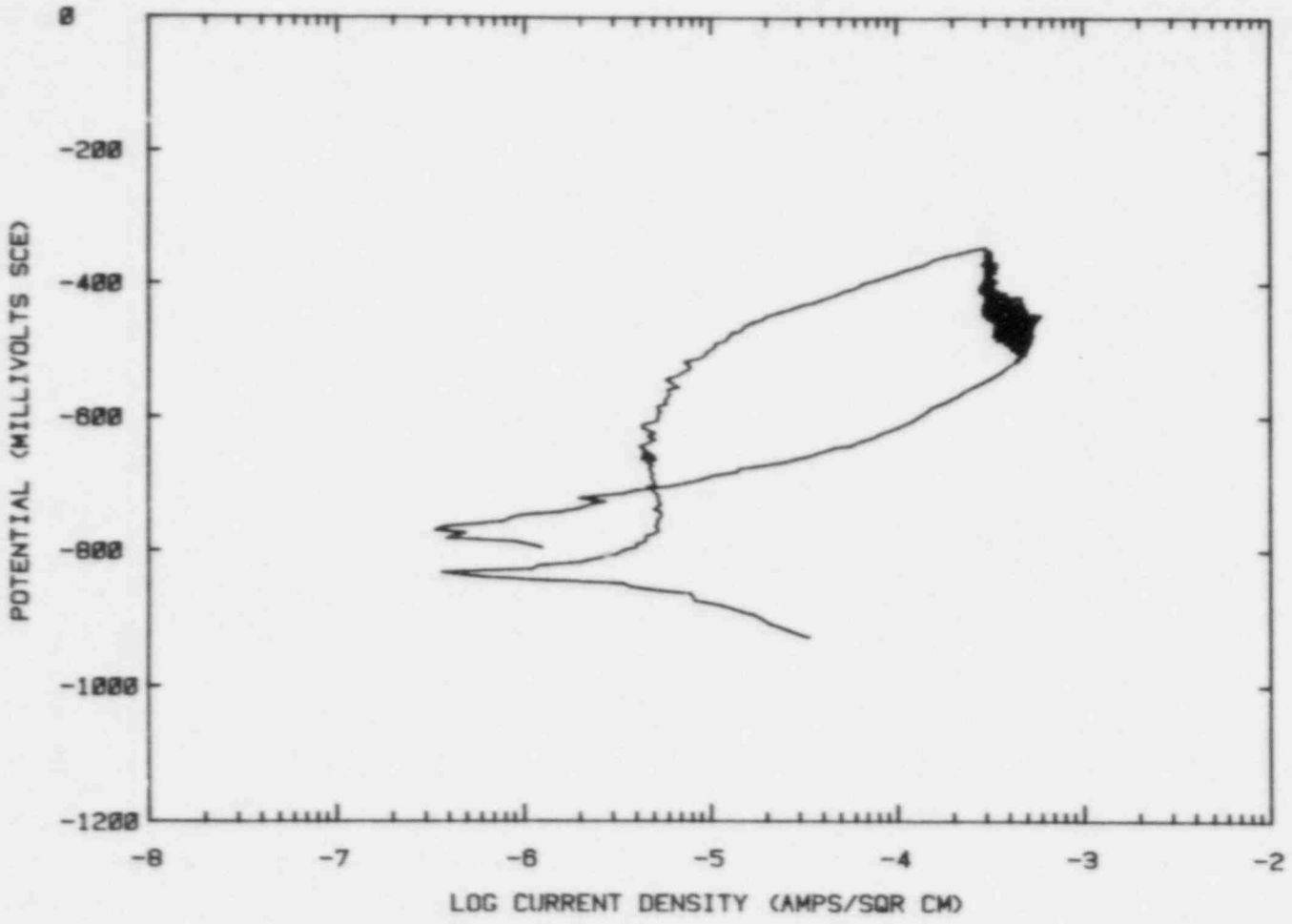

Figure 3.2. Potentiodynamic polarization curve for cast, doped BCL steel in basalt groundwater at 90 C polarized with a scan rate of 0.6 V/hr.

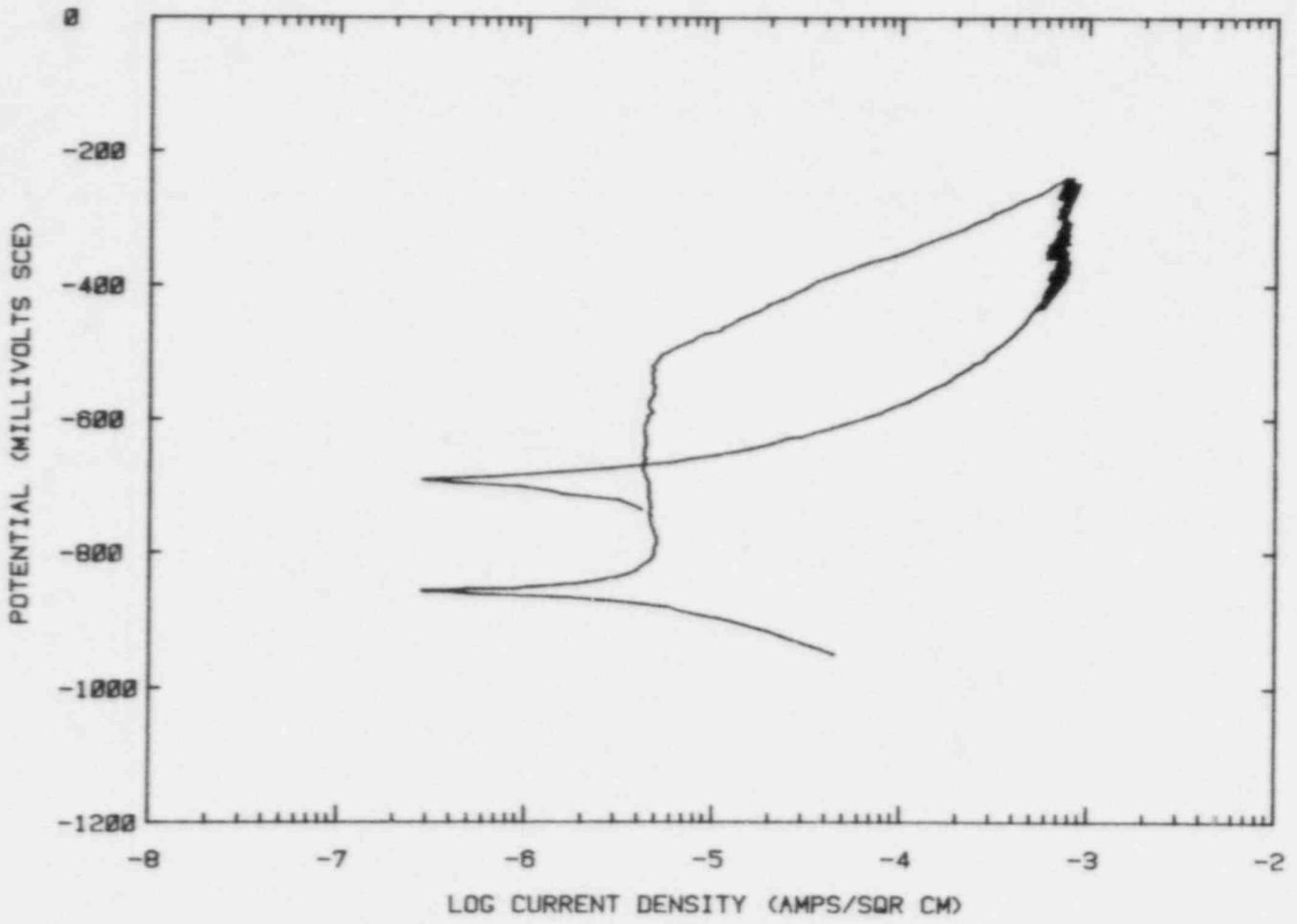

Figure 3.3. Potentiodynamic polarization curve for clean wrought BCL steel in basalt groundwater at 90 C polarized with a scan rate of 0.6 V/hr.

Table 3.2. Summary of results of potentiodynamic polarization tests performed on cast and wrought steels in deaerated basalt groundwater at 90 C and a scan rate of 0.6 V/hr.

Material		E_{cor}, Structure	E_{max}, V (SCE)	E_{pit}, V (SCE)	E_{prot}, V (SCE)	i_{cor}, V (SCE)	i_{max}, A/cm^2	i_{pas}, A/cm^2
Doped BCL Steel	Cast	-0.840	-0.745	-0.508	-0.698	3.7×10^{-6}	5.5×10^{-6}	4.6×10^{-6}
Doped BCL Steel	Wrought	-0.859	-0.793	-0.481	-0.659	6.8×10^{-6}	1.2×10^{-5}	5.7×10^{-6}
Clean BCL Steel	Cast	-0.859	-0.793	-0.471	-0.679	6.2×10^{-6}	1.0×10^{-5}	6.2×10^{-6}
Clean BCL Steel	Wrought	-0.859	-0.801	-0.508	-0.669	3.4×10^{-6}	5.2×10^{-6}	4.4×10^{-6}
Ferrovac E (1)		-0.869	-0.764	-0.432	-0.679	6.2×10^{-6}	1.2×10^{-5}	6.2×10^{-6}
Ferrovac E (2)		-0.754	(a)	-0.461	-0.764	1.9×10^{-7}	(a)	4.4×10^{-7}

(a) The free-corrosion potential of the specimen was more noble than the potential at maximum current (E_{max}).

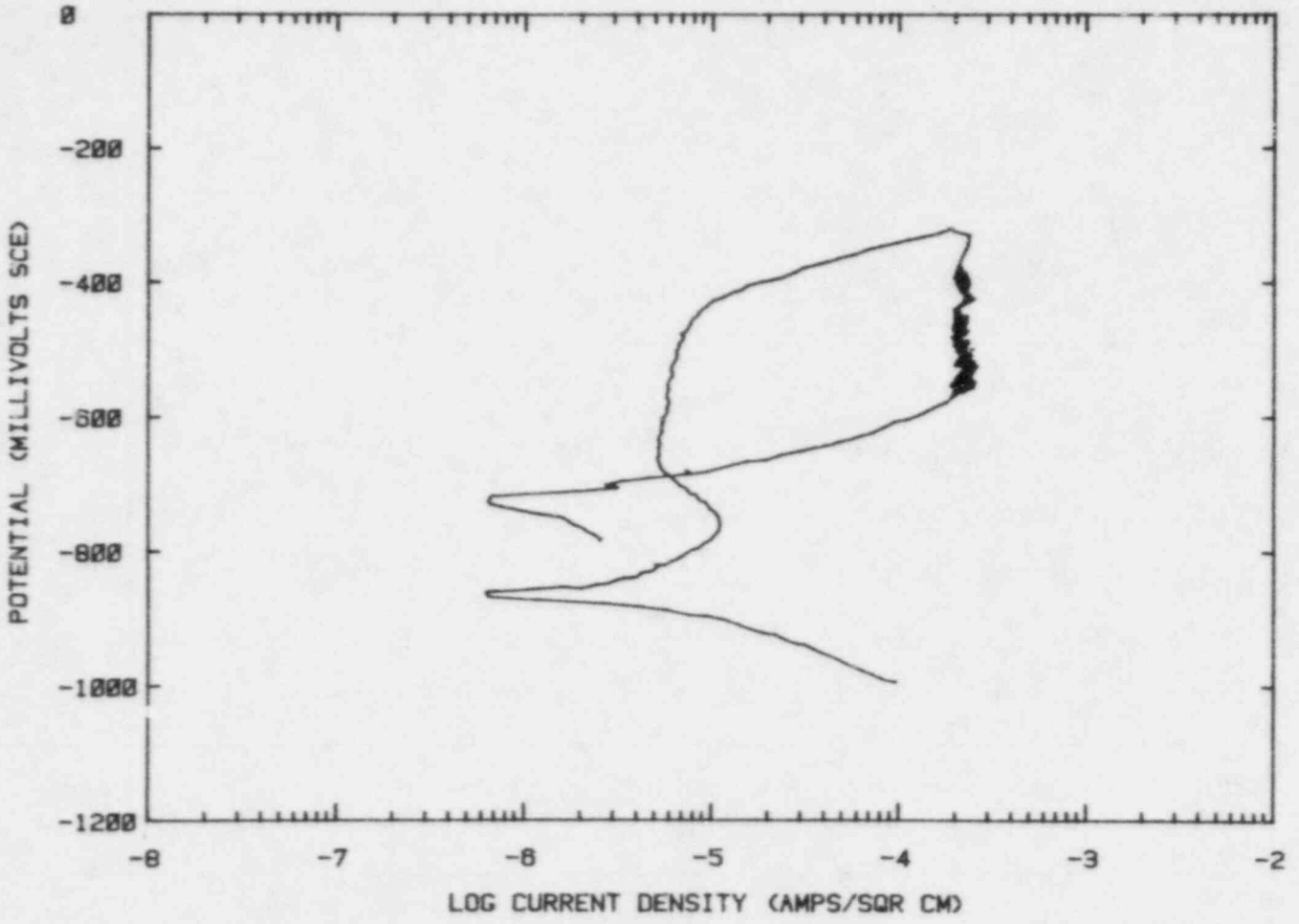

Figure 3.4. Potentiodynamic polarization curve for Specimen 1 of Ferrovac E in basalt groundwater at 90 C polarized with a scan rate of 0.6V/hr.

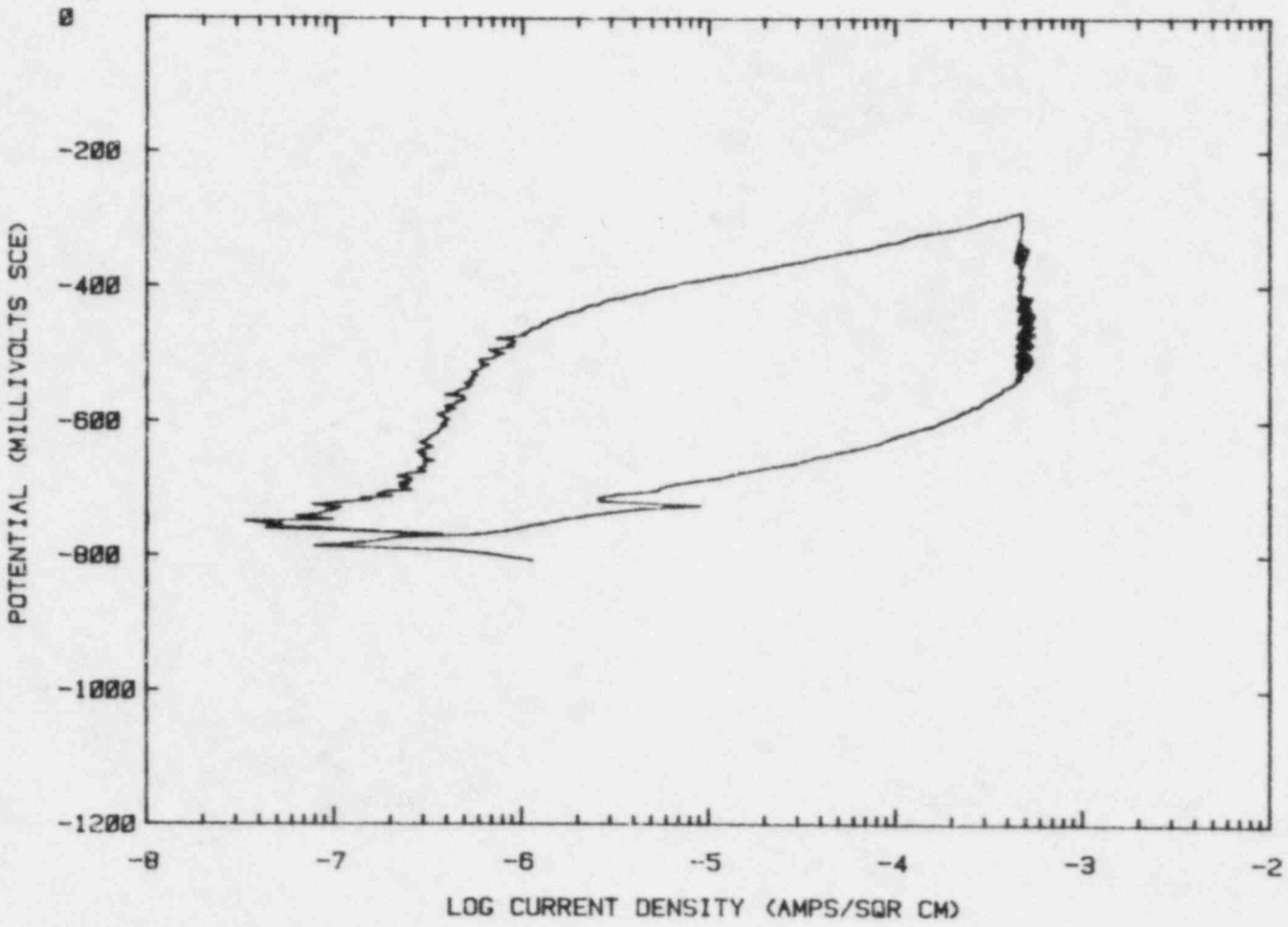

Figure 3.5. Potentiodynamic polarization curve for Specimen 2 of Ferrovac E in basalt groundwater at 90 C polarized with a scan rate of 0.6 V/hr.

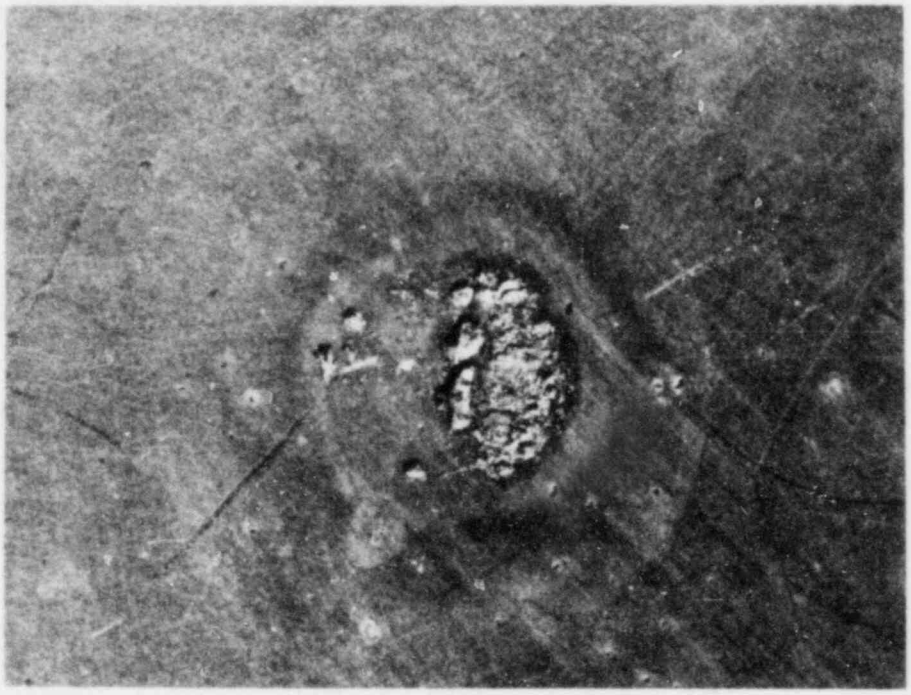

20X 6L615

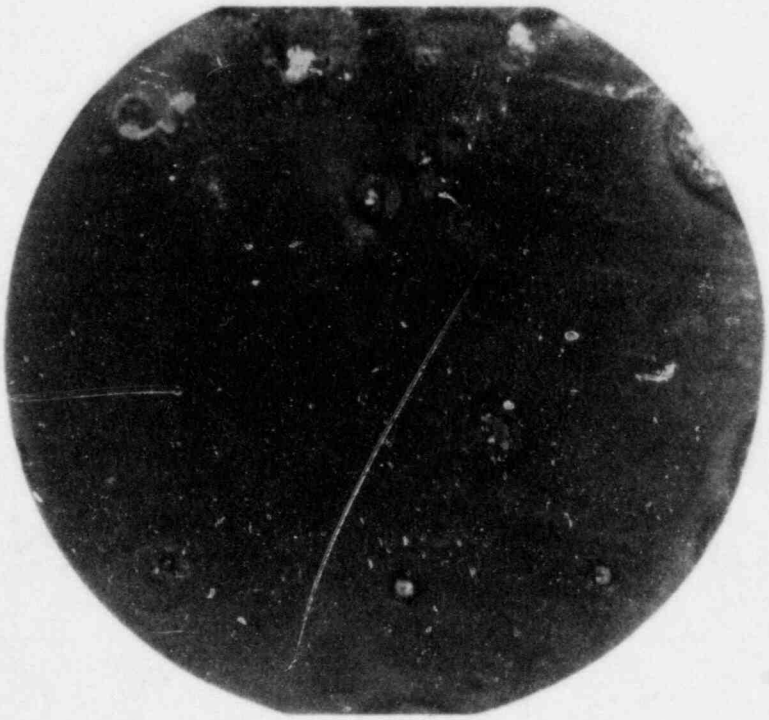

4X 6L614

Figure 3.6. Optical photographs of Ferrovac E Specimen 1 following potentiodynamic polarization testing in deaerated 1X basalt groundwater at 90 C.

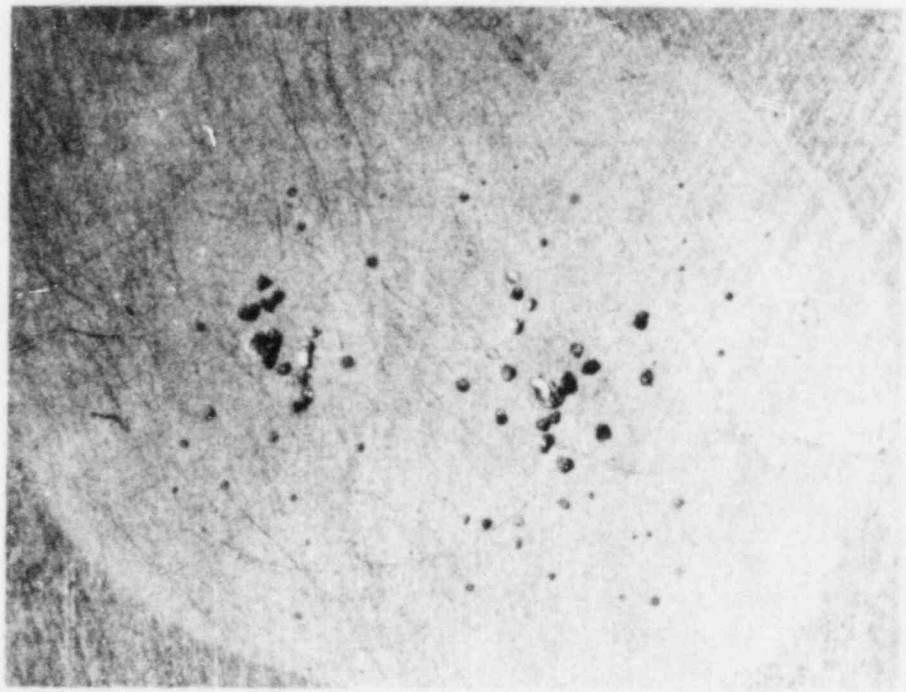

20X 6L617

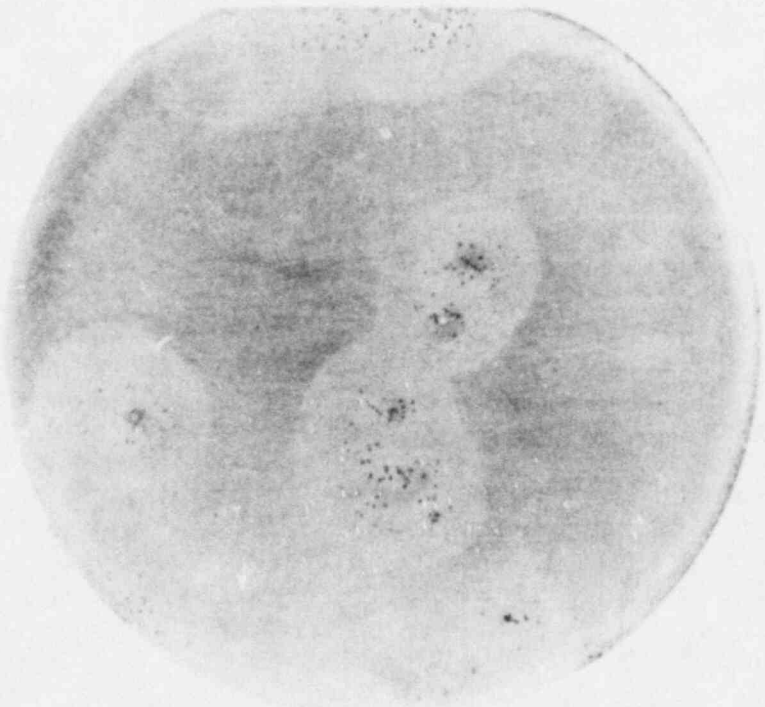

4X 6L616

Figure 3.7. Optical photographs of Ferrovac E Specimen 2 following potentiodynamic polarization testing in deaerated 1X basalt groundwater at 90 C.

to 1018 carbon steel does not have a marked effect on the electrochemical behavior in a simulated basalt repository environment. Since close correlation between electrochemical behavior and pit initiation has been established for many environments, these results indicate that minor variation in the composition of carbon steel or the use of a high purity steel will not have a marked influence on the pitting performance. The influence of steel composition on SCC cannot be fully assessed on the basis of these electrochemical data. Although the electrochemical behavior of Ferrovac E was not markedly different from 1018 carbon steel, it is well known that carbon content of steel can greatly influence SCC susceptibility, and the carbon content of these steels is considerably different. Thus, it is clear that properties other than the bulk electrochemical response must be considered in assessing the influence of metallurgical variables on SCC susceptibility. Since SCC in this system is intergranular in nature, the chemistry and electrochemistry of the grain boundaries, as influenced by bulk composition, also must be considered. In addition, the influence of steel composition on mechanical response of the material to the applied load must also be taken into account in assessing the influence of composition on SCC susceptibility.

3.1.1.2 Environmental Studies

Effect of Basalt Rock and Concentration of Basalt Groundwater

Potentiodynamic polarizaton curves were obtained on two of the steels characterized in Table 3.1: a wrought, doped BCL steel and a clean, cast BCL steel. These were tested in the standard basalt groundwater (1X) and a 10-fold concentration of this groundwater (10X) both in the presence of crushed basalt and in its absence. In the former tests, the solutions were equilibrated with crushed basalt by boiling overnight. Results of these studies, summarized in Figures 3.8 and 3.9, show small but systematic effects of groundwater chemistry on the electrochemical parameters. The corrosion potential (E_{cor}) and the potential at the current peak (E_{max}) shifted to slightly more negative values, and the passive current density (i_{pas}) decreased slightly upon increasing the solution concentration. A similar analysis of the effect of leaching of the basalt rock on these parameters indicated no systematic effect on the electrochemical parameters measured. Since the systematic shifts in these parameters were small, their relevance is difficult to ascertain with respect to waste-package performance.

Effect of Electrochemical-Potential Scan Rate

The effect of scan rate on the polarization behavior of several steels was studied in a 1X basalt groundwater at 90 C. These experiments provide information on the most likely potential ranges for stress-corrosion cracking susceptibility of the steels in repository environments. In the fast scan tests (18 V/hour), the curves are generated as soon as the specimen contacts the solution, whereas in the slow scan tests (0.6 V/hr), the specimens were allowed to equilibrate with the

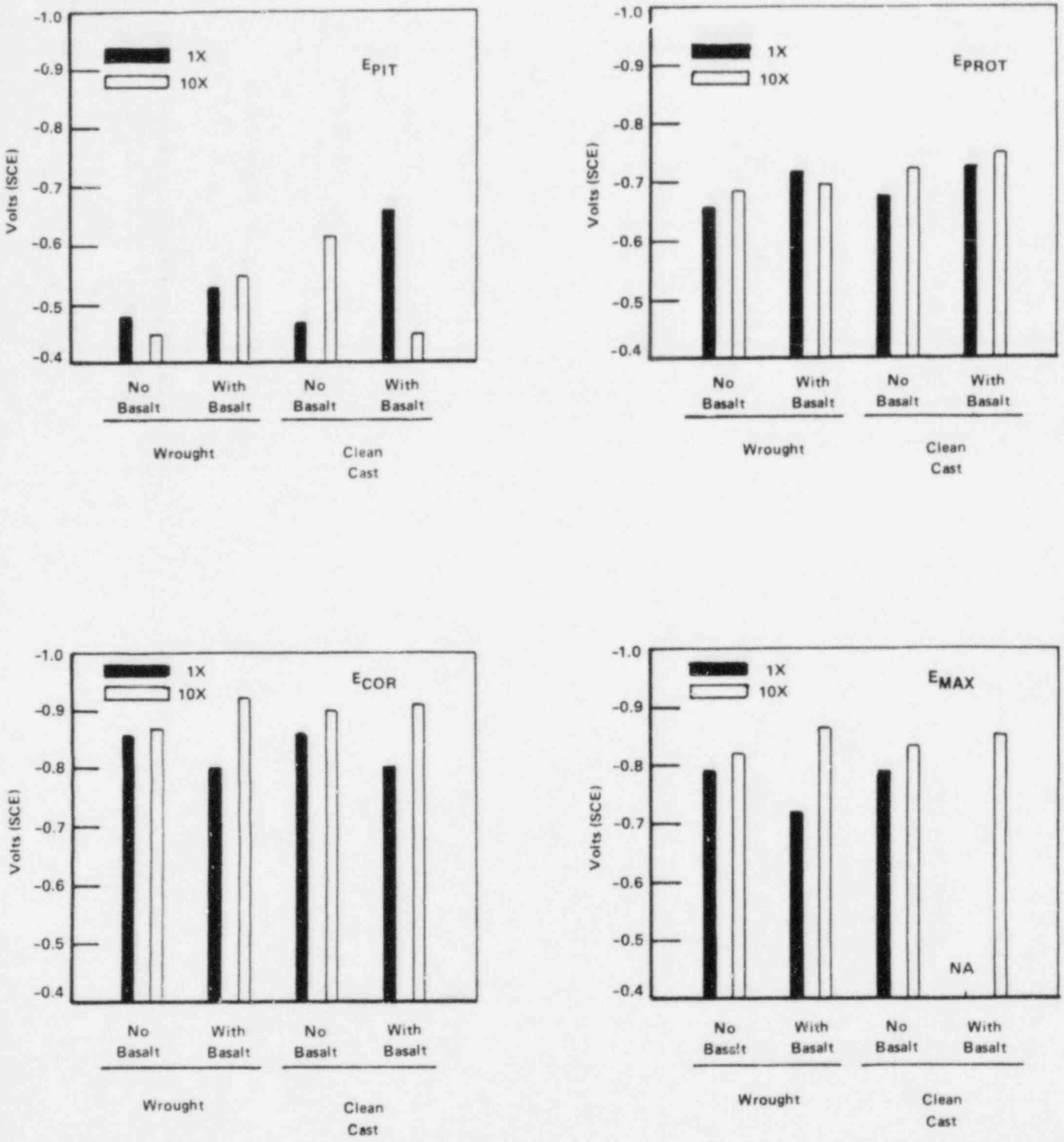

Figure 3.8. Electrochemical potential parameters taken from potentiodynamic polarization curves for wrought doped BCL steel and clean cast BCL steel in deaerated simulated basalt groundwater at 90 C.

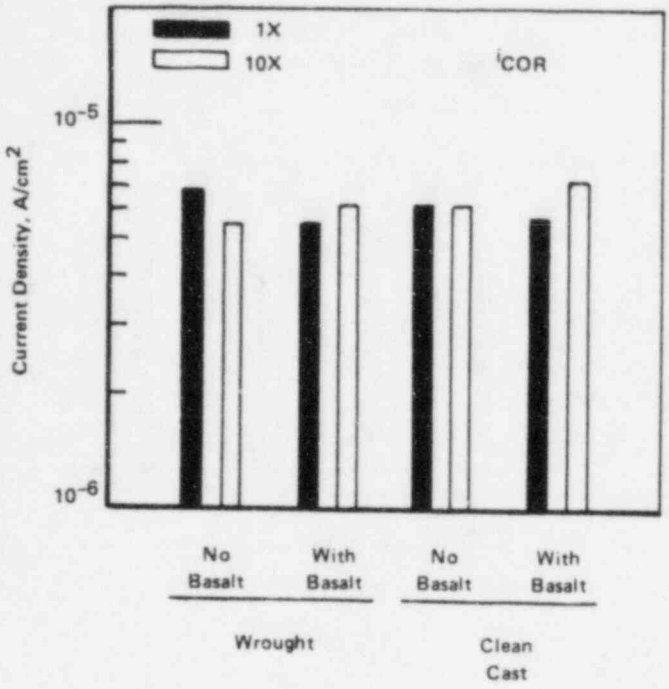

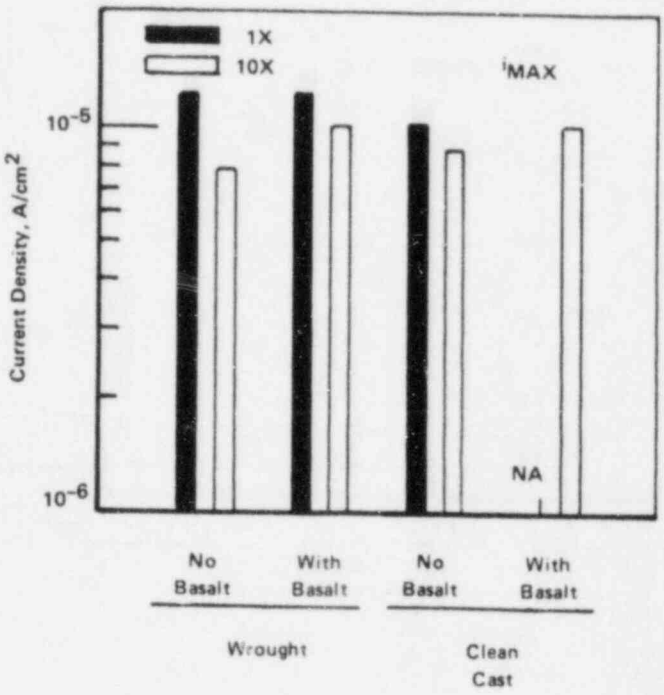

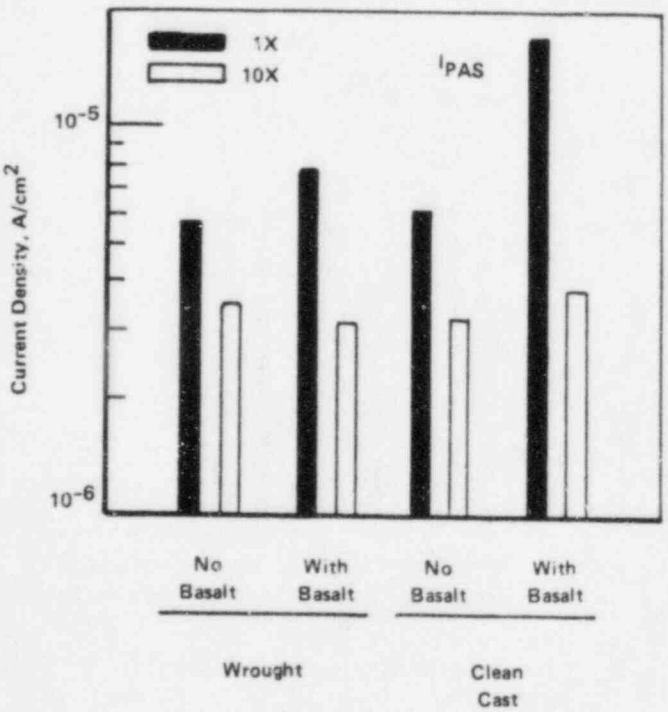

Figure 3.9. Current parameters taken from potentiodynamic polarization curves for wrought doped BCL steel and clean cast BCL steel in deaerated simulated basalt groundwater at 90 C.

solution overnight. The aim of the fast scan polarization tests is to obtain the maximum current density on relatively bare metal surfaces.

Results of these experiments, summarized in Figures 3.10 and 3.11 and Table 3.3, show that passive currents are considerably higher at the faster scan rates than at the lower scan rates, as expected. Empirically, it has been shown that stress-corrosion susceptibility of carbon steel reaches a maximum where the differences in current density between the fast and slow polarization scans are large. On this basis, one would expect that the most likely range for stress-corrosion cracking of carbon steel in basalt groundwater is between -0.78 V and -0.65 V (SCE). However, the differences in current between the fast and slow scans are small in comparison to potent cracking systems, and thus one would not expect a high degree of susceptibility to stress-corrosion cracking at 90 C in the 1X basalt groundwater.

Effect of Temperature

A potentiodynamic polarization curve was obtained for the wrought, doped BCL carbon steel in deaerated basalt groundwater at 250 C and at a scan rate of 0.6 V/hr. The results, given in Figure 3.12, show that the behavior of the steel at 250 C was qualitatively similar to that observed at 90 C, exhibiting an active-passive transition and definite pitting and protection potentials. Values for i_{cor}, i_{max}, and i_{pas} were somewhat higher at 250 C than at 90 C. The higher peak current may indicate that stress-corrosion cracking is more likely at 250 C than at 90 C. On the other hand, the hysteresis loop area at 250 C appears to be somewhat smaller than at 90 C, suggesting a greater tendency for pits to repassivate at the higher temperature. Because the polarization behavior is qualitatively similar at 250 C to that observed at 90 C, it was decided to perform the majority of polarization studies at 90 C.

Effect of Concentration of Species Present in the Groundwater

As discussed previously, results of the potentiodynamic polarization studies indicated that a uniform tenfold increase in chemical concentration of the groundwater did not have a pronounced effect on the electrochemical behavior. On the other hand, the literature survey[3.2] identified many species that are present in the groundwater or that may intrude into the repository or be generated by radiolysis that may significantly affect the localized corrosion behavior of carbon steel. Accordingly, electrochemical studies were undertaken to evaluate the influence of these species on electrochemical behavior. Because of the large number of species considered, a statistical approach was used.

A literature survey of the chemical species selected for the investigation was the basis for determining the high and low concentrations to be used in the experiments. The low concentration was based on that present in typical basalt groundwaters. The high concentration was typically 2 to 4 orders of magnitude higher than the low concentration.

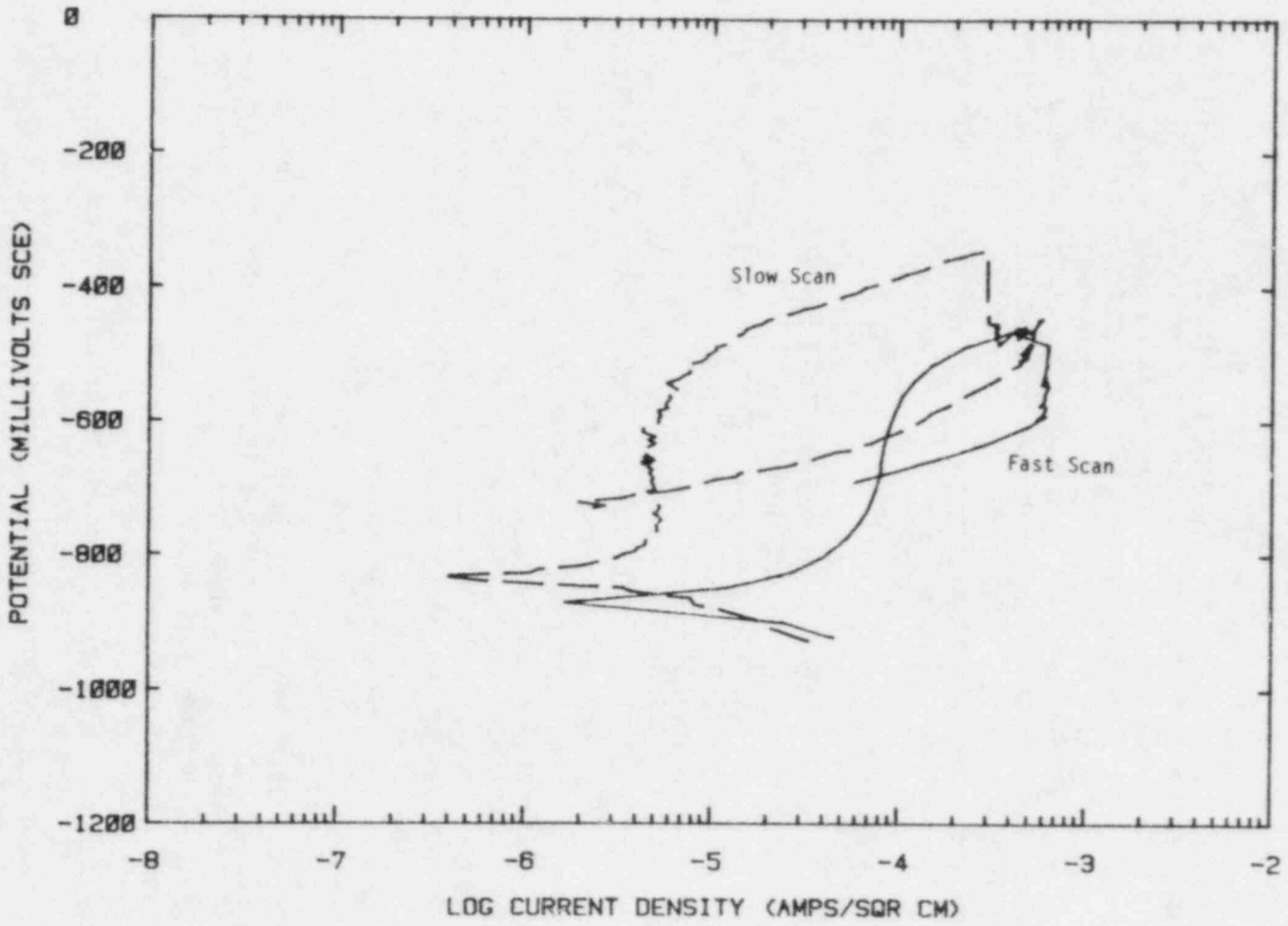

Figure 3.10. Effect of scan rate on the polarization behavior of cast doped BCL steel in deaerated basalt groundwater at 90 C.

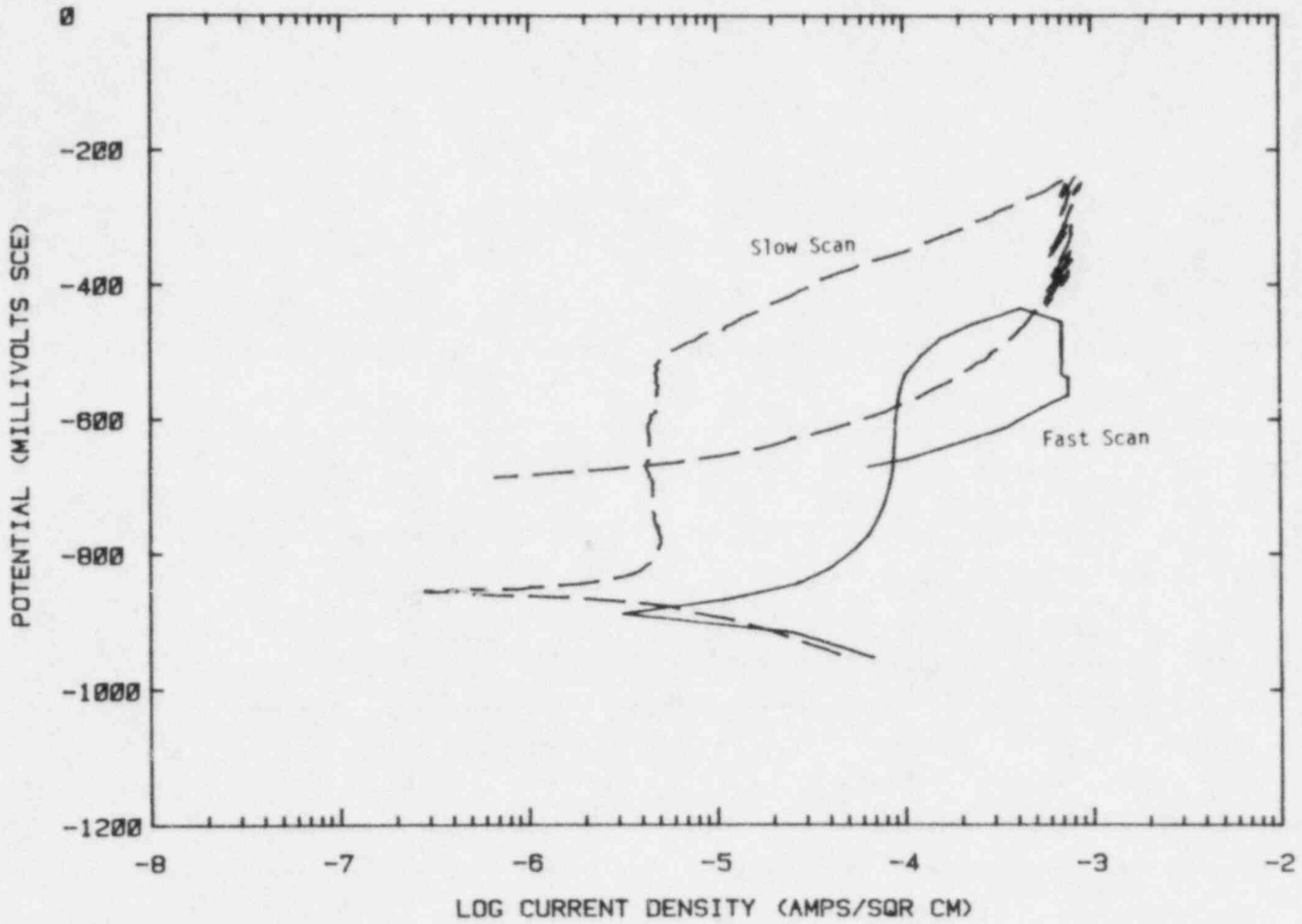

Figure 3.11. Effect of scan rate on the polarization behavior of clean wrought BCL steel in deaerated basalt groundwater at 90 C.

Table 3.3. Summary of results of potentiodynamic polarization tests performed on doped cast BCL steel and clean wrought steel in deaerated basalt groundwater at 90 C comparing fast scan rate and slow scan rate data.

Material	Scan Rate, V/hr	E_{cor}, V (SCE)	E_{max}, V (SCE)	E_{pit}, V (SCE)	E_{prot}, V (SCE)	i_{cor}, A/cm^2	i_{max}, A/cm^2	i_{pas}, A/cm^2
Doped Cast[a]	0.6	-0.858	-0.745	-0.508	-0.698	3.7×10^{-6}	5.5×10^{-6}	4.6×10^{-6}
Doped Cast	18	-0.886	(a)	-0.518	-0.669	1.9×10^{-5}	(a)	8.2×10^{-5}
Clean Wrought	0.6	-0.859	-0.801	-0.508	-0.669	3.4×10^{-6}	5.2×10^{-6}	4.4×10^{-6}
Clean Wrought	18	-0.896	(a)	-0.491	-0.649	1.6×10^{-5}	(a)	9.0×10^{-5}

(a) Polarization behavior did not exhibit a maximum current peak.

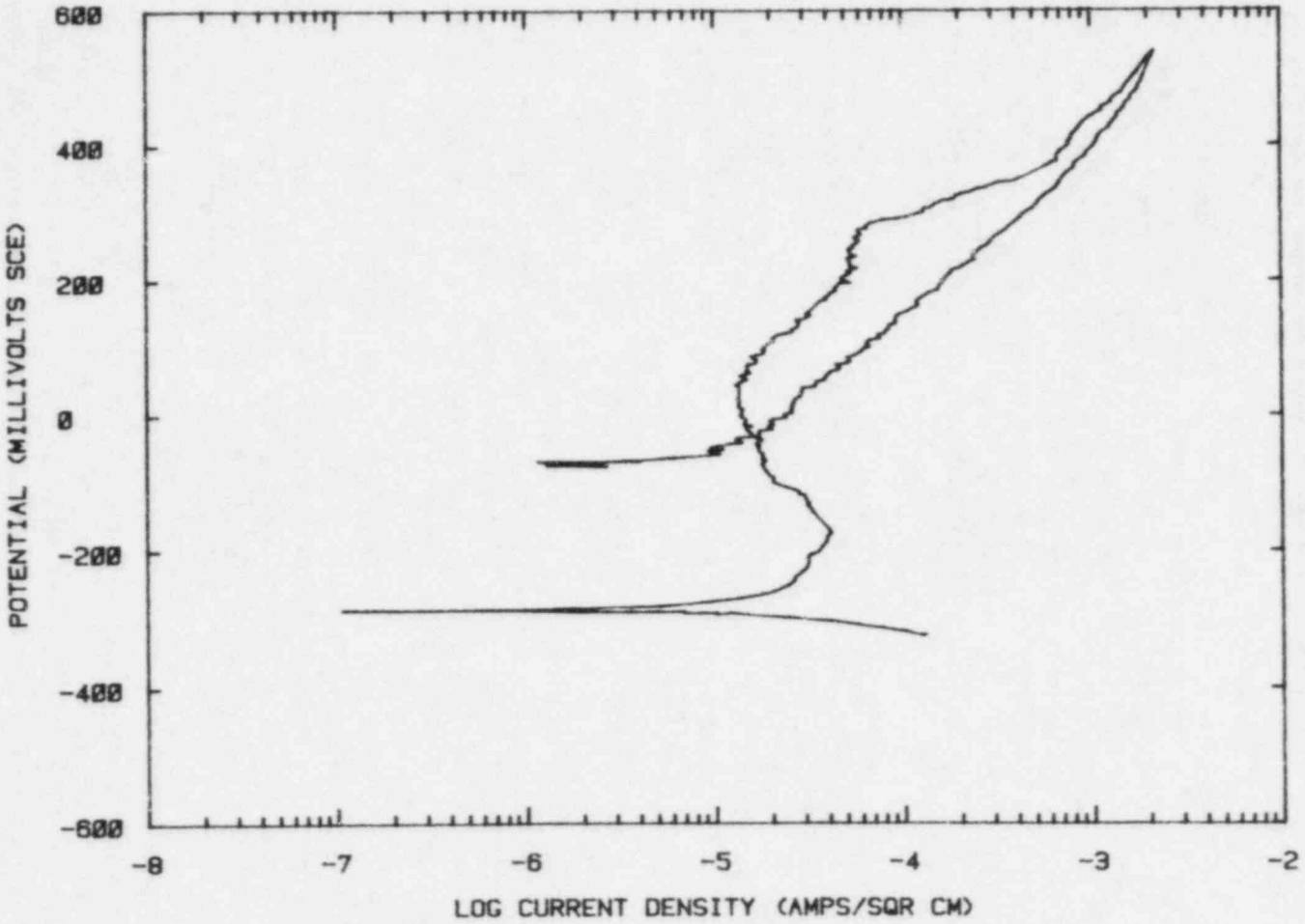

Figure 3.12. Potentiodynamic polarization curve for the wrought doped BCL steel in basalt groundwater at 250 C with a scan rate of 0.6 V/hr.

Table 3.4 gives the 15 species and their concentrations selected for examination during the preliminary 2-level design matrix. These include species present in the groundwater, those that may leach from the backfill, radiolysis products, and species that may intrude into the repository.

Table 3.5 shows typical concentrations which have been reported in the literature for the 15 species being examined in the present experiments, along with the concentrations of other species. Species such as sodium (Na^{+1}), potassium (K^{+1}), calcium (Ca^{+2}), and sulfate (SO_4^{-2}) were also included in the experimental matrix, but not as controlled variables. The concentrations of potassium and calcium were maintained constant, while sodium and sulfate ions were used to balance the cation and anion concentrations required for the 15 species to be added as variables. Justifications for the species examined in this task were presented in the first quarterly report.(3.4)

All of the experiments were performed on a commercially available, hot-rolled 1020 carbon steel at 90 C in argon-purified simulated groundwater solutions. The composition of the steel is given in Table 3.1. The parameters analyzed were E_{cor}, E_{prot}, E_{pit}, i_{cor}, i_{max}, and i_{pas}, as was defined in Figure 3.1. The studies, described in the following sections, were divided into 3 subtasks: the preliminary matrix, the main matrix, and effects of single species.

3.1.1.2.1 Preliminary Matrix of Experiments

The purpose of the preliminary matrix of experiments was to determine which of the 15 species discussed above have a significant effect on general corrosion, SCC, and pitting corrosion. The preliminary matrix was used as a screening test so that only species that significantly affect corrosion were examined in the main matrix.

To estimate the individual main effects of each of the fifteen species, a statistical design was used to define the optimal compositions of the test solutions. The statistical design was a partial factorial design of resolution IV. This design permits the main-effect terms of the fifteen variables to be estimated free and clear of other main-effect terms and of any two-factor interactions. Three-factor and greater interactions still confound the main-effect terms; however, these usually contribute only a small response compared to the main-effect-term response. Consequently, a good estimate of the main-effect terms could be calculated at the end of the screening matrix of experiments. Four experiments were also performed using the midpoint of each species concentration to provide an estimate of error for the polarization experiments.

At the completion of the screening matrix of experiments, a regression analysis was performed on the different corrosion parameters with the

Table 3.4. High and low concentrations of species selected for evaluation in the electrochemical experiments.

	Species	High Concentration	Low Concentration
1.	pH	9.3	6.0
2.	Cl^{-1}	100,000 ppm	100 ppm
3.	F^{-1}	10,000 ppm	10 ppm
4.	Fe^{+2}/Fe^{+3}	100 ppm	0.05 ppm
5.	Al^{+3}	1,000 ppm	0.1 ppm
6.	CO_3^{-2}/HCO_3^{-1}	1 M	0.001 M
7.	NO_3^{-1}/NO_2^{-1}	1,000 ppm [N]	0.1 ppm [N]
8.	PO_4^{-3}	1,000 ppm [P]	0.1 ppm [P]
9.	$BO_3^{-3}/B_4O_7^{-2}$	1,000 ppm [B]	1 ppm [B]
10.	SiO_3^{-2}	1,000 ppm [Si]	10 ppm [Si]
11.	H_2O_2	100 ppm	0
12.	ClO_4^{-1}	100 ppm	0
13.	O_2	2% (Vapor)	0
14.	CO	1% (Vapor)	0
15.	H_2	80% (Vapor)	1%

Table 3.5. Concentrations of species in basalt groundwater or in actual or simulated basalt repository environments.

	Ref. 3.5	Ref. (a)	Ref. 3.6	Ref. 3.7	Ref. 3.8	Ref. 3.9
1. pH	9.7(5.7)					
2. Cl^{-1}	98-297(500) ppm					
3. F^{-1}	11-42(50) ppm					4%[Fe_2O_3](d)
4. Fe^{+2}/Fe^{+3}	0-0.6(0.5)[Fe^{+2}] ppm	0.009 ppm				18%[Al_2O_3](d)
5. Al^{+3}	0.02(20) ppm	0.007 ppm				
6. CO_3^{-2}/HCO_3^{-1}	4-55/45-118(70/200) ppm					
7. NO_3^{-1}/NO_2^{-1}						
8. PO_4^{-3}		0.2[P] ppm				0.08%[P_2O_5](d)
9. $BO_3^{-3}/B_4O_7^{-2}$	0-1.5(5)[B^{+3}] ppm	1.3[B] ppm				
10. SiO_3^{-2}	30-170(3000)[Si] ppm				30[SiO_2] ppm	59%[SiO_2](d)
11. H_2O_2				0.34 ppm		
12. ClO_4^{-2}						
13. O_2				3.2 ppm	0.5%(c)	
14. CO						
15. H_2				0.02 ppm	76.6%(c)	
Na^{+1}	161-350(500)					2.2%(d)
K^{+1}	3-25(100)					0.7%[K_2O](d)
Ca^{+2}	0.8-10(100)					1.7%[CaO](d)
Mg^{+2}	0-0.2(50)					2.1%[MgO](d)
SO^{-2}	4-197(200)				300 ppm	
S^{-2}	0(100)					
N_2			25 ppm(b)		19.3%(c)	
CH_4			700 ppm(b)		0.3%(c)	
CO_2					2.3%(c)	
E_H	-0.5 to -0.53(+0.2 to -0.4)V_{SHE}					

(a) Data on trace elements from Well DC-6. Personal communications from Tom Jones to Jeff Means, 1983.
(b) Measurements at 25 C.
(c) Composition of gas phase for simulated irradiated Grande Ronde basalt groundwater.
(d) Composition of bentonite.

aid of a multiple regression routine on the MINITAB* statistical computer program. The regression analysis calculated the "F" ratio and the regression coefficient for each of the fifteen species. The "F" statistic is a ratio of two variances, i.e., the sum of squares explained by each factor when entered in the equation, divided by the residual mean square (error). In general, when the calculated "F" ratio for a factor is large, it means that a large amount of experimental variation is explained by this term compared to the error variation. If a calculated "F" ratio exceeds the appropriate tabulated "F" value, then it can be assumed that the solution variable has a statistically significant effect on a particular polarization parameter. A 90-percent probability that a species is significant is usually acceptable for most experimental work and implies that one accepts a 10-percent chance of being wrong in assuming that the factor has a significant effect.

The regression coefficients are multiplicative terms for the factors in a regression equation and were determined by a linear least square fit of the data. The regression coefficients determined in this study are calculated based on the high and low concentrations (+1 and -1) of the various chemical species. These factors are based on the design concentration range of the species indicated in Table 3.4. Because precipitation occurred in several solutions, the actual concentrations achieved in the test solutions were not the designed values. Therefore, the regression coefficients provide relative magnitudes of the measured effects only and are not meant to give a quantitative measure of the effects. Solutions are being analyzed, and actual chemical concentrations of the species examined will be used in the final analysis to provide the quantitative measure for the regression coefficients.

Polarization experiments were performed and polarization curves obtained for each of 33 solutions.(3.10) A wide range of behavior was observed by varying the concentration of the 15 species used in the screening matrix of experiments. Not all of the polarization parameters can be selected from the curves in all cases. Table 3.6 shows the polarization parameter values for 1018 carbon steel in solution 33. The variations in the polarization parameters for the four tests repeated for this solution indicate the reproducibility of the data obtained.

Results of the statistical analysis performed on the polarization data are given in Table 3.7. These data indicate the main effect for each of the 15 species on the six polarization parameters examined. The "F" value indicates the significance of the species, and the coefficient indicates the relative magnitude of the effect. Coefficients are given only for those species that have a significant effect, based on a

---

*Minitab Project, Statistics Dept., 215 Pond Laboratory, The Pennsylvania State University, University Park, PA, 16802, 1981.

75-percent or greater probability. For the majority of the discussions, a 90-percent or greater probability is typically required before an effect is considered significant. A positive coefficient indicates that an increase in concentration increases the value of the parameter, and a negative coefficient indicates than an increase in concentration of the species decreases the value of the parameter. Table 3.7 indicates that most species have an effect on at least one of the polarization parameters with the exceptions being perchlorate (ClO_4^-) and hydrogen (H_2), based on a 90-percent or greater probability of significance.

Table 3.6. Experimentally measured polarization parameters for solution 33 which represented the mid-point concentration of species defined in Table 3.4 (4 replicates, A-D).

Solution	i_{cor}, A/cm^2	E_{cor}, V(SCE)	i_{pas}, A/cm^2	E_{pit}, V(SCE)	E_{prot}, V(SCE)	$i_{max(fast)}$, A/cm^2
33A	2.50×10^{-6}	-.544	6.25×10^{-6}	-.293	-.576	1.12×10^{-4}
33B	1.10×10^{-6}	-.466	3.73×10^{-6}	-.31	-.576	1.17×10^{-4}
33C	1.37×10^{-6}	-.53	4.27×10^{-6}	-.232	-.576	8.97×10^{-5}
33D	1.48×10^{-6}	-.53	4.61×10^{-6}	-.31	-.576	1.11×10^{-4}

Table 3.8 summarizes the results of the statistical analysis for the main effects of the chemical species examined in the screening tests. Arrows are used to indicate the direction of the effect for each species that had a significant effect, based on a 90-percent or greater probability. Many of the effects were expected, such as O_2 and NO_3^- increasing E_{cor} and CO_3^{-2}/HCO_3^- decreasing E_{cor}. Other effects, such as Cl^- decreasing E_{cor}, were not particularly expected but can be explained since Cl^- would tend to make the steel more active and would thereby decrease E_{cor}. It is also noteworthy that several species had a significant effect on i_{pas}. Referring back to Table 3.7, NO_3^-/NO_2^- and $BO_3^{-3}/B_4O_7^{-2}$ had very large coefficients, indicating that these species greatly increased the passive current density with an increase in concentration, while SiO_3^{-2} and CO had large negative coefficients, indicating that these species greatly decreased i_{pas} with an increase in concentration.

Table 3.7. Results of statistical analysis indicating the effect of each chemical species on the polarization parameters measured by potentiodynamic polarization.

	E_{cor}		log i_{cor}		log i_{max}		log i_{pas}		E_{pit}		E_{prot}	
	F	Coef	F	Coef	F	Coef	F	Coef	F	Coef	F	Coef
pH	0.5		6.4	-0.34*	0.0		174	-0.18*	27	+0.31*	13	+0.22*
Cl	7.6	-0.06*	0.2		7.1	-0.23*	34	+0.06*	26	-0.25*	30	-0.32*
F	0.5		1.0		1.8	+0.11**	39	-0.08*	0.0		0.3	
Fe	0.9		0.9		0.2		86	+0.41*	0.0		0.3	
Al	1.1		0.8		0.0		36	+0.03*	1.7		0.1	
CO_3/HCO_3	8.4	-0.07*	0.3		25.1	+0.43*	3.6	-0.16**	2.9	+0.06**	0.9	
NO_3/NO_2	15.0	+0.09*	1.1		0.9		19	+0.64*	4.0	+0.13**	0.1	
PO_4	1.1		0.4		0.3		28	+0.10*	0.3		2.6	-0.10**
BO_3/B_4O_7	1.9	+0.03**	0.1		1.3		29	+0.78*	6.0	+0.14*	5.1	+0.13*
SiO_3	1.1		7.2	-0.36*	0.2		138	-0.85*	0.0		0.1	
H_2O_2	0.3		4.2	+0.27*	0.4		16	+0.25*	0.0		0.2	
ClO_4	0.2		0.1		0.0		1.2		0.2		1.3	
O_2	3.9	+0.05*	0.5		0.0		1.3		9.3	+0.13*	8.2	+0.15*
CO	0.1		0.1		0.0		22	-0.64*	1.1		0.0	
H_2	0.0		1.7	+0.17**	0.2		0.3		1.2		0.1	

*Greater than 90 percent probability that effect is significant.
**Greater than 75 percent but less than 90 percent probability that effect is significant.

Table 3.8. Summary of results of statistical analysis for the main effects of the chemical species based on a 90-percent or greater probability of significance.

	E_{cor}	log i_{cor}	log i_{max}	log i_{pas}	E_{pit}	E_{prot}
pH	-	↓	-	↓	↑	↑
Cl	↓	-	↓	↑	↓	↓
F	-	-	-	↓	-	-
Fe	-	-	-	↑	-	-
Al	-	-	-	↑	-	-
CO_3/HCO_3	↓	-	↑	-	-	-
NO_3/NO_2	↑	-	-	↑	-	-
PO_4	-	-	-	↑	-	-
BO_3/B_4O_7	-	-	-	↑	↑	↑
SiO_3	-	↓	-	↓	-	-
H_2O_2	-	↑	-	↑	-	-
ClO_4	-	-	-	-	-	-
O_2	↑	-	-	-	↑	↑
CO	-	-	-	↓	-	-
H_2	-	-	-	-	-	-

↑ means that an increase in the control parameter (e.g., pH) resulted in an increase in the response parameter. ↓ means that an increase in the control parameter resulted in a decrease in the response parameter.

The polarization parameter i_{max}, which is the maximum current density during the active peak as measured with the fast scan technique, has been used to indicate the tendency for stress-corrosion cracking. Generally, a higher stress-corrosion cracking tendency is indicated by a larger i_{max}. As expected, CO_3^{-2}/HCO_3^- produced a significant increase in i_{max} with increasing concentrations. Chloride, on the other hand, decreased i_{max} with increasing concentration. The effect of Cl was not expected and will be considered more closely in the main matrix of experiments.

Pitting behavior also was affected significantly by some of the species. Chloride, as expected, tended to decrease E_{pit} and E_{prot}, indicating more severe pitting conditions. Oxygen, BO_3/B_4O_7, and pH all tended to increase E_{pit} and E_{prot} with increasing concentration.

Based on the results of the statistical analysis, 11 species were selected to be examined in the main matrix of experiments. As shown in Table 3.8, H_2 and ClO_4^- had no effect on the polarization parameters measured, based on a 90-percent or greater probability of significance; therefore, these two species were removed from further consideration. It should be noted that ClO_4^- may have an effect that lasts for only a short period of time, and that it might have been overlooked in the present experiments. Therefore, it will be proposed that additional work be performed to consider the effects of ClO_4^-. The other two species that were not considered in the main matrix of experiments were Al^{+3} and PO_4^{-3}. Both of these species were removed since they only affected i_{pas} and the coefficients of the effects (see Table 3.7) were less than those of the other species. Fluoride also had only a small effect on i_{pas} but showed an effect on i_{max} with a probability of significance greater than 75 percent, but less than 90 percent. The decision, therefore, was made to retain fluoride in the main matrix.

Several of the two-factor interactions of the 15 species being examined were significant. Of particular interest to this program are interactions that are important when considering i_{max}, which indicates the tendency for stress-corrosion cracking, and when considering E_{pit} and E_{prot}, which indicate the tendency for pitting. However, the two-factor interactions were always confounded with several others, and individual two-factor interaction effects could not be determined from the preliminary matrix analysis.

3.1.1.2.2 Main Matrix of Experiments

The primary purpose of the main matrix of experiments was to examine the two-factor interactions that significantly affect corrosion behavior of carbon steel. Also, an improved estimate of the main effect of each of the 11 species in the main matrix of experiments was determined with the aid of the larger data base available. Table 3.9 shows the 11 species that were included in the main test matrix and the 21 two-factor interactions, that were also to be examined. The interactions included in Table 3.9 were based upon the results of the preliminary matrix analysis of group-interaction effects on the polarization parameters.

The design of the main matrix of experiments was accomplished with the computer aided design program called COED (Computer Optimized Experimental Design). The COED program is an interactive computer program that allows scientists involved in experimental investigation to plan their experiments to obtain maximum information at minimum cost. COED picks an optimal subset of experiments to be run from the total number of possible experiments. The selection process is based on determinant optimality theory; that is, it determines the experiments which minimize

the error of prediction at each of the possible experimental design points. COED can be used to generate an entire experimental design or to build upon an existing experimental effort.

Table 3.9. Main effects and interactions selected from screening tests to be examined in main test matrix.

Main Effects	Two-Factor Interactions	
pH	pH x Cl	Cl x H_2O_2
Cl	pH x CO_3	CO_3 x H_2O_2
F	pH x NO_3	CO_3 x O_2
Fe	pH x BO_3	NO_3 x BO_3
CO_3/HCO_3	pH x SiO_3	NO_3 x O_2
NO_3/NO_2	pH x H_2O_2	NO_3 x SiO_3
BO_3/B_4O_7	pH x O_2	BO_3 x SiO_3
SiO_3	pH x CO	BO_3 x H_2O_2
H_2O_2	Cl x CO_3	SiO_2 x O_2
O_2	Cl x NO_3	H_2O_2 x O_2
CO	Cl x BO_3	

In this case, the COED program was used to select 30 additional experiments which, when combined with the preliminary matrix experiments, would allow for the estimation of the 21 two-factor interactions listed in Table 3.9. The ability to estimate the main effects listed in the table carries over from the preliminary matrix. Table 3.10 gives the design matrix for the 30 additional test solutions which were selected by COED for the main matrix of experiments. The pluses and minuses refer to the high and low concentration values given in Table 3.4 except in the case of pH. In the main matrix of experiments, the nominal high and low values for pH were 11.5 and 6.0, respectively.

The combined data set (preliminary and main matrix) for each of the six polarization parameters was analyzed statistically as follows with the results reported in Tables 3.11 and 3.12. A full regression model including all eleven main effects and all 21 interaction terms was fitted to the data. To facilitate the comparison of widely varying species concentrations, all values (except for pH) were transformed to a -1 to +1 scale before the regression analysis was performed.

Table 3.10. Experimental design developed utilizing COED for main matrix of experiments.*

Experiment	pH	Cl	F	Fe	CO_3/HCO_3	NO_3/NO_2	BO_3/B_4O_7	SiO_3	H_2O_2	O_2	CO
37	+	+	-	+	+	+	-	-	-	-	+
38	+	-	+	-	+	+	-	+	+	-	-
39	+	+	-	-	-	+	-	+	+	+	-
40	+	+	-	+	+	-	-	+	+	+	-
41	+	-	-	+	-	+	+	+	+	+	+
42	-	-	-	-	+	+	-	+	-	-	+
43	-	+	-	-	+	+	+	-	+	-	+
44	+	-	+	-	-	+	+	+	-	-	+
45	-	+	-	+	-	-	+	+	+	+	+
46	+	-	-	-	+	+	+	-	+	-	-
47	+	-	-	+	-	+	-	-	-	+	-
48	+	+	+	-	-	+	-	-	+	-	+
49	+	-	+	-	+	-	+	+	-	+	-
50	+	-	+	-	-	-	-	-	+	+	+
51	+	-	-	+	+	+	+	-	-	+	+
52	+	-	-	+	-	-	-	+	+	-	-
53	+	+	-	+	-	-	+	+	-	+	+
54	+	+	-	-	-	-	-	-	-	-	-
55	+	+	+	-	+	-	+	-	+	+	-
56	+	-	-	+	-	-	+	-	+	-	-
57	-	-	+	+	-	+	+	+	+	-	-
58	+	-	-	+	+	-	-	+	-	-	+
59	-	-	+	+	+	+	-	-	+	+	+
60	+	+	-	-	+	+	+	+	-	-	-
61	-	-	-	+	-	-	+	-	-	+	+
62	+	+	+	+	+	-	+	-	-	-	-
63	+	+	+	-	+	-	+	+	+	-	+
64	+	+	+	+	-	+	+	-	+	+	-
65	+	+	-	+	+	+	-	+	-	+	+
66	+	-	-	+	+	-	-	-	+	+	+

*(+) and (-) refer to the high and low concentrations, respectively, as indicated in Table 3.4 (except for pH). Solutions 1 through 33 comprise the Preliminary Matrix.

Table 3.11. Main effects, intercept terms, and correlation coefficients resulting from statistical analysis of the combined preliminary and main-matrix data.

Main Effects	E_{cor} RC (OSL)[a]	log i_{cor} RC (OSL)	log i_{max} RC (OSL)	log i_{pas} RC (OSL)	E_{pit} RC (OSL)	E_{prot} RC (OSL)
pH	--	-0.87(0.00)	-0.47(0.00)	-0.52(0.00)	0.309(0.00)	0.120(0.00)
Cl	-0.072(0.01)	--	-0.14(0.05)	0.14(0.05)	-0.239(0.00)	-0.347(0.00)
F	--	--	0.18(0.01)	0.10(0.17)	--	--
CO_3	-0.39(0.01)	--	0.29(0.00)	-0.08(0.25)	0.143(0.00)	--
NO_3	0.076(0.00)	-0.20(0.03)	-0.11(0.14)	--	0.071(0.04)	--
BO_3	--	--	--	--	0.105(0.00)	0.134(0.00)
SiO_3	0.023(0.11)	-0.20(0.03)	--	-0.19(0.01)	--	--
H_2O_2	--	0.22(0.01)	--	0.14(0.04)	--	--
O_2	0.036(0.01)	--	--	--	0.066(0.06)	--
CO	0.021(0.15)	--	--	--	--	--
Intercept	-0.590	-5.54	-3.97	-5.04	0.061	-0.222
R^2-full[b]	72% (45%)	77% (54%)	72% (43%)	81% (57%)	86% (71%)	81% (59%)
R^2-final[c]	66% (57%)	68% (62%)	64% (55%)	75% (63%)	83% (78%)	76% (71%)

(a)RC = regression ccefficient; OSL = observed significance level. RC > 0 indicates that the parameter increases with increasing concentration; RC < 0 indicates that the parameter decreases with increasing concentration. A small OSL indicates that the term is significant.

(b)"R^2-full": coefficients of determination for the fitted regression models including all 32 terms.

(c)"R^2-final: coefficients of determination for the final model. The "R^2" term is the percentage of total variability explained by the model. The term in parentheses is the R^2 value after adjustment for degrees of freedom.

Table 3.12. Interaction effects resulting from statistical analysis of the combined preliminary and main matrix data.

Interaction Effects	E_{cor} RC (OSL)*	log i_{cor} RC (OSL)	log i_{max} RC (OSL)	log i_{pas} RC (OSL)	E_{pit} RC (OSL)	E_{prot} RC (OSL)
pH x Cl	-0.033(0.05)	0.16(0.11)	0.19(0.02)	--	--	-0.196(0.00)
pH x CO_3	0.030(0.08)	--	--	0.11(0.20)	0.186(0.00)	0.088(0.08)
pH x NO_3	-0.037(0.03)	--	--	--	-0.060(0.15)	--
pH x BO_3	--	--	-0.19(0.02)	-0.15(0.06)	-0.071(0.08)	--
pH x SiO_3	--	--	--	0.13(0.13)	--	0.077(0.12)
pH x H_2O_2	--	--	0.012(0.15)	--	--	--
pH x O_2	--	--	--	0.12(0.15)	-0.106(0.01)	-0.087(0.08)
Cl x CO_3	0.036(0.01)	-0.28(0.00)	--	-0.16(0.02)	0.183(0.00)	--
Cl x NO_3	--	0.20(0.03)	--	0.14(0.05)	--	--
Cl x BO_3	--	--	-0.14(0.06)	-0.19(0.01)	-0.072(0.04)	-0.104(0.01)
Cl x H_2O_2	--	--	-0.17(0.02)	-0.14(0.06)	--	--
CO_3 x H_2O_2	-0.030(0.04)	--	--	-0.11(0.12)	--	--
NO_3 x BO_3	--	--	--	--	-0.051(0.14)	--
NO_3 x SiO_3	--	--	--	-0.07(0.34)	--	--
NO_3 x O_2	-0.023(0.11)	0.17(0.06)	0.23(0.00)	0.22(0.00)	0.089(0.01)	0.083(0.05)
BO_3 x SiO_3	--	--	--	--	--	-0.081(0.06)
BO_3 x H_2O_2	--	0.022(0.02)	--	--	--	--
SiO_3 x O_2	0.029(0.05)	--	-0.12(0.12)	-0.14(0.06)	--	--
H_2O_2 x O_2	-0.027(0.07)	--	--	--	--	--

*RC = regression coefficient; OSL = observed significance level. RC > 0 indicates that the parameter increases with increasing concentration; RC < 0 indicates that the parameter decreases with increasing concentration. A small OSL indicates that the term is significant.

The transformation was accomplished by using the equation

$$X^* = (2X - M)/M$$

where X is the species concentration, M is the maximum concentration tested, and X* is the transformed species concentration. Note that X*=1 if X=M and X*=-1 if X=0 (where 0 equals the minimum concentration). The transformation formula for pH is

$$pH^* = (pH-8.75)/2.75 .$$

Thus, pH*=1 if pH=11.5 and pH*=-1 if pH=6.0 .

The transformed variables described above were used as the independent variables corresponding to the main effects. The independent variables corresponding to the interaction effects were formed by multiplying the transformed variables for the pair of species involved.

The "R^2-full" values reported in Table 3.11 are the coefficients of determination from the fitted regression models including all 32 terms. The R^2 term may be interpreted as the percentage of total variability explained by the model. The value in parentheses is the R^2 value after adjustment for degrees of freedom. Many of the terms in the full models contributed very little to their predictive ability. To arrive at final models for each of the polarization parameters, a stepwise regression analysis was performed. A stepwise regression analysis selects a best subset of independent variables to include in a regression model. Regardless of the method employed, the goal of a stepwise regression analysis is to eliminate insignificant terms and retain significant ones.

Three stepwise regression techniques were employed here. They are

1. Forward Selection. This technique begins with no variables in the model and adds variables one at a time. For each variable not in the model, an F statistic is calculated which reflects the variable's contribution to the model if it were to be included next. The variable contributing most to the model is added provided that the F statistic is significant at the 15 percent significance level. The procedure continues adding variables to the model until none of the variables excluded from the model meet the 15 percent significance level criterion.

2. Backward Elimination. This technique begins with all of the variables in the model and eliminates variables one at a time. For each variable in the model, an F statistic is calculated and the variable contributing least to the model is eliminated, provided that the F statistic is not significant at the 15 percent significance level. The procedure continues eliminating variables from the model until all of the variables in the model are significant at the 15 percent level.

3. Stepwise. This technique begins with no variables in the model. However, variables which are added to the model do not necessarily stay there. Variables are added one at a time using the same criterion as with forward selection. After a variable is added, however, a backward elimination is performed to delete any variable which does not contribute significantly to the model. This process continues until no variables can be added or deleted.

The final model for each polarization parameter was chosen to include each of the 32 terms (11 main effects and 21 interactions) that appeared in at least one of the three stepwise regression models. The coefficients of determination for the final model are reported in the "R^2-final" row of Table 3.11. Note that the R^2 values that are adjusted for degrees of freedom are higher for the final model than for the full model in all six cases. This is a reflection of the fact that the terms eliminated from the full models did not contribute significantly to their predictive ability.

The regression coefficients (RC) and intercept terms for the final model are also reported in Tables 3.11 and 3.12 along with the corresponding observed significance level (OSL). In each case, the OSL may be interpreted as the probability of observing a regression coefficient as large (in absolute value) as that observed under the hypothesis that the term is insignificant. Thus, a small OSL indicates that a term is significant. The regression coefficients for the main effects (Table 3.11) may be interpreted as one-half the change in the polarization parameter that would be produced by changing the concentration of the corresponding species from low to high. A positive coefficient indicates that the polarization parameter increases with increasing species concentration; a negative coefficient indicates a decrease with increasing species concentration. For example, E_{cor} increases approximately 0.152 units as the NO_3 concentration increases from zero to 1000 mg/l, and E_{pit} decreases approximately 0.478 units as the Cl concentration increases from zero to 100,000 mg/l. The regression coefficients for the interaction terms (Table 3.12) are the multipliers in the regression model for the individual interaction terms. If two species acted independently on the polarization parameter, the corresponding two-factor interaction regression coefficient would be zero.

Combining the intercept and regression coefficients into a final model gives, for example,

$$\log i_{cor} = -5.54 - 0.87\ (pH^*) - 0.20\ (NO_3^*)$$
$$-0.20\ (SiO_3^*) + 0.22\ (H_2O_2^*) + 0.16\ (pH^*)\ (Cl^*)$$
$$-0.28\ (Cl^*)\ (CO_3^*) + 0.20\ (Cl^*)\ (NO_3^*)$$
$$+0.17\ (NO_3^*)\ (O_2^*) - 0.22\ (BO_3^*)\ (H_2O_2^*)$$

as a predictive model for i_{cor}. The variables appearing in this model are the transformed species concentrations described earlier in this section. In each final model, some terms had no significant contribution and were thus excluded from that model. It should be noted that in Tables 3.11 and 3.12 the Fe main effect term and the pH x CO and CO_3 x O_2 interaction terms were excluded from all six final models.

The regression analysis was based on the design concentrations (Tables 3.6 and 3.7). Because of precipitation of some of the species, the actual concentrations which were present in the solution during the test differ from the design concentrations. Solution samples were obtained just prior to each test and these solutions will be analyzed early in the next fiscal year. Therefore, the results presented here are qualitative and at present a large significance will not be placed on the quantitative measure of the estimate for the regression coefficients.

Table 3.13 summarizes the results for the main effects of the chemical species presented in Table 3.11. For comparison purposes, the results of the preliminary matrix also are summarized in Table 3.13. These results show that the analyses of the preliminary and main matrices compare favorably for most of the response parameters. A few additional species that were not identified in the preliminary matrix were identified as significant in the main matrix. This behavior is not surprising and simply reflects the greater sensitivity to trends in the main matrix due to the larger data base.

Two additional species were shown to have an effect on i_{max}. An increase in the solution pH was shown to decrease i_{max} while an increase in F was shown to increase i_{max}. Two additional species were shown to have a beneficial effect on E_{pit}. An increase in both CO_3/HCO_3 and NO_3/NO_2 was shown to increase E_{pit}. Therefore, the only species found to promote pitting was Cl, which decreased both E_{pit} and E_{prot} when its concentration was increased. It has been suggested that E_{prot} is a more important parameter than E_{pit} when describing the beneficial and detrimental effects of species toward pitting. This would suggest that pH and BO_3/B_4O_7 are the two variables that would have the most beneficial effect toward pitting.

The passive current density, i_{pas}, was the only response parameter where there was a significant discrepancy between the preliminary and main matrix. The species, CO, BO_3, NO_3, Fe, and F were found to affect i_{pas} in the preliminary matrix, but not in the main matrix. Since the preliminary matrix was based on the minimum data needed to determine the main effects, it is possible that a single erroneous test biased the results. It is interesting to note that in the preliminary matrix, i_{pas} was the only parameter that the species Fe and CO affected; thus, these species will be omitted in future experiments.

Table 3.13. Summary of results of statistical analysis comparing main matrix with preliminary matrix.(a)

	E_{cor}	log i_{cor}	log i_{max}	log i_{pas}	E_{pit}	E_{prot}
pH	--	↓↓	-↓	↓↓	↑↑	↑↑
Cl	↓↓	--	↓↓	↑↑	↓↓	↓↓
F	--	--	-↑	↓-	--	--
Fe	--	--	--	↑-	--	--
CO_3/HCO_3	↓↓	--	↑↑	--	-↑	--
NO_3/NO_2	↑↑	-↓	--	↑-	-↑	--
BO_3/B_4O_7	--	--	--	↑-	↑↑	↑↑
SiO_3	--	↓↓	--	↓↓	--	--
H_2O_2	--	↑↑	--	↑↑	--	--
O_2	↑↑	--	--	--	↑↑	↑-
CO	--	--	--	↓-	--	--

(a) ↑ or ↓ : increase or decrease, respectively, in main matrix response parameter (E_{cor}, etc.) resulting from increase in control parameter (pH, Cl, etc.).

↑ or ↓ : increase or decrease, respectively, in preliminary matrix response parameter resulting from increase in control parameter.

-- : indicate that no effect was observed in either main or preliminary matrix.

Table 3.14 summarizes the findings for the two-factor interactions determined by the regression analysis of the main matrix data. The majority of interactions examined (15 out of 21) affected the behavior of at least one polarization parameter, based on a 85-percent or greater probability of significance. The two-factor interactions that affected at least three of the six polarization parameters examined were: pH x Cl, pH x CO_3, pH x BO_3, Cl x CO_3, Cl x BO_3, and NO_3 x O_2. The data show the importance of considering two-factor interactions when describing the polarization behavior, and therefore the corrosion behavior, of carbon steel in these environments.

Table 3.14. Two-factor interactions as determined by main matrix analysis (based on 85 percent or greater probability of significance).

	E_{cor}	log i_{cor}	log i_{max}	log i_{pas}	E_{pit}	E_{prot}
	(a)					
pHxCl	↓	↑	↑	--	--	↓
$pHxCO_3$	↑	--	--	--	↑	↑
$pHxNO_3$	↓	--	--	--	--	--
$pHxBO_3$	--	--	↓	↓	↓	--
$pHxSiO_3$[b]	--	--	--	--	--	--
$pHxH_2O_2$[b]	--	--	--	--	--	--
$pHxO_2$	--	--	--	--	↓	↓
pHxCO[b]	--	--	--	--	--	--
$ClxCO_3$	↑	↓	--	↓	↑	--
$ClxNO_3$	--	↑	--	↑	--	--
$ClxBO_3$	--	--	↓	↓	↓	↓
$ClxH_2O_2$	--	--	↓	↓	--	--
$CO_3xH_2O_2$	↓	--	--	--	--	--
CO_3xO_2[b]	--	--	--	--	--	--
NO_2xBO_3[b]	--	--	--	--	--	--
NO_3xSiO_3[b]	--	--	--	--	--	--
NO_3xO_2	--	↑	↑	↑	↑	↑
BO_2xSiO_3	--	--	--	--	--	↓
$BO_2xH_2O_2$	--	↓	--	--	--	--
SiO_3xO_2	↑	--	--	↓	--	--
$H_2O_2xO_2$	↓	--	--	--	--	--

(a) ↑ or ↓: increase or decrease in response parameter (E_{cor}, log i_{cor}, etc.) resulting from increase in the product of two control parameters (pHxCl, $pHxCO_3$, etc.).

Dashes indicate that no effect was observed.

(b) Interaction terms not included in the final model.

Several of these interaction effects will be examined further during the next year's research. Also, these two-factor interactions will be reanalyzed when the solution analyses become available during the next year's work.

3.1.1.2.3 Effect of Single Species

The purpose of these experiments was to examine the individual effects of each of the 15 species on the polarization behavior in the absence of the other species. This is to aid in interpreting the polarization behavior in the more complicated solutions. The statistical analyses performed in the prior sections determined the effects of the chemical species on specific polarization parameters. Although this approach is necessary to quantify main effects in the presence of other species and to determine interactive effects, it does not provide an entire picture of the polarization behavior change due to the addition of these chemical species. Therefore, in the experiments in this subtask, the base solution was standard (previously referred to as 1X) simulated basalt groundwater; one species at a time was increased to the level given in Table 3.7 and the resulting polarization behavior determined.

The polarization data for 1020 steel in groundwater indicate active-passive pitting behavior. In the following discussion, polarization analyses are compared with this behavior to determine the effects of adding various chemical species to the groundwater. The polarization behavior of 1020 steel in groundwater alone was compared to that of steel in groundwater with 100,000 g/m^3 Cl^- added. The addition of Cl^- resulted in a decrease in the pitting potential, E_{pit}, which was expected.

The addition of 10,000 g/m^3 F^- expanded the passive region for the steel in basalt groundwater by increasing E_{pit}. This effect was somewhat unexpected, but it is known that some species that promote passivation can promote SCC.

The addition of 100 g/m^3 each of Fe^{+2} and Fe^{+3} produced a slight increase in the passive current density and a slight decrease in the protection potential, E_{prot}. The decrease in E_{prot} indicates an increase in susceptibility to pitting and/or crevice corrosion.

The addition of 1000 g/m^3 Al^{+3} had a significant effect on the polarization behavior of 1020 steel. The passive current density was reduced. The pitting potential and E_{prot} were both greatly decreased; in fact, E_{prot} was more negative than the free-corrosion potential, E_{cor}, indicating that pitting and/or crevice corrosion could occur at E_{cor}. Crevice attack of the test coupon could account for the erratic i_{pas} observed.

Adding 1 M CO_3^{-2}/1 M HCO_3^- to the simulated basalt groundwater showed a very large effect. The current density of the active corrosion peak, i_{max}, increased nearly three orders of magnitude. An active peak of this magnitude (> 10 mA/cm^2) has been associated with SCC, and CO_3^{-2}/HCO_3^- is a known cracking environment. The passive current density also increased, and no pitting was observed.

The addition of 1000 g/m^3 each of NO_2^- and NO_3^-, known SCC agents, showed greatly decreased i_{pas} and increased E_{cor}. The NO_2^-/NO_3^- additions also greatly increased E_{pit} and E_{prot}.

Adding 1000 g/m^3 of PO_4^{-3}, a known SCC agent, produced active corrosion of the steel with no indication of passive-pitting behavior. The promotion of active corrosion may be important in propagating stress-corrosion cracks, assuming an active dissolution model for the mechanism of SCC in carbon steels.

The addition of 1000 g/m^3 each of BO_3^{-3} and $B_4O_7^{-2}$ increased the pitting potential, but no significant effect on active corrosion or the magnitude of i_{pas} was observed.

By adding 1000 g/m^3 of SiO_3^{-2}, the passive current density was greatly reduced, and E_{pit} greatly increased. Although E_{prot} was only slightly reduced, E_{cor} was increased to a value more positive than E_{prot}, indicating the possibility of pitting and/or crevice corrosion. The polarization behavior for SiO_3^{-2} additions is similar to that of NO_2^-/NO_3^-, a known cracking agent.

Adding 100 g/m^3 of H_2O_2, which acts as an oxidizer, significantly increased the total rate of the reduction reaction. This increase resulted in a large increase in E_{cor}. The polarization behavior indicates mostly active behavior, but an E_{prot} was observed, indicating pitting attack. Because $E_{prot} < E_{cor}$, pitting and/or crevice corrosion could have initiated at crevice sites created by the holder-specimen interface during exposure at E_{cor}.

The addition of 100 g/m^3 of ClO_4^- promoted passivation of the 1020 steel. The passive current density decreased, and E_{pit} increased. Although the magnitude of the effect is much less, it is similar to that for NO_2^-/NO_3^- and SiO_3^{-2} additions.

All the selected species affected the polarization behavior to some degree. The polarization experiments identified Al^{+3}, NO_2^-/NO_3^-, SiO_3^{-2}, and ClO_4^- as significantly decreasing i_{pas}; PO_4^{-3} and possibly Cl^- or H_2O_2 as promoting active corrosion; and CO_3^{-2}/HCO_3^- as producing a significant increase in i_{max} and still maintaining passive behavior. The differences in the effects in these single species experiments and the results of the statistical experiments is probably due to the presence of the other species during the statistical experiments. For example, Al^{+3} affected E_{pit} and E_{prot} when it was added to the standard

basalt groundwater (fairly low concentrations of species). In the statistical matrix of experiments, when several of the other species were present in high concentrations, Al^{+3} showed no systematic effect on E_{pit} or E_{prot}. Combining the effects observed from the single species test with those for the statistical matrix provided a more complete understanding of the affects of the chemical species on the corrosion behavior of carbon steel.

The potential effects of these species on SCC susceptibility were examined further by performing fast scan rate (18 V/hr) polarization curves for comparison with slow scan rate (0.6 V/hr) curves. In most cases, the fast scan curves are displaced to much higher current values than the slow scan curves. For example, with Al^{+3} added there are over two orders of magnitude difference in the currents at approximately -0.70 V (SCE). However, the fast-scan current is still only approximately 3×10^{-4} A/cm^2, which is low for the cracking environments previously studied. The CO_3^{-2}/HCO_3^- solution exhibited the general behavior expected of cracking agents, but i_{max} for the fast scan was actually less than i_{max} for the slow scan. This behavior is not readily explained except that the Cl^- and F^- present in the groundwater may have affected the polarization behavior observed; in other CO_3^{-2}/HCO_3^{-2} environments i_{max} for the fast scan is typically greater than i_{max} for the slow scan.

To summarize, statistically designed polarization studies were performed to examine the corrosion effects of chemical species which are either present in basalt groundwaters or are possible radiolysis products. The results of these studies showed that various combinations of these species can produce much more severe localized corrosion, both SCC and pitting, than the nominal basalt groundwater. Furthermore, the studies indicate that in considering the corrosion behavior of carbon steel, interaction effects between species can be very important.

3.1.2 Slow Strain Rate Studies

The objective of the slow strain rate studies is to assess the stress-corrosion cracking susceptibility of carbon steels in candidate repository environments. Specific environmental conditions (solution composition and electrochemical potential) are being selected on the basis of the results of a literature survey and the electrochemical studies. During this year, all of the tests were performed on a commercially available hot-rolled 1020 carbon steel having the composition shown in Table 3.1.

During the latter part of last year, several slow strain rate tests were performed on carbon steel specimens in 1X basalt groundwater at 90 C, over a range of potentials selected on the basis of the potentiodynamic polarization studies. Cracking was not observed or expected in this groundwater composition. During this year, a single test was performed in 1X basalt groundwater at 250 C at -250 mV (Ag/AgCl, saturated) and a

strain rate of 6×10^{-7} sec^{-1}. This potential was selected on the basis of the results of the potentiodynamic polarization experiments performed at 250 C. No cracking was found in the gauge length of the specimen.

In the literature survey,(3.2) several species which may be present in the repository were identified as potential stress-corrosion cracking agents. Of these, $FeCl_3$ or chloride + ferric oxides or hydroxides are potentially the most problematic, since chlorides are present in the groundwater and since corrosion of the overpack would generate ferrous ions which may be oxidized to ferric ions by radiolysis or oxygen ingress. Strauss and Bloom(3.11) first reported on the stress-corrosion cracking of low-carbon steels by ferric chloride solutions in 1961. Transgranular cracking was observed in pressurized capsule tests at 316 C at very low concentrations of ferric chloride, 0.001 M, and in aqueous slurries of FeOOH or Fe_2O_3 and NaCl. On the other hand, NaCl + Fe_3O_4 did not produce cracking (see Table 3.15).

Although the stress-corrosion cracking observed by Strauss and Bloom may be relevant to overpack performance, it had not been established whether stress-corrosion cracking of carbon steel will occur at lower temperatures, which are more typical of waste repositories, or in more complicated aqueous solutions containing typical groundwater species. Moreover, it was not evident from the original reference whether the cracking occurred in the vapor or in the liquid phase within the capsules. Accordingly, an experimental investigation was undertaken to reproduce the stress-corrosion cracking observed in the original reference and to examine the influence of temperature and solution chemistry on stress-corrosion cracking of low-carbon steels in these ferric-chloride solutions.

Initially, slow strain rate tests were performed on hot-rolled 1020 carbon steel in 0.001 M ferric chloride at 315 C over a range of strain rates to attempt to reproduce the stress-corrosion cracking data reported in the literature and to establish the optimum strain rate for subsequent stress-corrosion testing. Stress-corrosion cracking was readily produced in the liquid phase. The cracking was transgranular, with some branching (see Figure 3.13), and was similar in morphology to that reported by Strauss and Bloom.

A summary of the results of slow strain rate tests which were performed at various strain rates is given in Table 3.16. These data show that susceptibility, based on the maximum depth of cracking, was highest at the lowest strain rate. This is unfortunate, experimentally, since a slow strain rate test at 1×10^{-8}/sec may last several weeks or more. For all subsequent work, an intermediate strain rate, 1×10^{-7}/sec, was selected.

Table 3.15. Effect of various solutions and slurries containing Fe (III) and/or chloride on cracking at 316 C.[3.2]

	Capsule Contents	Result of Treatment*
(1)	0.001 M $FeCl_3$	Capsules cracked and leaked within 6 to 15 hours.
(2)	0.0001 M $FeCl_3$	Very shallow cracks were produced within 1 week.
(3)	0.0005 M $Fe_2(SO_4)_3$	No cracking observed within 1 week.
(4)	0.001 M $Fe(NO_3)_3$	No cracking observed within 1 week.
(5)	0.003 M NaCl	No cracking observed within 1 week.
(6)	0.001 M NaCl	No cracking observed within 1 week.
(7)	0.1 M NaCl	Slight attack at weld junction during 1 week.
(8)	1 M NaCl	Localized corrosion in martensite penetrated welds within 20 hours.
(9)	Aqueous slurry of Y-FeOOH containing 0.6% Cl^-	Capsules cracked and leaked within 6 hours.
(10)	Aqueous slurry of Y-FeOOH generated by corrosion in 0.0005% Cl^-	Capsules cracked and leaked within 12 hours.

*At least three and usually more capsules were given each treatment.

Table 3.15. Continued.

	Capsule Contents	Result of Treatment*
(11)	Aqueous slurry of Y-FeOOH generated by corrosion in high purity water	No cracking observed within 1 week.
(12)	Slurry of Y-FeOOH in line 11 and 0.0001 M $FeCl_3$	Capsules cracked and leaked 16 to 18 hours.
(13)	Aqueous slurry of α-FeOOH containing 0.01% Cl	Shallow cracks were produced within 1 week.
(14)	Supernatant liquid Y-FeOOH slurry in line 9	No cracking observed within 1 week.
(15)	Slurry of α-FeOOH in line 13 and liquid in line 14	Capsules cracked and leaked within 3 to 4 hours.
(16)	Slurry of α-FeOOH containing 0.001% Cl^- and 0.003 M NaCl	Moderately deep cracks were produced within 1 week.
(17)	Slurry of Y-Fe_2O_3 containing 0.01% Cl^- and 0.003% M NaCl	Moderately deep cracks were produced within 1 week.
(18)	Slurry of α-Fe_2O_3 containing 0.02% Cl^- and 0.003 M NaCl	Very deep cracks were produced within 1 week. One capsule cracked and leaked within 4 days.
(19)	Slurry of Fe_3O_4 containing < 0.01% Cl^- and 0.003 M NaCl	No cracking observed within 1 week.

*At least three and usually more capsules were given each treatment.

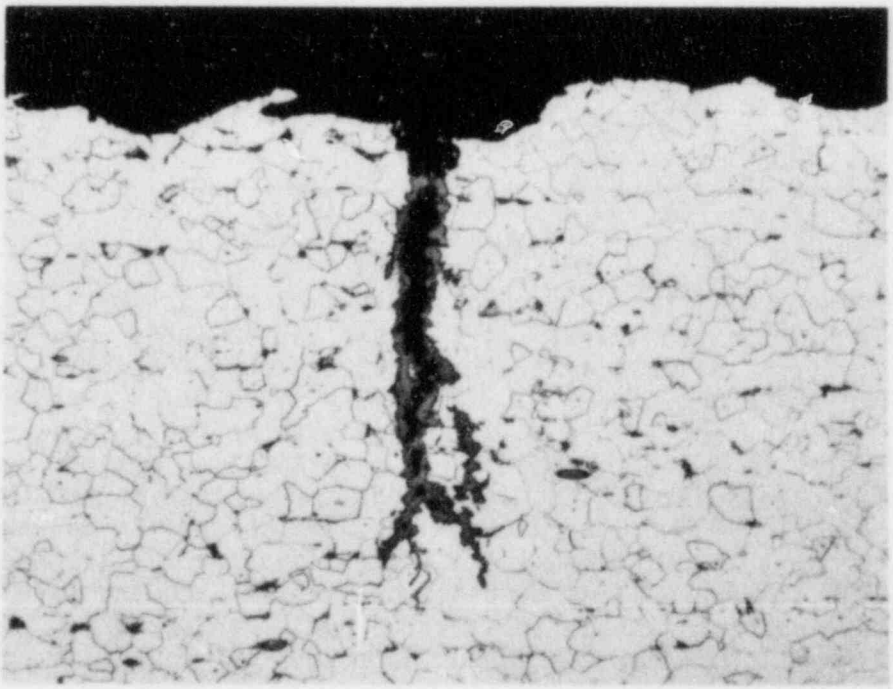

200X 7L773

Figure 3.13. Optical photograph of metallographic section of hot-rolled 1020 carbon steel specimen which was tested in 0.001 M $FeCl_3$ at 315 C and a strain rate of 1×10^{-8}/s.

Table 3.16. Summary of results of slow strain rate experiments performed on hot-rolled 1020 carbon steel in $FeCl_3$ solutions.

Strain Rate (s^{-1})	Solution Composition (M)	Temperature (C)	Maximum Crack Depth (mm)	Time to Failure (hours)	Crack Velocity (mm/s)
1×10^{-8}	1×10^{-3}	315	0.30	393	2.10×10^{-7}
6×10^{-8}	1×10^{-3}	315	0.11	146	2.09×10^{-7}
6×10^{-7}	1×10^{-3}	315	0.20	59.2	9.53×10^{-7}
1×10^{-7}	5×10^{-4}	315	0.28	282	2.75×10^{-7}
1×10^{-7}	5×10^{-4}	275	0.12	165	2.05×10^{-7}
1×10^{-7}	5×10^{-4}	250	0.14	148	2.67×10^{-7}
1×10^{-7}	5×10^{-4}	225	0.52	164	8.80×10^{-7}
1×10^{-7}	5×10^{-4}	200	0.45	188	6.65×10^{-7}
1×10^{-7}	5×10^{-4}	175	0.59	211	9.37×10^{-7}

Significant general attack occurred on the specimens exposed to the 1×10^{-3} M $FeCl_3$ solution at 315 C; accordingly, it was speculated that cracking would be at least as severe at lower $FeCl_3$ concentrations. Subsequent specimens tested in 5×10^{-4} M $FeCl_3$ solutions exhibited about the same susceptibility to cracking as those tested in 1×10^{-3} M $FeCl_3$ solutions, but the morphology of the attack was altered by the change in solution concentration. Whereas the cracks in specimens tested in 1×10^{-3} M $FeCl_3$ were generally well defined, with sharp tips, those tested in 5×10^{-4} M $FeCl_3$ exhibited blunt crack tips (see Figure 3.14). Lower $FeCl_3$ concentrations were not studied since 5×10^{-4} M $FeCl_3$ corresponds to about 50 ppm chloride, which is well below the nominal chloride concentration of basalt groundwater.

The effect of temperature on the stress-corrosion cracking of hot-rolled 1020 carbon steel was studied in 5×10^{-4} M $FeCl_3$ at a strain rate of 1×10^{-7}/sec. The results, summarized in Table 3.16 and Figures 3.15 and 3.16, show that crack depths and crack velocities exhibited minimums around 275 C and increased monotonically with decreasing temperature below that value.

The morphology of the cracking was similar over the temperature range studied with blunt crack tips. However, more corrosion products/oxides appeared to be present in the cracks at the lower temperatures. In addition, at the lowest temperature tested, there was considerable pitting on the gauge section of the specimen and the cracks appeared to have nucleated at the base of the pits; see Figures 3.17 and 3.18.

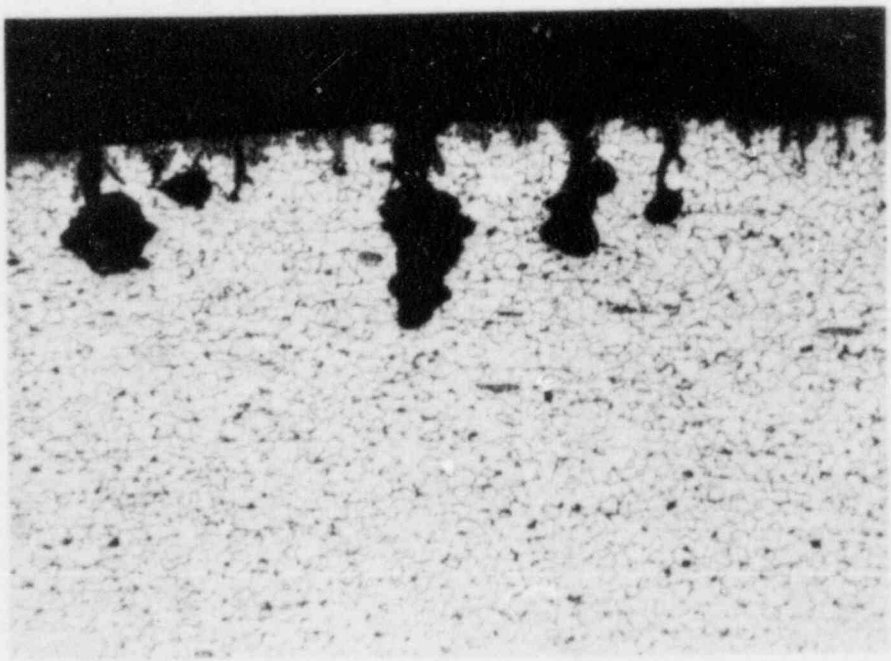

100X

8L343

Figure 3.14. Optical photograph of metallographic section of hot-rolled 1020 carbon steel specimen which was tested in 0.0005 M $FeCl_3$ at 315 C and a strain rate of 1×10^{-7}/s.

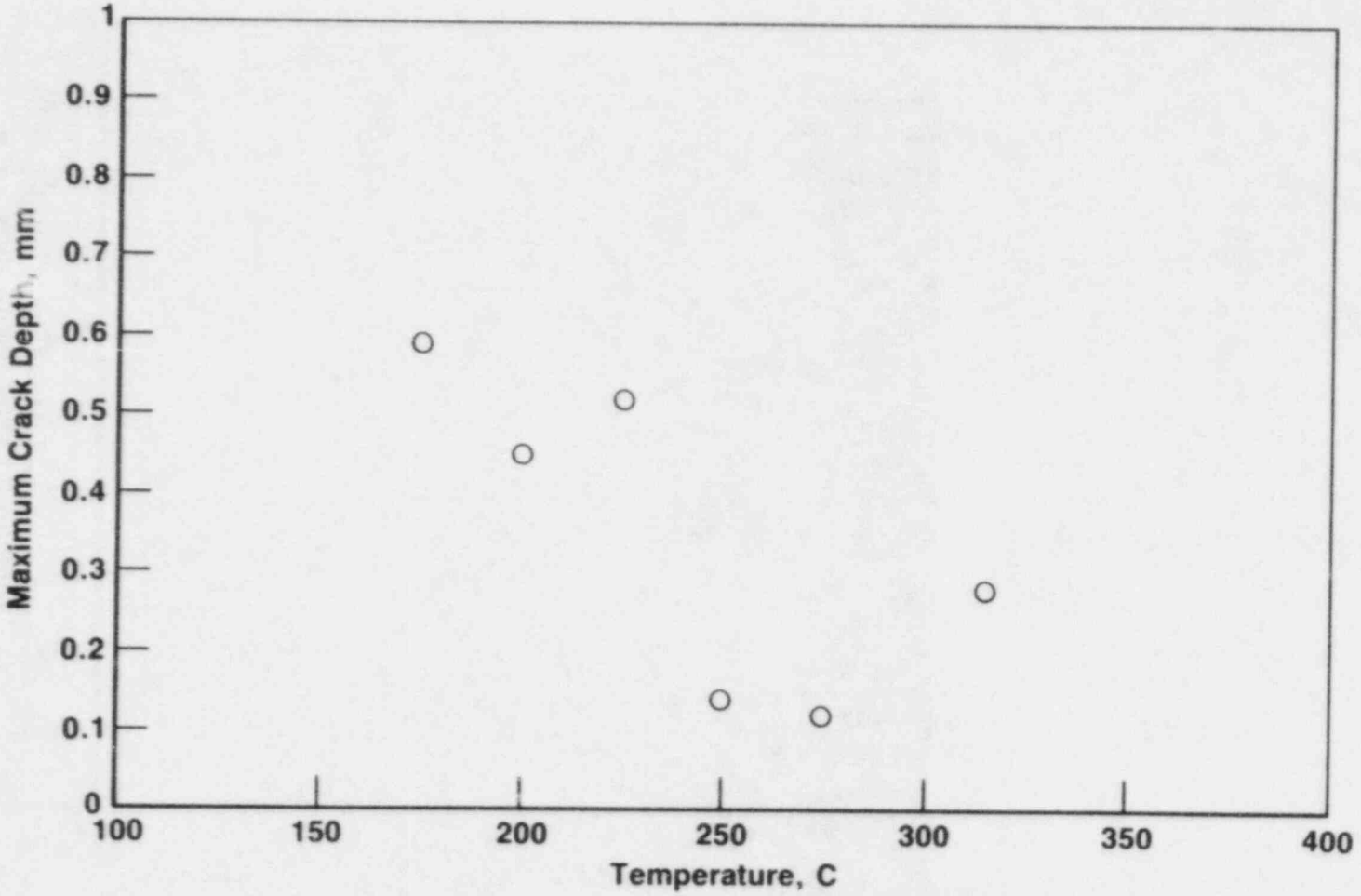

Figure 3.15. Effect of temperature on the maximum depth of cracking in slow strain rate specimens of hot-rolled 1020 carbon steel tested in 5×10^{-4} M $FeCl_3$ at a strain rate of 1×10^{-7} sec^{-1}.

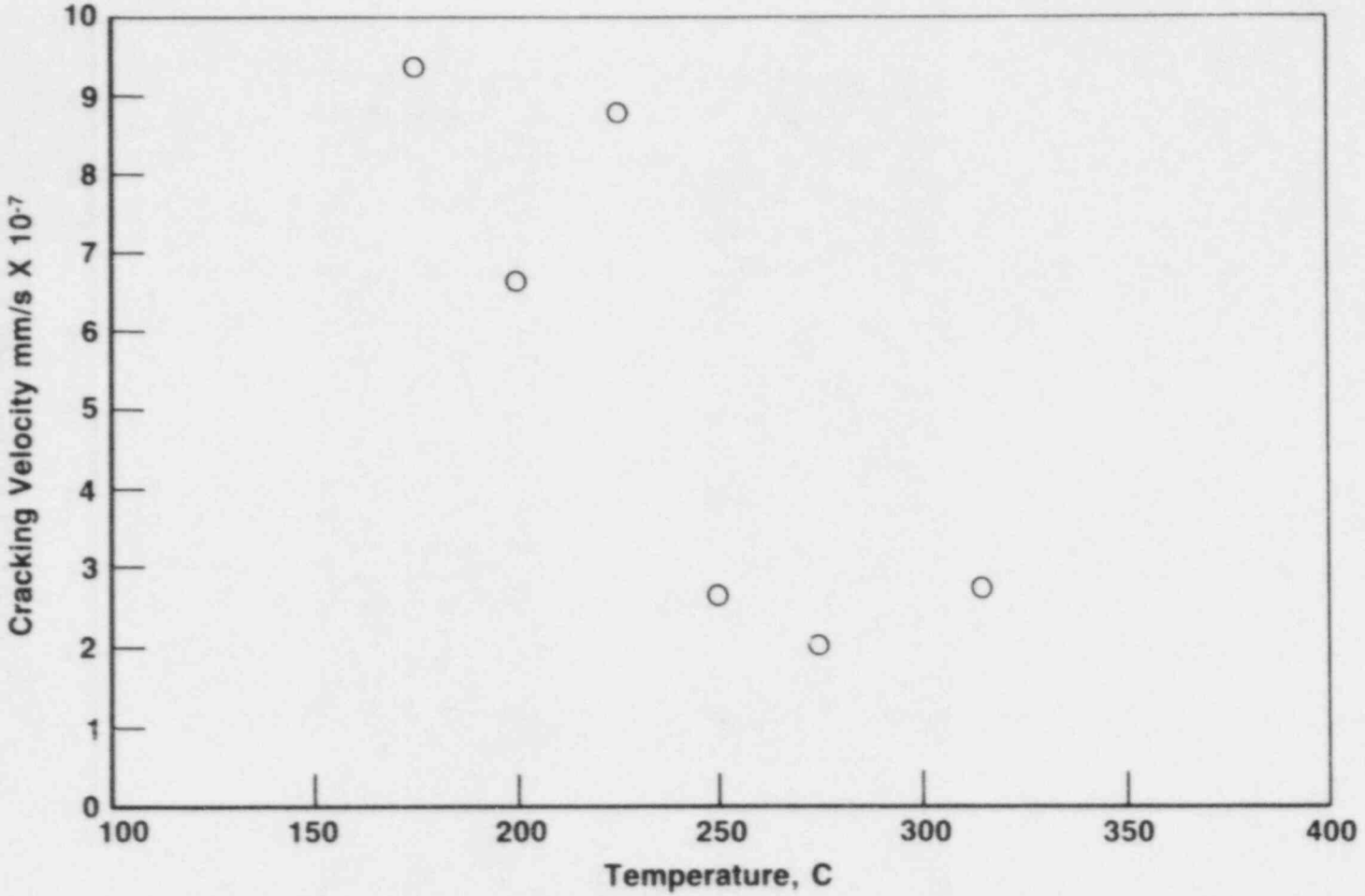

Figure 3.16. Effect of temperature on the cracking velocity in slow strain rate specimens of hot-rolled 1020 carbon steel tested in 5×10^{-4} M $FeCl_3$ at a strain rate of 1×10^{-7} sec^{-1}.

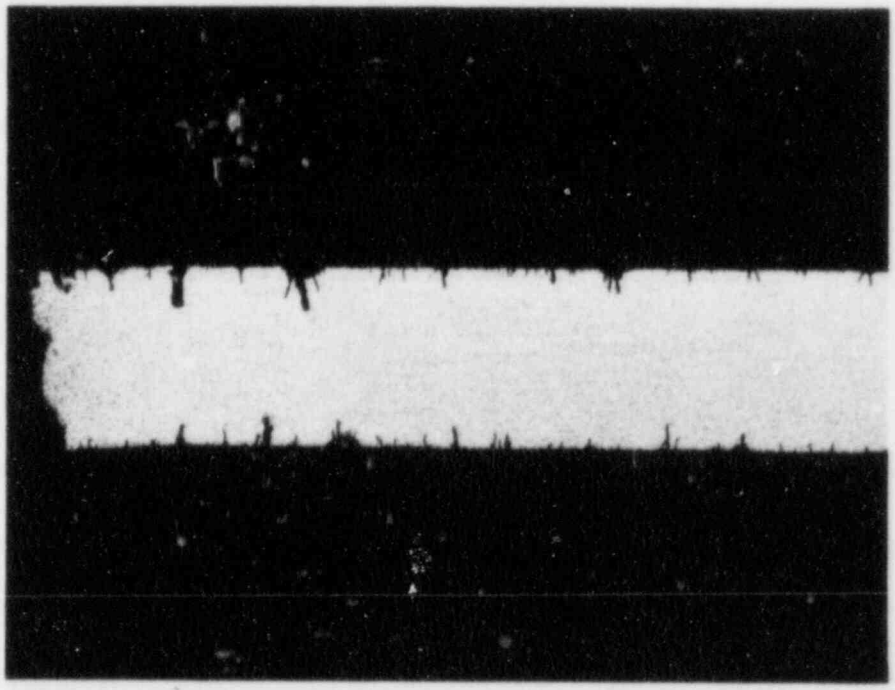

10X OM224

Figure 3.17. Optical photograph of metallographic section of hot-rolled 1020 carbon steel specimen which was tested in 0.005 M $FeCl_3$ at 175 C and a strain rate of 1 x 10^{-7}/sec.

100X OM223

Figure 3.18. Higher power optical photograph of one of the pits shown in Figure 3.17.

In conclusion, the results of the slow strain rate studies performed this year demonstrate that $FeCl_3$ is a potent stress-corrosion cracking agent for carbon steel at chloride concentrations that are typical of basalt groundwater. Moreover, the cracking appears to be most severe in the temperature range of interest for the repository, 150 to 250 C. It remains to be determined whether radiolysis will generate sufficient $FeCl_3$ to promote stress-corrosion cracking or whether the cracking will occur in the pH range that is more typical of the basalt repository.

3.1.3 Pitting-Kinetics Studies

Results of the potentiodynamic polarization experiments and autoclave exposures suggest that pit initiation in low-carbon steels is likely in basalt groundwater. The polarization curves exhibit considerable hysteresis on the reverse scans, and protection potentials are very near the corrosion potentials, even for deaerated solutions. In the autoclave exposures, pits actually were found on specimens exposed for approximately 1000 hours in a deaerated simulated basalt groundwater at 250 C.

Accordingly, experiments were undertaken to characterize the pit-propagation behavior of carbon steel in simulated basalt-repository environments. Two types of experiments were initiated: long-term exposures of "prepitted" specimens, and electrochemical pit-propagation experiments. Results of these experiments are discussed below.

3.1.3.1 Exposures of Prepitted Specimens

Simulated pits of various depths and aspect ratios (depth/diameter ratios) were mechanically drilled in specimens of hot-rolled 1018 carbon steel and are being exposed at 90 C in deaerated and in oxygenated basalt groundwater. The steel used in this study was commercially obtained, and its composition is given in Table 3.1. Prior to exposure, the depths of the pits were measured with a micrometer having a thin needle point; after exposure, the specimens were metallographically sectioned so that the morphology and depth of attack could be studied.

Four different pit diameters are examined: 5.1 mm (0.2 inch), 2.54 mm (0.10 inch), 1.35 mm (0.05 inch), and 0.53 mm (0.021 inch). For each diameter, there are three aspect ratios: 2:1, 5:1, and 10:1. Thus, for a 5.1-mm-diameter pit, the initial pit depths were 10 mm, 25 mm, and 50 mm. The overall specimen dimensions are about 40 mm long x 20 mm wide x 75 mm thick (in the dimension of the pit) and the specimens were machined from 7.6 cm (3 inches) x 15.2 cm (6 inches) strip steel.

Prior to exposure, the specimens were cleaned with acetone. Each of the pits was filled with the simulated basalt groundwater using a syringe, and the specimens were placed in high-density polyethylene vessels which contained 1 inch of crushed basalt rock. In each vessel, an electrical connection was attached to one specimen for subsequent potential

measurements. The basalt-groundwater solution was added and the vessels were sealed. They were then placed in oil baths, Luggin probes were connected, and the flow of nitrogen or oxygen was started (for deaerated and oxygenated solutions, respectively).

During the experiments, the electrochemical potential of one specimen in each vessel were monitored, and aliquots of solution were taken periodically for pH analysis. Results of the potential measurements are given in Figure 3.19. These data show that the potentials of the specimens in the deaerated vessels varied between about -700 and -750 mV (SCE) over the first 2 months of exposure, whereas the potentials of the specimens in the aerated vessels exhibited a marked increase after about 1 month of exposure and stabilized at about -220 mV (SCE).

The results of the pH measurements are given in Table 3.17. The measurements were taken frequently over the first several weeks of exposure to establish the trends, but less frequently thereafter to conserve the solutions and minimize contamination of the deaerated solutions with oxygen. These data show some interesting trends. The pH of all the solutions decreased over the first 24 hours from about 9.8 to about 7.5, and the pH of the deaerated solutions continued to decrease somewhat over the first 2 months of exposure. On the other hand, the pH of the aerated solutions increased over the 2-month period to values around 11.5. The mechanism for this pH increase is not fully understood but will be investigated.

Table 3.17. pH as a function of exposure time for simulated basalt groundwater solutions in contact with basalt rock and 1018 carbon steel specimens.

Exposure Time (hours)	pH			
	Oxygenated		Deaerated	
	Vessel 1	Vessel 2	Vessel 3	Vessel 4
0	9.8	9.8	9.8	9.8
24	8.0	7.6	7.0	7.4
72	7.4	7.4	7.2	7.8
168	7.5	7.5	7.5	7.5
336	7.8	7.9	7.5	7.5
1080	11.2	11.5	7.5	7.5
2208	11.2	11.5	6.5	6.6

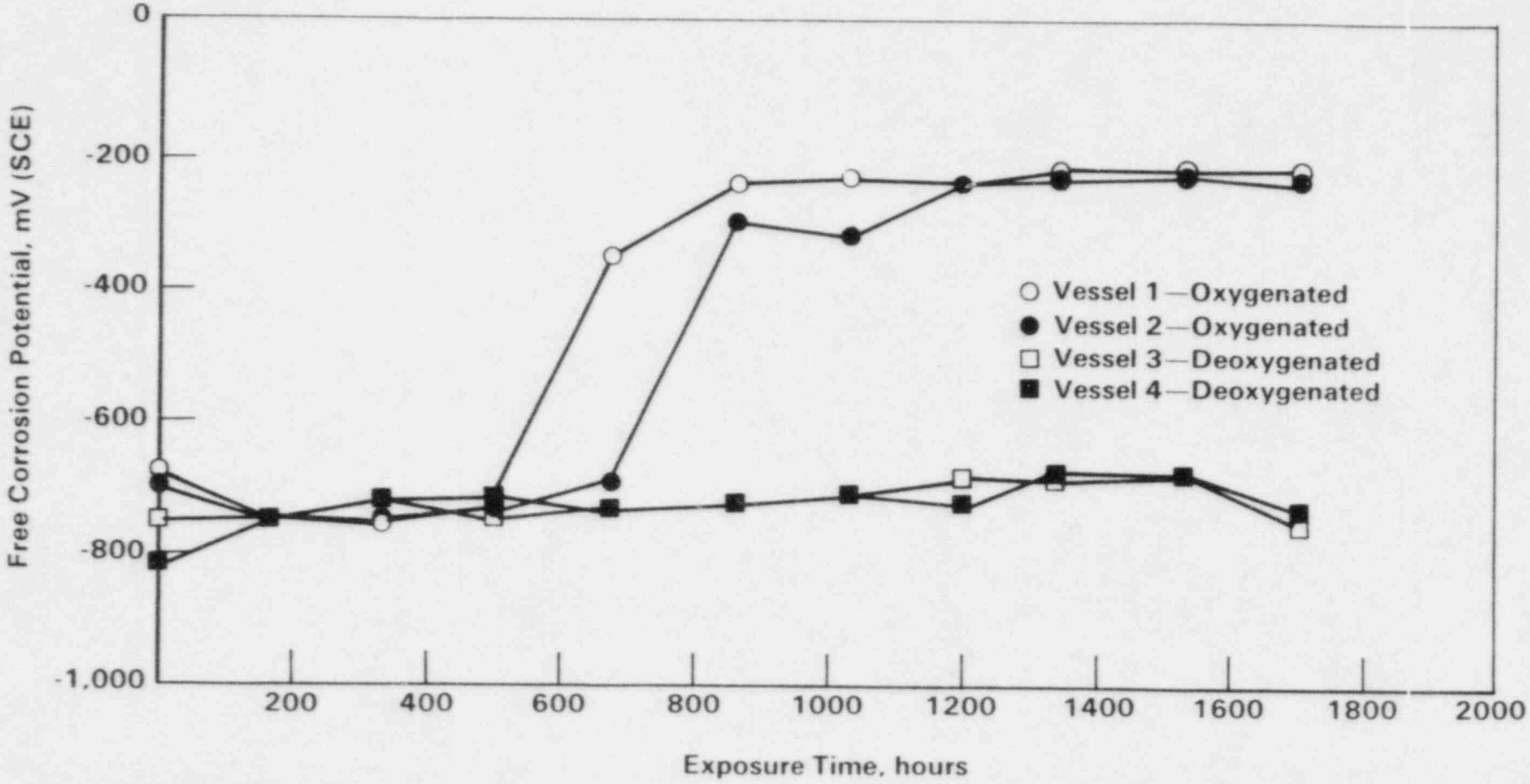

Figure 3.19. Electrochemical potential as a function of exposure time for mechanically prepitted 1018 carbon steel containing crushed basalt at 90 C.

Altogether, eight prepitted specimens were removed from the vessels and optically examined following four months of exposure. Specimens containing mechanically produced pits of each diameter were removed from both oxygenated and deaerated vessels. All specimens from the oxygenated vessels were covered with thick, red rust deposits, and the pits were all capped with corrosion products. On the other hand, specimens taken from the deaerated vessels were covered with thin black deposits, and the pits were not capped. Figure 3.20 illustrates some of these features as they appeared in specimens with 2.54-mm-diameter pits.

Following the optical examination, the specimens were metallographically sectioned, mounted, and polished, and the depths of the pits were measured with a microscope having a calibrated stage. No systematic trend in pit depth was evident from the data. The differences between the initial (preexposure) and the final pit depths varied by about $\pm$ 0.1 mm, which probably reflects the error in the measurement.

A close examination of the metallographic sections of the specimens exposed in the deaerated vessels did not indicate any evidence of appreciable attack. Similarly, the 5.1-mm, 2.45-mm, and 1.35-mm pits in the specimens exposed in the oxygenated vessels did not exhibit appreciable attack. (An optical photograph of a metallographic section of the specimen containing the 2.54-mm-diameter pits is shown in Figure 3.21.) On the other hand, the smallest-diameter pits exposed in the oxygenated vessels did show evidence of attack. The attack occurred over the entire pit for the lowest-aspect-ratio pit (2:1), whereas it occurred only near the mouth of the deeper pits. There is also evidence that the attack followed stringers in the midwall of the pits (see Figures 3.22 to 3.25).

Since attack was observed in the small-diameter pits in the oxygenated exposures, the absence of significant attack in the larger-diameter pits may simply indicate that long times are required to develop the acidic conditions necessary for pit propagation. The localization of the attack near the mouth of the deep, small-diameter pits is an interesting observation since it suggests that high-aspect-ratio pits are not stable in this system. A possible explanation for this behavior is that the solution conductivity in conjunction with high local currents limits the distance of separation of the cathode (on the external surface) and the anode within the pits.

3.1.3.2 Electrochemical Pit-Propagation Experiments

A schematic of the pit-propagation monitor is shown in Figure 3.26. Experimentally, the monitor is oriented vertically in a test cell containing an electrolyte, and the current flow between the base of the simulated pit and the boldly exposed surface is monitored as a function of exposure time. Current measurements provide an estimation of the rate of pit propagation; the rate measured may be somewhat nonconservative since the reduction reactions occurring on the pit base will contribute to pit propagation but will not be detected.

Oxygenated

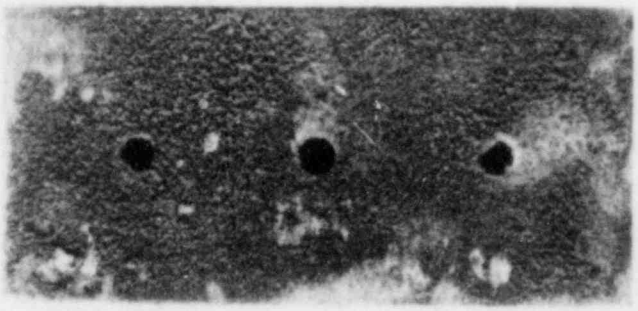

Deaerated

Figure 3.20. Low-power photograph of prepitted hot-rolled 1018 steel specimens following exposure in oxygenated and deaerated simulated basalt groundwater containing crushed basalt at 90 C.

Note that the pits on the specimen in the oxygenated solution are capped with corrosion products.

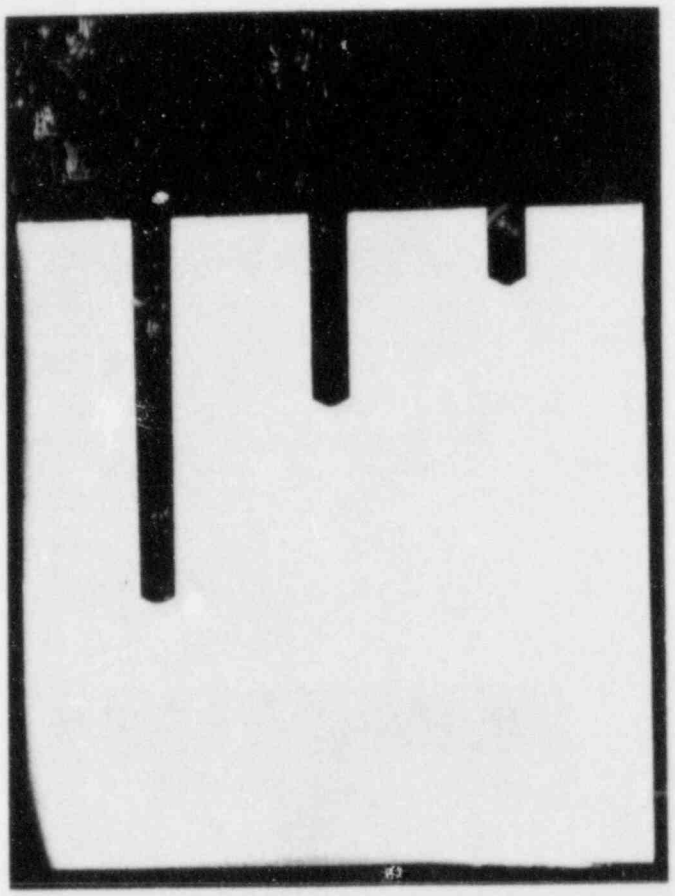

2X 7L701

Figure 3.21. Low-power optical photograph of metallographic section of prepitted (2.54-mm-diameter) specimen of hot-rolled carbon steel following exposure in oxygenated simulated basalt groundwater containing crushed basalt.

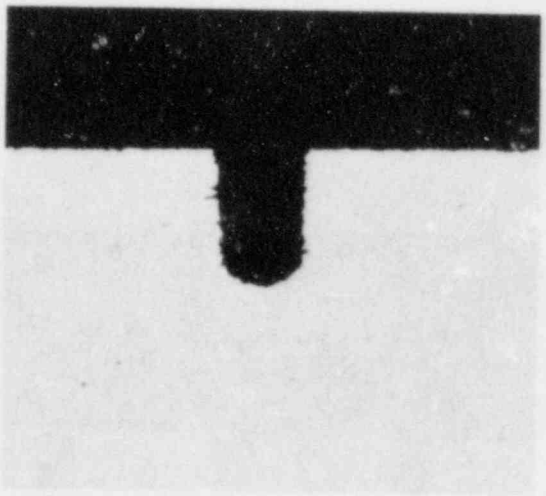

20X 7L708

Figure 3.22. Optical photograph of 2:1 aspect-ratio 0.53-mm-diameter pit.

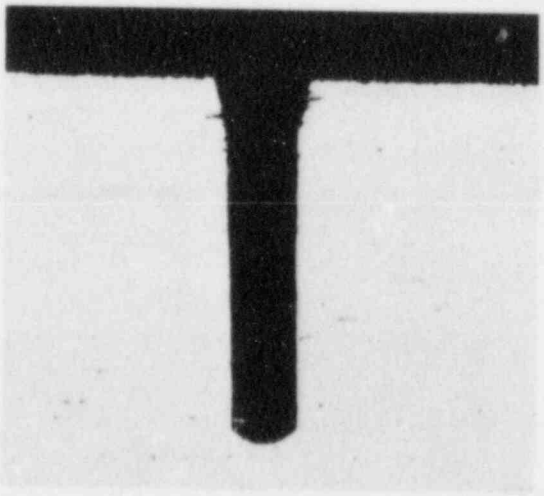

20X 7L707

Figure 3.23. Optical photograph of 5:1 aspect-ratio 0.53-mm-diameter pit

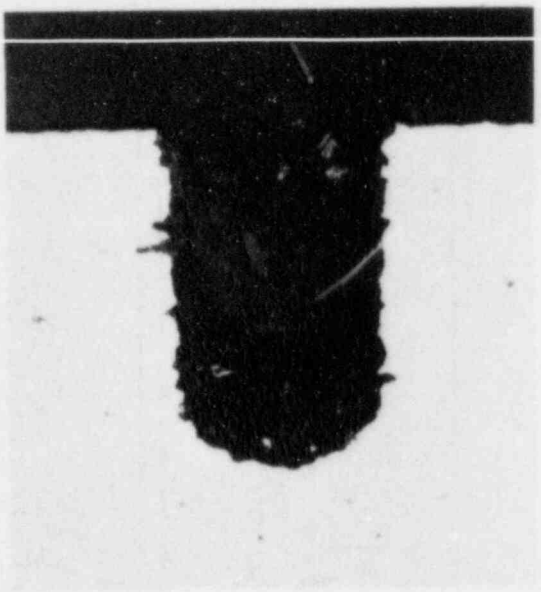

50X 7L711

Figure 3.24. Higher-power optical photograph of pit shown in Figure 3.22.

50X 7L710

Figure 3.25. Higher-power optical photograph of pit shown in Figure 3.23.

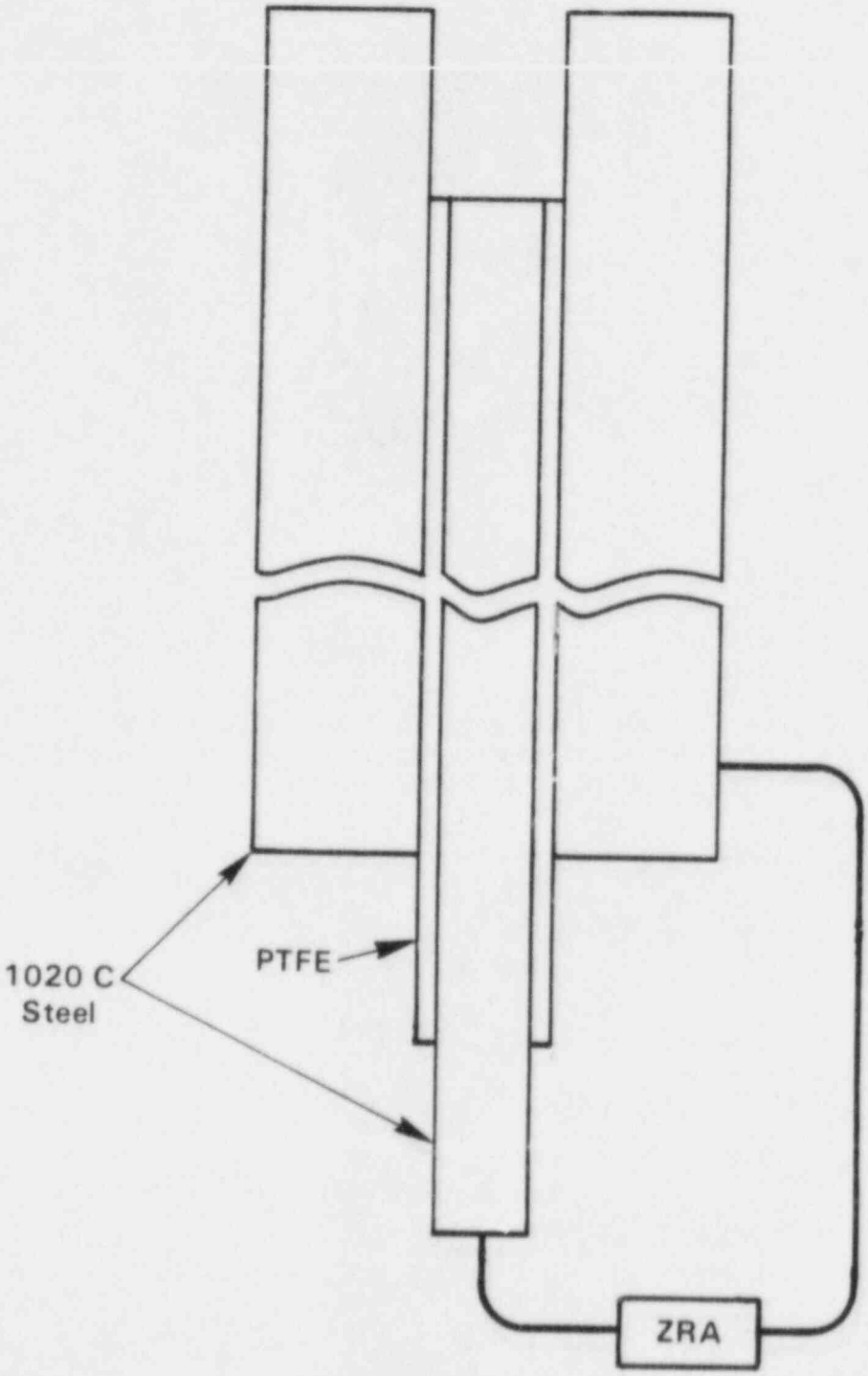

ZRA = Zero Resistance Ammeter

Figure 3.26. Schematic of pit-propagation monitor.

Several preliminary experiments were performed in oxygenated basalt groundwater at 75 C using two aspect ratios, 2:1 and 10:1. It was found that the pits did not initiate within about 1 week of exposure; currents were actually negative, indicating protection of the pit base. It is possible that this behavior was the result of the absence of a cap over the pits, which is necessary to prevent oxygen ingress into the pits and migration of protons out of the pits. Accordingly, the pits were stimulated for about 24 hours at 10 to 20 mA/cm^2 anodic current using a potentiostat and a platinum counter electrode. The boldly exposed portion of the pit monitor was allowed to corrode freely during this stimulation. Following stimulation, both pits initiated, and the 2:1-aspect-ratio pit stabilized at a current of about 50 $\mu A/cm^2$ (23 mil/yr). On the other hand, the 10:1-aspect-ratio pit did not stabilize, and eventually the current actually became cathodic. These results appear consistent with the results of the exposure tests in that the shallow pits propagated but the deep ones did not. However, an optical examination of the electrochemical pit-propagation monitors following exposure indicated that the 10:1-aspect-ratio pit had not fully occluded, which may account for the inability to stabilize pitting in this specimen.

Because of the difficulties encountered in consistently occluding the simulated pits, two artificial methods of occluding the pits were investigated: (1) packing the pit with an Fe_3O_4 slurry, and (2) plugging the pit mouth with a glass frit. Optical examination indicated that red oxides were present on the outside surfaces of the specimens but black oxides were adjacent to the metal, and that attack had occurred beneath the inner deposits. X-ray diffraction analyses were performed on both types of deposits, and it was found that the inner deposit is Fe_3O_4 and the outer deposit is primarily Fe_3O_4 with some γ-FeOOH and α-FeOOH. Accordingly, an Fe_3O_4 paste was chosen for packing the pits.

The cells were set up with aspect ratios of 3:1 in standard simulated basalt groundwater (pH 9.8). The cells were deaerated with nitrogen at 75 C for 24 hours and oxygen was then introduced at a flow rate of approximately 10 cc/min; the galvanic current flow between the inner pits and the boldly exposed surfaces was monitored as a function of time. Pitting was established almost immediately, as indicated by anodic currents flowing from the pits. The pitting currents were monitored during the course of the next five days. For the Fe_3O_4 pits, the currents fluctuated between 5.1 and 11.6 $\mu A/cm^2$; 2.17 $\mu A/cm^2$ is equal to 1 mil/yr for iron. Thus, the pitting rates were quite low. Pitting currents for the glass-plugged pits were even lower, varying between 0.51 and 1.2 $\mu A/cm^2$ over the five-day period.

Because of the low pitting rates observed, it was decided to attempt to stimulate the pits by anodically polarizing them; the specimens were galvanostated at 15 mA/cm^2 for 24 hours. For the Fe_3O_4-packed pit, approximately 400 mV of polarization was required to achieve the desired current. On the other hand, over 5 volts of polarization was required to achieve the same current density for the frit-plugged pit, suggesting that there were high electrical potential (IR) drops across the frit.

Upon termination of the polarization, the pitting currents were again measured and found to be cathodic. Over a period of two days the currents remained cathodic, at values ranging between < 1 $\mu A/cm^2$ and 72.5 $\mu A/cm^2$ for the Fe_3O_4 pit and between 11 $\mu A/cm^2$ and 18 $\mu A/cm^2$ for the frit-plugged pit.

Of the two techniques which were studied, it was concluded from the experiments that packing with Fe_3O_4 is the best method of occluding the pit. The experiment also demonstrated that anodic stimulation was detrimental to pit initiation since cathodic currents were measured afterwards. However, the zero-resistance ammeter was connected between the pit and bulk surface immediately following anodic stimulation. This produced cathodic currents, since the anodic stimulation made the pit more noble than the bulk surface. The cathodic currents produced an increase in pH within the pit, altering the pit environment. It was speculated that different results might have been obtained if the pit had remained uncoupled after anodic stimulation and the potential permitted to depolarize prior to coupling.

In a second experiment, both cells were set up with aspect ratios of 3:1 and the pits were packed with an Fe_3O_4 slurry. For the first 24 hours, nitrogen was bubbled through both cells; one cell (cell A) was left uncoupled, in the other (cell B), the pit was anodically stimulated at 15 mA/cm^2. After 24 hours, cell B was disconnected from the galvanostat, oxygen flow was started in both cells, and the potential differences between the pit and the boldly exposed surfaces were measured for both cells. For cell A, the pit was 15 mV negative to the boldly exposed surface, whereas for cell B, the pit was 20 mV positive (noble) to the boldly exposed surface. Over the next 24 hours, the pit in cell B maintained a noble potential of 15 to 20 mV with respect to the boldly exposed surface. Accordingly, the experiment was terminated. From this experiment, it was confirmed that anodic stimulation of the pit was not beneficial in pit initiation in this system.

Following the potential measurement on cell A, the pit and the boldly exposed surface were coupled through a zero-resistance ammeter and the current was monitored as a function of exposure time. During the first 50 minutes, the current increased from 43 $\mu A/cm^2$ to about 180 $\mu A/cm^2$. It then decreased over the next 1400 minutes and actually went negative after another 1125 minutes, indicating protection of the pit. Pitting reinitiated after about 1450 minutes of exposure, and currents increased over the next 2800 minutes to about 65 $\mu A/cm^2$. The current then fluctuated over the next 1200 minutes between 3 and about 65 $\mu A/cm^2$.

These current fluctuations may have resulted from inadequate control of the oxygen flow and temperature within the cell. To test the sensitivity of the pitting current to temperature and oxygen flow rate, these parameters were varied briefly during the course of the test. A 10 C drop in the temperature reduced the pitting current from 16.7 $\mu A/cm^2$ to 7.2 $\mu A/cm^2$. Varying the oxygen flow rate had a similar affect, with the current increasing with increasing oxygen flow rate.

Based on the observed dependence of the pitting current on the oxygen flow rate, it was concluded that the rate of pitting is controlled, to

some extent, by the kinetics of the reduction reaction. To test this hypothesis, the pit was disconnected from the boldly exposed carbon steel surface and connected to a platinum counter electrode. The current immediately increased several orders of magnitude to about 3.26×10^3 $\mu A/cm^2$ but decayed over the next 700 minutes to about 1.09×10^3 $\mu A/cm^2$--a value which is, nevertheless, considerably higher than values measured for the standard pit geometry.

Because of the problems encountered with temperature and oxygen control, the pit cell was redesigned. The TEFLON cell body was replaced with a double-walled PYREX* cell body. With the new design, the cell is heated by flowing heat-transfer fluid between the inner and outer cell walls. The heat transfer rate is much higher than in the previous design, and thus the cell temperature is not a function of the oxygen flow rate.

With the new cell design, one-week experiments were performed at three aspect ratios, 1:1, 5:1, and 10:1 in 1X basalt groundwater at 75 C and an oxygen-flow rate of 10 cc/min. Results of these experiments are given in Figure 3.27. These data show that, for the initial 4,000 minutes of exposure, the current densities were highest for the low-aspect-ratio pits and decreased with increasing exposure time. During the latter part of the tests, the currents were similar for all three aspect ratios and there was considerable variability in the data. It is interesting to note that in several instances, currents actually became cathodic for short periods of time during the course of the experiments.

Optical examination of the boldly exposed electrodes in situ during the experiments indicated that the electrodes initially passivated. However, corrosion initiated at several localized sites on the surfaces and grew from these sites, eventually covering the entire electrode surfaces with thick corrosion products. This process may account for the decrease in current with time observed for the low-aspect-ratio pits since the growth of the deposits would tend to decrease the effective cathodic area. In addition, the anodic sites on the boldly exposed surfaces probably competed for cathodic current with the simulated pit. The localized attack on the boldly exposed specimen also may account for the variability in the anodic currents measured as the initiation and destruction of pits on the boldly exposed surface would cause fluctuations in the electrochemistry of the system.

Following completion of the one-week exposures, the simulated pits were disconnected from the boldly exposed surfaces and polarization curves were obtained on the pits using a Luggin probe located at the mouth of the pits and a platinum counter electrode. The objective of these tests was to examine the electrochemical behavior of the pit and to estimate the magnitude of the IR drop down the pit. The latter was accomplished by periodically interrupting the current during the course of the experiment such that the IR-corrected polarization curve could be

---

*PYREX is a registered trademark of Corning Glass Works.

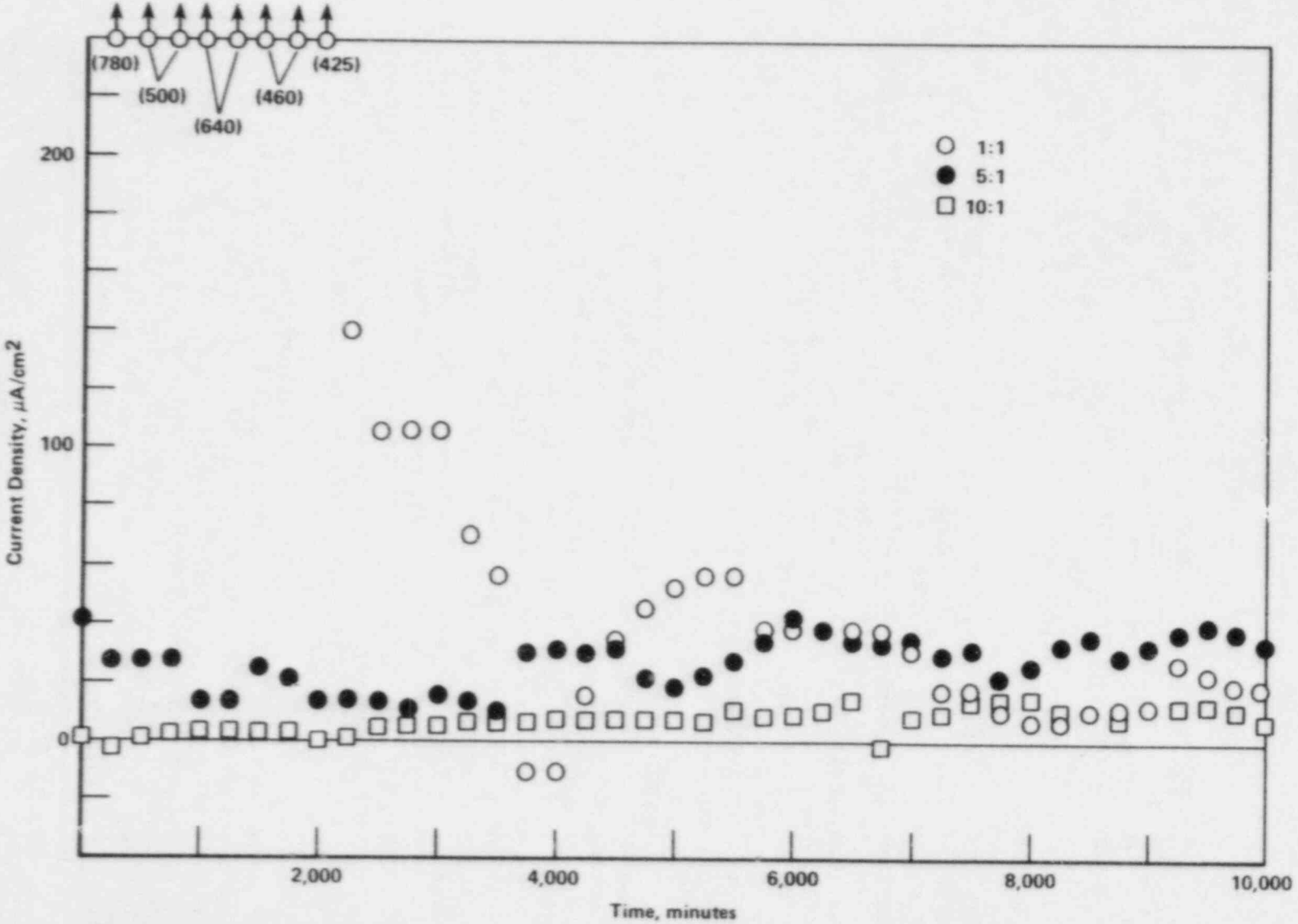

Figure 3.27. Current density as a function of exposure time for pit propagation experiments performed at aspect ratios of 1:1, 1:5, and 1:10 in aerated 1X basalt groundwater at 75 C.

obtained. Results of the experiments are given in Figures 3.28 through 3.30. These data show that the polarization behavior for all three aspect ratios was similar. On the forward scans, the curves exhibited non-linear behavior which could not be attributed totally to IR effects, suggesting that the electrode had filmed. On the reverse scans, significant hysteresis was observed, indicating that local breakdown of films had occurred. Subsequent examination of the pit specimens indicated the presence of films and sites of local film breakdown.

There were some differences between the performance of the different aspect ratio pits. The current density at a given overpotential was somewhat lower at the highest aspect ratio and the significant IR effects occurred at lower overpotentials. However, the IR effects were not appreciable, even for the highest-aspect-ratio pit, below about 200 mV of anodic polarization.

The observation of films on the simulated pits is a significant finding since it indicates that the pits were not freely corroding--a conclusion that is consistent with the low currents measured. This behavior may or may not be representative of in-service conditions; nevertheless, it produces nonconservative estimates of maximum pit propagation rates. Accordingly, efforts in the future will be directed toward obtaining upper-bound pit propagation rates by stimulating acidification within the pits.

To summarize, the results of the pitting studies clearly demonstrate that occluded-cell corrosion will propagate in simulated basalt groundwater at 90 C. However, the observed rates of localized attack are low, suggesting that the overpack life will not be greatly compromised. On the other hand, it has not been established whether the measured rates are conservative or whether they can be greatly accelerated by alteration in environment or geometry. These issues will be addressed in future work.

3.1.4 Future Work

In dealing with the steel-basalt system, statictical analyses of existing potentiodynamic polarization data will continue during the coming year, supplemented by additional experiments where necessary. The effects of several highly reactive, radiolytically produced species will be examined in more detail. In addition, a matrix of experiments will be carried out at temperatures higher than 90 C to examine the effects of credible repository temperatures on potentiodynamic polarization behavior. Slow strain rate studies will continue, focusing on confirmation of the results of the potentiodynamic polarization studies. The environmental metallurgical, and geometric factors contributing to pit propagation will continue under study to establish conservative pitting rates for carbon steel and to aid in the development of the pitting-corrosion model.

Preliminary studies of carbon steel in tuff groundwater will be initiated. These will include potentiodynamic polarization, U-bend, and slow strain rate tests.

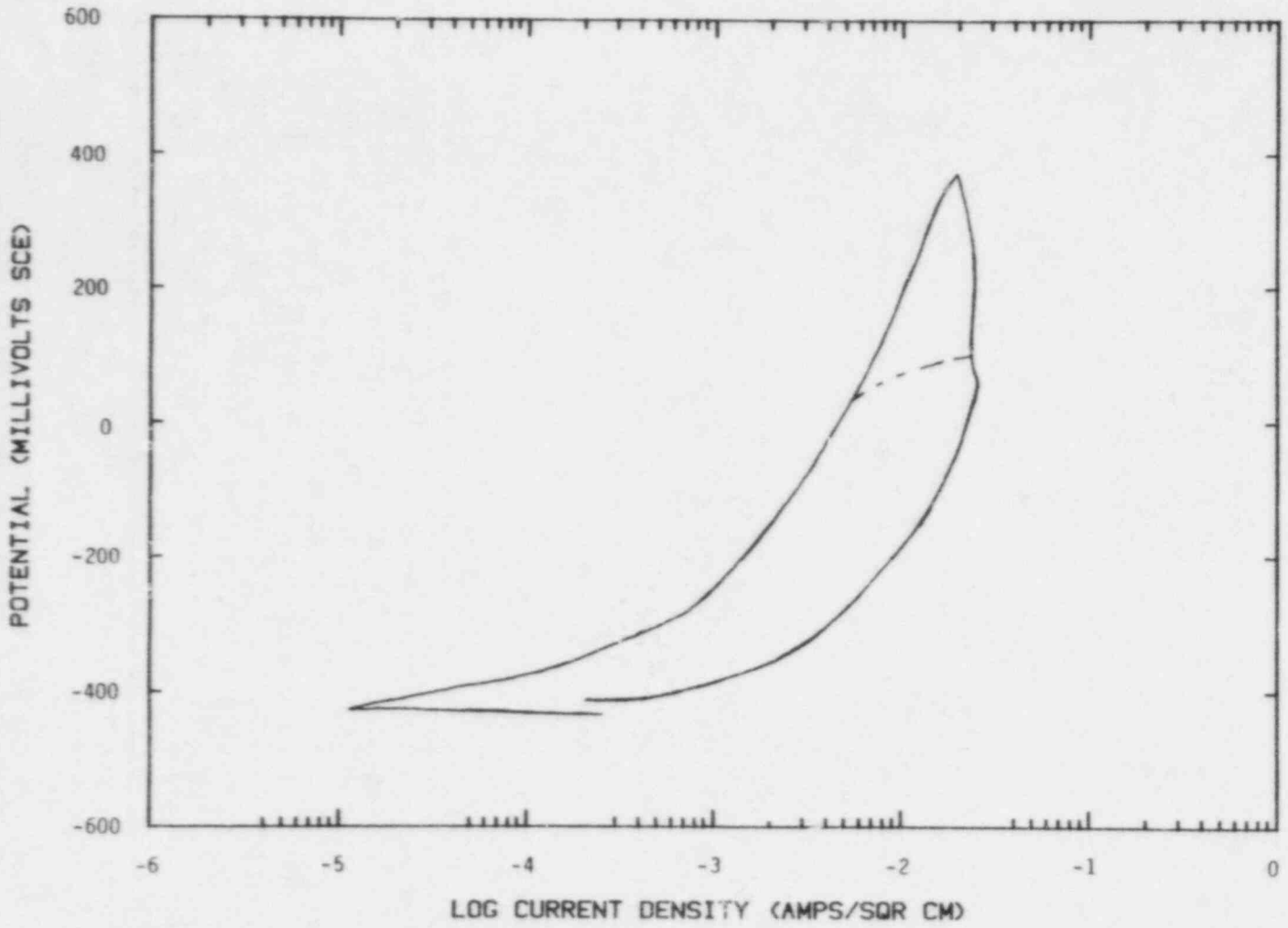

Figure 3.28. Potentiodynamic polarization curve for 1:1 aspect ratio pit in aerated 1X basalt groundwater at 75 C following 1-week exposure; scan rate 0.6 V/hr.

— — — — IR Corrected
———— IR Uncorrected

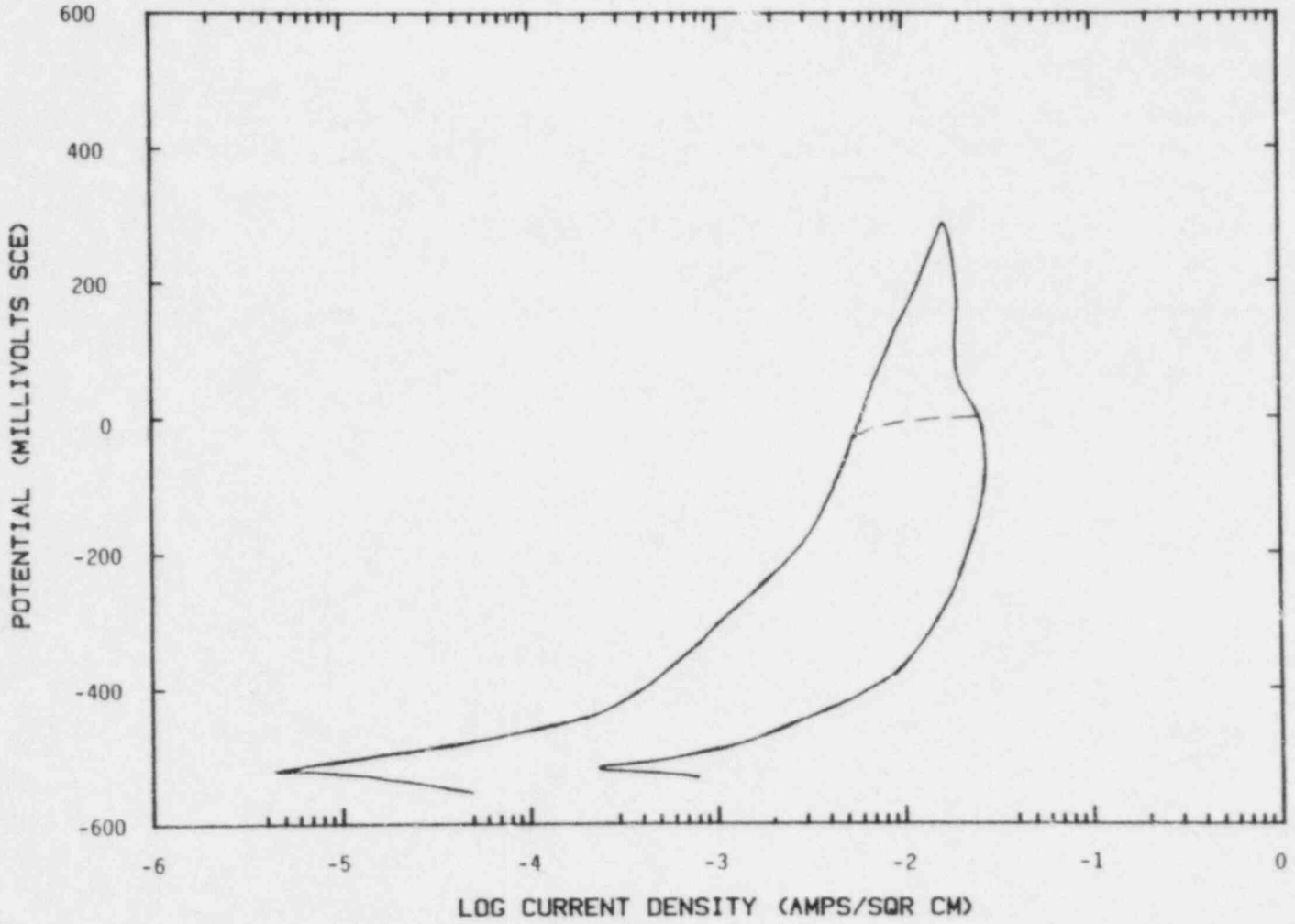

Figure 3.29. Potentiodynamic polarization curve for 1:5 aspect ratio pit in aerated 1X basalt groundwater at 75 C following 1-week exposure; scan rate 0.6 V/hr.

— — — — IR Corrected
———— IR Uncorrected

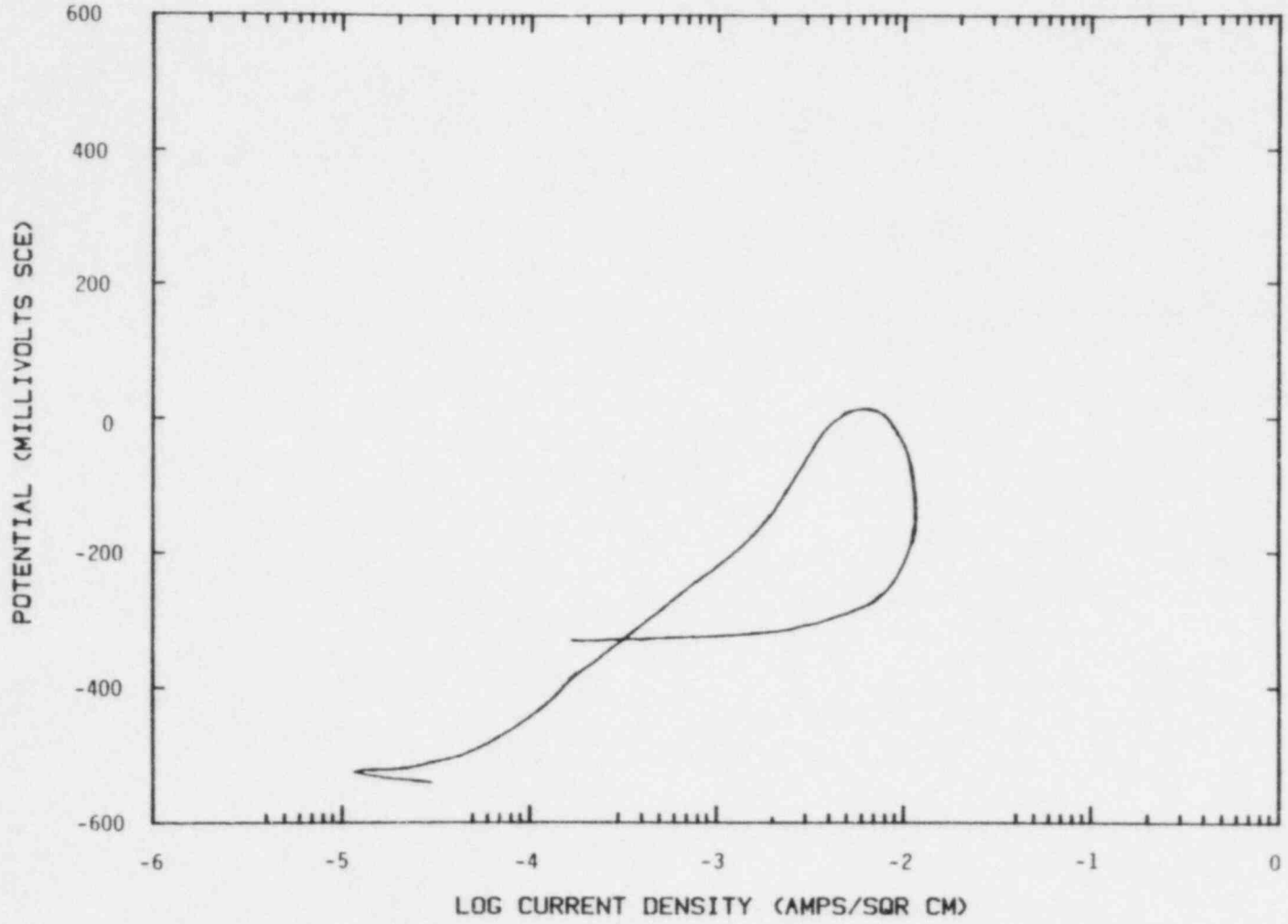

Figure 3.30. Potentiodynamic polarization curve for 1:10 aspect ratio pit in aerated 1X basalt groundwater at 75 C following 1-week exposure; scan rate 0.6 V/hr.

_____ IR Uncorrected

3.2 Hydrogen Embrittlement

During the second project year, experiments were conducted to determine the potential for hydrogen embrittlement of cast-steel overpacks from corrosion or radiolytic reactions. Although some of the results required verification, those experiments indicated that resistance to cracking can be reduced significantly by the action of hydrogen, particularly in specimens that are annealed after casting. The apparent high sensitivity to embrittlement of annealed specimens suggests that overpacks may become more susceptible to hydrogen embrittlement with increasing service time or as the result of welding. The microstructures of the overpack steel could change during long-term exposure at repository temperatures or during heating when the containers are welded.

During the third project year, experiments were performed to verify some of the observations made in the previous year. In addition, experiments were performed to evaluate the sensitivity to hydrogen embrittlement of cast, commercial-purity iron using sample ingots that were provided by Armco, Incorporated. Experiments were planned that would use welded cast-steel specimens to be provided by Manufacturing Sciences Corporation (MSC), but these specimens were not produced due to fabrication difficulties encountered by MSC.

3.2.1 Verification Tests on Cast Steel

The elastic-plastic fracture-toughness, or J-integral, experiment provides a measure of the work required to initiate and drive a crack through a ductile metal. By applying a constant, slow, crack-opening-displacement rate to the specimen and monitoring the load on the specimen and the crack length continuously, the energy release rate per unit of crack advance, which is equal to the J-integral, can be estimated. The plot of J-integral versus change in crack length is known as the J-resistance curve, which provides information regarding the material's resistance to cracking. Comparison between the material's J-resistance curve and the applied in-service J-integral, which results from the stress state in the container wall and the presence of a flaw, should allow calculation of the critical flaw size which the container can support and thereby contribute to failure criteria for estimation of containment life. The intersection of the J-resistance curve with the blunting line, which is a mathematically derived estimate of apparent artificial crack growth that results from crack-tip blunting, defines the elastic-plastic fracture toughness or resistance to crack initiation, J_{Ic}. The resistance to subsequent steady-ductile crack growth is given by the tearing resistance, which is the slope of the J-resistance curve, or by the tearing modulus, which is a nondimensional quantity proportional to the tearing resistance. The fracture toughness and the tearing resistance or tearing modulus are frequently used measures of resistance to ductile fracture.

The results of three sets of fracture-toughness tests from the previous year required verification because of inconsistency in the data. The

fracture toughness, J_{IC}, provides an indication of the material's resistance to crack initiation, whereas the tearing modulus, T, provides a measure of the material's resistance to unstable crack growth*. The data for the annealed "clean" (low sulfur and phosphorus) steel tested in nitrogen were not valid based on ASTM criteria to determine the J-resistance curves. Therefore, two additional tests were conducted in a nitrogen environment on the clean, annealed steel. In addition, the data for the "doped" steel (with sulfur and phosphorus added to levels typical of commercially available steel) in the as-cast condition indicated that the tearing modulus was slightly higher in hydrogen than in nitrogen. Because hydrogen should reduce (or have no effect on) the tearing modulus, those tests were repeated to determine whether this indication was genuine or simply a result of specimen-to-specimen variation in properties. Also, tests with the doped steel in the hot-rolled condition were repeated in hydrogen and in nitrogen.

Table 3.18 presents revised fracture-toughness data that include the results of the new tests. As expected, multiple testing of the as-cast doped steel revealed that the apparent moderate increase in tearing modulus in hydrogen was a result of specimen-to-specimen variation. The tearing-modulus values for that material ranged from 58 to 94 in nitrogen and from 49 to 95 in hydrogen, with little difference in the averages. The fracture toughness, J_{IC}, also varied widely in both environments. Hydrogen caused a greater reduction of J_{IC} in the as-cast doped steel than in the as-cast clean steel, although both steels exhibited approximately the same toughness in nitrogen.

The data in Table 3.18 show that in all cases hydrogen reduced the fracture toughness of the steel. Thus, a crack would initiate in an overpack at lower applied stress (or J integral) when hydrogen is present. This observation is consistent with previous studies of hydrogen embrittlement at Battelle and elsewhere, but by itself it would not necessarily indicate that premature failure by hydrogen embrittlement will occur. In many cases, a crack may initiate at low load or J-integral value but then would not propagate, provided that the tearing modulus is sufficiently high to resist further crack advance. However, if the tearing modulus is reduced by hydrogen, unstable crack growth is more likely, and premature failure can occur.

The tearing modulus was not significantly lower in hydrogen for the as-cast and wrought conditions; however, a large reduction in tearing modulus was observed for both the clean and the doped steels in the annealed condition. The observation of a significant tearing-modulus reduction in hydrogen for the annealed steels suggests that as microstructures change with time at slightly elevated temperatures, such as those in a repository, or when microstructural changes occur in the heat-affected zone during welding, sensitivity to hydrogen embrittlement may increase.

---

*$T = (E/\sigma_o^2)\ (dJ/da)$, where E is Young's modulus, σ_o is the flow stress, and dJ/da is the slope of the J-resistance curve.

Table 3.18. Revised fracture-toughness data for clean and doped steels.

Steel	Test	Fracture Toughness (J_{Ic}), psi-inch (MN/m)	Tearing Modulus $T = (E/\Delta\delta^2)(dJ/da)$
		Clean Steel	
As Cast	1000 psig N_2	575 (0.10)	67
	1000 psig H_2	420 (0.07)	72
Annealed	1000 psig N_2	542* (0.09)	152*
	1000 psig H_2	65 (0.01)	36
Wrought	1000 psig N_2	1,265 (0.22)	117
	1000 psig H_2	65 (0.01)	85
		Doped Steel	
As Cast	1000 psig N_2	658* (0.12)	77*
	1000 psig H_2	225* (0.04)	72*
Annealed	1000 psig N_2	245 (0.04)	181
	1000 psig H_2	30 (0.01)	36
Wrought	1000 psig N_2	605* (0.11)	65*
	1000 psig H_2	185* (0.03)	73*

*Based on results from new tests.

3.2.2 Commercial-Purity Iron

Twelve small laboratory ingots approximately 7 inches long, 3 inches wide, and 1 inch thick (approximately 17.8 cm long, 7.6 cm wide, and 2.5 cm thick) of commercial high-purity iron were provided by Armco for use in studies of hydrogen embrittlement and corrosion at Battelle and for studies of weldability at MSC. The ingots were produced in the laboratory but had chemical compositions that could be achieved in large castings produced using present practice at Armco. The chemical composition of one ingot from which specimens were prepared is presented in Table 3.19.

Table 3.19. Composition of iron ingot from which specimens were prepared.

Element	Content, weight percent*
Carbon	0.000
Manganese	0.004
Phosphorus	0.003
Sulfur	0.004
Silicon	0.170
Aluminum	0.001
Copper	0.068
Nickel	0.020
Chromium	0.045
Molybdenum	0.044
Vanadium	0.001

*Average of two emission-spectrographic analyses.

Metallographic sections were prepared from each of the castings. Figure 3.31 presents a photomicrograph of a transverse section through the ingot from which tensile specimens were prepared. The figure illustrates the solidification pattern and the very coarse grain size that was apparent in all of the castings. This coarse grain size is further illustrated in Figure 3.32. The photomicrographs in Figure 3.33 show very fine particles, which were present in the grains, and somewhat coarser particles that were present at the grain boundaries. These particles exhibited a lamellar structure (Figure 3.33b) and may have been fine pearlite precipitates, even though the bulk carbon content was

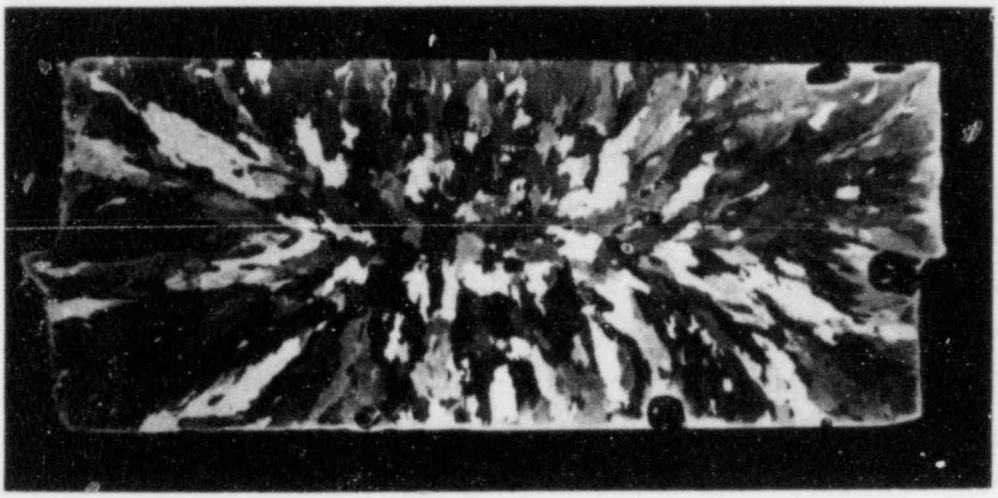

7L387

Figure 3.31. Transverse section through iron ingot from which tensile specimens were prepared.

25X Nital Etch 7L382

Figure 3.32. Microstructure of iron ingot in Figure 3.31.

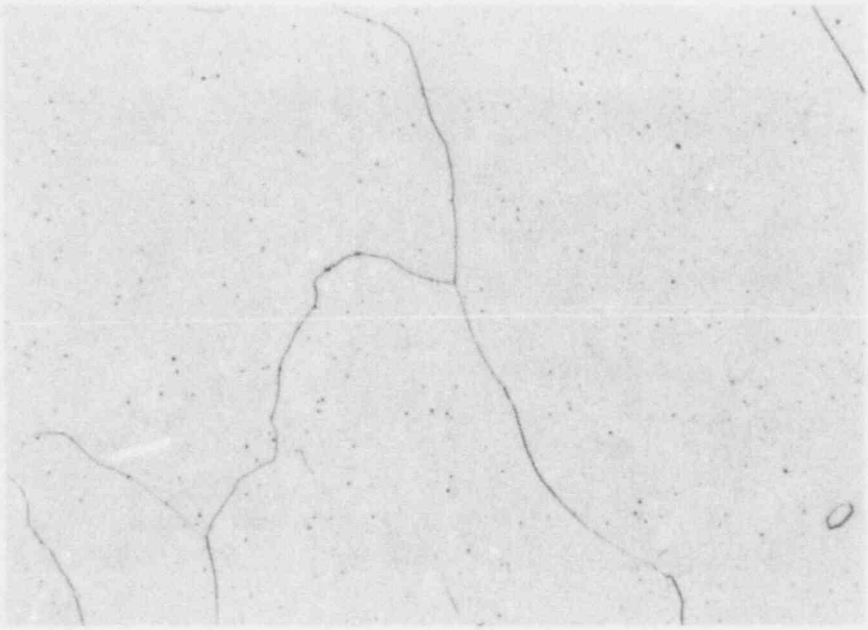

100X Nital Etch 7L368

a. Overall View

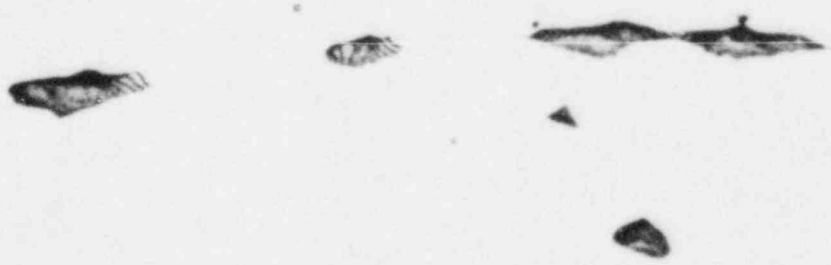

1000X Nital Etch 7L373

b. Grain-Boundary Precipitates

Figure 3.33. Photomicrographs of iron ingot showing fine precipitates at grain boundaries and in the matrix.

below the detectable level in spectrographic analysis. No inclusions were observed. It is interesting to note that the photomicrograph in Figure 3.33a was taken at the same magnification as were earlier photomicrographs of the steels.[3.1] Comparison between those photomicrographs indicates that the grain size of the commercially pure iron is approximately 5 times that of the cast steel studied previously in the as-cast condition.

3.2.2.1 Tensile Properties of Iron

Tensile specimens oriented longitudinally (tensile axis parallel to the pouring direction or the length of the ingot) and transversely (tensile axis perpendicular to the pouring direction and parallel to the width of the ingot) were tested in hydrogen and nitrogen. The longitudinal specimens had an 0.50-inch-diameter (1.3-cm-diameter) gage section that was 2.0 inches (5.1 cm) long, whereas the transverse specimens had a 0.25-inch-diameter (0.63-cm-diameter) gage section that was 1.0 inch (2.5 cm) long. The tests were conducted at an engineering strain rate of 10^{-4} sec^{-1}. The gas pressure was 1000 psig (6.9 MPa), and the tests were conducted at room temperature. An indication of the sensitivity of the material to embrittlement was obtained by comparing the tensile properties in those environments. Further information was obtained from fracture-toughness tests, which are discussed in a subsequent section.

The results of the tensile tests in the two environments are presented in Table 3.20. The results indicate that, as expected based on the previous studies and information in the literature, hydrogen had no effect on the strength properties. Hydrogen did reduce the ductility in both orientations, but to a greater extent in the transverse orientation. The reduction in area was decreased approximately 36 percent in the transverse specimens and approximately 17 percent in the longitudinal specimens. However, it should be noted that the absolute value of the reduction in area was greater for the transverse specimens in both environments. In neither case was the loss of reduction in area so great as to indicate severe hydrogen embrittlement.

3.2.2.2 Fracture-Toughness Properties of Iron

Fracture-toughness experiments were performed with compact-tension fracture-toughness specimens that were machined from the as-cast ingots. Experiments were conducted in 1000 psi (6.9 MPa) nitrogen and in 1000 psi (6.9 MPa) hydrogen to provide a relative indication of the degree of degradation of the resistance of the material to cracking by hydrogen. The experiments were intended to be standard elastic-plastic fracture-toughness experiments conducted in general accordance with ASTM Standard E813. However, as discussed later in this section, the behavior of the iron specimens was such that neither elastic-plastic nor linear-elastic (per ASTM Standard E399) standard fracture-toughness-measurement procedures could be followed.

Table 3.20. Tensile properties of iron.

Specimen Orientation[a]	Test Environment	Ultimate Tensile Strength ksi (MPa)	Yield Strength ksi (MPa)	Percent Elongation[b]	Reduction in Area (percent)
Longitudinal	1000 psig N_2	30.9 (213)	10.8 (74)	25.1	21.1
	1000 psig H_2	31.8 (219)	10.5 (72)	24.9	17.6
Transverse	1000 psig N_2	27.2 (188)	9.4 (65)	31.3	55.2
	1000 psig H_2	27.6 (190)	10.0 (69)	23.6	35.2

(a) Longitudinal orientation indicates that the specimen axis was oriented parallel to the pouring direction, or the length of the ingot. Transverse orientation indicates that the specimen axis was oriented transverse to the pouring direction, or parallel to the width of the ingot.

(b) Percent elongation was measured in a gage length that was equal to four times the diameter, in accordance with ASTM Standard E8-82, "Standard Methods of Tension Testing of Metallic Materials".

Figure 3.34 presents approximate J-resistance curves that were generated from the fracture-toughness-experiment data. There was some uncertainty in determining the actual crack lengths for reasons discussed later in this section. The J-resistance curves indicate that the fracture toughness (J_{Ic}) values in the nitrogen (reference) and hydrogen environments were approximately 440 psi-inch (0.08 MN/m) and 20 psi-inch (0.004 MN/m), respectively. As with many other materials, such as the cast steels that have been reported on previously, hydrogen dramatically reduced the resistance to initiation of ductile cracking. The tearing-resistance values also were extremely low, and a greater amount of rapid crack growth was observed in both environments than had been anticipated based on the cast steels.

These results suggest that fracturing proceeded in an elastic or brittle manner, with little or no plastic deformation preceding crack initiation. In essence, this is what occurred in the experiments, except that there was some ductile behavior prior to crack initiation--sufficient to rule out standard linear-elastic quantification of the fracture behavior. Continuous monitoring of crack length during the fracture-toughness experiments, using a direct-current electric-potential-drop method, provided an indication of the manner in which cracking occurred in this environment. In the nitrogen environment, the specimen was loaded elastically at first, and then plastic deformation at the crack tip occurred as the specimen was loaded further. Following what appeared to be a significant amount of plastic deformation, such that standard linear-elastic measures of fracture toughness, such as K_{Ic}, could not be determined with validity, a sudden drop in load was detected. This load drop was accompanied by a sudden rise in the signal from the electric-potential-drop probes, indicating a rapid increase in crack length. This "pop-in" form of crack initiation sometimes is observed in brittle, high-strength materials, but typically it is not preceded by any appreciable deformation. Thus, standard test methods could not be applied to interpret the results of these experiments.

However, some comparisons may be made between the cracking behavior in the nitrogen and hydrogen environments. Crack growth in the hydrogen environment proceeded in a manner similar to that described above for crack growth in nitrogen, except that pop-in crack initiation was preceded by a small amount of steady, possibly ductile, crack growth. This is reflected in the J-resistance curves, which indicate that hydrogen promoted a large reduction in resistance to crack initiation. However, because of the rapid nature of the subsequent pop-in cracking, the precise crack length indicated by the electric-potential-drop probes at a given point in an experiment was uncertain with the calibration procedure used. Thus, the J-resistance curves in Figure 3.34 are only approximate, and the extent of cracking in the hydrogen environment prior to pop-in is not known precisely.

The fracture-toughness-test results indicate that the iron samples that were studied underwent large reductions in J_{Ic} when exposed to hydrogen and had extremely low resistance to crack growth in both environments.

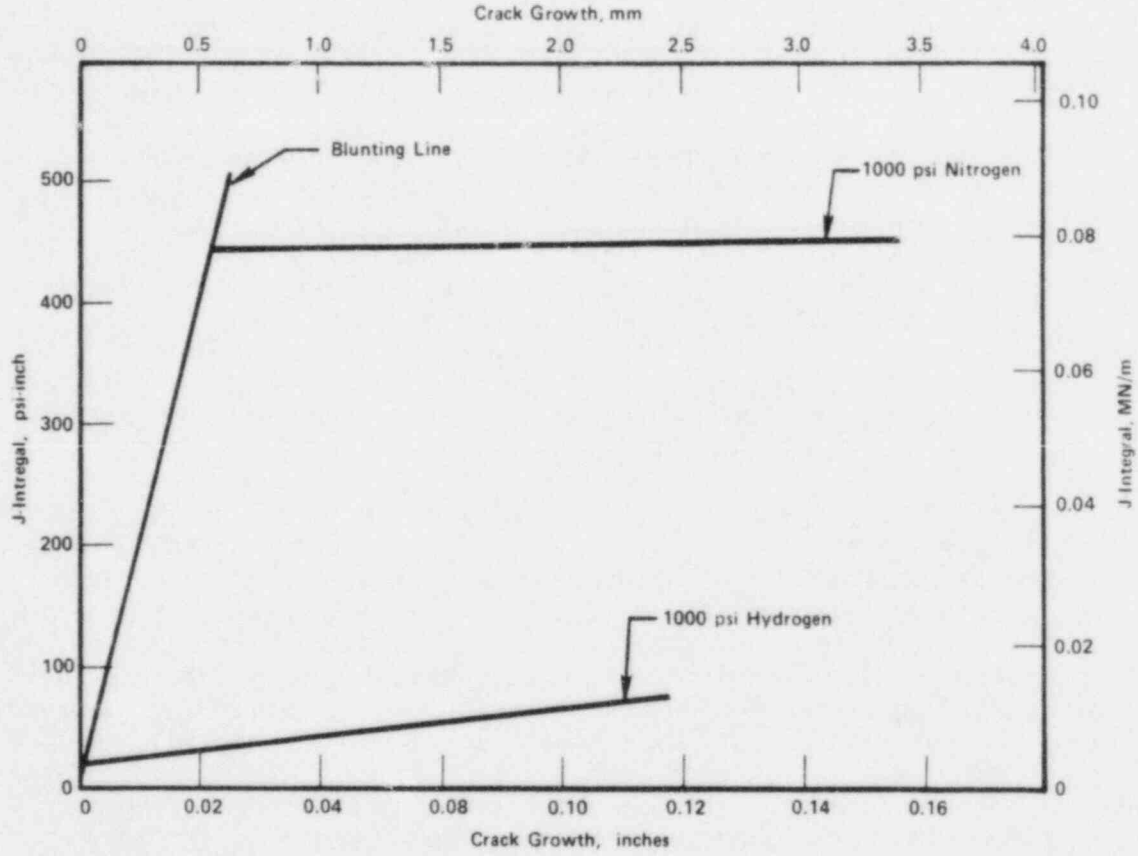

Figure 3.34. J-resistance curves for iron specimens.

In addition, observations during the tests suggest that the iron may be subject to rapid cracking, independent of environment. The presence of a hydrogen environment also promoted steady cracking prior to pop-in cracking. This behavior may indicate a sensitivity of this material to sustained-load subcritical crack growth. Therefore, subcritical-crack-growth experiments were performed to determine whether the iron was susceptible to this form of degradation. These experiments were non-standardized tests that have been developed recently at Battelle to evaluate the sensitivity of a relatively ductile material to subcritical-crack growth in an aggressive environment.

3.2.2.3 Subcritical Crack Growth in Iron

Subcritical-crack-growth experiments were conducted with fracture-toughness specimens in the following manner. Each specimen was fatigue precracked in the test environment, 1000 psi (6.9 MPa) nitrogen or 1000 psi (6.9 MPa) hydrogen. Then, a fixed load-line displacement was imposed on the specimen, and the load and crack length were monitored. If no subcritical crack growth was observed in a period of at least one hour, the displacement was increased and another one-hour hold period at fixed displacement was imposed. This sequence was repeated three times or until crack growth was detected.

The subcritical-crack-growth experiments provided no indication of crack growth at fixed displacement. In every load period, there was a small decrease in load and an apparent increase in crack length that was related to crack-tip relaxation processes. After completion of the test in nitrogen, the nitrogen was evaluated and replaced with hydrogen while the displacement was maintained. However, no crack growth was observed under those conditions, even when additional displacement increments were imposed. Thus, it appears that although the iron has low toughness in an inert environment and undergoes significant loss in J_{IC} in hydrogen, subcritical-crack growth is not likely.

3.2.3 Future Work

Hydrogen-embrittlement studies will be de-emphasized during the coming year, unless there is a significant change in the direction of DOE research. However, the issue of microstructural changes in cast steel resulting from welding or from long-term exposure to repository temperatures remains to be resolved. At present, it is planned that studies will be conducted with welded steel samples produced by MSC provided that those samples are made available.

3.3 Corrosion Correlations

Studies of corrosion correlations were continued, during the third year of this program, in the areas of general corrosion and pitting corrosion of container materials. Efforts in general corrosion research were directed toward development of a physically realistic model that would include processes of major importance in an actual repository. The

model was applied to some specific examples to illustrate effects brought about by varying certain parameters. Pitting-corrosion studies were directed toward an analysis of the evolution of the pit-depth distribution based on specific functional forms for the rates of pit generation and pit growth. In addition, the current associated with pitting corrosion was calculated based on the binary-electrolyte model of pit growth developed during the second project year.

3.3.1 Analysis of General Corrosion

Development of a comprehensive model for general corrosion of waste-package container materials has continued to be a subject of primary interest during the third year of this program. Processes that are included in this model are the following:

(1) Heat and mass transport in the aqueous solution outside the container walls

(2) Growth kinetics of an oxide film on the metal surface

(3) Radiolytic production of chemical species and homogeneous chemical reactions within the groundwater.

The mathematical formalism required to treat items 1 and 3 above was developed during the second project year and has been summarized in the pertinent annual report.[3.12] Two specific examples were considered in that report. The first involved an analysis of a heat-conduction problem, using a primary assumption that the temperature at the container surface decreases exponentially with time. The second example involved the mass transport, via chemical diffusion, of a single radiolytically produced, electrically neutral species--nominally O_2. Film-growth kinetics was not included in this example; instead, "maximum-rate" kinetics was assumed by imposing the boundary condition that the concentration of the species in the solution at the container surface was zero. Additional studies related to this example were carried out during the past year and are described below.

The second example discussed above was extended by including a second chemical species, i.e., an electrically neutral reducing species with which the oxidizing species can chemically react. In addition, the assumption of maximum-rate kinetics was relaxed by the inclusion of a model of film-growth kinetics and the appropriate coupling of this model with that for mass transport within the solution. Effects of including film growth were studied using the simpler example of just one chemical (oxidizing) species. The major results obtained from all these studies are presented below.

Clearly, the studies to date have involved highly simplified models of general-corrosion kinetics. This approach was selected in order to check the accuracy of the numerical procedure, evaluate effects of imposing various boundary conditions, and obtain an unambiguous

assessment of gross features of the corrosion process. The last item is of particular importance; such assessments are not readily made using complex corrosion models because of competitive and overlapping processes.

Presented below are the results of applying the general-corrosion formalism to three specific cases. In each case important aspects of the process are illustrated. As will be seen, each case required some extension of the overall modeling effort.

3.3.1.1 One Chemical Species, Maximum-Rate Kinetics

In the annual report for Year Two of this program,(3.12) the results of sample calculations were presented for a simplified general-corrosion model. The major assumptions used in this model are as follows:

- The behavior of one electrically neutral oxidizing species within the groundwater outside the container wall was considered. This species, nominally O_2, was assumed to be radiolytically produced.

- Mass transport of the dissolved species to the container surface occurred via chemical diffusion only, with cylindrical geometry being assumed for the surface.

- Aside from its radiolytic production, the dissolved species underwent no chemical reactions within the groundwater.

- The entire system was isothermal.

- A "maximum-rate" model was used, in the sense that the concentration of the dissolved species at the container wall was taken to be maintained at zero. In this approximation, film-growth kinetics did not, in any way, inhibit the rate of transfer of the species across the metal/groundwater interface.

- The gamma-field intensity, $I(r,t)$, measured at radial distance r from the axis of symmetry at time t, was taken to be

$$I(r,t) = I_0\left(\frac{r_0}{r}\right)\exp\left[-\lambda t - \varepsilon(r-r_0)\right] , \qquad (3\text{-}1)$$

  where I_0 is the intensity at the container surface, $r = r_0$ at time $t = 0$, λ is a radioactive-decay constant, and ε is the linear absorption coefficient characteristic of the surrounding medium.

In Equation 3-1, the 1/r factor represents geometric spreading of the gamma field. The first term in the argument of the exponential function describes the decay with time of the gamma-field intensity and the

second term describes absorption of the gamma radiation by the groundwater medium. In this and subsequent examples reported here, units were normalized by setting I_o, r_o, and λ equal to unity.

The local rate of production of the chemical species, being proportional to $I(r,t)$, was expressed as gI, where g is a parameter chosen to be dimensionless so that the production rate is likewise dimensionless.

The concentration field characterizing the species, $c(r,t)$, was computed for three different cases, i.e.,

- $g = 1, \varepsilon = 1$
- $g = 10, \varepsilon = 1$
- $g = 10, \varepsilon = 2$

using the following initial and boundary conditions:

- $c(r = 1, t > 0) = 0$
- $c(1 < r < 5, t = 0) = c(r = 5, t > 0) = 1.$

In this manner, effects of increasing the production rate and the linear absorption coefficient were both evaluated.

During the past year, further consideration was given to these three cases. In particular, the rate of general corrosion was calculated as a function of time for each case. This rate is proportional to the rate at which the oxidizing species is transported across the container surface which, on the basis of this model, is in turn proportional to

$$\frac{\partial c}{\partial t}(r = 1, t) \quad .$$

In addition, the total depth of penetration of the corrosion layer into the metal, which is proportional to

$$\int_0^t \frac{\partial c}{\partial r}(r = 1, t) \, dt \quad ,$$

was also calculated for each case as a function of time. The results are illustrated in Figures 3.35 and 3.36. Since we are presently interested only in relative variations of corrosion rates and penetration depths, these quantities are plotted in terms of normalized, dimensionless units, the precise definitions of which are unimportant for present purposes.

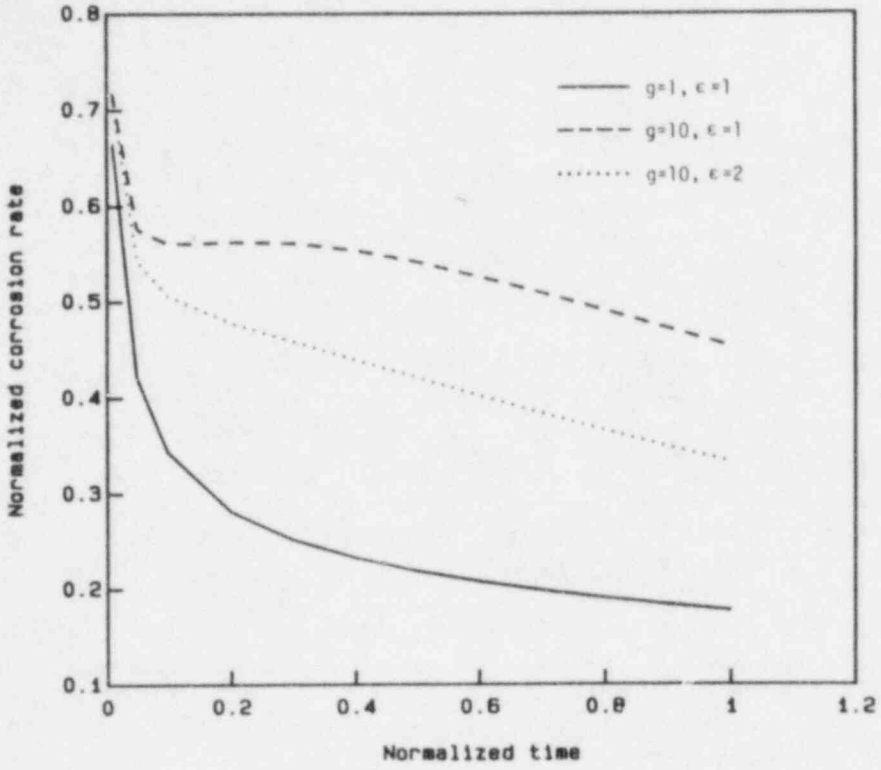

Figure 3.35. Calculated rates of general corrosion as a function of time.

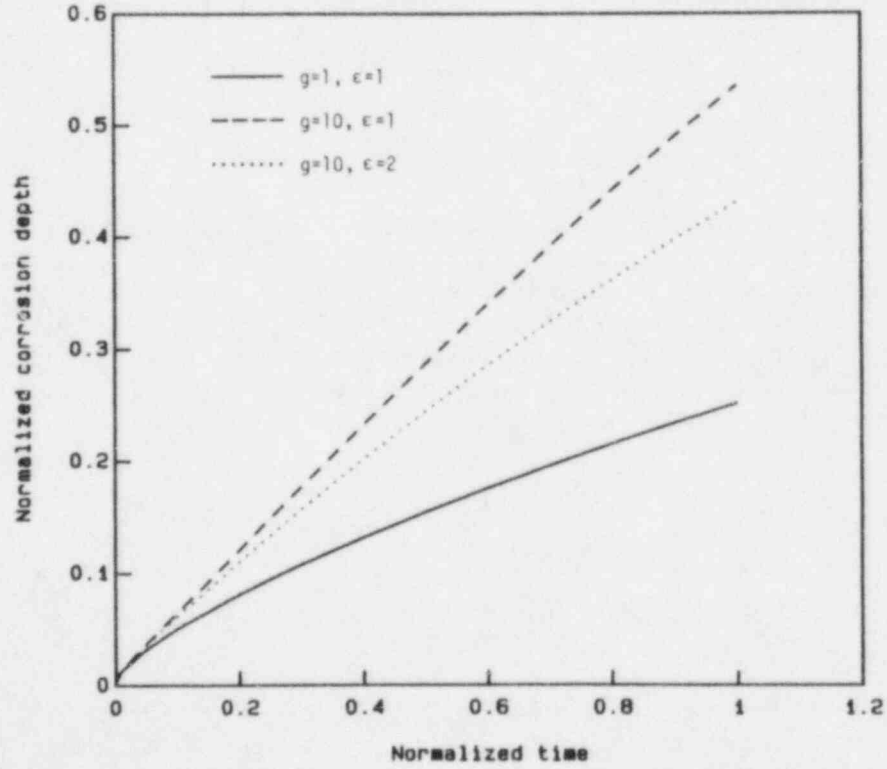

Figure 3.36. Calculated depth of penetration by general corrosion as a function of time.

The calculated corrosion rates are plotted in Figure 3.35. For the case $g = 1$, $\varepsilon = 1$, the corrosion rate decreases monotonically with time. For the case $g = 10$, $\varepsilon = 1$, which corresponds to a large increase in the production rate of the oxidizing species relative to the previous case (for which $g = 1$), the corrosion rate at any given time generally is significantly higher than the corresponding rate for $g = 1$, $\varepsilon = 1$ calculated at the same time. The corrosion rate even experiences a period during which it increases with time. This behavior results, of course, from the much greater amount of the oxidizing species that is generated for $g = 10$. Finally, the case $g = 10$, $\varepsilon = 2$ illustrates the effect of increasing the linear absorption coefficient by a factor of two. Comparison of the cases $g = 10$, $\varepsilon = 1$ and $g = 10$, $\varepsilon = 2$ shows that the corrosion rate is indeed reduced by increasing ε, although the resultant curve still lies well above that for the case $g = 1$, $\varepsilon = 1$.

The corrosion depth calculated for these same three cases is plotted in Figure 3.36 on the same time scale as in Figure 3.35. As would be expected from the results presented in Figure 3.35, the corrosion depth, at a given time, is indeed largest for the case $g = 10$, $\varepsilon = 1$, and smallest for the case $g = 1$, $\varepsilon = 1$.

From the results of this highly idealized analysis, it appears that radiolytic production of oxidizing species could indeed have a significant effect on the overall kinetics of general corrosion. A major objective of this particular task is to quantify further our understanding of this effect through the use of more physically realistic radiolysis models and through the inclusion of film-growth kinetics on the container surface.

3.3.1.2 Two Chemical Species, Maximum-Rate Kinetics

A natural extension of the simplified model discussed immediately above would be to introduce a second chemical species, i.e., an electrically neutral reducing species with which the oxidizing species can react chemically. Again assuming radial cylindrical symmetry, the mass transport of the ith species ($i = 1, 2$ for the two species) can be described in terms of the following partial differential equation:

$$\frac{\partial c_i}{\partial t} = D_i \frac{1}{r} \frac{\partial}{\partial r} \left(r \frac{\partial c_i}{\partial r} \right) + g_i I - a c_1 c_2 - b_i c_i \qquad (3\text{-}2)$$

where $c_i(r,t)$ is the concentration of species i in the water (i.e., for $r > 1$ in our normalized units.)

The right-hand side of Equation 3-2 is simply a sum of terms that represent different mechanisms which can cause c_i to vary with time. The first term represents chemical diffusion, with D_i being the diffusion coefficient. The second term represents the rate of radiolytic production, with I being given by Equation 3-1. The third represents loss of

species i by chemical reaction with the other species, with "a" being the pertinent rate constant. As expressed in Equation 3-2, the reaction is assumed to be of second order, with species i and j being "lost" in equal amounts when the reaction occurs. Of course, it would be a simple matter to generalize this reaction-rate term to account for other types of reactions, in which case the rate constant, a, would accordingly differ for the two cases, i = 1 and 2, in order to maintain stoichiometry. The fourth term accounts for loss of species i as a result of a pseudo-first-order chemical reaction of that species with another, unspecified species that is assumed to exist in virtually infinite supply.

Clearly, for the special case for which a = 0, there is no coupling between c_1 and c_2 (taking i = 1 and 2 for the oxidizing and reducing species, respectively). For this case, c_1 would exhibit behavior identical to that presented above for the first example.

The initial and boundary conditions selected for this second example were the same as for the first example as far as the oxidizing species is concerned. In addition, for the reducing species, it was assumed that

- $c_2 (r > 1, t = 0) = 0$
- $c_2 (r = 5, t > 0) = 0$
- $\frac{\partial c_2}{\partial r} (1, t) = 0.$

Moreover, values assumed for other parameters were $g_i = 10$ and $b_i = 0$ for i = 1 and 2, and $\epsilon = 2$. Hence, effects of a pseudo-first-order reaction were not included in this example. Also, a value of unity was selected for D_i, i = 1 and 2, as well as for the rate constant, a.

Some results of these calculations are shown in Figures 3.37 and 3.38, in which profiles of the concentrations of the oxidizing and reducing species are plotted for various times. For comparison, the results of a similar one-species calculation (equivalent to the first example) are also given in Figure 3.39. Again, these latter results could have been generated by the two-species model by setting a equal to zero. Comparing Figures 3.37 and 3.39, the results are similar for short times, but at longer times the reaction that takes place between the two radiolytic species reduces the concentration of the oxidizing species and thus must also reduce the corrosion rate. In Figure 3.40 we plot a normalized measure of the corrosion rate as a function of time for both models, and the difference between the two predicted corrosion rates is evident. Finally, in Figure 3.41 we plot a normalized measure of the corrosion depth or wastage as a function of time.

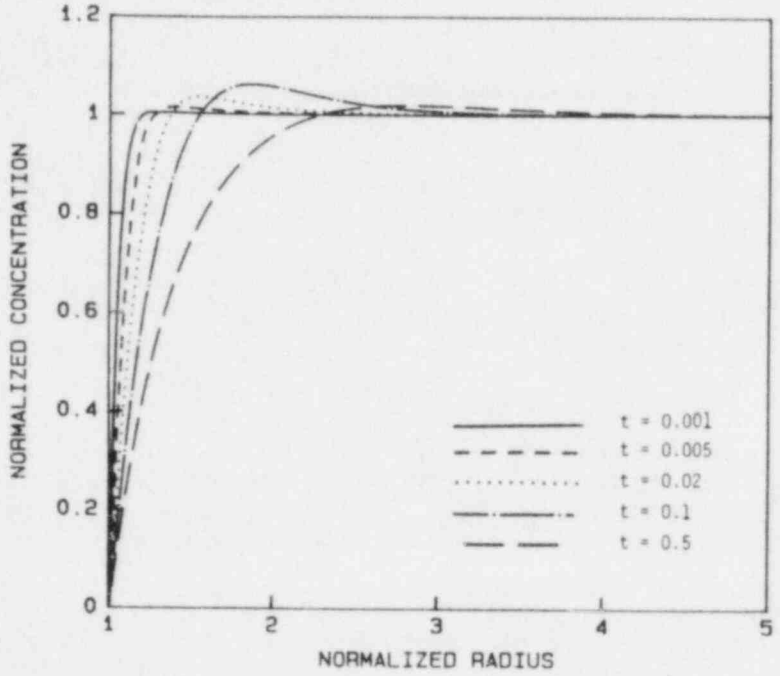

Figure 3.37. Concentration profiles for the oxidizing radiolytic species, as calculated by the two-species model using maximum-rate kinetics for corrosion.

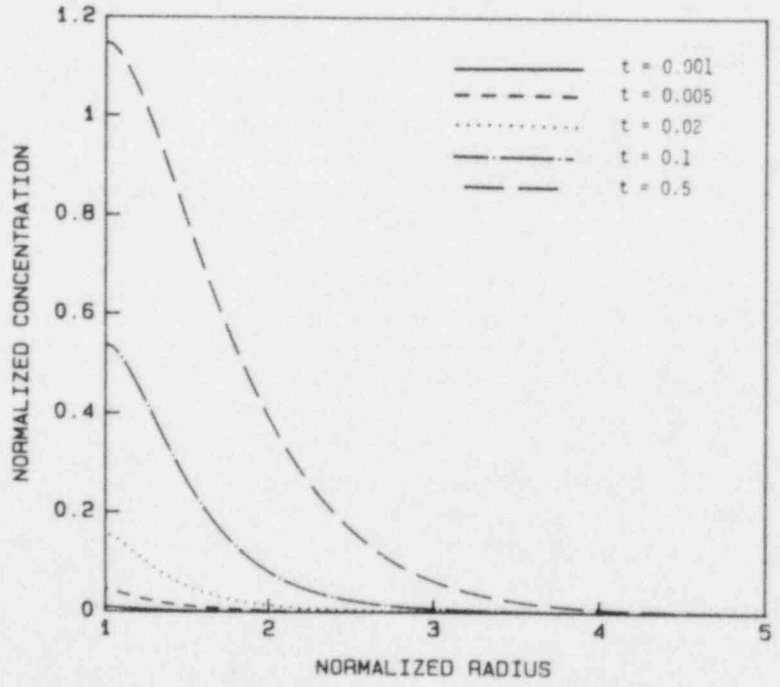

Figure 3.38. Concentration profiles for the reducing radiolytic species, as calculated by the two-species model using maximum-rate kinetics for corrosion.

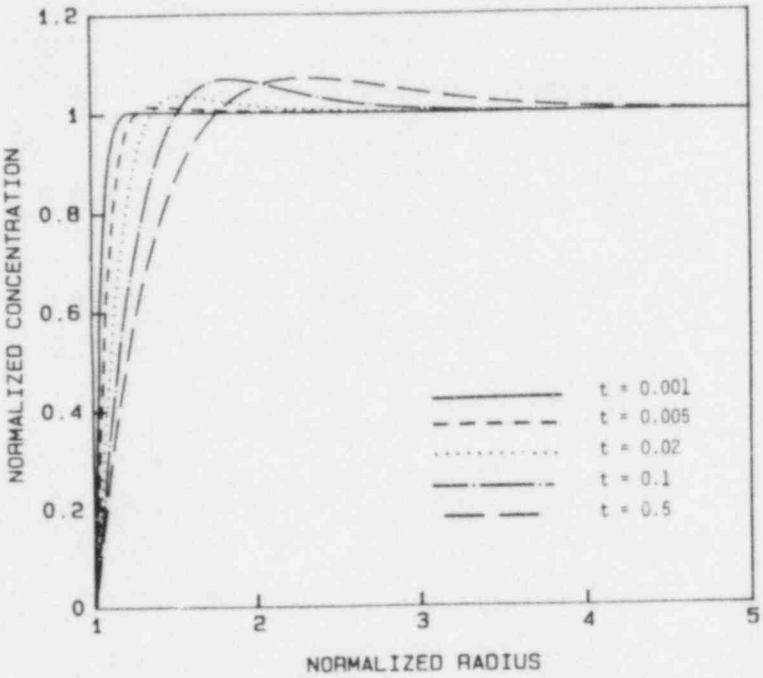

Figure 3.39. Concentration profiles for the oxidizing radiolytic species, as calculated by the one-species model using maximum-rate kinetics for corrosion.

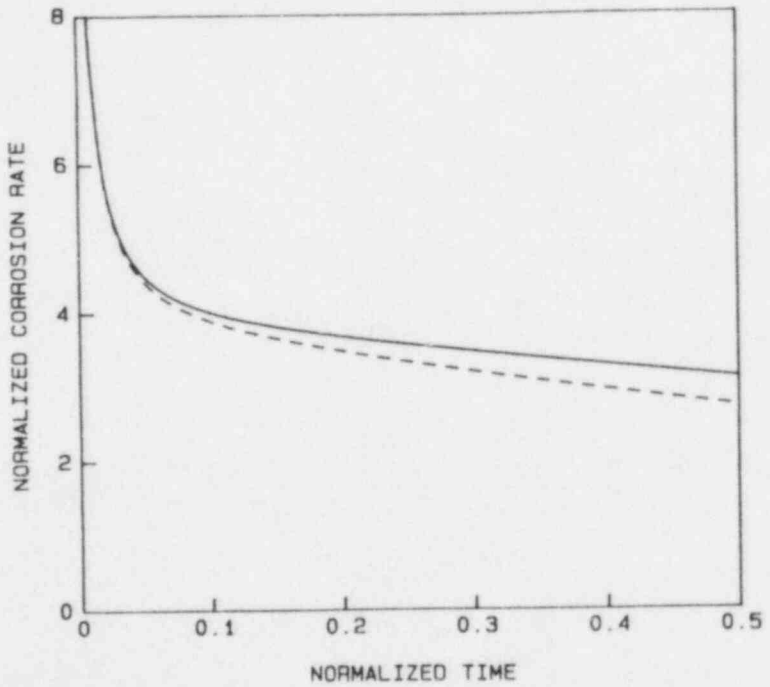

Figure 3.40. Corrosion rate as a function of time as calculated by the one-species model (solid) and two-species model (dash) using maximum-rate kinetics for corrosion.

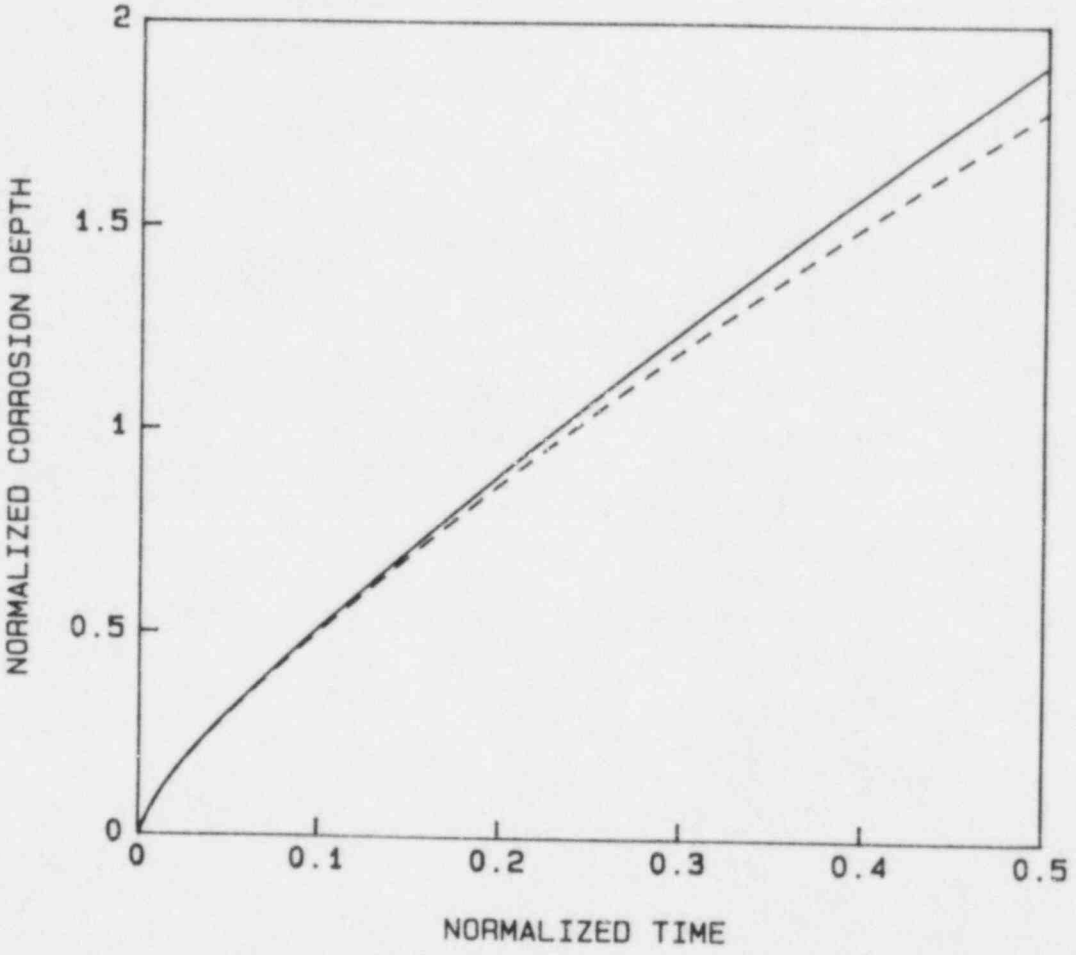

Figure 3.41. Corrosion depth as a function of time as calculated by the one-species model (solid) and two-species model (dash) using maximum-rate kinetics for corrosion.

3.3.1.3 Inclusion of Film-Growth Kinetics

In another refinement of the general corrosion model, the boundary condition at the container/groundwater interface has been generalized to account for the kinetics of film growth on the metal surface. For this purpose, the film-growth model of Chao, Lin, and Macdonald[3.13] was used. This point-defect model describes the rate of growth of a passive film in terms of the transport of oxide species through the film, and is summarized by the following expression which is valid for a fixed groundwater pH:

$$\frac{dL}{dt} = \frac{A_1 \exp\left(\frac{-2\alpha V_{ext}}{RT}\right)\left[B_1 \exp\frac{2FV_{ext}}{RT} - 1\right]}{\exp\left(\frac{2FEL}{RT}\right) - 1} \qquad (3\text{-}3)$$

where L is the wastage at time t, A_1 and B_1 are constants (although they vary with pH), V_{ext} is the external potential, F is the Faraday constant, R is the gas constant, T is the absolute temperature, and E is the electric field strength within the oxide (assumed constant).

A complicating factor in the application of Equation 3-3 is that V_{ext} generally depends upon the concentrations of oxidizing and reducing species, [OX] and [RE], respectively, at the container/groundwater interface, according to the relation

$$V_{ext} = V^{\circ}_{ext} + \frac{RT}{F} \ln\left(\frac{[OX]}{[RE]}\right) \qquad (3\text{-}4)$$

where V°_{ext} is a constant. Hence, V_{ext} changes as these concentrations change.

Of course, Faraday's law must still be applied at the container surface, i.e.,

$$\frac{dL}{dt} = \frac{D_o v}{n}\frac{\partial c_o}{\partial r}\,(r = 1) \qquad (3\text{-}5)$$

where D_o is the diffusivity of the oxidizing species, v is the molar volume of the metal, n is the number of molecules of the oxidizing species necessary to oxidize one atom of metal, and c_o is the concentration of the oxidizing species with $c_o(r = 1) = [OX]$. Although we are considering only a single oxidizing species here, a more general treatment would require a summation of the contributions of all the oxidizing

species that may be present. Clearly, we continue to assume that the oxidizing species is neutral.

Upon comparison of Equations 3-3 to 3-5, we find that inclusion of film-growth kinetics at the container surface results in a boundary condition that is far more complex than that for maximum-rate kinetics, which was simply $c_O(r = 1) = 0$ for the oxidizing species. Of course, the boundary condition for the neutral reducing species, regardless of whether or not film growth is accounted for, is

$$\frac{\partial c_r}{\partial r} (r = 1) = 0$$

where $c_r(r = 1) = [RE]$, again considering for the present the existence of only a single reducing species.

Imposing the boundary condition represented in Equations 3-3 to 3-5 clearly is not a simple matter, since it consists of a complex relationship between concentration gradients and concentrations measured in the groundwater at the container surface. In general, its imposition can be accomplished only through the application of a numerical, iterative procedure. Briefly, this was carried out by taking the difference between the right-hand side of Equation 3-3 and that of Equation 3-5, at each time step of the calculation, and applying a secant method to determine conditions for which that difference is zero.

One additional computational aspect that is noted here is that the concentration gradient at $r = 1$ is somewhat more difficult to calculate than the gradient elsewhere. Normally, we use a central-difference approximation with accuracy of order h^2 where h is the step size. A central difference cannot be taken in this case since the function is not defined for $r < 1$. Therefore, we use a one-sided difference approximation with accuracy of order h^2 to calculate the concentration gradient at $r = 1$. For an arbitrary function u that be evaluated for arguments greater than or equal to x,

$$\frac{du}{dx} = \frac{4u(x + h) - 3u(x) - u(x + 2h)}{2h} + O(h^2) \qquad (3\text{-}6)$$

where h is the step size and $O(h^2)$ denotes terms of order h^2. The error in Equation 3-6 is about twice that of our usual central-difference approximation for the derivative.

One test calculation was carried out in which the film-growth model was included. This calculation was essentially the same as that presented above based on the one-species model, except that the boundary condition

based on the assumption of maximum-rate kinetics was replaced with Equations 3-3 to 3-5. For this calculation, the following additional data were used: $A_1 = B_1 = 1$, $D_O v/n = 1$, $FE/(RT) = 10^5$, $FV_{ext}/(RT) = 1/300$. In addition, the singularity at $L = 0$ predicted by Equation 3.3 was avoided by selecting an initial value of $L = 10^{-4}$.

Corrosion rates and depths for this calculation are shown in Figures 3.42 and 3.43, while concentration profiles for various times are shown in Figure 3.44. These results may be compared with those for the one-species maximum-rate model shown in Figures 3.39 to 3.41. Inclusion of the film-growth model results in a much more rapid decrease of the corrosion rate with time than that predicted using the maximum-rate model. The calculated corrosion depths are also correspondingly smaller. Since the rate of consumption of the oxidizing species is so much smaller as a result of including film-growth effects, the concentration of this species builds up to much higher levels, as seen from comparison of Figures 3.39 and 3.44.

3.3.2 Analysis of Pitting Corrosion

Studies carried out thus far on this program in the area of pitting corrosion have been centered on three principal aspects of the overall process:

- Pit-generation kinetics
- Pit-growth kinetics
- Evolution of the pit-depth distribution.

The greatest emphasis thus far has been placed on the last two aspects, in which substantial progress has been made[3.14]. Presented below is a summary of research on pitting corrosion carried out during the past year.

3.3.2.1 Pit-Generation Kinetics

Some effort was devoted during the past year to studies of pit generation kinetics, about which there is still relatively little knowledge. However, it does appear to be possible to make use of existing theoretical models of pit initiation, in conjunction with a more empirical description of the rate at which pits are formed on a metal surface. These would be used to develop a physically reasonable description of the overall pit-generation process.

As has already been pointed out[3.14], the approach would use an existing model[3.15] for the induction time for pitting at an "average" site. The model would then account for a statistical distribution of induction times about that for the "average" site through the application of essentially empirical techniques. The remaining problem would be to select a statistical distribution that would adequately describe the gross features of pit-generation kinetics.

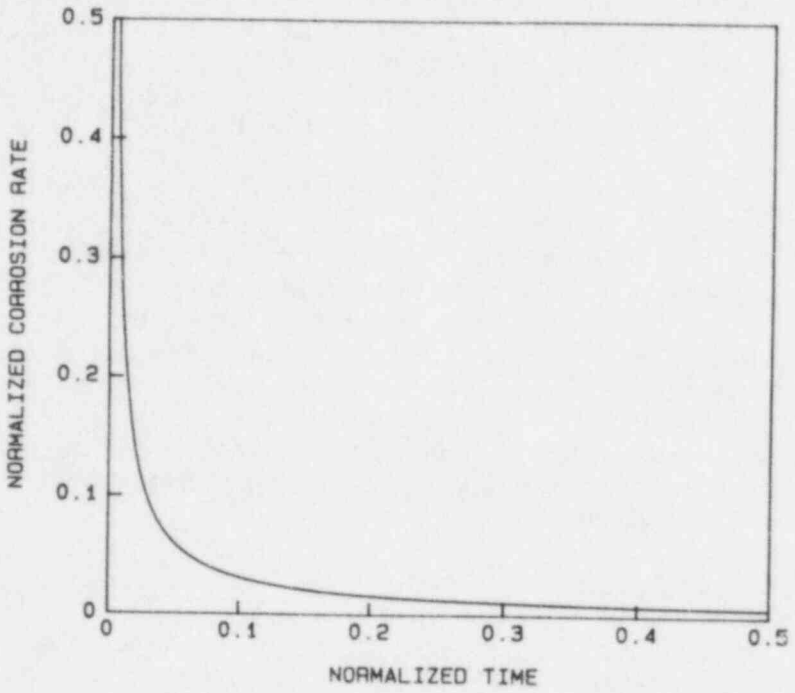

Figure 3.42. Corrosion rate as a function of time as calculated by the one-species model using the point-defect model for film growth.

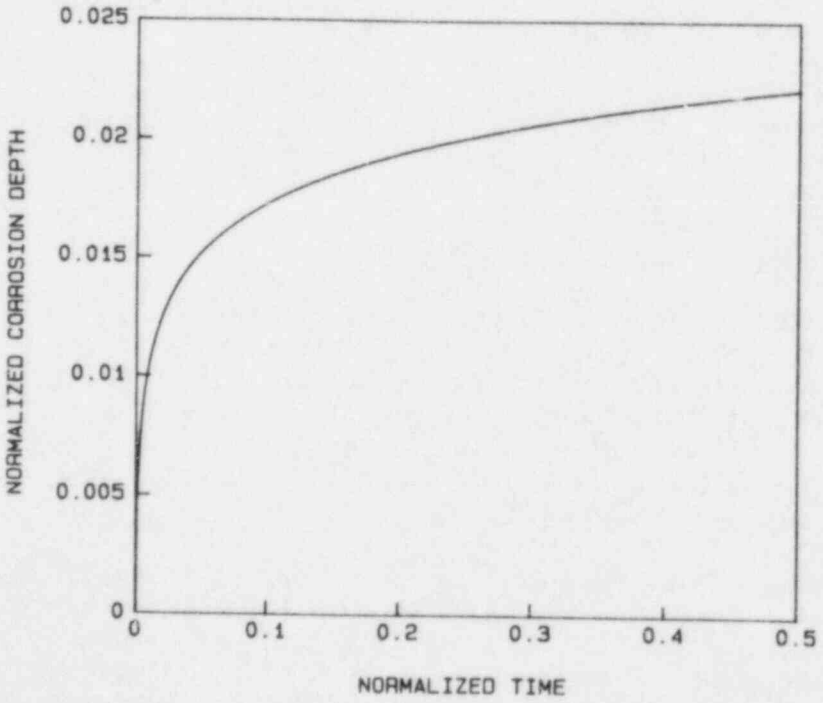

Figure 3.43. Corrosion depth as a function of time as calculated by the one-species model using the point-defect model for film growth.

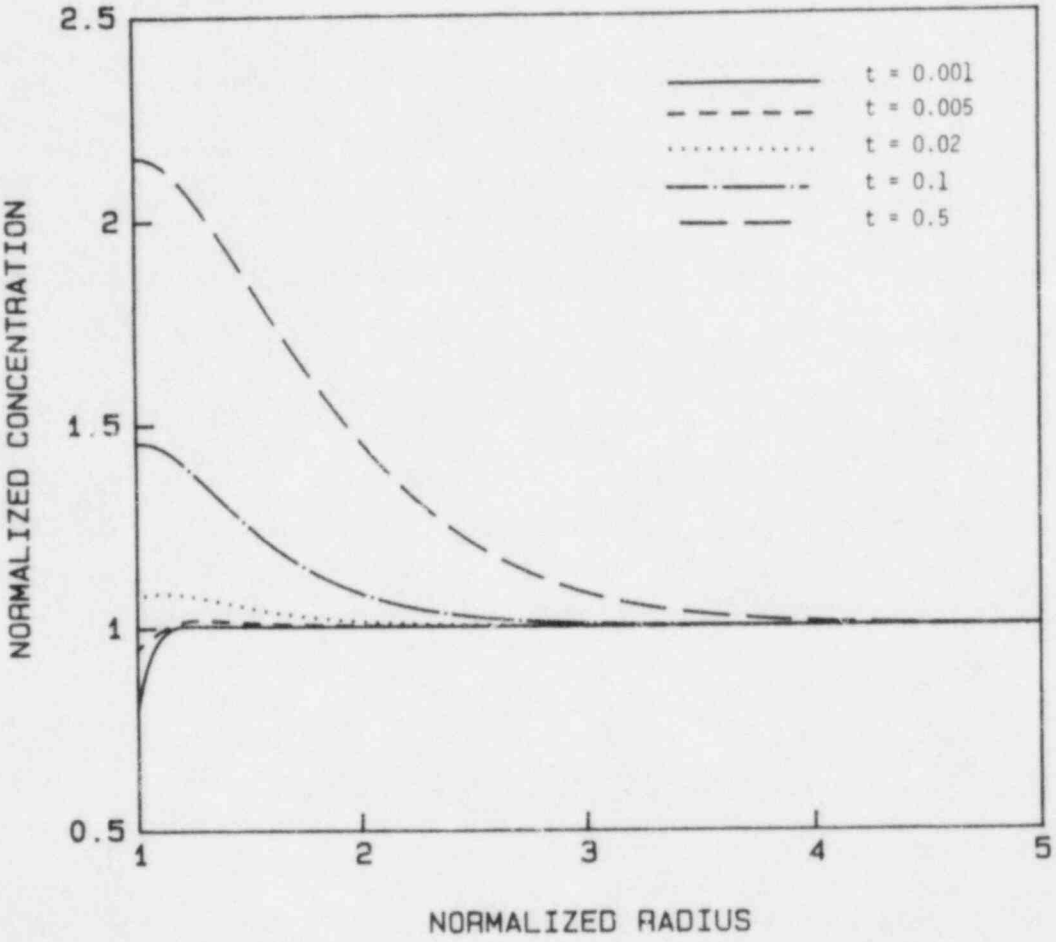

Figure 3.44. Concentration profiles for the oxidizing radiolytic species, as calculated by the one-species model using the point-defect model for film growth.

For example, the time-dependent pit-generation rate, G(t), which is defined as the number of pits generated per unit area of surface per unit time, may be a "peaked" type. Janik-Czachor and Ives[3.16] described the gross features of such behavior, which are that G(t) rises from zero to a maximum value and then falls to zero once again, using a very simple $\sin^2(0.2t)$ function.

During the past year, an improved approach to describing pit-generation kinetics was explored, based on a more flexible generation-rate function, i.e., one that could be more readily brought into accord with corresponding experimental data. Specifically, the function that was used was the Weibull distribution function, which has long been used to describe statistically based phenomena related to various aspects of the behavior of materials.

For present purposes, we express the Weibull distribution as

$$G(t) = \frac{mN_\infty}{\tau^m} (t - t_o)^{m-1} \exp\left[-\left(\frac{t - t_o}{\tau}\right)^m\right] \quad , \tag{3-7}$$

which is applicable for $t > t_o$ and with $G(t) = 0$ for $t \leq t_o$. Here, N_∞, m, τ, and t_o are certain characteristic parameters. In particular, the instantaneous total number of pits per unit area of metal surface, N(t), is given by

$$N(t) = \int_{t_o}^{t} G(t)dt = N_\infty \left\{1 - \exp\left[-\left(\frac{t - t_o}{\tau}\right)^m\right]\right\} \tag{3-8}$$

so that N_∞ is the total pit concentration on the surface at asymptotically large times. It is noted that effects of overlap of growing pits, which have been discussed elsewhere[3.17], are not considered here.

For $m > 1$, the function G(t) given by Equation 3-7 rises smoothly from zero beginning at time $t = t_o$, "peaks" at time t_{max} which is given by

$$t_{max} = t_o + \tau \left(1 - \frac{1}{m}\right)^{1/m} \quad , \tag{3-9}$$

and then decreases monotonically with time, approaching zero asymptotically.

The time t_{max} can be chosen to be the characteristic incubation time, as predicted from first principles[3.15]. Values of N_∞, τ, and m can then

be chosen that would yield generation-rate behavior that is consistent with experimental data. Such choices may, however, have to be inferred from pit-depth-distribution measurements, which are more likely to be made than direct measurements of the pit-generation rate itself. Theoretical relationships between pit-generation rate and the time-dependent pit-depth distribution have already been established for some elementary cases[3.16-3.18]. Some applications of the above analysis of pit-generation kinetics to studies of the variation with time of the pit-depth distribution are presented next.

3.3.2.2 Evolution of Pit-Depth Distribution

Let $h(t, t_g)$ be the depth of a pit, at time t, which had been generated at time $t_g \leq t$. We assume here that h exhibits power-law dependence upon time, i.e.,

$$h = a(t - t_g)^b \tag{3-10}$$

where a and b are positive parameters, independent of t, t_g, and h. Many types of pit growth have been found to satisfy a relationship of this general type, as has been discussed elsewhere[3.19]. Moreover, it was shown[3.18], for this particular growth-rate expression, that the pit-depth distribution function, f(h,t), defined such that f(h,t)dh is the number of pits per unit area of surface, at time t, that have depth between h and h+dh, is related to G(t) through the expression

$$f(h,t) = \frac{1}{ab}\left(\frac{h}{a}\right)^{\frac{1-b}{b}} G\left(t - \left(\frac{h}{a}\right)^{\frac{1}{b}}\right) \tag{3-11}$$

for $h < a\,(t - t_o)^b$, assuming that pit generation begins at time t_o (taken as zero in Reference 3.18) and that $f(h,t) = 0$ for $h > a\,(t - t_o)^b$, where G(t) is an arbitrary pit-generation-rate function. It was assumed, in the derivation of Equation 3-11, that deactivation of growing pits did not occur.

For the specific case in which G(t) is given by Equation 3-7, we can use Equation 3-11 to show that

$$f(h,\,t) = \frac{mN_\infty}{a\tau^b}\left(\frac{h}{a\tau^b}\right)^{\frac{1-b}{b}}\left[\frac{t - t_o}{\tau} - \left(\frac{h}{a\tau^b}\right)^{\frac{1}{b}}\right]^{m-1}$$

$$\cdot \exp\left\{-\left[\frac{t - t_o}{\tau} - \left(\frac{h}{a\tau^b}\right)^{\frac{1}{b}}\right]^m\right\}, \tag{3-12}$$

which is valid for $t > t_o$ and $h < a(t - t_o)^b$. Also, $f(h,t) = 0$ for $t < t_o$ and $h > a(t - t_o)^b$.

We now illustrate the application of this analysis to some specific examples. However, rather than choosing values for all the pertinent parameters, it is convenient to first reduce all quantities that appear in the various expressions to dimensionless form. Examination of Equations 3-7, 3-8, and 3-12 shows that natural choices for such quantities are

$$g \equiv \frac{\tau}{mN_\infty} G \tag{3-13}$$

$$n \equiv \frac{N}{N_\infty} \tag{3-14}$$

$$T \equiv \frac{t - t_o}{\tau} \tag{3-15}$$

$$H \equiv \frac{h}{a\tau^b} \tag{3-16}$$

$$F \equiv \frac{ab\tau^b}{MN_\infty} f \tag{3-17}$$

in which case Equations 3-7, 3-8, and 3-12 respectively, are reduced to

$$g = T^{m-1} \exp\ (-T^m) \tag{3-18}$$

$$n = 1 - \exp\ (-T^m) \tag{3-19}$$

$$F = H^{\frac{1-b}{b}} \left(T - H^{\frac{1}{b}}\right)^{m-1} \exp\ \left[-\left(T - H^{\frac{1}{b}}\right)^m\right] \tag{3-20}$$

with Equation 3-20 being valid within the range $T > 0$ and $H < T^b$, and with $F = 0$ for $T < 0$ and $H > T^b$. The only input parameters that are now needed in Equations 3-18 to 3-20 are m and b.

Some specific numerical examples were selected to illustrate these results. First, the value b = 0.5 was selected for all the examples, since this corresponds closely to the value of 0.49 reported by Marsh[3.20] for carbon-steel nuclear-waste containers. Using this value of b, Equations 3-18 and 3-19 are plotted in Figures 3.45a and 3.45b, respectively, for m = 2, 3, and 4. Moreover, the pit-depth distribution at selected times is plotted for these three examples in Figures 3.46 to 3.48 using Equation 3-20.

The effect of increasing the value of m is seen, in Figure 3.45a, to reduce the pit-generation rate at short and long times; that is, to essentially shorten the duration over which most of the pits are generated. This behavior is also reflected in Figure 3.45b, which shows that the total pit concentration approaches its saturation level more quickly as m is increased.

The "spreading" of the pit-depth distribution with increasing time is illustrated for these cases in Figures 3.46 to 3.48. Although some differences in properties of the distribution function at the same given value of T are seen to exist for the different values of m, gross features of the general shape are similar in all three cases.

3.3.2.3 Pitting Current

In the most recent annual report[3.19] on this program, a pit-growth model was developed based on the well-known transport theory characterizing an infinitely dilute solution of a "binary electrolyte", i.e., a solution containing one cation species and one anion species. (The general theory of binary electrolytes has been presented in detail by Newman[3.21].) Ionic-transport processes of both chemical diffusion and electromigration were included. Pit growth was assumed to occur as a result of anodic dissolution of the metal, the dissolved metal taken as the cation species in the solution.

The principal goal of our original analysis was to predict the time dependence associated with pit growth. However, the experimental studies of pit growth, reported in Section 3.1 of this report, have demonstrated a strong sensitivity of pitting current to certain experimental conditions. Accordingly, attention was also directed to an analysis of the pitting current, as predicted on the basis of the binary-electrolyte model, to assess its dependence on pertinent experimental parameters. The results are summarized below, using nomenclature that is consistent with that used in Reference 3.19.

Recalling that the pit model involves a cylindrical pit with ionic transport taking place one-dimensionally along the length of the pit,

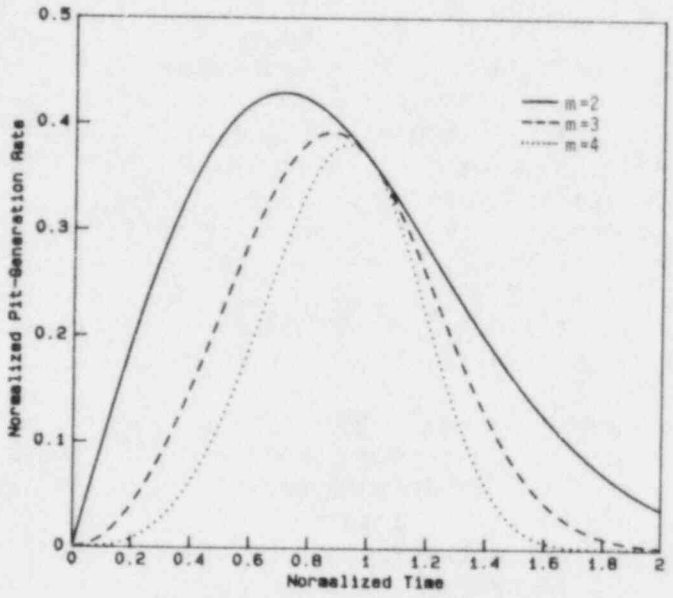

(a) g vs. T, after Equation 3-18

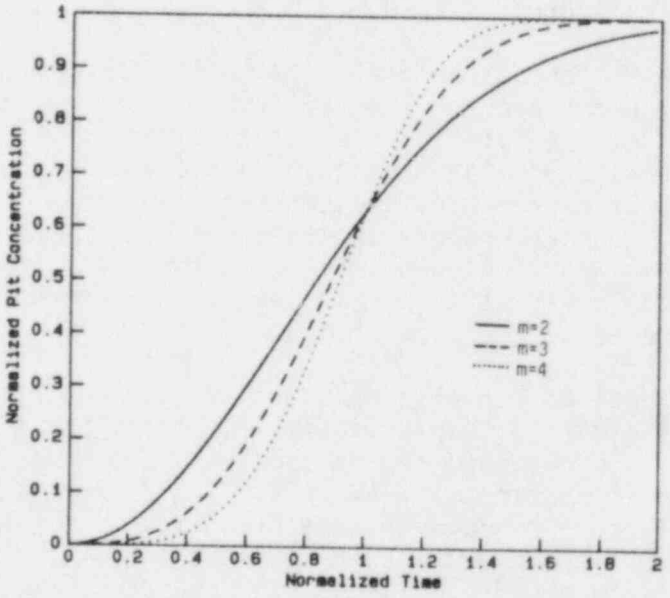

(b) n vs. T, after Equation 3-19

Figure 3.45. Variation of pit-generation rate and pit concentration with time, as calculated by the pitting-corrosion model.

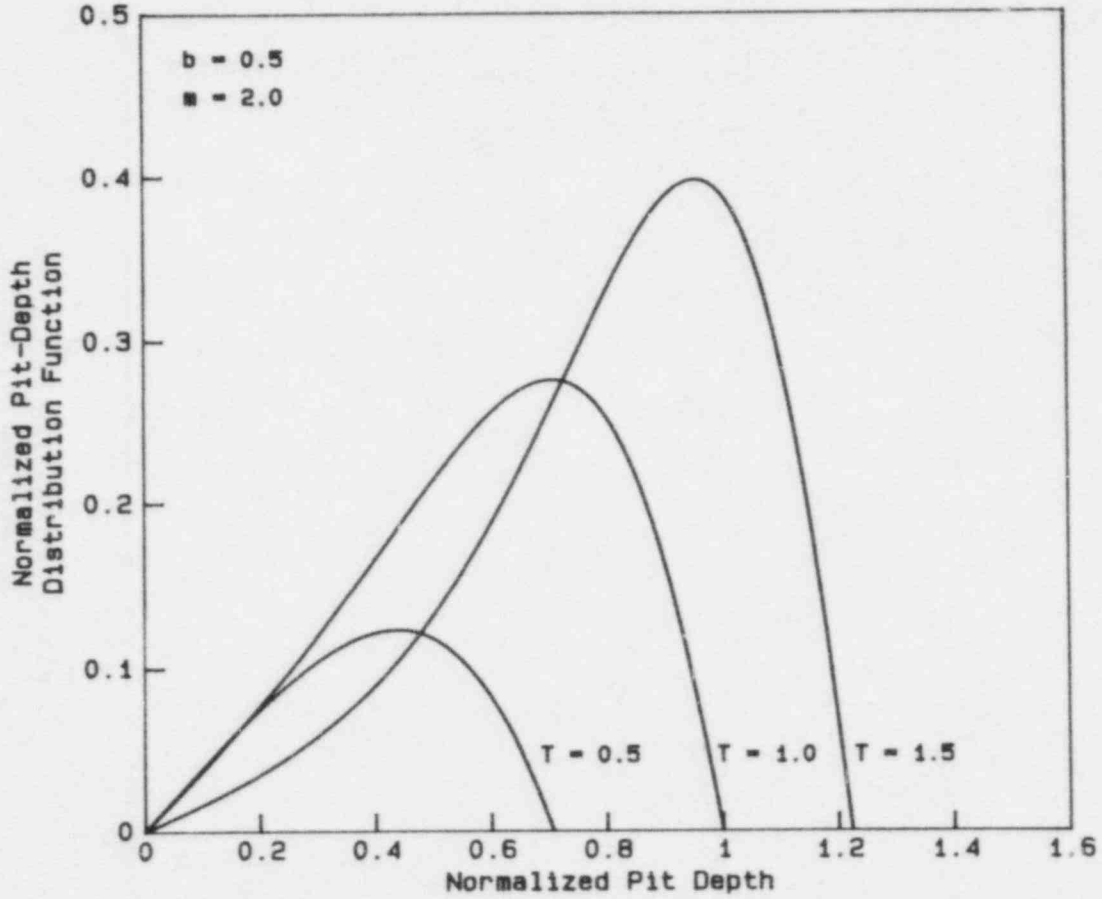

Figure 3.46. Calculated pit-depth distributions (F vs. H, after Equation 3-20) for m = 2 and selected values of T.

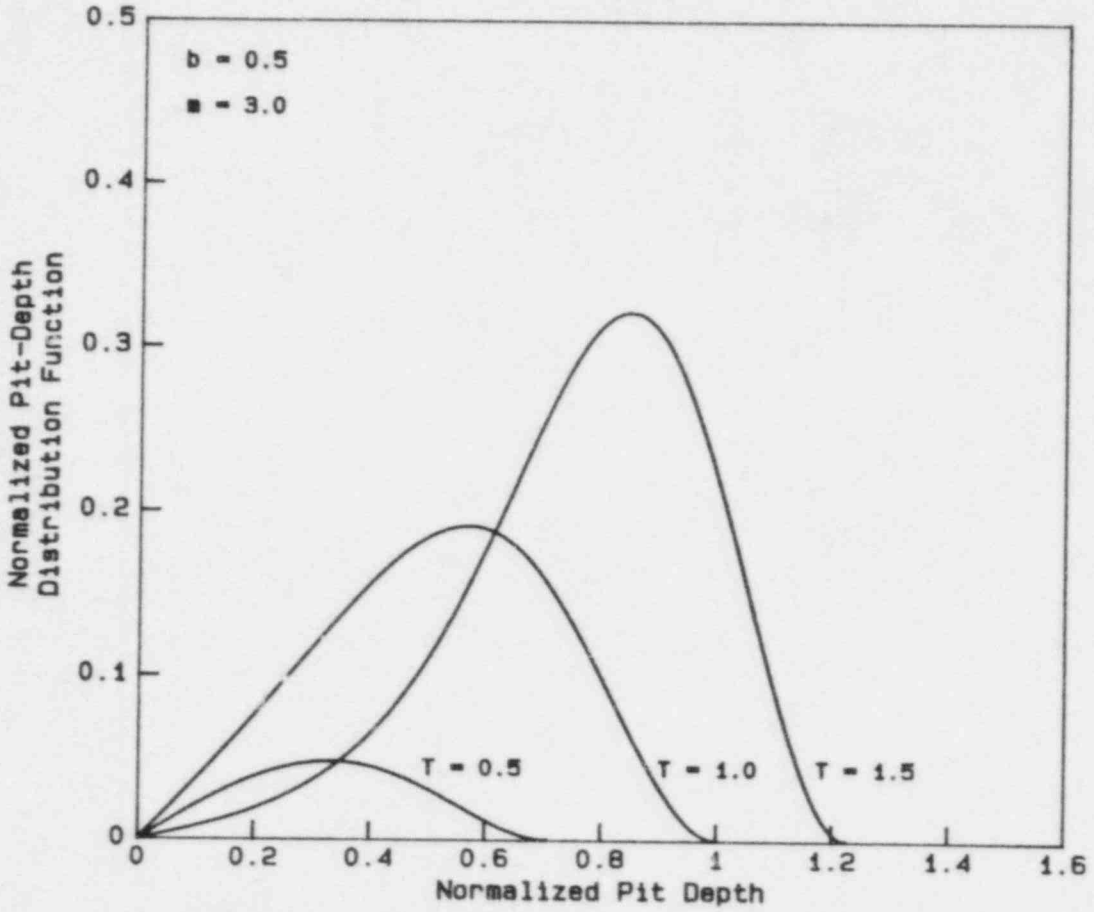

Figure 3.47. Calculated pit-depth distributions (F vs. H, after Equation 3-20) for m = 3 and selected values of T.

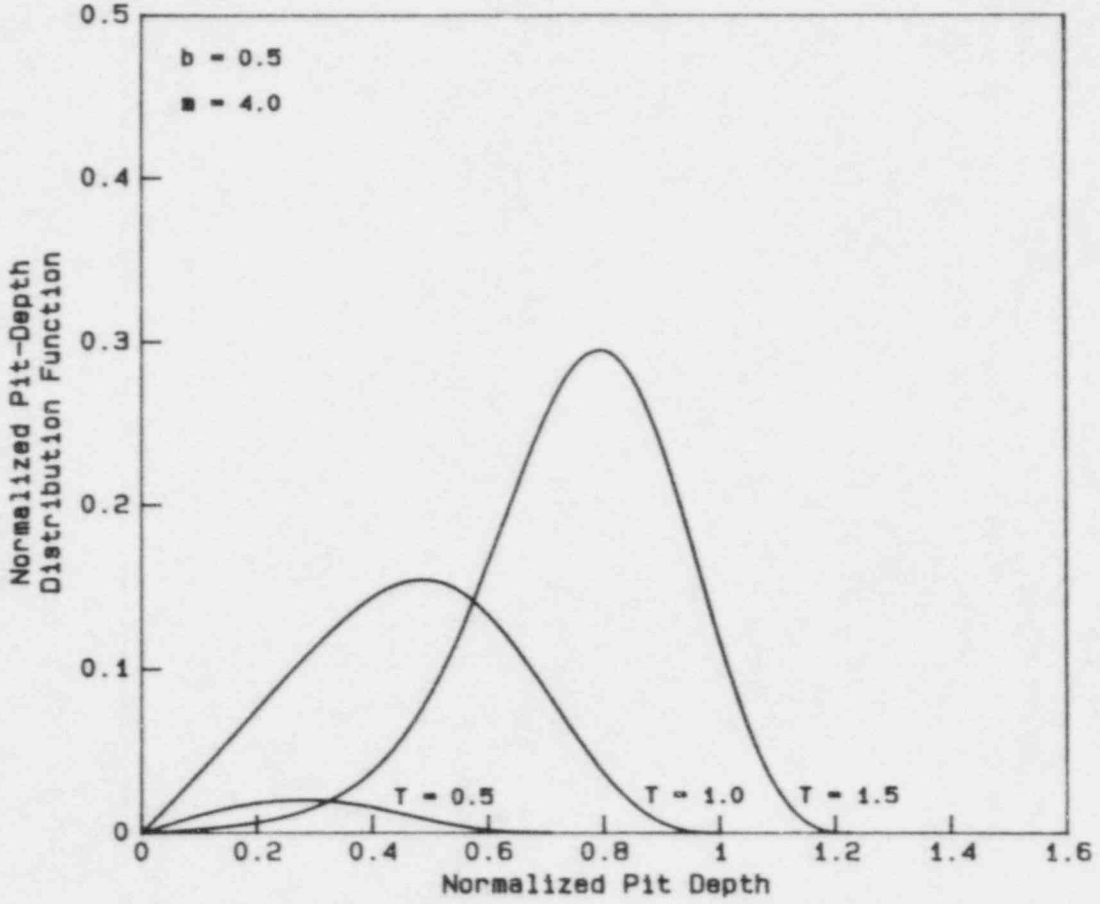

Figure 3.48. Calculated pit-depth distributions (F vs. H, after Equation 3-20) for m = 4 and selected values of T.

the current density, i, associated with growth of a single pit is given by

$$i = F\,(z_+ N_+ + z_- N_-) \tag{3-21}$$

where F is the Faraday constant, z_+ and z_- are the respective numbers of proton charges associated with the cation and anion, and N_+ and N_- are the respective flux values of cations and anions along the pit length. Since the anion does not undergo chemical reaction at the pit base, and since it is assumed that no homogeneous chemical reactions take place within the solution, it follows that $N_- = 0$ everywhere inside the pit. In this case Equation 3-11 reduces to

$$i = F z_+ N_+ \quad . \tag{3-22}$$

From Equation 3.25 of Reference 3.19, it follows that

$$N_+ = -D_+ \left(\left| \frac{z_+}{z_-} \right| + 1 \right) \frac{c_+(h) - c_+(0)}{h} \tag{3-23}$$

where D_+ is the cation diffusion coefficient and $c_+(0)$ and $c_+(h)$ are the respective cation concentrations in the solution at the pit mouth and pit base, with h being the instantaneous pit depth. (The sign convention in the development of this model is such that $N_+ < 0$ implies cation flow away from the pit base.) Moreover, from Equation 3.23 of Reference 3.22, one can show that

$$c_+(h) = c_+(0) \exp \left(\frac{z_- F}{RT} \left[\phi(0) - \phi(h) \right] \right) \tag{3-24}$$

where R is the gas constant, T is the absolute temperature, and $\phi(0)$ and $\phi(h)$ are the respective values of electrostatic potential at the pit mouth and pit base.

Combining Equations 3-22 to 3-24,

$$i = F z_+ D_+ \left(\left| \frac{z_+}{z_-} \right| + 1 \right) \frac{c_+(0)}{h} \left\{ 1 - \exp \left(\frac{z_- F}{RT} \left[\phi(0) - \phi(h) \right] \right) \right\} \quad . \tag{3-25}$$

Clearly, Equation 3-25 constitutes a relationship between the pitting current and the potential difference across the pit length. One limiting case which is of particular interest is that for which $c_+(h) \gg c_+(0)$. This corresponds to the assumption that the concentration of dissolved metal immediately adjacent to the base of the pit far

exceeds that at the pit mouth, which is adjacent to the bulk solution. For this special case, Equation 3-25 becomes

$$i = -Fz_+D_+\left(\left|\frac{z_+}{z_-}\right| + 1\right)\ \frac{c_+(0)}{h}\ \exp\left(\frac{z_-F}{RT}\ [\phi(0) - \phi(h)]\right) . \qquad (3\text{-}26)$$

Equation 3-26 can be equivalently expressed in the alternative and somewhat more familiar form

$$\phi(0) = \phi(h) - \frac{RT}{|z_-|F}\ \ln\left(\frac{i}{i_o}\right) \qquad (3\text{-}27)$$

where the minus sign on the right-hand side of Equation 3-26 has been dropped, and where

$$i_o \equiv Fz_+D_+\left(\left|\frac{z_+}{z_-}\right| + 1\right)\ \frac{c_+(0)}{h} \quad . \qquad (3\text{-}28)$$

It is clear from either Equation 3-26 or 3-27 that the pitting current is indeed sensitive to a number of parameters. For instance, assuming the h^{-1} factor on the right-hand side of Equation 3-26 is the only factor therein that actually varies with h, it follows that i varies as h^{-1} and that the pitting current therefore decreases as the pit becomes deeper. Likewise, if experimental conditions cause a variation of the potential at the crevice mouth, $\phi(0)$, the relative effect on i would be substantially greater because of the exponential dependence of i upon $\phi(0)$. Such an effect may, in fact, be related to the relatively high pitting currents that were measured in Battelle experiments involving the use of a platinum counter electrode (see Section 3.1 of this report).

3.3.3 Future Work

During the coming year, film-growth kinetics will be fully implemented into the overall general-corrosion model, and more realistic models for radiolytic production of chemical species will be used. The water-chemistry model, which so far has been used on in waste-form dissolution studies, will be explicitly applied to the general-corrosion analyses.

The pitting-corrosion model will continue to be developed, focusing on the evolution of the pit-depth distribution, the time-dependence of the pitting current, and the effects of radiolysis on pit growth. Experimental validation of the pitting-corrosion model will continue.

3.4 Mechanical Degradation Analyses

A small effort was undertaken, during the past year of this program, toward analysis of mechanical-degradation of waste-package components.

Because of the emphasis that had been placed on including water-chemistry effects in other aspects of the separate-effects modeling studies, it was decided that this emphasis would be continued in this effort as well. The specific task that was carried out consisted primarily of an analysis of mechanical and water-chemistry-related factors that may contribute to the susceptibility of a low-carbon-steel container material to stress-corrosion cracking (SCC). Actual modeling of the SCC process itself is a problem of great complexity and beyond the scope of this research. Possible sources of stress, a necessary ingredient in SCC, were also considered.

The investigation reported below was based entirely upon the assumption of basalt groundwater. For other groundwaters, such as tuff, appropriate modifications would be required.

Some of the mechanical and electrochemical parameters that can influence the SCC behavior of low-carbon steel in a basalt repository are the following:

(1) Water chemistry (including chemical composition and related characteristics of the groundwater)

(2) Temperature at the overpack/backfill interface

(3) Water flow rate

(4) Stresses (thermal, residual, hydrostatic and lithostatic, as well as internal pressure due to helium generation inside the containers)

(5) Radiolysis (which actually comes under the water-chemistry heading but is treated here as a separate item)

(6) Heat-transfer characteristics of the container-backfill interface

(7) Galvanic corrosion (only of concern if the overpack is penetrated).

Not included in the list are material-related parameters such as change in microstructure due to strain aging, thermal aging, and radiation-induced swelling. Welding the overpack to close it will also influence the cracking behavior of the material, and the area so heated may be the most susceptible to cracking. In the following paragraphs, a brief discussion of the role of these various factors is discussed in general terms. The discussion is based on the estimated and expected near-field repository conditions in basalt as presented in Reference 3.23.

3.4.1 Water Chemistry and Temperature

Water chemistry in the basalt repository may be the single most important variable in determining the stress-corrosion cracking behavior of carbon-steel overpack material. In addition to other species, the water contains chlorides, sulfates, carbonates, and bicarbonates[3.23]. In general, carbon steel is known to crack in chlorides and carbonate/bicarbonate environments. Other species, such as nitrates and hydroxides, are also known to enhance SCC-susceptibility. Although these last two species are present in insignificant concentrations, their concentration may increase due to heat-transfer characteristics of the overpack/backfill interface, flow rate of the groundwater past the container, radiolysis, and the temperature at the interface. The flow rate is expected to be small in a basalt repository[3.23]. Its influence simply may be the transport of species to and from the overpack surface.

There is considerable evidence in the literature that SCC of carbon steel occurs by the film-rupture and anodic-dissolution mechanism[3.24]. This being the case, one could reasonably postulate that a balance between aggressive ions (e.g., Cl^-, SO_4^-, F^-) and passivating ions (e.g., HCO_3^-, CO_3^{-2}), in addition to the Eh of the solution, may be critical in determining the SCC behavior of carbon steel.

The Eh of the groundwater will be primarily determined by the presence of oxygen in the repository. Reference 3.23 indicates that during the initial period (operations period), oxygen will be present and the Eh of the water therefore will be oxidizing. During the thermal period, the oxygen trapped in the repository will be consumed and the Eh of the water will become reducing. However, radiolysis of groundwater is believed to produce strongly oxidizing species (e.g., H_2O_2 and HO_2). It is therefore not clear at present what Eh conditions will be experienced by the carbon-steel overpack in the repository. However, the presence of a variety of species could produce cracking over a rather wide range of Eh, depending on the pH of the water[3.25]. Since the groundwater pH is expected to range from approximately 6 to 9[3.23], there exists a distinct possibility of cracking of the carbon-steel overpack. In addition, under stagnant conditions the pH could be forced beyond these expected bounds.

Another important aspect of the cracking process has been described by Ford[3.25], who suggested that cracking is encountered where a protective film (phosphate, carbonate, magnetite, etc.) is initially stable but then ruptures to produce soluble metastable species. This is, in general, the basis for the film-rupture anodic-dissolution model mentioned earlier. It is important that the possibility of a similar model be examined for carbon steel in a typical basalt environment. Because of the complex chemistry involved, this may not be simple. Westerman et al[3.26] conducted corrosion experiments on a ductile iron in oxic basalt groundwater at 250 C with and without irradiation. After 5 months of exposure, analcime and nontronite were found to be the

corrosion products under unirradiated conditions. Under irradiated conditions, acmite and nontronite were found to be present on the specimen surface. These researchers found that the type of corrosion product depended not only upon the irradiated or unirradiated condition, but also upon exposure length and the specific type of material[3.26].

The corrosion products discussed above will depend not only on the groundwater chemistry, irradiation, and exposure duration, but also on the temperature. Reference 3.23 suggests that the temperature in the repository will be fairly high during the operating period as well as during the thermal period. Although few data are available above 100 C, carbon steel susceptibility to SCC generally increases with increasing temperature. This factor will have to be investigated further.

3.4.2 Radiolysis

The manner in which radiolysis of the groundwater will influence the container-degradation process is the least understood factor of all. Its influence will depend upon water chemistry and the nature of the material itself. In pure water, radiolysis produces strong oxidizing agents such as peroxides. Hydrogen is liberated in the radiolysis process and could cause hydrogen embrittlement. A detailed review of the available literature on radiolysis of water has been prepared by Glass[3.27] and the following discussion is taken primarily from that work. The noted reactions by no means represent a complete listing. Additional work in this area is being conducted at Battelle as part of this project (see Section 4.2).

When water is gamma-radiated, the primary species produced within 10^{-11} to 10^{-10} second are:

$$H_2O \xrightarrow{\gamma} H_2,\ H_2O_2,\ H,\ OH,\ e^-_{aq},\ H_3O^+.$$

It is believed that the following reactions are responsible for the production of hydrogen atoms and molecules[3.27]:

$$e^-_{aq} + H_3O^+ \longrightarrow H + H_2O \qquad (3\text{-}29)$$

$$H_2O \xrightarrow{\text{Excited}} H + OH \qquad (3\text{-}30)$$

$$e^-_{aq} + H_2O \longrightarrow H + OH^-_{aq} \qquad (3\text{-}31)$$

$$e^-_{aq} + e^-_{aq} \xrightarrow{2H_2O} H_2 + 2\ OH^- \qquad (3\text{-}32)$$

$$e^-_{aq} + H \xrightarrow{H_2O} H_2 + OH^- \qquad (3\text{-}33)$$

$$H + H \longrightarrow H_2 \quad (3\text{-}34)$$

$$H_2O \xrightarrow{\text{Excited}} H_2 + O \quad . \quad (3\text{-}35)$$

Reaction 3-29 is considered to be the primary reaction for hydrogen atom production, espectially in acidic solution. Reaction 3-32 is primarily responsible for hyrogen-molecule production, especially in neutral or basic solution[3.27]. In acidic solution, reaction 3-29 followed by 3-34 may play a major role in the production of molecular hydrogen.

The primary reaction responsible for the production of molecular H_2O_2 is:

$$OH + OH \longrightarrow H_2O_2 \quad . \quad (3\text{-}36)$$

There are additional reactions which inhibit or destroy the molecular products and re-form water. For example,

$$OH + H_2O_2 \longrightarrow H_2O + HO_2 \quad (3\text{-}37)$$

$$e^-_{aq} + H_2O_2 \longrightarrow OH^- + OH \quad (3\text{-}38)$$

$$H + H_2O_2 \longrightarrow H_2O + OH \quad (3\text{-}39)$$

$$H_2 + OH \longrightarrow H_2O + H \quad . \quad (3\text{-}40)$$

In the presence of oxygen, the following reactions may occur:

$$O + O_2 \longrightarrow O_3 \quad (3\text{-}41)$$

$$O + H_2O \longrightarrow H_2O_2 \quad . \quad (3\text{-}42)$$

What influence these reactions will have on the SCC behavior of carbon steel is not yet known. What is known is that H_2O_2, OH, and HO_2 are strong oxidizing agents, whereas H, e^-_{aq}, and H_2 are strong reducing agents (e^-_{aq} is reducing in neutral solution, while H is reducing in acidic solution[3.27]). Also, H_2 and H_2O_2 are the major stable products.

The primary effect of the species (e.g., salts) added to pure water is to reduce or eliminate the radiolytic intermediates, generating new species not present in pure water. In concentrated solutions (>0.1M), the ionic strength and structure of water may influence the rates of reactions of the primary species with each other and with species generated from solutes that may be present[3.27]. Anions are the most effective in this regard. In the presence of concentrated Cl^-, for example, the H_2O_2 yield is decreased significantly while H_2 yield is increased slightly as compared to yield from pure water. The presence of Br^- has a similar effect.

The presence of gases can also alter the radiation chemistry. Gases such as O_2, CO, and CO_2 tend to be electron acceptors; e.g.,

$$e^-_{aq} + O_2 \longrightarrow O_2^- \quad . \tag{3-43}$$

Such electron-scavenging reactions tend to decrease the H_2 yield. In the presence of various gas mixtures, stable products are formed; for example,

$$2\ H_2 + O_2 \underset{\longleftarrow}{\overset{\text{radiation}}{\longrightarrow}} 2\ H_2O$$

$$N_2 + 3H_2 \underset{\longleftarrow}{\overset{\text{radiation}}{\longrightarrow}} 2\ NH_3$$

$$H_2O + N_2 + 2.5\ O_2 \longrightarrow 2\ HNO_3 \quad .$$

It is clear that the interaction of the complex water chemistry with radiation will produce a wide variety of constituents. Based on present knowledge, hydrogen and hydrogen peroxide production may be the most significant factors. Townsend et al[3.28] noted that H_2O_2 promotes passivation of the steel by the formation of a film of Fe_2O_3 due to the increased activity of oxygen available from the breakdown of H_2O_2. This effect could be beneficial in prolonging the life of the material. But the authors also noted that the presence of sodium chloride, in amounts as little as 0.005N, overcomes the passivating effect of 3 g/liter hydrogen peroxide, and that increasing amounts of chloride result in increasing rates of film breakdown[3.28]. The dual effect of chloride is apparent here. It not only decreases the H_2O_2 yield from the radiolysis of water, but also accelerates film breakdown on the steel surface. Such interactions need to be studied further to understand their influence on SCC of carbon steel. Such efforts have been undertaken at Battelle[3.29] where a model has been developed for the radiolysis of water containing ferrous and ferric ions.

3.4.3 Stresses

The four primary sources of stress on the container will be hydrostatic pressure, lithostatic pressure, thermal stresses, and build-up of helium pressure. In addition to these service-related stresses, residual stresses from the fabrication process could play an important role in determining the stress state of the container.

From a modeling standpoint, one could develop a fracture-mechanics-based methodology to predict the rate at which a crack will grow. Alternatively, knowing the stress and the size of a pre-existing flaw in the material, one could predict whether or not this flaw will grow, i.e., whether or not the stress-intensity, K, lies below the threshold value K_{ISCC} for SCC. Still another option will be to establish the maximum acceptable pre-existing flaw size that will not propagate in service, based on the stress intensity experienced by the flaw and the K_{ISCC} of the material. In this regard, it will be important to develop K_{ISCC} data for the material in the basalt-groundwater environment. Because a standard does not exist for K_{ISCC} determination, and because of the long design life of the container, it will be important that K_{ISCC} be determined for long exposures.

In addition to the above-noted considerations, there are other factors to be considered in the development of K_{ISCC}. K_{ISCC} is environment-specific and also depends upon temperature. Any fluctuation in stress (for example, cyclic loading due to thermal fluctuations) could result in a significant reduction of K_{ISCC}. Since such fluctuations are likely to occur, it may be undesirable to design a container solely on consideration of K_{ISCC}.

3.4.4 Future Work

Mechanical-degradation processes associated with the waste package will continue to be examined througout the remainder of the program. Stress-corrosion cracking will continue to be emphasized, because of its potential importance, and other environmentally assisted fracture mechanisms will also be evaluated.

3.5 References for Section 3

(3.1) "Long-Term Performance of Materials Used for High-Level Waste Packaging", D. Stahl and N. E. Miller (Compilers), NUREG/CR-3427, Vol. 4, Annual Report (June 1984), pp. 3-67 ff, 3-87 ff.

(3.2) J. A. Beavers, N. G. Thompson, and R. N. Parkins, "Stress-Corrosion Cracking of Low-Strength Steels in Candidate High Level Waste Repository Environments", Topical Report, NUREG/CR-3861, to be published, 1984.

(3.3) T. E. Jones, "Reference Material Chemistry--Synthetic Groundwater Composition", RHO-BW-St-37 P (April 1982).

(3.4) "Long-Term Performance of Materials Used for High-Level Waste Packaging", D. Stahl and N. E. Miller (Compilers), NUREG/CR-3900, Vol. 1, (September 1984), pp. 319-323 ff.

(3.5) "Appendix D: Range of Environmental Parameters", Draft NUREG-1076, ORNL, 1984.

(3.6) W. J. Gray, "Gamma Radiolysis Effects on Grande Ronde Basalt Groundwater", RHO-BW-SA-315 P (presented at the Materials Research Society Symposium-Scientific Basis for Nuclear Waste management, Boston, MA, November 14-17, 1983).

(3.7) S. A. Simonson, and W. L. Kuhn, "Predicting Amounts of Radiolytically Produced Species in Brine Solution", PNL-SA-11426 (presented at the Materials Research Society Symposium-Scientific Basis for Nuclear Waste Management, Boston, MA, November 14-17, 1983.

(3.8) E. P. Grause, C. Brewster, and P. Soo, "Determination of the Waste Package Environments for a Basalt Repository: Phase 1--Gamma Irradiation Conditions in the Absence of Methane", BNL-NUREG-24297, Draft Report, (February 1984).

(3.9) NRC Nuclear Waste Geochemistry '83, Proceedings of the U.S. Nuclear Regulatory Commission, Reston, Virginia, August 1983, p. 245.

(3.10) "Long-Term Performance of Materials Used for High-Level Waste Packaging", D. Stahl and N. E. Miller (Compilers, NUREG/CR-3900, Volume 3, (May 1985), pp. 3-7 ff.

(3.11) M. B. Strauss and M. C. Bloom, "Cracking of Low Carbon Steel by Ferric Chloride Solutions", Corrosion 16 (11) 553t.

(3.12) "Long Term Performance of Materials Used for High-Level Waste Packaging", D. Stahl and N. E. Miller (Compilers), NUREG/CR-3427, Vol. 4, BMI-2113 (June 1984), pp. 3-106 ff.

(3.13) C. Y. Chao, L. F. Lin, and D. D. Macdonald, "A Point Defect Model for Anodic Passive Films", J. Electrochem. Soc., 128 (1981) 1187.

(3.14) "Long-Term Performance of Materials Used for High-Level Waste Packaging", D. Stahl and N. E. Miller (Compilers), NUREG/CR-3427, Vol. 4, BMI-2113 (June 1984), pp. 3-121 ff.

(3.15) L. F. Lin, C. Y. Chao, and D. D. MacDonald, J. Electrochem. Soc., 128 (1981) 1194.

(3.16) M. Janik-Czachor and M. B. Ives, in Passivity of Metals, R. P. Frankenthal and J. Kruger (Editors). Electrochem. Soc. (Princeton, N. J., 1978), p. 369.

(3.17) "Long-Term Performance of Materials Used for High-Level Waste Packaging", D. Stahl and N. E. Miller (Compilers), NUREG/CR-3405, Vol. 1, BMI-2105 (July 1983), pp. 6-18 ff.

(3.18) "Long-Term Performance of Materials Used for High-Level Waste Packaging", D. Stahl and N. E. Miller (Compilers), NUREG/CR-3427, Vol. 4, BMI-2113 (June 1984), pp. 3-132 ff.

(3.19) "Long-Term Performance of Materials Used for High-Level Waste Packaging", D. Stahl and N. E. Miller (Compilers), NUREG/CR-3427, Vol. 4, BMI-2113 (June 1984), pp. 3-124 ff.

(3.20) G. P. Marsh, Trans. Am. Nucl. Soc., 45 (1983) 292.

(3.21) J. S. Newman, Electrochemical Systems, Prentice-Hall, Inc. (Englewood Cliffs, N. J., 1973), pp. 223 ff.

(3.22) "Long-Term Performance of Materials Used for High-Level Waste Packaging", D. Stahl and N. E. Miller (Compilers), Annual Report, Year Two, NUREG/CR-3427, BMI-2113, Vol. 4 (June 1984), pp. 3-114 ff.

(3.23) Review of DOE Waste Package Program, P. Soo (Ed.), NUREG/CR-2482, BNL-NUREG-51494, Vol. 2 (April, 1983), Brookhaven National Laboratory.

(3.24) R. N. Parkins, "Environmental Aspects of Stress Corrosion Cracking in Low Strength Ferritic Steels", in Stress Corrosion Cracking and Hydrogen Embrittlement of Iron Base Alloys, R. W. Staehle et al. (Eds.), National Association of Corrosion Engineers, Houston, Texas (1977).

(3.25) F. P. Ford, "Mechanisms of Stress-Corrosion Cracking", Report No. 82CRD083, General Electric, Schenectady, New York (1982).

(3.26) R. E. Westerman, S. G. Pitman, and J. L. Nelson, "General Corrosion, Irradiation Corrosion, and Environmental-Mechanical Evaluation of Nuclear Waste Package Structural Barrier Materials", PNL-4364, UC-70, Battelle Pacific Northwest Laboratory (1982).

(3.27) R. S. Glass, "Effects of Radiation on the Chemical Environment Surrounding Waste Canisters in Proposed Repository Sites and Possible Effects on the Corrosion Process", SAND81-1677, Sandia National Laboratory (1981).

(3.28) H. E. Townsend, H. J. Cleary, and L. Allegra, "Breakdown of Oxide Films on Steel Exposed to Chloride Solutions", Corrosion, Vol. 37, No. 7, pp. 384-391 (July, 1981).

(3.29) "Long Term Performance of Materials Used for High-Level Waste Packaging", D. Stahl and N. E. Miller (Compilers), NUREG/CR-3900, Vol. 2 (July-September, 1984).

4. INTEGRATED SYSTEM PERFORMANCE

The purpose of the system performance task is to obtain a better understanding of the phenomena that affect the long-term performance of waste packages at the system level. Knowledge gained in these studies will aid in assessing the adequacy of system-performance models for nuclear waste packages.

During the past year, emphasis has been placed on water-chemistry studies, the radiolysis of aqueous solutions containing ferric and ferrous species, the development of a mechanism for the radiolysis of solutions containing chloride species, and construction and further planning of the integral experiments.

The water-chemistry studies will improve our understanding of the water chemistry in the vicinity of the waste package by providing information on how the corrosion of the metallic barriers and the dissolution of the waste form alter the local water chemistry. Phenomena such as corrosion of the metallic barriers and dissolution of the waste form may be affected in turn by such changes in the local water chemistry. The water-chemistry studies will also provide information on the chemical speciation of radionuclides released from the waste form. This information will be useful for assessing the transport rate of these radionuclides through the waste package.

The groundwater-radiolysis studies will provide information on the concentrations of the radiolytic species in the vicinity of the waste package. These species may affect both the corrosion of the metallic barriers and the chemical speciation of the radionuclides released from the waste form. Radiolysis can influence the expected containment period of a waste package as well as the release rate of radionuclides from the waste package to the repository environment after the containment is breached.

The integral experiments are being assembled to provide a means of assessing the relative importance of various combined-effects processes which may affect the long-term performance of nuclear waste packages. These experiments will also provide information on the performance of spent-fuel waste forms in environments approximating that of a potential repository. These experiments will also provide data which can be used to benchmark the radiolysis and water-chemistry models that are under development.

4.1 Water Chemistry

The study of water chemistry is an important part of any theoretical treatment of waste-package performance. It is generally considered that water is the only credible medium for transport of radionuclides away from the repository. In addition, the composition of groundwater and its presence or absence are major factors in determining the modes and rates of degradation for all components of the repository. Since water

is both a transport medium and a participant in a large number of degradation mechanisms, it plays an important role in coupling many processes. It is therefore desirable to build a model of water chemistry that can interface easily with descriptions of many other phenomena. Our work has been directed at producing such a model. Our intention has not been to produce a highly detailed water-chemistry code, but rather to investigate the interactions between various phenomena by using a small water-chemistry code as a tool.

Our work to date has used two water-chemistry programs: a Battelle-developed water-chemistry code, which handles a small number of species; and WATEQ[4.1], which handles a significantly larger set of species. WATEQ was intended for analyzing field data rather than for modeling, and it was not feasible to adapt WATEQ for modeling. On the other hand, when using our water-chemistry code, we were concerned that neglecting so many species would impair the accuracy of our work. Therefore, our usual procedure has been to use the small model for most of our calculations and, where possible, to check selected results against output from WATEQ. In some cases, the calculated results have been compared with those of experiments. For example, the calculated pH produced by our code for synthetic Grande Ronde basalt groundwater was 9.90[4.2]. This is in good agreement with the experimental value of 9.74 ± 0.10 reported by Jones[4.3].

A major expansion of Battelle's water-chemistry code was carried out during the past year. This consisted of an expansion of the number of chemical species accounted for within the code, as well as certain other improvements. For example, we wanted to include the elements aluminum, potassium, and fluorine and to strengthen our treatment of iron. This has been accomplished by making appropriate modifications of the program and incorporating thermodynamic data from the WATEQ data base. A total of 34 species are now treated. Among other changes in the program, treatment of the carbonate-bicarbonate system has been improved. The current list of species treated includes:

e^-	H_2O	H^+	OH^-
H_2	Na^+	Mg^{2+},	$MgOH^+$
Ca^{2+}	$CaOH^+$	Fe^{2+}	$FeOH^+$
$Fe(OH)_2$	$Fe(OH)_3^-$	Fe^{3+}	$FeOH^{2+}$
$Fe(OH)_2^+$	$Fe(OH)_3$	$Fe(OH)_4^-$	K^+
Al^{3+}	$AlOH^{2+}$	$Al(OH)_2^+$	$Al(OH)_4^-$
H_3BO_3	$H_2BO_3^-$	H_2CO_3	HCO_3^-
CO_3^{2-}	Cl^-	F^-	H_4SiO_4
	$H_2SiO_4^{2-}$	SO_4^{2-}	$H_3SiO_4^-$.

Coding and testing of the new version is complete. Although the new version has not yet been heavily used, preliminary comparisons of results from the two versions indicate that the old version underestimated the effect of buffering resulting from the carbonate-bicarbonate reaction. This may reduce the pH calculated for a repository environment. While the magnitude of the error has not been determined, the inaccuracies of the previous version are conservative; that is, the higher pH predicted by the earlier version would be expected to correspond to rates of waste-form dissolution that are too high.

Further expansion of our water-chemistry code is not planned for the immediate future. Testing of the current computer code will be completed, and it will then be integrated into our model for glass dissolution. However, additional expansion is likely to be required when attention on this program focuses on spent-fuel waste forms rather than glasses.

4.2 Groundwater Radiolysis

Radiolysis of groundwater in the vicinity of the waste package can alter the local water chemistry, thereby affecting the long-term performance of waste packages. Effects on the local water chemistry can include changes in pH and oxygen potential, as well as the production of additional species which may have a deleterious effect on the waste-package materials. As reported previously, other investigators have observed that gamma radiation may have adverse effects on the time-to-failure performance measure for metal components exposed to water[4.4,4.5].

One objective of these studies is to develop a generalized model for analyzing the radiolysis of both unaltered groundwater systems and groundwater systems whose composition has been altered by the presence of other materials such as packing and corrosion products. This model will provide information on the expected concentrations of radiolysis products in the vicinity of the metallic components of waste packages. The information obtained will aid the canister-materials task of the program by guiding the selection of appropriate solution compositions for corrosion experiments. The model will also provide a means of assessing the abbreviated groundwater-radiolysis model, which is part of the general corrosion model described in Section 3.3, and will provide a vehicle for determining effective rate constants for reactions included in the water-radiolysis component of the corrosion model.

The first step in the approach taken in these studies was to develop a description for the radiolysis of pure water that might contain hydrogen and/or oxygen. This description is being extended to account for the presence of anions and cations which may be present in significant amounts in groundwaters of interest. As the description of groundwater radiolysis is developed, it is being benchmarked against experimental data from the literature. As part of this effort, gamma-energy deposition calculations were performed to determine energy deposition rates to groundwater and the materials surrounding spent fuel and commercial

high-level waste packages. Results of these energy deposition calculations have been reported previously[4.6]. In those studies, several mechanisms for the radiolysis of water were evaluated on the basis of their ability to predict the behavior of water-radiolysis experiments described in the literature. Of these, the mechanism presented by Rosinger and Dixon[4.7] was chosen as a basis for developing a generalized description of groundwater radiolysis.

Work performed during this past year has been directed toward studies of the radiolysis of ferrous solutions relevant to basalt systems. A mechanism being developed for radiolysis of solutions containing chloride ions is also described.

4.2.1 Radiolysis of Alkaline Ferrous Systems

Calculations were performed using the mechanism developed this year for the radiolysis of groundwaters containing iron. This mechanism is shown in Table 4.1. Development of the mechanism has been reported earlier[4.8]. These calculations simulate the performance of aqueous systems containing ferrous ions under conditions that may be similar to those expected in a basalt repository.

The calculations were performed for a 60 R/hr gamma field with a solution of pH 9.8. The initial dissolved-hydrogen concentration was estimated to be 4×10^{-10} mole/l. This estimate was calculated using a Bunsen absorption coefficient of 0.0175 for hydrogen in water and a hydrogen partial pressure of 5×10^{-7} atm calculated assuming a standard dry atmosphere. Initial dissolved-oxygen concentrations used in these calculations were 4×10^{-10}, 6×10^{-5}, and 6×10^{-4} mole/l. The median value was chosen as a mid-range value of measurements of the oxygen concentration for a simulation of a waste-package environment[4.9]. The initial ferrous concentration was set at 10^{-5} mole/l and was allowed to vary to reflect production and depletion by the model.

Calculations for the radiolysis of a closed ferrous system with an initial dissolved-oxygen concentration of 6×10^{-5} mole/l are shown in Tables 4.2 and 4.3. Table 4.2 shows the time-dependence of Fe^{2+} and FeOOH. In this model, FeOOH represents a range of precipitates, and the yield is given in moles/l to allow for comparison with other species treated in the model. As shown in this table, the ferrous ion is effectively converted to the precipitate species over a 100-hour time period.

Table 4.3 shows the relative concentrations of aqueous species in solution during this conversion process. These data indicate that the second hydrolysis product of the ferric species is predominant, followed by the first hydrolysis product, and then the ferric ion. Knowledge of these concentrations can be useful when modeling corrosion phenomena and planning corrosion-research experiments.

Table 4.4 shows the effects of the initial dissolved-oxygen concentration on the conversion of ferrous ions to ferric species. Although the

Table 4.1. Reactions added to the Rosinger and Dixon mechanism that complement the description of groundwaters containing iron.

Fe^{2+}	+	OH	→	$FeOH^{2+}$				**k = 3.2E08
$FeOH^{2+}$	+	H^+	→	Fe^{3+}	+	H_2O		k = 1.5E09
Fe^{2+}	+	e^-	→	Fe^+				k = 1.2E08
Fe^+	+	OH	→	$FeOH^+$				k = 2.8E08
$FeOH^+$	+	H^+	→	Fe^{2+}	+	H_2O		k = 1.3E09
Fe^+	+	H_2O_2	→	Fe^{2+}	+	$OH + OH^-$		k = 5.29E01
Fe^+	+	O_2^-	→	Fe^{2+}	+	O_2^{2-}		k = 3.52E08
H	+	Fe^{2+}	→	FeH^{2+}				k = 1.38E06
FeH^{2+}	+	H^+	→	Fe^{3+}	+	H_2		k = 1.06E06
Fe^+	+	H	→	FeH^+				k = 1.2E06
FeH^+	+	H^+	→	Fe^{2+}	+	H_2		k = 9.3E03
Fe^{2+}	+	H_2O_2	→	Fe^{3+}	+	$OH + OH^-$		k = 6.0E01
Fe^{2+}	+	O_2^-	→	Fe^{3+}	+	O_2^{2-}		k = 4.0E08
Fe^{3+}	+	e^-	→	Fe^{2+}				k = 2.0E10
Fe^{3+}	+	O_2^-	→	Fe^{2+}	+	O_2		k = 4.0E08
Fe^{3+}	+	H	→	Fe^{2+}	+	H^+		k = 1.0E08
H	+	OH^-	→	e^-	+	H_2O		k = 1.8E07
Fe^{3+}			→	$FeOH^{2+} + H^+$	-	H_2O		k = 3.0E07
$FeOH^{2+}$	+	H^+	→	Fe^{3+}	+	H_2O		k = 4.7E09
$FeOH^{2+}$			→	$Fe(OH)_2^+ + H^+$	-	H_2O		k = 6.1E04
$Fe(OH)_2^+$	+	H^+	→	$FeOH^{2+}$	+	H_2O		k = 8.0E09
*$Fe(OH)_2^+$	+	$Fe(OH)_2^+$	→	FeOOH	+	$FeOH^{2+}+H_2O$		k = 5.0E02

*FeOOH represents a range of products associated with the precipitation of ferric species.

**Sources of the rate constants are identified in Reference 4.8.

Table 4.2. Fe^{2+} oxidation in radiolysis of an aqueous system containing dissolved oxygen.*

Time	Fe^{2+} Concentration (mole/l)	FeOOH Concentration (mole/l)
0	1.0×10^{-5}	0
10 minutes	9.9×10^{-6}	3.5×10^{-10}
1 hour	9.6×10^{-6}	6.6×10^{-8}
100 hours	2.9×10^{-20}	9.99×10^{-6}

*Conditions: Dose Rate = 60 R/hr
pH = 9.8
Initial dissolved O_2 concentration = 6×10^{-5} mole/l.

Table 4.3. Aqueous ferric species present during radiolysis of an aqueous solution containing dissolved oxygen.**

Time	Fe^{3+} Concentration (mole/l)	$FeOH^{2+}$ Concentration (mole/l)	$FeOH_2^{+}$ Concentration (mole/l)
0	0	0	0
10 minutes	2.5×10^{-18}	1.3×10^{-12}	6.2×10^{-8}
1 hour	3.9×10^{-18}	7.8×10^{-12}	3.7×10^{-7}
100 hours	2.7×10^{-20}	3.4×10^{-13}	6.7×10^{-9}

**Conditions: Initial concentration of Fe^{2+} = 1.0×10^{-5} mole/l
Dose Rate = 60 R/hr
pH = 9.8
Initial dissolved O_2 concentration = 6×10^{-5} mole/l.

Table 4.4. Effect of initial dissolved oxygen concentration on radiolytic oxidation of ferrous ions.

Species	Oxygen Concentration (mole/l)	Time		
		10 Minutes	1 Hour	100 Hours
Fe^{2+}	$4x10^{-10}$	$9.9x10^{-6}$	$9.7x10^{-6}$	$1.9x10^{-7}$
$Fe(OH)_2^+$	$4x10^{-10}$	$3.0x10^{-8}$	$1.6x10^{-7}$	$1.0x10^{-7}$
FeOOH	$4x10^{-10}$	$8.8x10^{-11}$	$1.3x10^{-8}$	$7.1x10^{-6}$
Fe^{2+}	$6x10^{-5}$	$9.9x10^{-6}$	$9.6x10^{-6}$	$2.9x10^{-20}$
$Fe(OH)_2^+$	$6x10^{-5}$	$6.2x10^{-8}$	$3.7x10^{-7}$	$6.7x10^{-9}$
FeOOH	$6x10^{-5}$	$3.5x10^{-10}$	$6.6x10^{-8}$	$1.0x10^{-6}$
Fe^{2+}	$6x10^{-4}$	$1.0x10^{-6}$	$9.7x10^{-6}$	$5.1x10^{-20}$
$Fe(OH)_2^+$	$6x10^{-4}$	$4.5x10^{-8}$	$2.8x10^{-7}$	$7.1x10^{-9}$
FeOOH	$6x10^{-4}$	$1.9x10^{-10}$	$3.7x10^{-8}$	$1.0x10^{-6}$

oxygen concentration was varied over more than 10 orders of magnitude, the calculated concentrations of FeOOH and the second hydrolysis product of the ferric ion were within one order of magnitude of the concentrations calculated for the various cases. This is because the model accounts for the oxidation of ferrous species to ferric species through reactions with radiolysis products and not through direct reaction with dissolved oxygen. Effects of oxygen therefore act indirectly in the mechanism through the influence of the dissolved-oxygen concentration on the concentrations of the radiolysis products.

4.2.2 Mechanism for the Radiolysis of Solutions Containing Chloride

Table 4.5 lists referenced elementary reactions taken from the literature which describe interactions between Cl^- and radiolytic species. Reaction 1 describes the formation of HCl as a result of reaction between hydrogen and chloride. Reactions 2, 3, and 4 describe reactions between HCl and radiolytic species. One product of these reactions is the Cl radical. Reactions 5 and 6 describe the behavior of this species, and reaction 6 describes the combination of two Cl radicals to form dissolved Cl_2. Although a study of reaction 6 was not found in the literature, it was added to account for recombination. Reactions 7, 8, and 9 describe the reactions of this species with H and OH radicals. Species formed include HOCl and ClO. Reaction 10 describes the interaction between atomic oxygen and ClO.

Rate constants for these reactions at 298 K are shown in Table 4.6 along with the literature reference. Rate constants 1-5 were calculated from expressions reported in the literature. The rate constant for reaction 6 was estimated as an order-of-magnitude upper-bound rate constant which assumes that the recombination process is rapid. Rate constants for reactions 7-10 were reported in the literature in units of cm^3/molecule-sec and were converted to l/mole-sec in Table 4.6.

This mechanism does not account for the long-term behavior of HOCl, nor does it account for interactions between chloride species and ferric species. These aspects of the behavior of the system will receive attention in the near term.

4.3 Integral Experiments

The selection of combined effects to be targeted for detailed study is often based upon engineering judgment. When applying the knowledge from such studies to the formulation of a system description or to the assessment of licensing applications, one must have some basis for determining that important combined-effects processes have not been omitted. Thus, there is a need for a test to provide investigators with a reasonably realistic view of the processes that may contribute to waste-package degradation. Such a test may help to confirm the importance of some processes which were believed to be important and may identify others which were not considered previously. The result will

Table 4.5. Reactions to account for interactions between chlorides and radiolytic species.

Reaction Number	Reaction	Reference
1	$H + Cl^- \rightarrow HCl + e^-$	4.10
2	$e^- + HCl \rightarrow H + Cl^-$	4.10
3	$H + HCl \rightarrow Cl + H_2$	4.11
4	$OH + HCl \rightarrow H_2O + Cl$	4.12
5	$H_2 + Cl \rightarrow HCl + H$	4.13
6	$Cl + Cl \rightarrow Cl_2$	--
7	$H + Cl_2 \rightarrow Cl + HCl$	4.11
8	$OH + Cl_2 \rightarrow Cl + HOCl$	4.11
9	$OH + Cl_2 \rightarrow ClO + HCl$	4.11
10	$O + ClO \rightarrow Cl + O_2$	4.11

Table 4.6. Rate constants at 298 K for reactions shown in Table 4.5.

Reaction Number	Rate Constant (l/mole-sec)	Reference
1	3.9×10^{8}	4.10
2	2.1×10^{9}	4.10
3	2.65×10^{7}	4.11
4	4.86×10^{8}	4.12
5	1.59×10^{3}	4.14
6	1×10^{10}	(estimated)
7	1.2×10^{10}	4.11
8	4.04×10^{7}	4.11
9	4.04×10^{5}	4.11
10	3×10^{10}	4.11

be the establishment of a technical basis for identifying the level of detail necessary in a system model or a licensing application.

The primary purpose of the integral experiments is to provide scoping information that will help to identify potentially important combined effects. The secondary purpose of these experiments is to provide qualitative information on corrosion phenomena, release rates, and water chemistry for spent fuel and commercial high-level waste packages.

The apparatus to be used in these experiments has been completed. The apparatus consists of 29 parallel test trains which operate in a once-through configuration. Each test train is supplied with fluid via separate channels of a peristaltic pump. This ensures control of the flow rate through each of the parallel test sections. The test sections which contain the test samples are enclosed in an oven inside a hot cell. This oven will be maintained at 90 C for the duration of the experiment. The pump, sampling ports, and other support equipment are located in a service area adjacent to the hot cell enclosure. The pump will deliver fluid to the test chambers at a rate of 1 ml/day for the majority of the test sections and 10 ml/day for other selected test sections. During operation of the experiment, fluid samples will be collected from the effluent and analyzed for radionuclides and other cations. During the course of the tests, pH, Eh, and dissolved oxygen measurements will be made on samples of the fluids entering and leaving selected test chambers.

Early in the fourth year, spent-fuel specimens will be prepared and loaded into the apparatus. The tests will be conducted for approximately one year. A search for combined effects will be made by post-test examinations in the fifth year.

4.4 References for Section 4

(4.1) A. H. Truesdell and B. F. Jones, "WATEQ, A Computer Program for Calculating Chemical Equilibria of Natural Waters", U.S. Geol. Surv. J. Res., 2, 223, 1974.

(4.2) "Long-Term Performance of Materials Used for High-Level Waste Packaging", D. Stahl and N. E. Miller (Compilers), NUREG/CR-3427, Vol. 1 (August 1983), pp 5-1 ff.

(4.3) Jones, T. E., "Reference Material Chemistry--Synthetic Groundwater Composition", RHO-BW-ST-37 P (April 1982).

(4.4) Takashi Furuya, et al., "Study on γ-ray Irradiation Effects on Corrosion Resistance of Alloys for Storage of High-Level Waste Packages", JAERI-M 82-061 (1982).

(4.5) T. D. Chikalla and J. A. Powell, "Nuclear Waste Management Semi-Annual Progress Report", (October 1982-March 1983), PNL-4250-3 (1983).

(4.6) "Long-Term Performance of Materials Used for High-Level Waste Packaging", D. Stahl and N. E. Miller (Compilers), NUREG/CR-3427, Vol. 4, Annual Report (June 1984).

(4.7) E.L.J. Rosinger and R. S. Dixon, "Mathematical Modeling of Water Radiolysis: A Discussion of Various Methods", AECL-5958 (1977).

(4.8) "Long-Term Performance of Materials Used for High-Level Waste Packaging", D. Stahl and N. E. Miller (Compilers), NUREG/CR-3900, Vol. 1 (September 1984) and Vol. 2 (January 1985).

(4.9) P. Soo, "Review of Waste Package Verification Tests", NUREG/CR-3091, Vol. 3 (February 1984).

(4.10) H. F. Calcote and D. E. Jensen, "Reactions in Flames", in Ion Molecule Reactions, R. F. Gould, Editor, American Chemical Society, pp 311-312 (1966).

(4.11) L. M. Lowenstein and J. G. Anderson, "Rate and Product Measurements for the Reactions of OH with Cl_2, Br_2, and BrCl at 298 K: Trend Interpretations", J. Phys. Chem., 88 (1984), pp 6277-86.

(4.12) L. F. Keyser, "High Pressure Flow Kinetics: A Study of the OH + HCl Reaction from 2 to 100 Torr", J. Phys. Chem., 88 (1984), pp 4750-8.

(4.13) R. W. Ramette, "Photon-Initiated Hydrogen-Chlorine Reaction", J. Chem. Ed., 61 (8) (1984), pp 722-723.

(4.14) D. L. Baulch, et al., "Vol. 1--Homogeneous Gas Phase Reactions of the H_2-O_2 System", Evaluated Kinetic Data for High Temperature Reactions, CRC Press.

5. QUALITY ASSURANCE

Quality assurance surveillance of the various program activities continues. One new procedure was prepared during this quarter, making a total of 36 approved QA procedures and 2 approved work instructions for the program.

A summary of the procedures which are being used to conduct the experimental program is given in Table 5.1. Included is the procedure number, the current revision number, the title, and the status.

Quality assurance surveillance activities will continue. Procedures will be revised and new ones prepared as necessary to meet program requirements.

Table 5.1. Status of NRC waste packaging program QA procedures.

Procedure No.	Title	Status
WF-PP-1 Revision 0	Procedures for Record Keeping and Documentation for NRC Waste Form System Model Development	Approved
WF-PP-5 Revision 0	Procedures for Record Keeping and Documentation for Separate Effects Model Development	Approved
WF-PP-10 Revision 0	Laboratory Procedure for Preparation of Glasses for NRC Waste Form Project	Approved
WF-PP-11 Revision 1	Laboratory Procedures for Preparation of Teflon-Leach Containers	Approved
WF-PP-14 Revision 1	Laboratory Procedure for Leaching Glass Samples	Approved
WF-PP-16 Revision 0	Laboratory Procedure for Operating the Orton Dilatometer	Approved
WF-PP-20 Revision 0	Procedure for Determining the Corrosion Rates of Alloys at High Temperatures	Approved
WF-PP-25 Revision 0	Procedure for Preparation of Carbon-Steel Casting	Approved
WF-PP-26 Revision 0	Procedure for Preparation of Steel Hydrogen-Embrittlement Test Specimens	Approved
WF-PP-26.1 Revision 0	Procedure for Preparation of Hydrogen-Embrittlement Test Specimens from Steel or Iron Samples	Approved

Table 5.1. Continued.

Procedure No.	Title	Status
WF-PP-27 Revision 4	Procedure for J-Testing Compact Tension Specimens	Approved
WF-PP-27.1 Revision 1	Procedures for Performing Subcritical-Crack-Growth Tests with Compact Tension Specimens	Approved
WF-PP-28 Revision 1	Procedure for Performing Tension Tests of Steel Specimens	Approved
WF-PP-29 Revision 0	Procedure for Conducting Hydrogen-Absorption Experiments	Approved
WF-PP-30 Revision 0	Laboratory Procedure for Preparation, Cleaning, and Evaluation of Titanium Grade-12 Specimens for Corrosion Studies of the Overpack Performance for the NRC Waste Packaging Program	Approved
WF-PP-31 Revision 0	Laboratory Procedure for Preparation, Cleaning, and Evaluation of Cast and Wrought Carbon Steel Specimens for Corrosion Studies of the Overpack Performance for the NRC Waste Packaging Program	Approved
WF-PP-32 Revision 0	Procedure for Preparation of Brine A for Corrosion Testing Under Simulated Repository Conditions	Approved
WF-PP-33 Revision 0	Procedure for Preparation of Simulated Basalt Groundwater Solution	Approved
WF-PP-33.1 Revision 0	Procedure for Preparation of Basalt Rock for Use in Corrosion Studies for the NRC Waste Packaging Program	Approved

Table 5.1. Continued.

Procedure No.	Title	Status
WF-PP-34 Revision 0	Procedure for Preparation of Simulated Tuff Groundwater Solutions	To be Written
WF-PP-35 Revision 1	Procedure for Performing Autoclave Exposures for Corrosion Tests in Simulated Brines	Approved
WF-PP-35.1 Revision 0	Procedure for Performing Autoclave Exposures for Corrosion Tests in Simulated Brines Using Sealed Internal Canister	Approved
WF-PP-36 Revision 0	Procedure for Performing Stagnant Autoclave Exposures for Corrosion Tests in Simulated Basalt or Tuff Groundwaters	Approved
WF-PP-37 Revision 0	Laboratory Procedure for Preparing Polarization Resistance Specimens, Performing Polarization Resistance Measurements and Evaluating Polarization Resistance Data	Approved
WF-PP-37.1 Revision 0	Laboratory Procedure for Performing Eh and Corrosion Potential Measurements in Autoclave Exposures in Simulated Basalt and Tuff Groundwater	Approved
WF-PP-37.2 Revision 0	Laboratory Procedure for Determination of the Polarization Behavior of Metal Specimens at Ambient Pressure	Approved
WF-PP-38 Revision 0	Procedure for Preparing and Evaluation of U-Bend Specimens for Stress Corrosion Studies of Overpack Materials for the NRC Waste Packaging Project	Approved
WF-PP-38.1 Revision 0	Procedure for Performing and Evaluating 3 Point Bend Beam Specimens for Stress Corrosion Studies of Overpack Materials for NRC Waste Package Program	Approved
WF-PP-39 Revision 0	Procedure for Preparing, Testing and Evaluating Crevice Corrosion Specimens of Titanium Grade-12 and Cast Steel	Approved

Table 5.1. Continued.

Procedure No.	Title	Status
WF-PP-40 Revision 0	Laboratory Procedures for Preparation, Cleaning, and Evaluation of Thermogalvanic and Heat-Transfer Specimens	Approved
WF-PP-41 Revision 0	Laboratory Procedures for Determination of Corrosion Rates Under Heat-Transfer Conditions	Approved
WF-PP-42 Revision 0	Laboratory Procedure for Determination of Thermogalvanic Corrosion Rates	Approved
WF-PP-43 Revision 0	Procedure for Welding Titanium Grade-12 Plate for Use in Corrosion Studies of Overpack Materials for NRC Waste Isolation Project	Approved
WF-PP-44 Revision 0	Procedure for Welding Cast and Wrought Steel Specimens	To be Written
WF-PP-45 Revision 0	Laboratory Procedure for Preparing and Evaluating Slow Strain-Rate Specimens and for Performing Slow Strain-Rate Tests	Approved
WF-PP-45.1 Revision 0	Laboratory Procedures for Performing Slow Strain-Rate Tests Under Potentiostated Conditions	Approved
WF-PP-46 Revision 0	Procedure for Preparation of Titanium Grade-12 Corrosion Specimens with Metallic Iron Embedded in the Surface	Approved
WF-PP-47 Revision 0	Procedure for Preparing Specimens and Performing Electrochemical Pit Propogation Experiments on Carbon Steel	Approved

APPENDIX A

GLASS-CRYSTALLINITY EXPERIMENT SAMPLE PREPARATION

1. INTRODUCTION

This appendix provides details on the sample preparation and laboratory procedures used in the glass-crystallinity experiment discussed in Section 2.2. This experiment was performed to develop the data on volume fraction of crystallization and crystal size needed for evaluating the corrosion characteristics of devitrified glass.

The method of response-surface exploration can be used to develop the time, temperature, and nuclei concentrations that should lead to the required volume-fractions-crystallized and crystal sizes. This method is a statistical design that can be used to find maximum and minimum response conditions without knowledge of exact, functional relationships. For the variables to be explored, a central composite design can be used to accommodate quadratic effects in all the variables and should be adequate for the present purposes. This design is presented pictorially in Figure A.1; the corresponding coordinates are presented in Table A.1. As discussed in Section 2.2, the coordinates are based on the following initial values of the experimental variables:

Variable	Low	High
T (C)	550	850
τ (hours)	4	44
N_p (#/cc)	10^6	10^9

2. LABORATORY PROCEDURE

MCC 76-68 glass was crushed into a powder using a Wooley Beuhler crushing apparatus with crushing surfaces composed of carbon steel. The glass was crushed and sieved at 325 mesh. The coarse fraction was recycled through the Wooley Beuhler until all of the powder passed through the 325 mesh screen. Stock suspensions containing 5 g/liter each of the glass and RuO_2 powder were prepared using deionized water which had a specific conductivity of less than 1.0 micromho/cm. After equilibration for 168 hours, 100-ml aliquots of the stock suspensions were used to prepare suspensions at different pH values. Reagent-grade nitric acid (HNO_3) or potassium hydroxide (KOH) were used to adjust the suspension pH values. The pH-adjusted suspensions were allowed to equilibrate for 168 hours prior to determination of their electrophoretic mobilities.

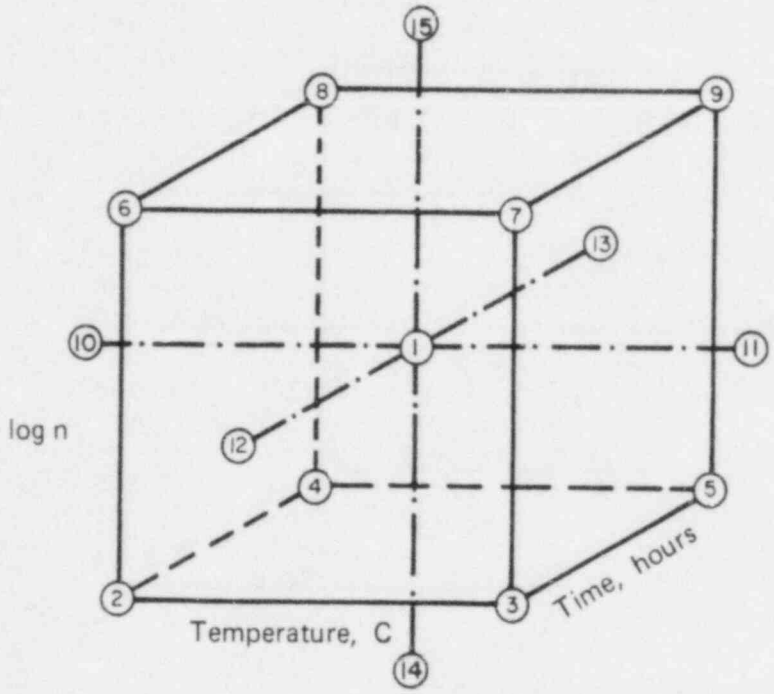

Figure A.1. Coordinates and levels of central composite design.

Table A.1. Coordinates and levels of central composite design.

Point	Coordinates	T (C)	t (hours)	log N_p
1	(0,0,0)	700	24	7.5
2	(-1,-1,-1)	610	12	6.6
3	(1,-1,-1)	790	12	6.6
4	(-1,1,-1)	610	36	6.6
5	(1,1,-1)	790	36	6.6
6	(-1,-1,1)	610	12	8.4
7	(1,-1,1)	790	12	8.4
8	(-1,1,1)	610	36	8.4
9	(1,1,1)	790	36	8.4
10	(-1.68,0,0)	550	24	7.5
11	(1.68,0,0)	850	24	7.5
12	(0,-1.68,0)	700	4	7.5
13	(0,1.68,0)	700	44	7.5
14	(0,0,-1.68)	700	24	6
15	(0,0,1.68)	700	24	9

The electrophoretic mobility (EM) and the zeta potential (ZP) of the suspended particles are needed to determine the condition that leads to maximum dispersion and mixing of the MCC 76 68 glass powder and the RuO_2 powder.

The EMs of the suspensions as a function of solution pH were determined using the horizontal cell of a Rank Brothers Mark II Particle Electrophoresis Apparatus (Rank Brothers, Cambridge, U.K.). At least 5 particles were tracked at each electrode polarization on the EM measurements. The ZP was calculated from the EM using the Smoluchowski equation:

$$ZP = \frac{4\pi\eta}{e} EM$$

where η is absolute viscosity and e is absolute permittivity of the solvent. For water at 23.5 C, the temperature at which the measurements were made, the Smoluchowski equation reduces to:

$$ZP\ (23.5\ C) = 12.57 \times EM$$

with ZP in millivolts and EM in units of microns per second per volt per centimeter. Values for viscosity and absolute permittivity are obtained from the CRC Handbook of Chemistry and Physics*. The absolute permittivity is calculated by multiplying the relative permittivity (i.e., dielectric constant) by the permittivity of vacuum.

The pH of each suspension was determined using an Orion Model 811 pH meter connected to a research-grade pH electrode and a single-junction reference electrode. Standard buffer solutions supplied by Orion were used to calibrate the pH measurements.

Particle sizes were determined using a Horiba CAPA 500 centrifugal particle-size analyzer (Horiba, Inc., Irvine, California). Its method of operation combines centrifugation with light-turbidity to measure particle-size distributions from 0.02 microns to tens of microns. Particle-size distributions of the suspensions at various solution pHs were measured in aqueous solution. The 5 g/liter powder-concentration suspensions were too concentrated to measure the turbidity with the Horiba particle-size analyzer. Therefore, the suspensions were centrifuged to decrease the particle concentration and then sonicated with a Heat Systems 1/2-inch-diameter ultrasonic horn to redisperse the particles to measurable turbidity ranges (i.e., light-absorbance values of 1.0 to 0.75).

---

*R. C. Weast, Handbook of Chemistry and Physics, 58th Edition, Chemical Rubber Company (1977-78).

The median size of the particles in suspension varied very little as a function of pH, EM, or ZP. This finding may indicate either that the sonication prior to particle size analysis breaks up weak coagules or that ZP has little effect at the particle concentrations used in these measurements. The second possibility implies that in the highly concentrated suspensions used to prepare batch mixes of glass and RuO_2, solution-pH conditions that give the maximum ZP should be used. This will ensure optimum dispersion of the suspensions to minimize homocoagulation prior to mixing of the glass and RuO_2 suspensions.

The EM and ZP data give isoelectric points equal to pH = 6.9 and pH = 5.1 for the glass and RuO_2 suspensions, respectively. This result gives a range of pH from 5.1 to 6.9 in which heterocoagulation between the glass and RuO_2 particles may take place. Thus, mixing procedures may be designed to optimize or minimize this process.

The general approach to optimizing the homogeneity of the glass and RuO_2 mixture should:

1. Minimize homocoagulation by avoiding the isoelectric points of the two powders.

2. Maximize mixing of the two powders via heterocoagulation or complete dispersion of the mixture. The latter requires that the glass and RuO_2 particles remain in suspension or settle at the same rate.

For ease of experimental procedure, melts were made from powdered glass and RuO_2 mixed according to the maximum dispersion method. The procedure requires minimum coagulation in the suspension mixture; this is achieved by mixing solutions of nearly equal pH. A RuO_2 suspension is prepared at pH 9.0 by ammonium hydroxide (NH_4OH) additions. This suspension is mixed with an equilibrium suspension of the glass at pH 9.70. The final pH of the mixture will be between pH 9.0 and pH 9.7, where both the glass and RuO_2 are negatively charged. Two dispersions, one intended to provide 10^6 particles/cm^3 and the other 10^9 particles/cm^3, were prepared.

After melting at 1150 C, the glasses were cast into bars and annealed at 450 C. Petrographic thin sections were prepared from two bars with concentrations of nucleating particles of 10^6 and 10^9 per cc. For reference, a sample of undoped MCC 76-68 was similarly prepared. Photographs of these thin sections in transmitted light at 250X are presented in Figures A.2 and A.3. The doped specimens clearly show a concentration of black particles. Since the only difference between these specimens and the undoped reference is the addition of RuO_2, those black particles must be dispersed RuO_2. The micrographs reveal that although some agglomerates remain, the RuO_2 particles, for the most part, are uniformly dispersed.

250X

a. Undoped

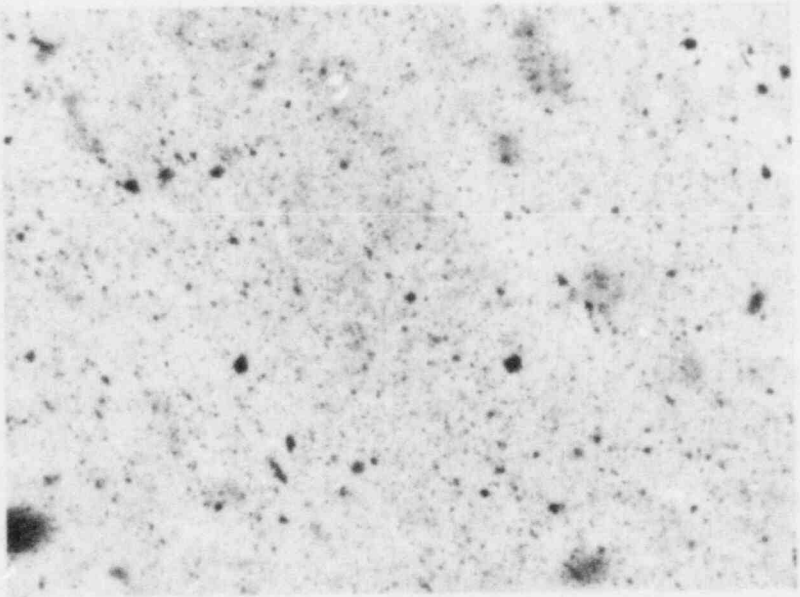

250X

b. Doped at 10^6 particles/cc

Figure A.2. Photomicrographs of thin sections of RuO_2-doped MCC 76-68.

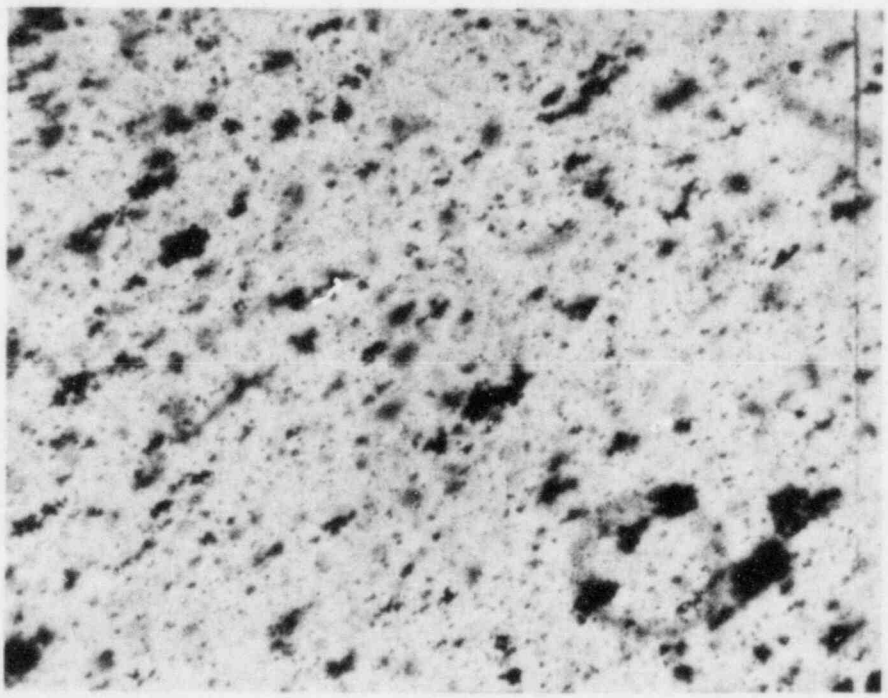

250X

Doped at 10^9 particles/cc

Figure A.3. Photomicrograph of thin section of RuO_2-doped MCC 76-68.

These results indicate that the method of preparation provides the needed uniform dispersion of RuO_2 particles in the glass. Stock suspension A, with RuO_2 concentration of 50 µg/ml, and stock suspension B, with RuO_2 concentration of 2.5 mg/ml, were each adjusted to a pH of 9. These suspensions were then used to prepare all glass samples according to Table A.2.

Table A.2. Additions of RuO_2 suspensions.

log N_p	Design Coordinate[a]	Stock Suspension Used	Amount Added[b] (ml)
6	-1.68	A	5
6.6	-1	A	20
7.5	0	B	3.2
8.4	1	B	25
9.0	1.68	B	100

(a)"Z" coordinate in Table A.1.
(b)Added to 100 g MCC 76-68 glass powder in 300 ml of water.

The listed volumes of RuO_2 suspensions A or B were added to 100 g of MCC 76-68 glass powder that had been equilibrated in pure water for at least three days. The RuO_2 suspension was added to the glass suspension in an Osterizer laboratory blender, after which the liquid was quickly poured into a clean plastic beaker and dried at 120 C. These blended powders were melted in preheated fireclay crucibles at 1200 C for two hours in an electrically heated furnace. Bars approximately 1 cm x 1 cm x 10 cm were cast into heated graphite molds and annealed for 1-1/2 hours at 450 C, followed by cooling at furnace rate to room temperature. Specimens approximately 6 mm thick were cut from the bars and heated according to the conditions set forth in Table A.1. For comparative purposes, a specimen of MCC 76-68 glass that did not contain RuO_2 additions was included at each time/temperature condition. After treatment, the air-quenched samples were mounted in epoxy, polished, and subjected to analysis by reflected-light microscopy.

3. Experimental Results

Reflected-light microscopy of the specimens revealed that the experimental parameters presented in Figure A.1 and Table A.1 did induce crystal growth in the glass. Typical examples of the resultant morphologies are presented in Figure A.4. The micrographs of treated specimens represent the body diagonal from (-1,-1,-1) through (0,0,0) to (1,1,1) in Figure A.1. These conditions are "least severe", "moderate", and "most severe" in temperature, time, and concentration of heterogeneous nuclei. For comparative purposes, the reference, or undoped, MCC 76-68 sample corresponding to the (1,1,1) coordinate is also presented in Figure A.4. The sample is very similar to a completely untreated, or as-received, MCC 76-68 glass sample. The large crystals are typical of those present in MCC 76-68 and are not randomly distributed in the glass. In contrast, the crystals in the heated specimens are different in morphology from those of the reference specimen, and those treated under the "most severe" condition are distinctly different from the other treated samples.

All the treated and reference specimens were examined by quantitative microscopy using a Cambridge, Model Q10, image analyzer. The data presented in Table A.3 are a summary of these analyses for the treated specimens. A similar summary for the reference specimens is presented in Table A.4. The data in Table A.4 indicate that without the addition of RuO_2, variations in treatment time and temperature produce no significant variation in mean particle size or mean volume fraction. In fact, the observed confidence band for mean particle size overlaps that for untreated MCC 76-68, while the observed confidence band for mean volume fraction nearly includes the mean value for untreated MCC 76-68. Therefore, without the RuO_2 addition, the treatment time and temperature have very little effect on crystallinity changes. In contrast, the data in Table A.3 indicate that with the addition of RuO_2, both the volume fraction crystallized and the particle diameter are changed by the experimental conditions.

4. Statistical Analysis

An assessment of the effects of temperature, T, heating time, t, and the logarithm of the number of nucleating sites, $\log(N_p)$, on each of two dependent variables was explored through regression analysis. The dependent variables are the average volume fraction crystalized (V_c) and the average diameter of the crystals formed during the experiment. Preliminary regression analyses indicated that none of the parameters T, t, or $\log(N_p)$, or their squared terms or interactions were significant as predictors of mean particle diameter. Consequently, no analysis results are reported for this dependent variable.

Several statistical models were evaluated for V_c. Plots of the residuals from preliminary analyses indicate that the variance of V_c increases as the magnitude of V_c increases. Therefore, one analysis

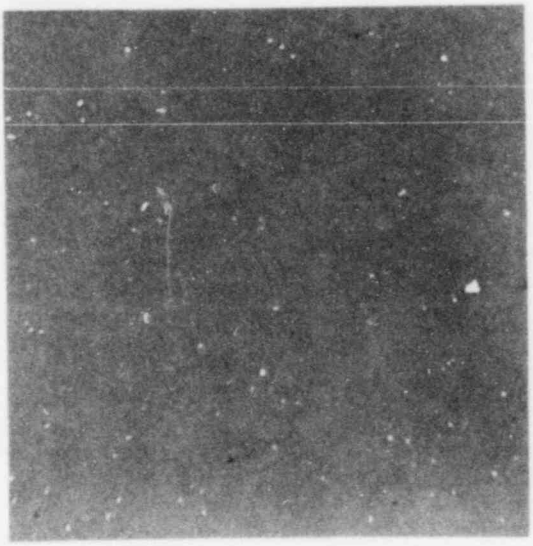

(-1, -1, -1)
(610C, 12h, 6.6)

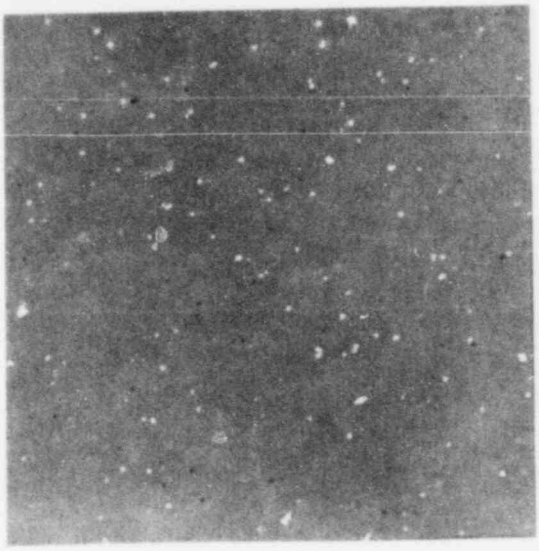

(0, 0, 0)
(700C, 24h, 7.5)

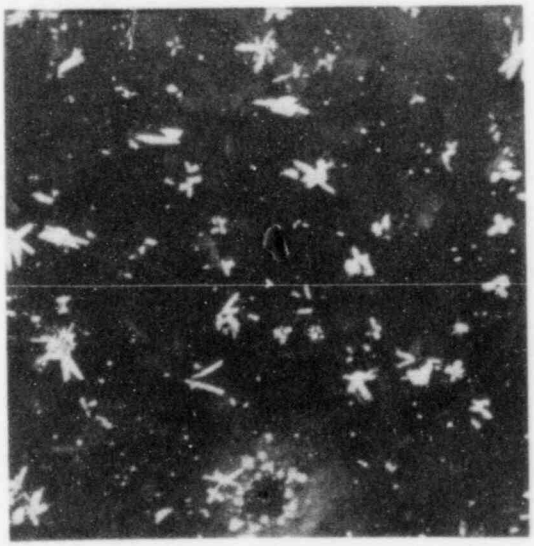

(1, 1, 1)
(790C, 36h, 8.4)

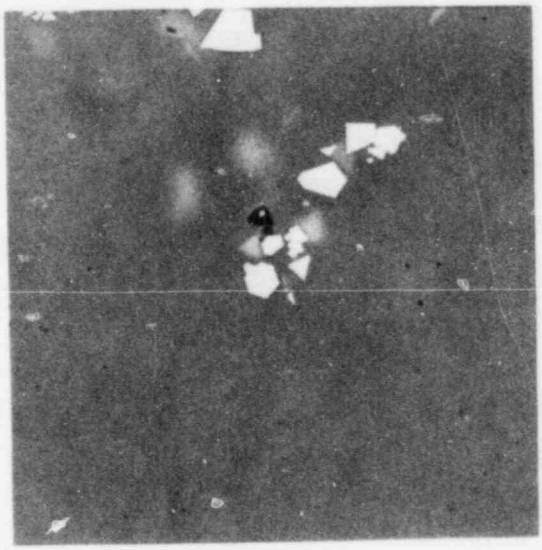

MCC 76-68
(790C, 36h)

Figure A.4. Typical reflection micrographs from crystallinity experiment (500X).

Table A.3. Quantitative microscopy results for treated MCC 76-68 glass (800X).

Coordinates[a]	Temp, C	t, hours	log(N_p)	V_c, %[b]	n[c]	$\bar{d}$, μm[d]
(0,0,0)	700	24	7.5	0.83	768	0.98
(-1,-1,-1)	610	12	6.6	0.66	572	1.15
(1,-1,-1)	790	12	6.6	0.88	729	0.91
(-1,1,-1)	610	36	6.6	0.49	317	1.22
(1,1,-1)	790	36	6.6	0.95	933	0.80
(-1,-1,1)	610	12	8.4	0.29	387	0.69
(1,-1,1)	790	12	8.4	4.34	3201	1.96
(-1,1,1)	610	36	8.4	0.28	336	0.96
(1,1,1)	790	36	8.4	7.40	2373	2.79
(-1.68,0,0)	550	24	7.5	0.31	430	0.69
(1.68,0,0)	850	24	7.5	0.93	709	0.74
(0,-1.68,0)	700	4	7.5	4.48	447	3.97
(0,1.68,0)	700	44	7.5	0.75	760	0.86
(0,0,-1.68)	700	24	6	0.35	578	1.38
(0,0,1.68)	700	24	9	5.83	2058	2.36

(a)From Figure A.1 and Table A.1.

(b)Average of 10 random fields taken in each sample.

(c)Total number of particles observed in 10 fields.

(d)Mean particle diameter.

Table A.4. Quantitative microscopy results for reference samples.

Condition[a]	Temp, C	t, hours	V_C, %[b]	n[c]	$\bar{d}$, μm[d]
1	610	12	5.40	419	2.13
2	610	36	4.69	401	1.45
3	700	24	4.84	593	1.51
4	790	12	4.06	822	0.89
5	790	36	5.45	895	0.98
6	790	44	4.99	429	1.99
mean value	-	-	4.91	-	1.49
95% confidence band	-	-	±0.42	-	±0.10
MCC 76-68	(e)	(e)	5.54	373	1.97
95% confidence band	-	-	(f)	-	±0.36

(a)MCC 76-68 without RuO_2.

(b)Selected fields containing crystals.

(c)Total number of particles counted.

(d)Mean particle diameter in each field.

(e)As-received sample; no exposure to any experimental conditions.

(f)Insufficient data.

variation was to apply a logarithmic transformation, $\log(V_c)$, to V_c for the purpose of stabilizing its variance. The results of the statistical models investigated may be summarized by the output from a stepwise regression of both V_c and $\log(V_c)$ using a full second-order model that includes linear, squared, and interaction terms for T, t, and $\log(N_p)$. All terms were included in the original models and individual terms were eliminated systematically until all terms remaining in the models were statistically significant ($P < 0.10$). The stepwise regression models produced for volume fraction crystallized are

$$V_c = 1.92 + 0.94\ T + 1.36\ \log(N_p) + 1.31\ [T\ \log(N_p)]$$

$$\log(V_c) = 0.14 + 0.28\ T - 0.15\ T^2 + 0.22\ \log(N_p) + 0.27\ [T\ \log(N_p)] \quad .$$

All coefficients in these models are significant ($P < 0.10$) as predictors of V_c and $\log V_c$. Table A.5 presents exact significant probabilities for all tests of the individual regression coefficients. The T-test indicates whether including a given term adds any important information to the model. The T-test statistic leads to the significance probability, expressed as a percentage in Table A.5; a significance probability of less than 5 percent indicates a significant relationship between the dependent and independent variables. The adjusted R^2 values reported in Table A.5 can be interpreted as the proportion of total variability explained by the model, adjusted for the number of degrees of freedom associated with the model.

For the purposes of the statistical analysis, T = (actual temperature - 700 C)/90 and $\log (N_p)$ = (actual log of number of nucleating sites - 7.5)/0.9. These values for T and $\log (N_p)$ apply to the values shown in Table A.5 and those indicated in the above regression equations.

In conclusion, the experiment failed to yield any empirical information about the relationship of mean particle diameter to any of the other variables. This result implies that most temperatures were too low to permit significant crystal growth rates. However, the temperature and logarithm of the number of nucleating sites are directly related to the average volume fraction of crystals produced. Due to the small number of experimental conditions for which large values of V_c were produced, selection of either the model for V_c or the model for $\log (V_c)$ as the better model for volume fraction crystallized must be based on a priori knowledge of the crystallization process.

5. CRYSTALLIZATION PATH

Fracture surface specimens of conditions (-1,-1,-1), (0,0,0), and (1,1,1) were prepared. Each was etched in 1-percent HF solution for 30 seconds to create relief between the crystals and the glass matrix. These samples and a similarly prepared sample of MCC 76-68 glass were

Table A.5. Regression coefficients with their corresponding T-tests and significance probabilities resulting from a stepwise regression of V_C and $\log(V_C)$ on full second-order models.

Dependent Variable: V_C		Adjusted R^2 = .5698	
Variable[a,b] Name	Regression Coefficient	T-Test Statistic	Significance Probability
Intercept	1.91846	-	-
T	0.94579	2.26	4.49%
log (N_p)	1.35868	3.25	0.77%
(T) log (N_p)	1.31333	2.40	3.49%

Dependent Variable: $\log(V_C)$		Adjusted R^2 = .6853	
Variable[a,b] Name	Regression Coefficient	T-Test Statistic	Significance Probability
Intercept	0.1411	-	-
T	0.2804	3.68	0.42%
T^2	-0.1512	1.82	9.83%
log (N_p)	0.2219	2.91	1.55%
(T) log (N_p)	0.2747	2.76	2.01%

(a) T = (Actual Temperature - 700 C)/90.

(b) $\log(N_p)$ = (Actual log of the number of nucleating sites - 7.5)/0.9.

subjected to scanning electron microscopy (SEM) and energy-dispersive X-ray analysis (EDX) in an attempt to define the crystal phases produced by the experimental variables. Representative micrographs and the corresponding EDX spectra are presented in Figures A.5 through A.9. As can be observed in these figures, the morphology and composition of the crystalline phases are changed markedly by the experimental conditions. Crystals phases enriched in zinc, iron, titanium, and lanthanum are produced. However, the data gathered to date are insufficient to permit speculation about the course of crystallization. Nevertheless, comparison of these data to similar spectra for MCC 76-68 presented in Figure A.10 imply a marked difference between "native" and heterogeneously nucleated crystals, while the bulk glasses, as shown in Figure A.11, are identical. These data indicate that more work in this area is warranted.

6. CONCLUSIONS

The inclusion of heterogeneous nuclei in MCC 76-68 glass heat-treated at temperatures and times comparable to those present during waste-form cooling can significantly change the volume fraction of crystals. The ranges of temperature and time explored to date indicate that 5 percent, by volume, of a crystalline phase can be easily produced. The lack of a statistically significant time variable likely results from slow growth in the temperature regime explored in this experiment. However, initial data indicate that changes in crystal morphology and composition are brought about by heterogeneous nucleation onto RuO_2 particles.

The ranges of temperature, time, and RuO_2 concentration that have been explored have not yielded data that can be used to generate specimens with V_c in excess of 5 percent or with two distinctly different crystal sizes. However, a preliminary empirical equation describing crystallization has been developed. Therefore, to improve this equation and, as a result, to produce the specimens needed for leaching/corrosion experiments, this effort should continue.

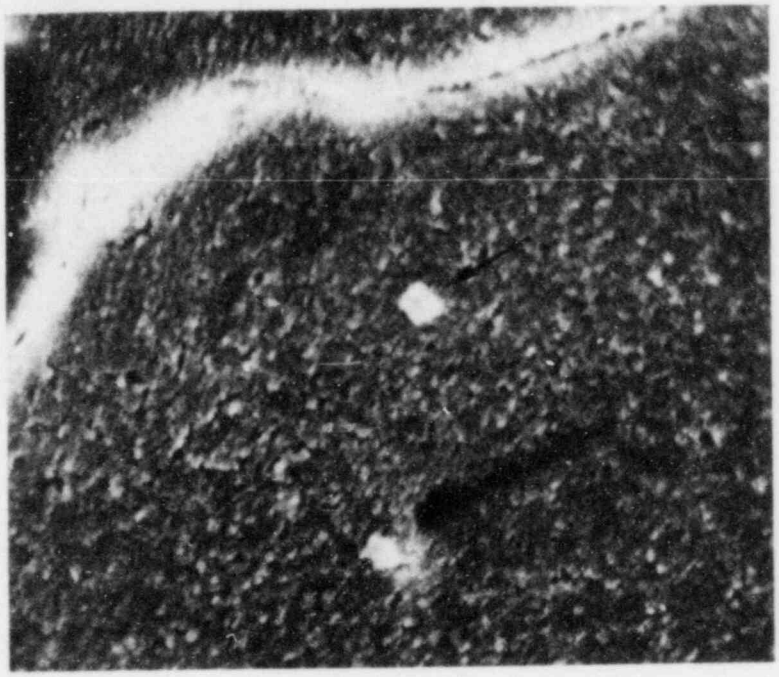

a. SEM 3000X

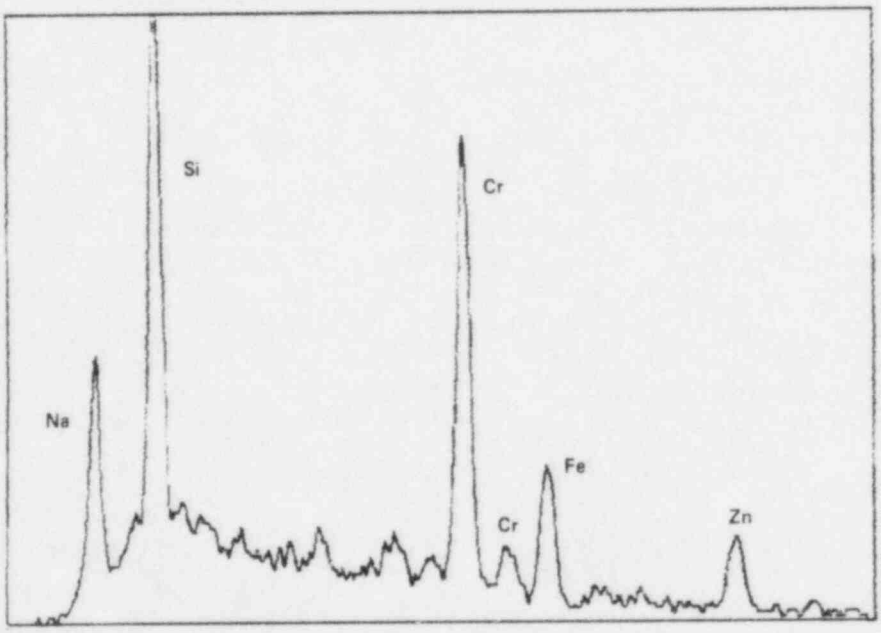

b. EDX spectrum

Figure A.5. SEM micrograph and EDX spectrum for condition (-1,-1,-1)

a. SEM 3000X

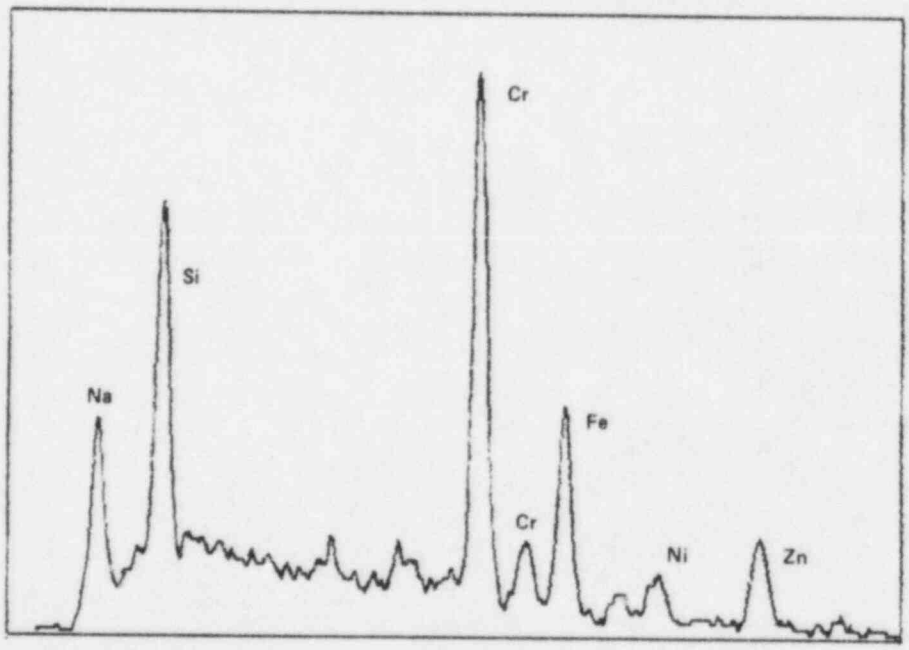

b. EDX spectrum

Figure A.6. SEM micrograph and EDX spectrum for condition (0,0,0).

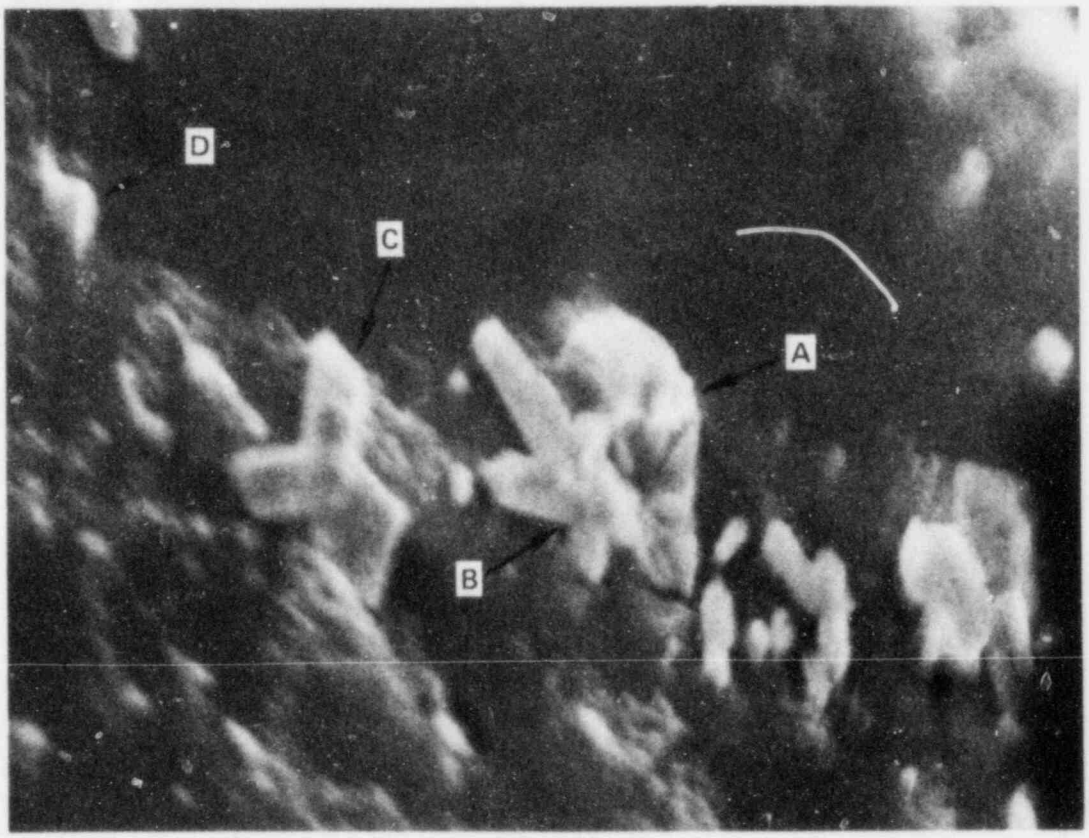

SEM 4000X

Figure A.7. SEM micrograph showing crystalline morphologies A to D for condition (1,1,1).

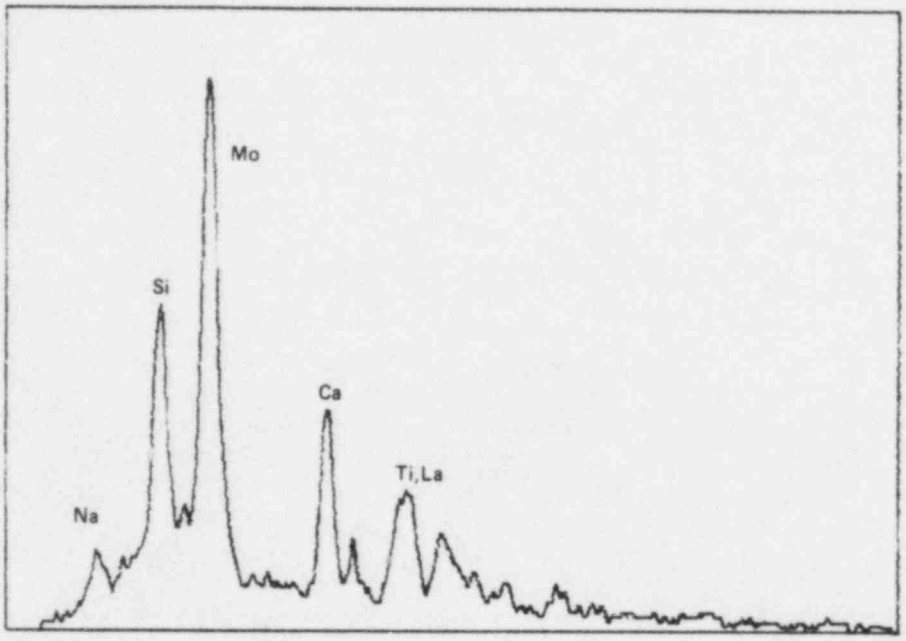

a. Morphology A

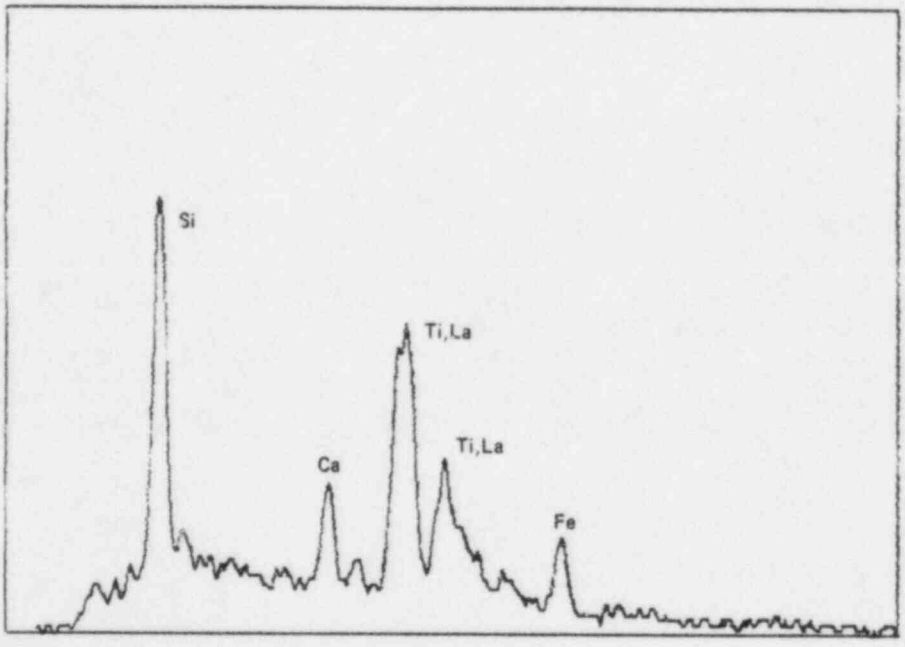

b. Morphology B

Figure A.8. EDX spectra for crystalline morphologies A and B in Figure A.7.

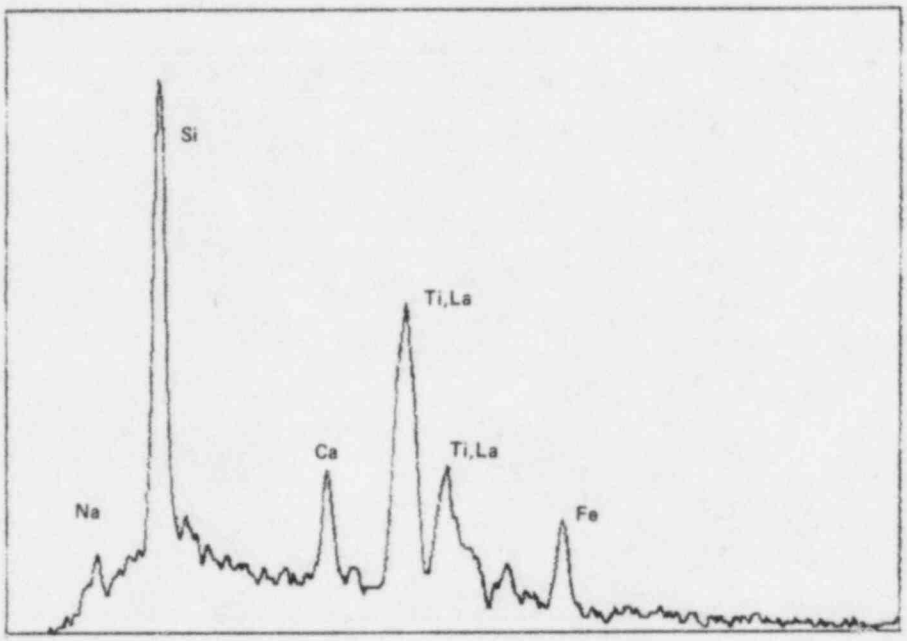

a. Morphology C

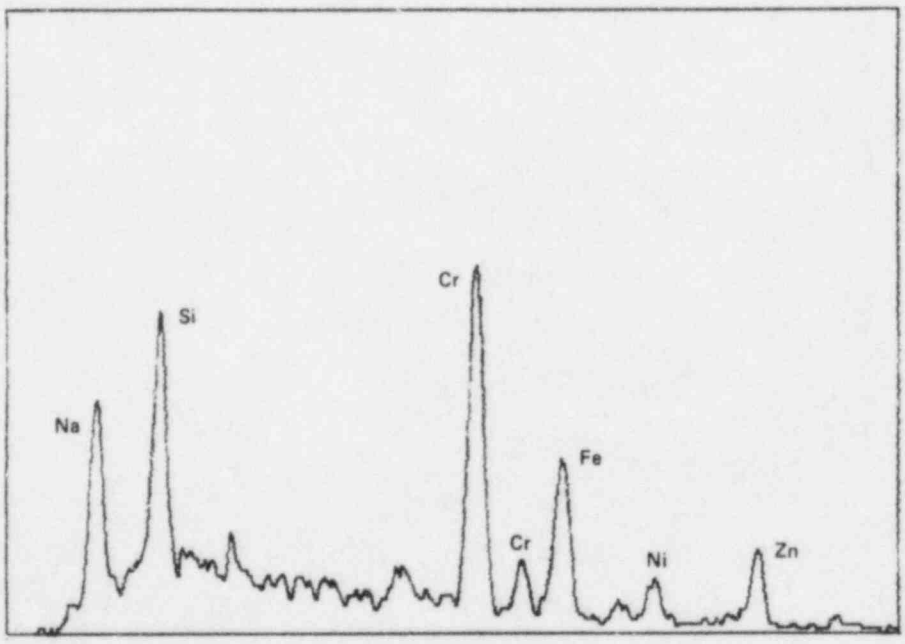

b. Morphology D

Figure A.9. EDX spectra for crystalline morphologies C and D in Figure A.7.

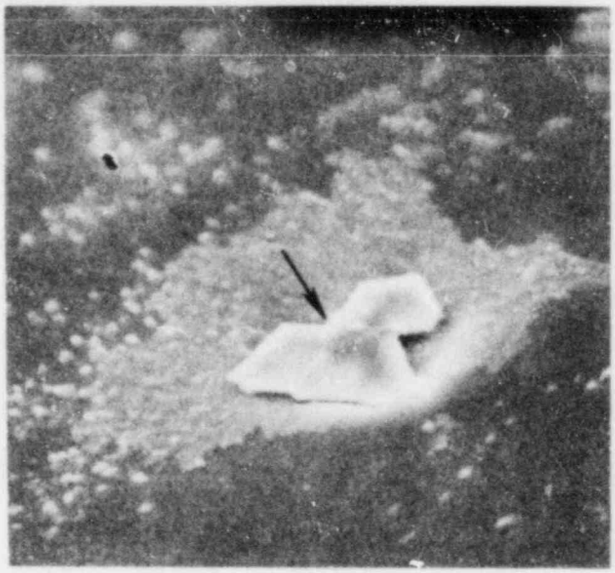

a. SEM 3000X

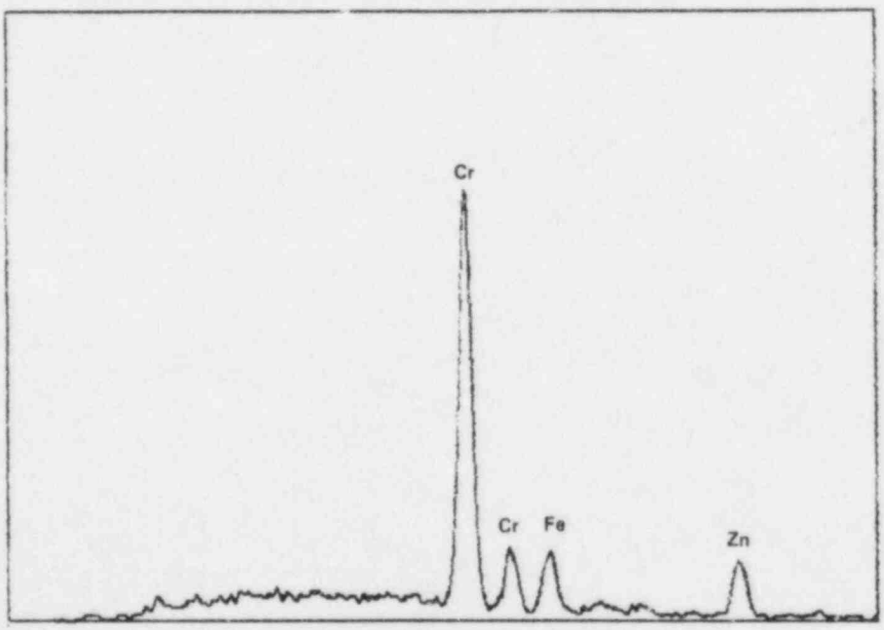

b. EDX spectrum

Figure A.10. SEM micrograph and EDX spectrum for "native" crystal in MCC 76-68.

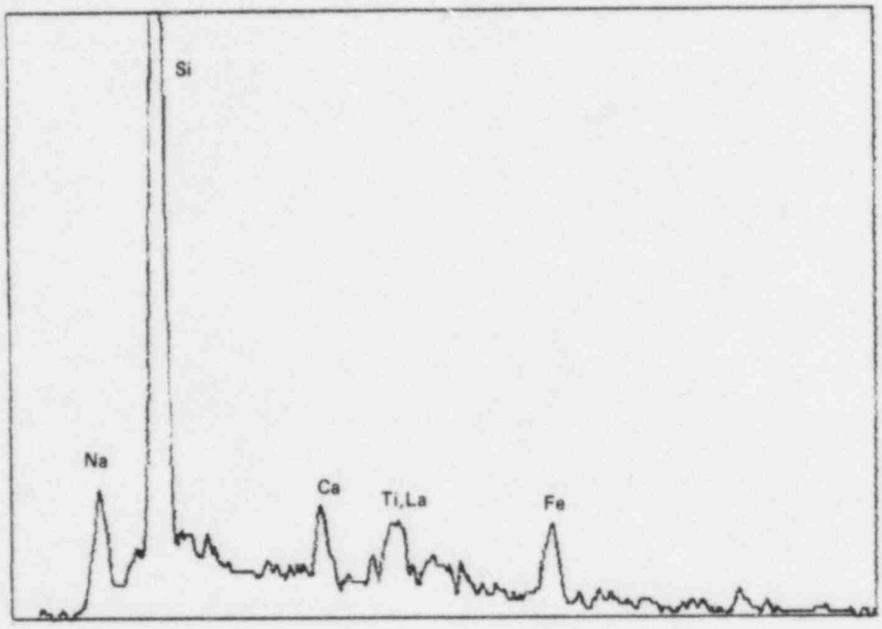

a. MCC 76-68

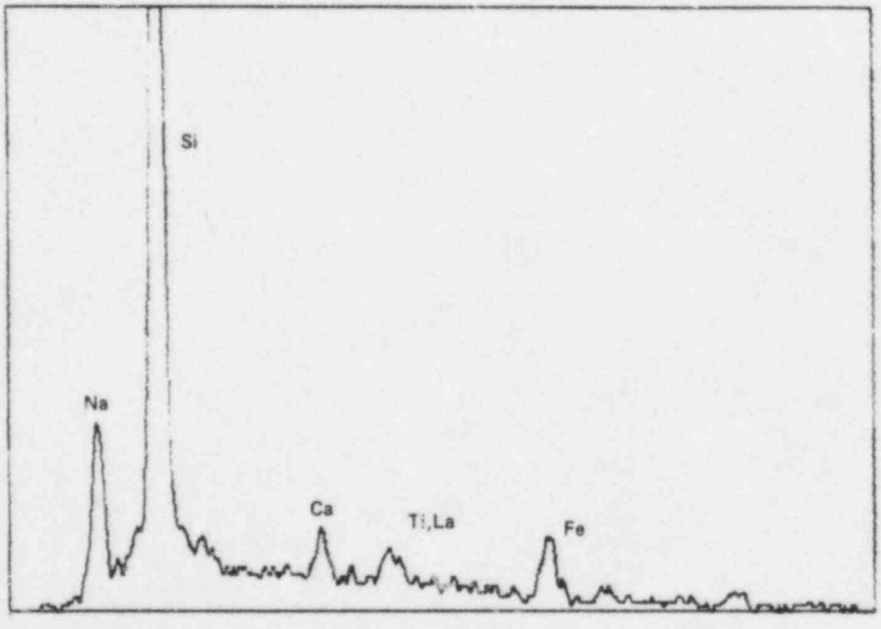

b. (1,1,1): 790 C, 36 hrs, $\log(N_p) = 8.4$

Figure A.11. EDX spectra for bulk glass in untreated MCC 76-68 and specimen treated at (1,1,1) condition.

DISTRIBUTION LIST

Office of Regulatory Research
Division of Radiation Programs and Earth Sciences
Mail Stop 1130 SS
U.S. Nuclear Regulatory Commission, Washington, D.C. 20555

Attn: Division Director/Deputy Director
E. F. Conti, Chief, Waste Management Branch
F. A. Costanzi
J. R. Randall
M. B. McNeil
K. S. Kim, Project Manager (15)

Division of Waste Management, NMSS
Mail Stop 623 SS
U.S. Nuclear Regulatory Commission, Washington, D.C. 20555

Attn: Division Director/Deputy Director
Chief, Engineering Branch
E. A. Wick
M. Tokar
K. C. Chang
Document Control Center

Division of Waste Management, NMSS
U.S. Nuclear Regulatory Commission
1955 Jadwin Ave - Suite 310A
Richland, WA 99352

Attn: R. Cook, BWIP Site Rep.

Advisory Committee on Reactor Safeguards
Mail Stop H-1016
U.S. Nuclear Regulatory Commission, Washington, D.C. 20555

Attn: Waste Management Subcommittee
R. C. Tang

Battelle's Columbus Laboratories
505 King Avenue
Columbus, Ohio 43201-2693

Attn: D. Stahl, Program Manager (50)

DISTRIBUTION LIST (Continued)

Martin J. Steindler
Argonne National Lab.
Argonne, IL 60439

Donald G. Schweitzer
Brookhaven National Lab.
Upton, NY 11973

Peter Soo
Brookhaven National Lab.
Upton, NY 11973

David Martin
Iowa State University
Ames, IA 50011

Harold Wollenberg
Lawrence Berkeley Lab.
Berkeley, CA 94720

Nestor Ortiz
Sandia National Lab.
Albuquerque, NM 87185

Pedro B. Macedo
Catholic University of America
Washington, D.C. 20064

Robert Williams
Electric Power Research Institute
P.O. Box 10412
Palo Alto, CA 94301

William P. Reed
U.S. Department of Commerce
National Bureau of Standards
Washington, D.C. 20234

Ray Walton
U.S. Department of Energy
Washington, D.C. 20545

John E. Mendel
Materials Characterization Center
Pacific Northwest Lab.
Richland, WA 99352

Larry Hench
University of Florida
Gainesville, FL 32611

David E. Clark
University of Florida
Gainesville, FL 32611

Joseph Mascara
MS 5650 NL
U.S. Nuclear Reg. Comm.
Washington, DC 20555

Ken W. Stephens
The Aerospace Corp., Suite 400
955 L'Enfant Plaza, S.W.
Washington, DC 20024

Robert S. Dyer
Office of Radiation Programs (ANR-461)
U.S. Environmental Protection Agency
401 M Street, S.W.
Washington, DC 20460

Lorenzo Ricks
Office of Energy Research
U.S. Department of Energy
Washington, D.C. 20545

Larry Evans
Armco Research Center
703 Curtis Avenue
Middletown, OH 45043

Woody Swope
Armco Stainless Steel Division
P.O. Box 1697
Baltimore, MD 21203

M. John Plodinec
Savannah River Laboratory
Aiken, SC 29808

Dennis R. Floyd
Manufacturing Sciences Corp.
711 Walnut Street
Boulder, CO 80302

DISTRIBUTION LIST (Continued)

Martin A. Molecke
Sandia National Lab.
Albuquerque, NM 87185

Neville Pugh
National Bureau of Standards
Washington, D.C. 20234

Nicholas Grant
Department of Metallurgy
Massachusetts Institute
of Technology
Cambridge, MA 02139

Jerome Kruger
Corrosion Section
National Bureau of Standards
Washington, D.C. 20234

Don J. Bradley
Waste Package Programs
Battelle Pacific Northwest Labs
Richland, WA 99352

Allen G. Croff
Oak Ridge National Laboratory
P.O. Box X
Oak Ridge, TN 37830

Lynn Hobbs
Department of Materials Science
Massachusetts Institute of
Technology
77 Massachusetts Avenue
Cambridge, MA 02139

Richard E. Westerman
Pacific Northwest Lab.
P.O. Box 999
Richland, WA 99352

Thomas D. Chikalla
Pacific Northwest Lab.
P.O. Box 999
Richland, WA 99352

John Crandall
Savannah River Lab.
Aiken, SC 29808

Edward J. Hennelly
Savannah River Lab.
Aiken, SC 29808

Arthur A. Bauer
Office of Crystalline Rock Development
Battelle Memorial Institute
505 King Avenue
Columbus, OH 43201

Michael Smith
Basalt Waste Isolation Projects
Rockwell Hanford Operation
Richland, WA 99352

Kenneth Russell
Department of Materials Science
and Engineering
Massachusetts Institute of
Technology
Cambridge, MA 02139

Robert H. Doremus
Materials Engineering Department
Rensselaer Polytechnic Institute
Troy, NY 12181

David C. Kocher
Oak Ridge National Lab.
P.O. Box X
Oak Ridge, TN 37830

Stanley Wolf
DOE/BES
Washington, D.C. 20585

Neville Moody
Sandia Livermore Lab.
Livermore, CA 94550

Donald E. Clark
ONWI
Battelle Memorial Institute
505 King Avenue
Columbus, OH 43201

Martin Seitz
Argonne National Lab.
Argonne, IL 60439

*U.S. GOVERNMENT PRINTING OFFICE: 1985-461-721:20245

NRC FORM 335 (11.81)

U.S. NUCLEAR REGULATORY COMMISSION

BIBLIOGRAPHIC DATA SHEET

1. REPORT NUMBER (Assigned by DDC)
NUREG/CR-3900, Vol. 4
BMI-2127

4. TITLE AND SUBTITLE (Add Volume No., if appropriate)
Long-Term Performance of Materials Used for High-Level Waste Packaging
Annual Report - April 1984-April 1985

2. (Leave blank)

3. RECIPIENT'S ACCESSION NO.

7. AUTHOR(S)
Compiled by D. Stahl and N. E. Miller

5. DATE REPORT COMPLETED
MONTH June YEAR 1985

9. PERFORMING ORGANIZATION NAME AND MAILING ADDRESS (Include Zip Code)
Battelle's Columbus Laboratories
505 King Avenue
Columbus, Ohio 43201-2693

DATE REPORT ISSUED
MONTH July YEAR 1985

6. (Leave blank)

8. (Leave blank)

12. SPONSORING ORGANIZATION NAME AND MAILING ADDRESS (Include Zip Code)
Division of Radiation Programs and Earth Sciences
Office of Nuclear Regulatory Research
U.S. Nuclear Regulatory Commission
Washington, DC 20555

10. PROJECT/TASK/WORK UNIT NO.

11. FIN NO.
B6764

13. TYPE OF REPORT
Annual

PERIOD COVERED (Inclusive dates)
April 1984 - April 1985

15. SUPPLEMENTARY NOTES

14. (Leave blank)

16. ABSTRACT (200 words or less)

Waste form experimentation has focused on borosilicate glass, using the reference composition MCC 76-68. An experiment investigated the influence of continuous contact between the glass specimen and the leachate on the results of corrosion studies. It was found that precipitates formed during cooling can affect the results. Other experiments evaluated the influence of crystallization on glass waste-form performance and the influence of organic acid on the waste-form and radionuclide mobility in groundwater. Models were used to analyze glass dissolution, including the reprecipitation of dissolved glass species. The effect of groundwater species on the electrochemistry of steels is being analyzed to evaluate susceptability to pitting and stress-corrosion cracking. Species identified as potential cracking agents are being investigated by slow strain rate experiments. Hydrogen embrittlement studies of steel showed annealed cast steel to be more sensitive to embrittlement. Realistic general and pitting corrosion models are being developed, based on known principles of mass transport and radiolytic production. Mechanical and water-chemistry-related stresses which influence mechanical degradation were evaluated. Groundwater-radiolysis and water-chemistry studies are continuing as part of the integrated system performance task.

17. KEY WORDS AND DOCUMENT ANALYSIS

17a. DESCRIPTORS

High-level waste
Waste package
Waste form/container/overpack

17b. IDENTIFIERS/OPEN-ENDED TERMS

18. AVAILABILITY STATEMENT
Unlimited

19. SECURITY CLASS (This report)
Unclassified

21. NO. OF PAGES

20. SECURITY CLASS (This page)
Unclassified

22. PRICE
$

NRC FORM 335 (11.81)

UNITED STATES
NUCLEAR REGULATORY COMMISSION
WASHINGTON, D.C. 20555